Vibration and Aeroelasticity of Advanced Aircraft Wings Modeled as Thin-Walled Beams
–Dynamics, Stability and Control

Zhanming Qin

Dissertation submitted to the Faculty of the
Virginia Polytechnic Institute and State University
in partial fulfillment of the requirements for the degree of

Doctor of Philosophy
in
Engineering Mechanics

Prof. Romesh C. Batra
Prof. David Gao
Prof. Daniel J. Inman
Prof. Liviu Librescu, Chair
Prof. Surot Thangjitham

October 2, 2001
Blacksburg, Virginia

Keywords: Aeroelasticity, Thin-Walled beam, Dynamics, Aeroelastic intabilities, Passive/ActiveControl

Vibration and Aeroelasticity of Advanced Aircraft Wings Modeled as Thin-Walled Beams

–Dynamics, Stability and Control

Zhanming Qin

(ABSTRACT)

Based on a refined analytical anisotropic thin-walled beam model, aeroelastic instability, dynamic aeroelastic response, active/passive aeroelastic control of advanced aircraft wings modeled as thin-walled beams are systematically addressed. The refined thin-walled beam model is based on an existing framework of the thin-walled beam model and a couple of non-classical effects that are usually also important are incorporated and the model herein developed is validated against the available experimental, Finite Element Anaylsis (FEA), Dynamic Finite Element (DFE), and other analytical predictions. The concept of indicial functions is used to develop unsteady aerodynamic model, which broadly encompasses the cases of incompressible, compressible subsonic, compressible supersonic and hypersonic flows. State-space conversion of the indicial function based unsteady aerodynamic model is also developed. Based on the piezoelectric material technology, a worst case control strategy based on the minimax theory towards the control of aeroelastic systems is further developed. Shunt damping within the aeroelastic tailoring environment is also investigated.

The major part of this dissertation is organized in the form of self-contained chapters, each of which corresponds to a paper that has been or will be submitted to a journal for publication. In order to fullfil the requirement of having a continuous presentation of the topics, each chapter starts with the purely structural models and is gradually integrated with the involved interactive field disciplines.

Dedication

To my parents, for their love, support and great expectation

Acknowledgements

First of all, I wish to thank my advisor, Professor Liviu Librescu, for his resourceful help, constant encouragement, unabating enthusiasm and great expectation. Without his great patience, this work would never have been finished. It is by the inspiring discussions and close interactions with him that my hope was reinvigorated once again and that I learned how to steadfastly move to the next step.

I also wish to thank all my committee members: Professors Romesh C. Batra, David Y. Gao, Daniel J. Inman and Surot Thangjitham for their help, patience and for devoting time from their busy schedule to serving on my committee.

Many thanks are expressed to Professors Leonard Meirovitch and Dean T. Mook in the Department of Engineering Science and Mechanics, Jan N. Lee and Layne Watson in the Department of Computer Science for their crystally clear lectures on the master level.

I would like to express my most profound thanks and gratitude to my parents for their sustaining love, dedication and support at all their possible levels.

High appreciations are also expressed to my brothers, sisters and sister-in-laws, for their constant encouragement and help during the past years.

Special thanks are expressed to Tongze Li, Johnny Yu, for their invaluable suggestions at my critical time. I also gratefully recognize the following friends for their help: Jianxin Zhao, Lizeng Sheng and Wei Peng and Caisy Ho.

During the rocky road of the past five years, I would like to express my warmest thanks to Professor Henneke, the head of the Department of Engineering Science and Mechanics, for his patience and generosity to manage to provide financial support for me. I also wish to express my gratitude to Mrs. Tickle Loretta, the graduate secretary of the Department of Engineering Science and Mechanics, and Professor Glenn Kraige in the Department of Engineering Science and Mechanics, for their help and constructive advice.

When staying at the Computer Lab of the Department of Engineering Science and Mechanics, I was deeply impressed by the readiness for help from Tim Tomlin, the system manager of the Computer Lab.

Many thanks are expressed towards my dear friends Peirgiovanni Marzocca and Axinte

Ionita, for their friendship and help.

Finally, I wish to express my gratitude to God, for His mercy and grace, to provide me such a benign environment to let me grow.

Contents

List of Figures

List of Tables

Nomenclature

$(\dot{X}, \ddot{X})$	$(\partial X/\partial t, \partial^2 X/\partial^2 t)$
$(\dot{\hat{X}},\ \ddot{\hat{X}})$	defined as $(\partial \hat{X}/\partial \tau,\ \partial^2 \hat{X}/\partial \tau^2)$
$(\hat{X}',\ \hat{X}'')$	$(\partial \hat{X}/\partial \eta,\ \partial^2 \hat{X}/\partial \eta^2)$
$(\Omega,\ F,\ H)$	(ohms, farad, henrys); unit of resistance, capacity, and inductance, respectively
$(\triangleq,\ \equiv)$	abbreviation or definition of notations
(s, z, n)	local coordinates for the cross section
(X', X'')	$(\partial X/\partial y,\ \partial^2 X/\partial y^2)$
$[\theta_{n1}/\theta_{n2}]_{n3}$	lay-up scheme of the wing walls
$A\!\!\!R,\ \eta$	wing aspect ratio and the non-dimensional spanwise coordinate, $L/b,\ \eta = y/L$
$\bar{C}_{ij}$	transformed elastic modulus in the beam local coordinate system
$\bar{M}_x,\ \bar{M}_y,\ \bar{M}_z$	external stress couples on the beam tip (Eq. 1.15)
$\bar{Q}_x,\ \bar{Q}_z$	applied transverse shear forces at the beam tip
$\bar{T}_y$	applied beam axial force at the beam tip
Δb_p	width of the piezoceramic patch
Δh_p	thickness of the piezoceramic patch
δ	operator of variation
ϵ_{ij}^S	electric permittivity coefficient of piezoelectric material
$\eta,\ \Lambda$	non-dimensional spanwise coordinate($\eta \equiv y/L$) and sweep angle
$\gamma_{sy}^0;\ \gamma$	contour-wise shear strain; damping ratio

γ_{yz}, γ_{yx}	transverse shear measures of the cross section
$\hat{I}_c$	electric current across the electrode
$\hat{I}_t$, $\hat{I}_w$, $\hat{r}$	non-dimensional parameters related to the torsion, warping and rotatory inertia of the cross-section, respectively (see Appendix B)
$\hat{P}_m$	non-dimensional peak reflected pressure of the blast, $bP_m/(2b_1U_n^2)$
$\hat{P}_{electric}$	rate of work done by the electric field within the piezoceramic patch, $\hat{V}_c \cdot \hat{I}_c$
$\hat{P}_{resistor}$	rate of electric energy dissipated by the resistor, $\hat{V}_c^2/R_c$
$\hat{V}$	applied voltage on the piezoceramic patch
$\hat{V}_c$	voltage induced on the piezo. patch
Λ_g, Λ_e	geometric and effective sweep angle, respectively, $\tan\Lambda_e = \tan\Lambda_g/\sqrt{1 - M_{flight}^2}$
$\lambda_m(\mathcal{P})$	operator, returning the maximum eigenvalue of matrix $\mathcal{P}$
$\mathbf{G}_c$	control gain matrix
$\mathcal{L}$, $\mathcal{L}^{-1}$	Laplace and inverse Laplace transform operator, respectively
μ	Lagrangian multiplier in Eq. 4.39a
μ_0, μ_1	non-dimensional parameters in Appendix B
∇	gradient operator
$\oint_c$	integral along the contour
ω_i	natural frequency of i*th* mode
ω_{hr}	$(\sqrt{a_{33}/(b_1L^4)})_{\theta=\pi/2}$
ϕ_W, ψ_K	Wagner and Küssner's function, respectively
ψ	torsional function
ρ_∞	mass density of the free stream
$\rho_{(k)}$	mass density of the k*th* layer
σ_{ij}, ε_{ij}	stress, strain components
τ	non-dimensional time, U_nt/b
τ_p	non-dimensional gust gradient or phase duration of blast

θ	ply angle
ε_{yy}^{0}, ε_{yy}^{n}	on and off-contour axial normal strains, respectively
$a(s)$	geometric quantity
a_{ij}	1-D stiffness coefficients (Eq. 1.19)
A_{ij}, B_{ij}	stretching, bending-stretching coupling coefficient, respectively
b, d, L	normal semi-width and semi-depth of the beam cross section and semi-span length, respectively
b_1	mass density of the wing per unit span, including contribution from piezo patches
B_w	bimoment (in Eq. 1.18)
b_w	bimoment of the external force per unit span
B_{ij}	local bending-stretching coupling stiffness quantities
C_{ij}^{E}	elastic modulus of piezoelectric material
C_c	value of capacity of the capacitor in the shunt circuit
C_p	value of capacity of the electrode pair
C_{ij}	elastic modulus of the material used in the host structure in the principal material coordinate system
$C_{L\phi}$	local lift curve slope
D/Dt	substantial derivative with respect to dimensional time
D_{ij}	local bending stiffness quantities
E_r, D_r	electric field intensity, electric displacement, $r = \overline{1,3}$
E_{11}, E_{22}, E_{33}, E_{12}, E_{13}, E_{23}	Young's modulus of orthotropic materials in the material coordinate system
E_{ij}	Young's moduli of orthotropic materials in the material coordinate system
e_{ij}	piezoelectric coupling coefficient
F_w	measure of primary warping function (Fig. 1.2)
G_{sy}	effective membrane shear stiffness
$H(\tau)$	Heaviside's step function

h_s	thickness of the wall of the host wing, i.e., not including Δh_p
$h_{(k)}, h$	thickness of the k*th* layer and thickness of the wall, respectively
I_1, I_2, ..., I_9	inertial terms, see Appendix A
K_{ij}	reduced stiffness coefficients (Eq. 1.9)
L	length of the beam (Fig. 1.1)
l	number of lag terms adopted in approximating each of the unsteady aerodynamic indicial functions
L_{ae}, L_g, L_b	unsteady aerodynamic loads and lift due to gust and blast, respectively
L_{yy}, L_{sy}	stress couples (Eq. 1.9)
m	number of the structural modes actually truncated in the calculation
m_l	number of the layers in the wall
M_x, M_y, M_z	1-D stress couples (in Eq. 1.18)
m_x, m_y, m_z	external moments per unit span, about x, y, z axes, respectively
M_{design}, θ_{design}	conditions under which the control is *nominally* designed
M_{Flight}	Mach number of flight speeed, $M_{Flight} \equiv U_\infty / a_\infty$
M_{flight}, θ_{flight}	*actual* flight conditions
n, N	number of aerodynamic lag terms used for the approximation of the Wagner's function and the number of polynomials used in the shape functions, respectively
N_{sy}, N_{yy}, N_{ny}	stress resultants (Eq. 1.9)
OL, CL	open-loop and close-loop, respectively
p	Laplace transformed counterpart of non-dimensional time variable
P_m	dimensional peak reflected pressure of the blast
p_x, p_y, p_z	external forces per unit span
Q_x, Q_z	shear forces in x, z directions (Eq. 1.18)
R_c	value of electric resistance of the resistor in the shunt circuit
r_n	geometric quantity (Fig. 1.2)

S_i, σ_i	*Cauchy* strain and stress components in Voigt notation form, $i = \overline{1,6}$
t, t_0; τ, τ_0	dimensional; non-dimensional time variables, respectively, $\tau \equiv U_n t/b$
T, V, W_e	kinetic energy, internal elastic potential and work of external forces, respectively
T_y	generalized beam axial force per unit span (Eq. 1.18)
T_{ae}, T_g, T_b	twist moments about the reference axis induced by the unsteady aerodynamic load, the gust and blast aerodynamic loads, respectively
U_∞, U_n	streamwise and chordwise free stream speed, respectively, $U_n = U_\infty \cos\Lambda$
V_G	peak gust velocity
$w_{0.5c}$, $w_{0.75c}$; $\hat{w}_{0.5c}$, $\hat{w}_{0.75c}$	dimensional; non-dimensional downwash at the semi-chord, three quarter chord, respectively
w_0, ϕ, θ_x; $\hat{w}_0$, $\hat{\phi}$, $\hat{\theta}_x$	dimensional; non-dimensional rigid body translations in z direction, rotation about the reference axis and transverse shear measures of the cross-section, respectively
X^T	transpose of the matrix or vector X
$X_{r\times s}$	an $r \times s$ matrix X
$\boldsymbol{\Psi}_u$, $\boldsymbol{\Psi}_v$, $\boldsymbol{\Psi}_w$, $\boldsymbol{\Psi}_\phi$, $\boldsymbol{\Psi}_x$, $\boldsymbol{\Psi}_z$	admissible shape functions (Eq. 1.26)
$\int_{-b}^{b}$, $\int_{-1}^{1}$	dimensional and non-dimensional airfoil integral, respectively
$\mathbf{I}_{m\times m}$	identity matrix with order m
$\mathbf{X}_{m\times n}$	$\mathbf{X}$ is a $m \times n$ matrix
(μ_{12}, μ_{13}, μ_{23})	Poisson's ratios of orthotropic materials in material coordinate system
(θ_x, θ_z, ϕ)	rotations of the cross section with respect to x, y, z axes, respectively(Fig. 1.2)
(u_0, v_0, w_0)	3 rigid body translations along x, y, z directions, respectively (Fig. 1.2)
CAS	circumferentially asymmetric stiffness, lay-up configuration
CUS	circumferentially uniform stiffness, lay-up configuration
DFE	dynamic finite element approach

Chapter 1

On a Shear-Deformable Theory of Anisotropic Thin-Walled Beams: Further Contribution and Validation

Abstract

Within the basic framework of an existing anisotropic thin-walled beam model, a couple of non-classical effects are further incorporated and the model thereby developed is validated. Three types of lay-up configurations, namely, the cross-ply, circumferentially uniform stiffness (CUS), and circumferentially asymmetric stiffness (CAS) are investigated. The solution methodology is based on the Extended Galerkin's Method (EGM) and the non-classical effects on the static responses and natural frequencies are investigated. Comparisons of the predictions by the present model with the experimental data and other analytical as well as numerical results are conducted and pertinent conclusions are outlined. This work is the first attempt to validate a class of refined thin-walled beam model that has been extensively used towards the study, among others, of dynamic response, static aeroelasticity and structural/aeroelastic feedback control.

---

[0] A slightly different version of this chapter has been submitted to the *Journal of Composite Structures* for publication

1.1 Introduction

Stimulated by the vast potential advantages provided by new composite materials, the anisotropic composite thin-walled beam structures are likely to play a crucial role in the construction of actual and future generation of high performance vehicles. The extensive research activities related to the thin-walled beams in the past have covered a broad range of domains such as aeroelastic tailoring [18, 25], smart materials/structures [15, 22], as well as the theoretical issues prompted by the multitude of the unusual effects inherent in this kind of structures. It is more than sure that this research trend will continue and get intensified in the years ahead. Among the unusual effects of the composite thin-walled beam structures, those contributed from warping and warping restraint [2, 9, 11, 17, 26, 27], transverse shear strain, 3-D strain effect [2, 10, 26, 33], and non-uniformity of the transverse shear stiffness within the structure [2, 9, 26], have been identified to have significant influence on the prediction accuracy of the models. Due to the complex influence of these non-classical effects, it is vital to validate the related models. In fact, during the last two decades, a number of analytical models for thin-walled beams have been proposed in specialized contexts and validated either numerically or experimentally [1, 3–5, 8, 10, 11, 26, 31, 32]. On the other hand, a refined thin-walled beam theory originally developed in [17, 27] has been extensively used for the study, among others, of dynamic response/structural feedback control (see e.g., [12–16, 19, 22, 27, 29]) and static aeroelasticity [14, 18, 27, 30]. However, for this beam model, *no validation* against the experimental and analytical predictions provided by other models of thin-walled beams is available in the literature. Moreover, the 3-D strain effect, the non-uniformity of contour-wise shear stiffness have not been accounted for in the model. In this chapter, a refined thin-walled beam model that is based on the previous work in Refs. [2, 17, 27] is developed and validated against the available data from experiments, finite element method and other analytical models. In order to be reasonably self-contained, the basic elements of the formerly developed theory to be used will be presented next. For more details on the former model, the reader is referred to Refs. [2, 17, 21, 27, 29].

1.2 Basic Assumptions

A single-cell, closed cross-section, fiber-reinforced composite thin-walled beam is considered in the present chapter. For its geometric configuration and the chosen coordinate system that is usually adopted in the analyses of aircraft wings, see Figs. 1.1 and 1.2. Towards its modeling, the following assumptions are adopted:

(1) The cross-sections do not deform in their own planes, i.e., no inplane deformations are allowed;

(2) Transverse shear effects are incorporated. In addition, it is stipulated that transverse shear strains γ_{xy} and γ_{yz} are uniform over the entire cross-sections;

(3) In addition to the warping displacement on the contour (referred to as primary warping), the off-contour warping (referred to as the secondary warping) is also incorporated;

(4) In order to account for the 3D effect of the strain components within the cross-section, it is assumed that over the entire cross-section, σ_{nn} is negligibly small when deriving the stress-strain constitutive law [2, 10]. The hoop stress resultants N_{ss} and N_{sn} are also negligibly small when compared with the remaining ones;

(5) The deformations are small and the linear elasticity theory is applied.

It is noted that based on assumption (1), strain ε_{nn}, ε_{ss}, γ_{ns} should be zero for each cross-section, but as reported in [10, 33], this assumption will result in over-prediction of stiffness quantities. As an alternative, it is assumed that the corresponding stress or stress resultants are zero. This is the essence of assumption (5).

1.3 Kinematics

Based on the assumptions mentioned above, the following representation of the 3-D displacement quantities is postulated:

$$u(x, y, z, t) = u_0(y, t) + z\phi(y, t); \quad w(x, y, z, t) = w_0(y, t) - x\phi(y, t); \tag{1.1a}$$

$$v(x, y, z, t) = v_0(y, t) + [x(s) - n\frac{dz}{ds}]\theta_z(y, t) + [z(s) + n\frac{dx}{ds}]\theta_x(y, t) - [F_w(s) + na(s)]\phi'(y, t) \tag{1.1b}$$

where

$$\theta_x(y, t) = \gamma_{yz}(y, t) - w_0'(y, t); \theta_z(y, t) = \gamma_{xy}(y, t) - u_0'(y, t); a(s) = -(z\frac{dz}{ds} + x\frac{dx}{ds}) \tag{1.2}$$

In the above expressions, $\theta_x(y, t)$, $\theta_z(y, t)$ and $\phi(y, t)$ denote the rotations of the cross-section about the axes x, z and the twist about the y axis, respectively, $\gamma_{yz}(y, t)$ and $\gamma_{xy}(y, t)$ denote the transverse shear strain measures.

The warping function in Eq.(1.1b) is expressed as

$$F_w(s) = \int_0^s [r_n(s) - \psi(s)]ds \tag{1.3}$$

in which the torsional function $\psi(s)$ and the quantity $r_n(s)$ are expressed as

$$\psi(s) = \frac{\oint_C r_n(\bar{s})d\bar{s}}{h(s)G_{sy}(s)\oint_C \frac{d\bar{s}}{h(\bar{s})G_{sy}(\bar{s})}}; \quad r_n(s) = z\frac{dx}{ds} - x\frac{dz}{ds} \tag{1.4}$$

where $G_{sy}(s)$ is the effective membrane shear stiffness, which is defined as [2]:

$$G_{sy}(s) = \frac{N_{sy}}{h(s)\gamma_{sy}^0(s)} \tag{1.5}$$

Notice that for the thin-walled beam theory considered herein, the six kinematic variables, $u_0(y, t)$, $v_0(y, t)$, $w_0(y, t)$, $\theta_x(y, t)$, $\theta_z(y, t)$, $\phi(y, t)$, which represent 1-D displacement measures, constitute the basic unknowns of the problem. When the transverse shear effect is ignored, Eq. (1.2) degenerates to $\theta_x = -w_0'$, $\theta_z = -u_0'$, and as a result, the number of basic unknown quantities reduces to four. Such a case leads to the classical, unshearable beam model.

The strains *contributing* to the potential energy are:

Spanwise strain:

$$\varepsilon_{yy}(n,s,y,t)=\varepsilon^0_{yy}(s,y,t)+n\varepsilon^n_{yy}(s,y,t) \tag{1.6a}$$

where

$$\varepsilon^0_{yy}(s,y,t)=v_0{}'(y,t)+\theta_z{}'(y,t)x(y,t)-\phi''(y,t)F_w(s) \tag{1.6b}$$

$$\varepsilon^n_{yy}(s,y,t)=-\theta_z{}'(y,t)\frac{dz}{ds}+\theta_x{}'(y,t)\frac{dx}{ds}-a(s)\phi''(y,t) \tag{1.6c}$$

are the axial strain components associated with the primary and secondary warping, respectively.

Tangential shear strain:

$$\gamma_{sy}(s,y,t)=\gamma^0_{sy}(s,y,t)+\psi(s)\phi'(y,t) \tag{1.7a}$$

$$\textit{where } \gamma^0_{sy}(s,y,t)=\gamma_{xy}\frac{dx}{ds}+\gamma_{yz}\frac{dz}{ds}=[u_0'+\theta_z]\frac{dx}{ds}+[w_0'+\theta_x]\frac{dz}{ds} \tag{1.7b}$$

Transverse shear strain measure:

$$\gamma_{ny}(s,y,t)=-\gamma_{xy}\frac{dz}{ds}+\gamma_{yz}\frac{dx}{ds}=-[u_0'+\theta_z]\frac{dz}{ds}+[w_0'+\theta_x]\frac{dx}{ds} \tag{1.8}$$

1.4 Constitutive Equations

Based on the assumption (5), the stress resultants and stress couples can be reduced to the following expressions:

$$\begin{Bmatrix} N_{yy} \\ N_{sy} \\ L_{yy} \\ L_{sy} \end{Bmatrix}=\begin{bmatrix} K_{11} & K_{12} & K_{13} & K_{14} \\ K_{21} & K_{22} & K_{23} & K_{24} \\ K_{41} & K_{42} & K_{43} & K_{44} \\ K_{51} & K_{52} & K_{53} & K_{54} \end{bmatrix}\begin{Bmatrix} \varepsilon^0_{yy} \\ \gamma^0_{sy} \\ \phi' \\ \varepsilon^n_{yy} \end{Bmatrix} \tag{1.9a}$$

$$N_{ny} = [A_{44} - \frac{A_{45}^2}{A_{55}}]\gamma_{ny} \tag{1.9b}$$

in which the reduced stiffness coefficients K_{ij} are defined in Appendix A.

1.5 The Governing System

The governing equations and boundary conditions can be systematically derived from the Extended Hamilton's Principle ([20], pp. 82-86), which states that the true path of motion renders the following variational form stationary:

$$\int_{t_1}^{t_2} (\delta T - \delta V + \overline{\delta W_e})\, dt = 0 \tag{1.10a}$$

with

$$\delta u_0 = \delta v_0 = \delta w_0 = \delta\theta_x = \delta\theta_z = \delta\phi = 0 \quad \text{at } t = t_1,\, t_2 \tag{1.10b}$$

where T and V denote the kinetic energy and strain energy, respectively, while $\overline{\delta W_e}$ denotes the virtual work due to external forces. These are defined as:

Kinetic energy

$$T = \frac{1}{2}\int_0^L \oint_C \sum_{k=1}^{m_l} \int_{h_{(k)}} \rho_{(k)}[(\frac{\partial u}{\partial t})^2 + (\frac{\partial w}{\partial t})^2 + (\frac{\partial v}{\partial t})^2] dndsdy, \tag{1.11}$$

Strain energy

$$\begin{aligned} V &= \frac{1}{2}\int_\tau \sigma_{ij}\varepsilon_{ij}\, d\tau \\ &= \frac{1}{2}\int_0^L \oint_C \sum_{k=1}^{m_l} \int_{h_{(k)}} [\sigma_{yy}\varepsilon_{yy} + \sigma_{sy}\gamma_{sy} + \sigma_{ny}\gamma_{ny}]_{h_{(k)}}\, dndsdy \end{aligned} \tag{1.12}$$

Virtual work of external forces:

$$\begin{aligned} \overline{\delta W_e} = &\int_0^L \{p_x(y,t)\delta u_0(y,t) + p_y(y,t)\delta v_0(y,t) + p_z(y,t)\delta w_0(y,t) \\ &+ m_x(y,t)\delta\theta_x(y,t) + (m_y(y,t) + b_w'(y,t))\delta\phi(y,t) + m_z(y,t)\delta\theta_z(y,t)\}\, dy \\ &+ \left(\bar{Q}_x\delta u_0 + \bar{Q}_z\delta w_0 + \bar{T}_y\delta v_0 + \bar{M}_x\delta\theta_x + \bar{M}_z\delta\theta_z + \bar{M}_y\delta\phi + \bar{B}_w\delta\phi'\right)\big|_0^L \end{aligned} \tag{1.13}$$

where p_x, p_y, p_z are the external forces per unit span length and m_x, m_y, m_z the moments about x, y, z axes , respectively. b_w is the bimoment of the external forces [27]. After lengthy manipulations, the equations of motion expressed in terms of 1-D stress resultant and stress couple measures are:

$$\delta u_0 : \quad Q'_x + p_x - I_1 = 0 \tag{1.14a}$$

$$\delta v_0 : \quad T'_y + p_y - I_2 = 0 \tag{1.14b}$$

$$\delta w_0 : \quad Q'_z + p_z - I_3 = 0 \tag{1.14c}$$

$$\delta \phi : \quad M'_y - B''_w + m_y + b'_w - I_4 + I'_9 = 0 \tag{1.14d}$$

$$\delta \theta_x : \quad M'_x - Q_z + m_x - I_5 = 0 \tag{1.14e}$$

$$\delta \theta_z : \quad M'_z - Q_x + m_z - I_6 = 0 \tag{1.14f}$$

Boundary conditions:

$$\delta u_0 : \ u_0 = \bar{u}_0 \quad \text{or} \quad Q_x = \bar{Q}_x \tag{1.15a}$$

$$\delta v_0 : \ v_0 = \bar{v}_0 \quad \text{or} \quad T_y = \bar{T}_y \tag{1.15b}$$

$$\delta w_0 : \ w_0 = \bar{w}_0 \quad \text{or} \quad Q_z = \bar{Q}_z \tag{1.15c}$$

$$\delta \phi : \ \phi = \bar{\phi} \quad \text{or} \quad -B'_w + M_y = \bar{M}_y - I_9 \tag{1.15d}$$

$$\delta \phi' : \ \phi' = \bar{\phi}' \quad \text{or} \quad B_w = \bar{B}_w \tag{1.15e}$$

$$\delta \theta_x : \quad \theta_x = \bar{\theta}_x \quad \text{or} \quad M_x = \bar{M}_x \tag{1.15f}$$

$$\delta \theta_z : \quad \theta_z = \bar{\theta}_z \quad \text{or} \quad M_z = \bar{M}_z \tag{1.15g}$$

For unshearable beam model, the equations of motion are reduced to:

$$\delta u_0 : \quad M''_z + p_x + m'_z - I_1 - I'_8 = 0 \tag{1.16a}$$

$$\delta v_0 : \quad T'_y + p_y - I_2 = 0 \tag{1.16b}$$

$$\delta w_0 : \quad M''_x + p_z + m'_x - I_3 - I'_7 = 0 \tag{1.16c}$$

$$\delta\phi\ :\quad M_y' - B_w'' + m_y + b_w' - I_4 + I_9' = 0 \tag{1.16d}$$

Boundary conditions:

$$\delta u_0\ :\ u_0 = \bar{u}_0 \quad \text{or} \quad M_z' - I_8 = \bar{Q}_x \qquad \delta u_0'\ :\ u_0' = \bar{u}_0' \quad \text{or} \quad M_z = \bar{M}_z \tag{1.17a}$$

$$\delta v_0\ :\ v_0 = \bar{v}_0 \quad \text{or} \quad T_y = \bar{T}_y \tag{1.17b}$$

$$\delta w_0\ :\ w_0 = \bar{w}_0 \quad \text{or} \quad M_x' - I_7 = \bar{Q}_z \qquad \delta w_0'\ :\ w_0' = \bar{w}_0' \quad \text{or} \quad M_x = \bar{M}_x \tag{1.17c}$$

$$\delta\phi\ :\ \phi = \bar{\phi} \quad \text{or} \quad -B_w' + M_y = \bar{M}_y - I_9 \tag{1.17d}$$

$$\delta\phi'\ :\ \phi' = \bar{\phi}' \quad \text{or} \quad B_w = \bar{B}_w \tag{1.17e}$$

The 1-D stress resultant and stress couple measures are defined as follows:

$$\begin{aligned}
T_y(y,t) &= \oint_C N_{yy}ds & M_z(y,t) &= \oint_C (xN_{yy} - L_{yy}\frac{dz}{ds})ds \\
M_x(y,t) &= \oint_C (zN_{yy} + L_{yy}\frac{dx}{ds})ds & Q_x(y,t) &= \oint_C (N_{sy}\frac{dx}{ds} - N_{ny}\frac{dz}{ds})ds \\
Q_z(y,t) &= \oint_C (N_{sy}\frac{dz}{ds} + N_{ny}\frac{dx}{ds})ds & B_w(y,t) &= -\oint_C [F_w(s)N_{yy} + a(s)L_{yy}]ds \\
M_y(y,t) &= \oint_C N_{sy}\psi(s)ds
\end{aligned} \tag{1.18}$$

In terms of the basic 1-D displacement measures, their expressions are:

$$\left\{\begin{array}{c} T_y \\ M_z \\ M_x \\ Q_x \\ Q_z \\ B_w \\ M_y \end{array}\right\} = \begin{bmatrix} a_{11} & a_{12} & a_{13} & a_{14} & a_{15} & a_{16} & a_{17} \\ a_{12} & a_{22} & a_{23} & a_{24} & a_{25} & a_{26} & a_{27} \\ a_{13} & a_{23} & a_{33} & a_{34} & a_{35} & a_{36} & a_{37} \\ a_{14} & a_{24} & a_{34} & a_{44} & a_{45} & a_{46} & a_{47} \\ a_{15} & a_{25} & a_{35} & a_{45} & a_{55} & a_{56} & a_{57} \\ a_{16} & a_{26} & a_{36} & a_{46} & a_{56} & a_{66} & a_{67} \\ a_{17} & a_{27} & a_{37} & a_{47} & a_{57} & a_{67} & a_{77} \end{bmatrix} \left\{\begin{array}{c} v_0' \\ \theta_z' \\ \theta_x' \\ (u_0' + \theta_z) \\ (w_0' + \theta_x) \\ \phi'' \\ \phi' \end{array}\right\} \tag{1.19}$$

In conjunction with Eqs. (1.14, 1.19), the most general form of the governing equations of the thin-walled beams can be derived. In general, for anisotropic and heterogeneous materials, the stiffness matrix in Eq. (1.19) is fully populated. As a result,the governing equations are completely coupled [21, 29] implying that the beam undergoes a coupled motion involving bendings, twist, extension, transverse shearing and warping. Assessment of these couplings on various problems and their proper exploitation should constitute an important task towards a rational design of these structures, and towards the proper use of the exotic material characteristics. However, for the purpose of validation, the following special cases will be investigated, namely, cross-ply, CUS, and CAS lay-ups (see e.g., [11, 17, 24, 26]). The CAS is also referred to as the symmetric lay-up, and the CUS as the anti-symmetric lay-up [26]. All the above lay-ups in the test are on box beams.

1.6 Governing systems for the Cross-ply, CUS and CAS configurations

Specialization of the lay-up configuration yields special elastic couplings. For the test beams configured by the CUS lay-up, the elastic couplings are split into two independent groups, one group featuring extension-twist coupling, while the other group featuring bending-transverse shear coupling [26]. For the test beams configured by the CAS lay-up, the elastic couplings are also exactly split into two independent groups, one group experiencing extension-transverse shear coupling, while the other group experiencing bending-twist coupling; for the test beams configured by the cross-ply lay-up, the elastic couplings completely disappear.

The force-displacement relationships that reveal in full the associated elastic couplings involved are:

Force-displacement relations for cross-ply lay-up configuration

$$\begin{Bmatrix} T_y \\ M_z \\ M_x \end{Bmatrix} = \begin{bmatrix} a_{11} & & \\ & a_{22} & \\ & & a_{33} \end{bmatrix} \begin{Bmatrix} v_0' \\ \theta_z' \\ \theta_x' \end{Bmatrix} \tag{1.20a}$$

$$\begin{Bmatrix} Q_x \\ Q_z \\ B_w \\ M_y \end{Bmatrix} = \begin{bmatrix} a_{44} & & & \\ & a_{55} & & \\ & & a_{66} & \\ & & & a_{77} \end{bmatrix} \begin{Bmatrix} (u_0' + \theta_z) \\ (w_0' + \theta_x) \\ \phi'' \\ \phi' \end{Bmatrix} \tag{1.20b}$$

Force-displacement relations for CUS lay-up configuration

$$\begin{Bmatrix} T_y \\ M_y \end{Bmatrix} = \begin{bmatrix} a_{11} & a_{17} \\ a_{17} & a_{77} \end{bmatrix} \begin{Bmatrix} v_0' \\ \phi' \end{Bmatrix} \tag{1.21a}$$

$$\begin{Bmatrix} M_z \\ M_x \\ Q_x \\ Q_z \\ B_w \end{Bmatrix} = \begin{bmatrix} a_{22} & 0 & 0 & a_{25} & 0 \\ 0 & a_{33} & a_{34} & 0 & 0 \\ 0 & a_{34} & a_{44} & 0 & 0 \\ a_{25} & 0 & 0 & a_{55} & 0 \\ 0 & 0 & 0 & 0 & a_{66} \end{bmatrix} \begin{Bmatrix} \theta_z' \\ \theta_x' \\ (u_0' + \theta_z) \\ (w_0' + \theta_x) \\ \phi'' \end{Bmatrix} \tag{1.21b}$$

Force-displacement relations for CAS lay-up configuration

$$\begin{Bmatrix} T_y \\ Q_x \\ Q_z \end{Bmatrix} = \begin{bmatrix} a_{11} & a_{14} & a_{15} \\ a_{14} & a_{44} & 0 \\ a_{15} & 0 & a_{55} \end{bmatrix} \begin{Bmatrix} v_0' \\ (u_0' + \theta_z) \\ (w_0' + \theta_x) \end{Bmatrix} \tag{1.22a}$$

$$\begin{Bmatrix} M_z \\ M_x \\ B_w \\ M_y \end{Bmatrix} = \begin{bmatrix} a_{22} & 0 & 0 & a_{27} \\ 0 & a_{33} & 0 & a_{37} \\ 0 & 0 & a_{66} & 0 \\ a_{27} & a_{37} & 0 & a_{77} \end{bmatrix} \begin{Bmatrix} \theta_z' \\ \theta_x' \\ \phi'' \\ \phi' \end{Bmatrix} \tag{1.22b}$$

The governing equations and the associated boundary conditions for the above lay-ups in terms of the basic unknowns can then be obtained.

Cross-ply lay-up configuration:

$$\delta u_0 : \quad a_{44}(u_0'' + \theta_z') + p_x - I_1 = 0 \tag{1.23a}$$

$$\delta v_0 : \quad a_{11} v_0'' + p_y - I_2 = 0 \tag{1.23b}$$

$$\delta w_0 : \quad a_{55}(w_0'' + \theta_x') + p_z - I_3 = 0 \tag{1.23c}$$

$$\delta \phi : \quad a_{77}\phi'' - a_{66}\phi^{(IV)} + m_y + b_w' - I_4 + I_9' = 0 \tag{1.23d}$$

$$\delta \theta_x : \quad a_{33}\theta_x'' - a_{55}(w_0' + \theta_x) + m_x - I_5 = 0 \tag{1.23e}$$

$$\delta \theta_z : \quad a_{22}\theta_z'' - a_{44}(u_0' + \theta_z) + m_z - I_6 = 0 \tag{1.23f}$$

CAS lay-up configuration:

$$\delta u_0 : \quad a_{14} v_0'' + a_{44}(u_0'' + \theta_z') + p_x - I_1 = 0 \tag{1.24a}$$

$$\delta v_0 : \quad a_{11}v_0'' + a_{14}(u_0'' + \theta_z') + a_{15}(w_0'' + \theta_x') + p_y - I_2 = 0 \tag{1.24b}$$

$$\delta w_0 : \quad a_{15}v_0'' + a_{55}(w_0'' + \theta_x') + p_z - I_3 = 0 \tag{1.24c}$$

$$\delta \phi : \quad a_{27}\theta_z'' + a_{37}\theta_x'' + a_{77}\phi'' - a_{66}\phi^{(IV)} + m_y + b_w' - I_4 + I_9' = 0 \tag{1.24d}$$

$$\delta \theta_x : \quad a_{33}\theta_x'' + a_{37}\phi'' - a_{15}v_0' - a_{55}(w_0' + \theta_x) + m_x - I_5 = 0 \tag{1.24e}$$

$$\delta \theta_z : \quad a_{22}\theta_z'' + a_{27}\phi'' - a_{14}v_0' - a_{44}(u_0' + \theta_z) + m_z - I_6 = 0 \tag{1.24f}$$

CUS lay-up configuration:

$$\delta u_0 : \quad a_{34}\theta_x'' + a_{44}(u_0'' + \theta_z') + p_x - I_1 = 0 \tag{1.25a}$$

$$\delta v_0 : \quad a_{11}v_0'' + a_{17}\phi'' + p_y - I_2 = 0 \tag{1.25b}$$

$$\delta w_0 : \quad a_{25}\theta_z'' + a_{55}(w_0'' + \theta_x') + p_z - I_3 = 0 \tag{1.25c}$$

$$\delta \phi : \quad a_{17}v_0'' + a_{77}\phi'' - a_{66}\phi^{(IV)} + m_y + b_w' - I_4 + I_9' = 0 \tag{1.25d}$$

$$\delta \theta_x : \quad a_{33}\theta_x'' + a_{34}(u_0'' + \theta_z') - a_{25}\theta_z' - a_{55}(w_0' + \theta_x) + m_x - I_5 = 0 \tag{1.25e}$$

$$\delta \theta_z : \quad a_{22}\theta_z'' + a_{25}(w_0'' + \theta_x') - a_{34}\theta_x' - a_{44}(u_0' + \theta_z) + m_z - I_6 = 0 \tag{1.25f}$$

The general expressions for boundary conditions remain the same as given above.

1.7 Solution Methodology

Due to the complex boundary conditions and complex couplings involved in the above equations, it is difficult to generate proper *comparison functions* ([20], pp. 385) that fulfil all the geometric and natural boundary conditions. Therefore, in order to solve the above equations in a general way, the extended Galerkin's method (EGM) [12, 23] is used. The underlying idea of this method is to select weight functions that need only fulfill the geometric boundary conditions, while the effects of the natural boundary conditions are kept in the governing equations. When the linear combination of these weight functions are capable to satisfying the natural boundary conditions, the convergence rate is usually excellent [23]. For the thin-walled beams to be investigated here, this method leads to both symmetric mass and stiffness matrices. To illustrate its implementation, only the basic formulae for the CAS test beams will be displayed in the following.

Let

$$\begin{aligned} u_0(y,t) &\equiv \boldsymbol{\Psi}_u^T(y)\mathbf{q}_u(t), \quad v_0(y,t) \equiv \boldsymbol{\Psi}_v^T(y)\mathbf{q}_v(t), \quad w_0(y,t) \equiv \boldsymbol{\Psi}_w^T(y)\mathbf{q}_w(t), \\ \phi(y,t) &\equiv \boldsymbol{\Psi}_\phi^T(y)\mathbf{q}_\phi(t), \quad \theta_x(y,t) \equiv \boldsymbol{\Psi}_x^T(y)\mathbf{q}_x(t), \quad \theta_z(y,t) \equiv \boldsymbol{\Psi}_z^T(y)\mathbf{q}_z(t) \end{aligned} \tag{1.26}$$

where the shape functions $\boldsymbol{\Psi}_u(y)$, $\boldsymbol{\Psi}_v(y)$, $\ldots$, $\boldsymbol{\Psi}_z(y)$ are required to fulfil only the geometric boundary conditions.

In following the procedure developed in [16], the use of Eqs. (1.24, 1.15) results in the discretized equations of motion:

$$[\mathbf{M}]\{\ddot{\mathbf{q}}\} + [\mathbf{K}]\{\mathbf{q}\} = \{\mathbf{Q}\} \tag{1.27a}$$

where

$$\{\mathbf{q}\} = \left[\begin{array}{cccccc} \mathbf{q}_u^T & \mathbf{q}_v^T & \mathbf{q}_w^T & \mathbf{q}_\phi^T & \mathbf{q}_x^T & \mathbf{q}_z^T \end{array}\right]^T \tag{1.27b}$$

$$\mathbf{M} = \int_0^L \left[\begin{array}{cccccc} \begin{array}{c} b_1 \\ \boldsymbol{\Psi}_u \Psi_u^{\mathrm{T}} \end{array} & \mathbf{0} & \mathbf{0} & \mathbf{0} & \mathbf{0} & \mathbf{0} \\ & \begin{array}{c} b_1 \\ \boldsymbol{\Psi}_v \Psi_v^{\mathrm{T}} \end{array} & \mathbf{0} & \mathbf{0} & \mathbf{0} & \mathbf{0} \\ & & \begin{array}{c} b_1 \\ \boldsymbol{\Psi}_w \Psi_w^{\mathrm{T}} \end{array} & \mathbf{0} & \mathbf{0} & \mathbf{0} \\ & & & \begin{array}{c} (b_4 + b_5)\boldsymbol{\Psi}_\phi \Psi_\phi^{\mathrm{T}} \\ +(b_{10} + b_{18})\boldsymbol{\Psi}'_\phi {\Psi'}_\phi^{\mathrm{T}} \end{array} & \mathbf{0} & \mathbf{0} \\ & \mathbf{S}ymm & & & \begin{array}{c} (b_4 + b_{14}) \\ \boldsymbol{\Psi}_x \Psi_x^{\mathrm{T}} \end{array} & \mathbf{0} \\ & & & & & \begin{array}{c} (b_5 + b_{15}) \\ \boldsymbol{\Psi}_z \Psi_z^{\mathrm{T}} \end{array} \end{array}\right] dy \tag{1.27c}$$

$$\mathbf{K} = \int_0^L \begin{bmatrix} a_{44}\boldsymbol{\Psi}'_u\boldsymbol{\Psi}'^T_u & a_{14}\boldsymbol{\Psi}'_u\boldsymbol{\Psi}'^T_v & \mathbf{0} & \mathbf{0} & \mathbf{0} & a_{44}\boldsymbol{\Psi}'_u\boldsymbol{\Psi}^T_z \\ & a_{11}\boldsymbol{\Psi}'_v\boldsymbol{\Psi}'^T_v & a_{15}\boldsymbol{\Psi}'_v\boldsymbol{\Psi}'^T_w & \mathbf{0} & a_{15}\boldsymbol{\Psi}'_v\boldsymbol{\Psi}^T_x & a_{14}\boldsymbol{\Psi}'_v\boldsymbol{\Psi}^T_z \\ & & a_{55}\boldsymbol{\Psi}'_w\boldsymbol{\Psi}'^T_w & \mathbf{0} & a_{55}\boldsymbol{\Psi}'_w\boldsymbol{\Psi}^T_x & \mathbf{0} \\ & & & \begin{array}{c} a_{77}\boldsymbol{\Psi}'_\phi\boldsymbol{\Psi}'^T_\phi \\ +a_{66}\boldsymbol{\Psi}''_\phi\boldsymbol{\Psi}''^T_\phi \end{array} & a_{37}\boldsymbol{\Psi}'_\phi\boldsymbol{\Psi}'^T_x & a_{27}\boldsymbol{\Psi}'_\phi\boldsymbol{\Psi}'^T_z \\ & \mathbf{S}ymm & & & \begin{array}{c} a_{33}\boldsymbol{\Psi}'_x\boldsymbol{\Psi}'^T_x \\ +a_{55}\boldsymbol{\Psi}_x\boldsymbol{\Psi}^T_x \end{array} & \mathbf{0} \\ & & & & & \begin{array}{c} a_{22}\boldsymbol{\Psi}'_z\boldsymbol{\Psi}'^T_z \\ +a_{44}\boldsymbol{\Psi}_z\boldsymbol{\Psi}^T_z \end{array} \end{bmatrix} dy \tag{1.27d}$$

$$\mathbf{Q} = \left\{ \begin{array}{l} \int_0^L p_x\boldsymbol{\Psi}_u dy + \bar{Q}_x\boldsymbol{\Psi}_u(L) \\ \int_0^L p_y\boldsymbol{\Psi}_v dy + \bar{T}_y\boldsymbol{\Psi}_v(L) \\ \int_0^L p_z\boldsymbol{\Psi}_w dy + \bar{Q}_z\boldsymbol{\Psi}_w(L) \\ \int_0^L (m_y + b'_w)\boldsymbol{\Psi}_\phi dy + [\bar{M}_y\boldsymbol{\Psi}_\phi(L) + \bar{B}_w\boldsymbol{\Psi}'_\phi(L)] \\ \int_0^L m_x\boldsymbol{\Psi}_x dy + \bar{M}_x\boldsymbol{\Psi}_x(L) \\ \int_0^L m_z\boldsymbol{\Psi}_z dy + \bar{M}_z\boldsymbol{\Psi}_z(L) \end{array} \right\} \tag{1.27e}$$

The inertial coefficients b_1, b_4, b_5, b_{10}, b_{14}, b_{15}, b_{18} in Eq. (1.27c) are defined in the Appendix A.

In order to validate the convergence of the above method, a typical cantilevered uniform aircraft wing [7] is used. Its geometric and material specifications are provided in Ref. [7]. Also provided in Ref. [7] are the exact solutions and the predictions by other methods (finite element method and dynamic finite element method (DFE)). The comparisons of the eigenfrequencies and eigenmodes up to the first six order are conducted. The eigenfrequency results are shown in Table 1.1 and the eigenmode shapes are shown in Figs. 1.3 and 1.4. Compared with the mode shapes listed in Ref. [7] (using the DFE method), the EGM gives the same mode shapes. It is noted that only 7 simple polynomials (x^i, $i = 1, 2, 3, ..., 7$) are used in the EGM. Tables 1.2, 1.3, 1.4, 1.5 display the prediction accuracy of the eigenfrequencies of anisotropic thin-walled beams with different configurations by the EGM method against the exact results.[1] Clearly, the convergence and accuracy are excellent. Also to be noted is that in order to provide accurate and robust numerical

---

[1] The exact results are taken from *Static/dynamic exact solutions of a refined anisotropic thin-walled beam model*, by Z. Qin and L. Librescu, to be submitted for publication

solutions, the *Cholesky* decomposition technique ([20], pp. 280-283) is adopted for the numerical implementation of matrix inversions. It is interesting to note that Ref. [28] conducted the comparisons of using EGM and the Laplace Transform Method (LTM) to predict the steady-state deflection amplitude at the beam tip subject to a harmonically oscillating load, and the accuracy of the predictions was excellent.

1.8 Test Cases

In order to quantitatively validate the accuracy and capabilities of the developed beam model, thin-walled box beams configured with the cross-ply, CUS and CAS lay-ups are considered. Both the responses subject to various types of static loading and characteristics of the natural frequencies are investigated. A number of comparisons are performed against the experimental (see e.g., [3, 5, 26]) and theoretical predictions available in literature (see e.g., [1, 3, 10, 11, 26, 31, 32]). Among them, the theoretical predictions cover refined finite element beam models, 3D finite element models, and other theoretical beam models. The material properties of thin-walled beams used in the static validation are summarized in Table 1.6; the geometric features of the beams is summarized in Table 1.7, while the lay-ups are specified in Table 1.8.

1.9 Validation

As has been correctly pointed out by Jung *e*t al. [9], the former beam model developed by Song [27], Librescu and Song [17] will yield erroneous results for the CAS lay-up beams specified in the test cases. The main purpose here is to investigate if that model has the potential, after the 3-D strain effect and the non-uniformity of G_{sy} are further incorporated, to provide good and consistent correlation compared with the experimental results and the analytical predictions by other models.

Before plunging ourselves into the details of the discussion, it is appropriate to point out several significant simplifications that can be drawn from the test beams. For the thin-walled CAS test cases, due to the balanced lay-ups on the webs (left and right walls), the stiffness coefficient a_{15} is zero. The coefficient a_{27} is much smaller than a_{37}, a_{22}, a_{55} and a_{77} for all the lay-ups tested ($< 2\%$), therefore, a_{27} can be ignored. Then the whole governing system (including the associated boundary conditions) can be split into two groups: one group involving extension-lateral bending-lateral transverse shear motions; while the other group involving twist-vertical bending-vertical transverse shear motions [29].

Figures 1.5 and 1.6 display the prediction results of the cross-ply test beams under 4.45 N tip bending shear load and 0.113 N-m tip torque. Compared with the experimental data (see Ref. [11] for the source of the experimental data) and other analytical results (e.g., a higher-order shear-deformable beam model by Kim and White [11]), the present beam model provides good correlation. As indicated in Ref. [11], the warping and transverse shear effects are small for the uncoupled lay-up configurations.

Figures through 1.7 to 1.11 show the prediction results of the thin-walled CUS test beams under 0.113 N-m tip torque, 4.45N tip shear load and 4.45 N tip extension load. It is noted that in Fig. 1.11, a remarkable transverse shear effect on the bending slope is observed. The unshearable model yields only 62% of the bending slope at the beam tip predicted by the shearable counterpart. Compared with the experimental data, for all the thin-walled CUS test cases, predictions by the present model show good agreement with the experimental data.

Figures through 1.12 to 1.18 display the prediction results of the thin-walled CAS test beams under 4.45 N tip shear load and 0.113 N-m tip torque. Also shown in the figures are predictions based on several other beam models [10, 11, 26, 31, 32], among which, the beam models by Kim and White [10, 11], Suresh and Nagaraj [31] are featured by higher-order shear-deformable beam theories. It is noted that the sources of the experimental data, Beam FEA model can be traced through Ref. [11]. Also notice that the present model yields consistent lower predictions of induced twist angle under the tip shear loads. For all thin-walled CAS test cases, the present model shows good and consistent correlation.

The above investigations are for the static responses. Compared with the static validation, there are very few experimental data available in literature on the dynamic validation of the thin-walled beam models (see Refs. [1, 4, 6, 8]).

The dynamic validation are based on the data provided in Refs. [1, 4]. The material, geometric and lay-up specifications are listed in Table 1, Ref. [4], and are not included here. The prediction results by the present model are listed in Table 1.9. Results reveal that the present model produce a good agreement with the experimental data. Notice that lower predictions of the natural frequencies of the CAS test beams are obtained by Armanios and Badir [1], even though transverse shear flexibility was not considered in the latter model.

It is reminded that equations developed in Refs. [17, 21, 27, 29] stipulate uniform membrane shear stiffness along the contour. This assumption is justified by the beams previously used (with constant contour-wise G_{sy}). However, for the walls composed of lay-ups with different stiffness along the contour, this assumption is no longer valid [9, 26]. It was later modified by Bhaskar and Librescu [2] to account for the non-uniformity of the shear stiffness. For the test cases, as was demonstrated by Smith and Chopra [26], the non-uniformity of the contour-wise membrane shear stiffness has a significant influence on the prediction of the static responses. Figures through 1.19 to 1.21 reveal the influence of non-uniformity of membrane shear stiffness G_{sy} on the twist angle and bending slope of CAS test beams subject to tip shear load and tip torque. It is noted that compared with the predictions by non-uniform contour-wise shear model, the uniform contour-wise shear model results in some degree of discrepancies that increase rapidly when the ply angle increases from 15^0 to 45^0. Intuitively, when the ply angle angle of the test beams is zero, the walls of the cross section become transversely isotropic. In this case, G_{sy} is constant along the contour, which illustrates the very small discrepancy on the CAS1 test cases (θ=15^0). In Fig. 1.21, for CAS3 test beam, the uniform shear stiffness model predicts only 50% of the deformation predicted by the non-uniform one. Figures 1.22 and 1.23 show the dynamic influence of the non-uniformity of G_{sy}. It is observed that for ply angles between 20^0 and 60^0 or -60^0 and -20^0, the influence becomes noticeable.

1.10 Conclusions

A refined thin-walled beam model based on an existing thin-walled beam model is developed and validated against experimental and analytical results available. Significant improvement of the prediction accuracy is achieved and for all the validation cases, compared with other analytical models cited in this paper, the present beam model yields good and consistent correlation against the experimental data. Non-classical effects such as transverse shear and non-uniformity of membrane shear stiffness along the contour can significantly influence the accuracy of predictions (both static and dynamic). Elastic couplings complicate the influences of these non-classical effects. The solution methodology based on the extended Galerkin's Method provides a superior convergence rate and accuracy.

1.11 References

[1] E. A. Armanios and A. M. Badir. Free vibration analysis of anisotropic thin-walled closed-section beams. *AIAA Journal*, 33(10):1905–1910, 1995.

[2] K. Bhaskar and L. Librescu. A geometrically non-linear theory for laminated anisotropic thin-walled beams. *International Journal of Engineering Science*, 33(9):1331–1344, 1995.

[3] R. Chandra and I. Chopra. Experimental-theoretical investigation of the vibration characteristics of rotating composite box beams. *Journal of Aircraft*, 29(4):657–664, 1992.

[4] R. Chandra and I. Chopra. Structural response of composite beams and blades with elastic couplings. *Composites Engineering*, 2(5-7):347–374, 1992.

[5] R. Chandra, A. D. Stemple, and I. Chopra. Thin-walled composite beams under bending, torsional and extensional loads. *Journal of Aircraft*, 27:619–626, 1990.

[6] D. S. Dancila and E. A. Armanios. The influence of coupling on the free vibration of anisotropic thin-walled closed-section beams. *International Journal of Solids and Structures*, 35(23):3105–3119, 1998.

[7] S. M. Hashemi and J. M. Richard. A dynamic finite element (DFE) method for free vibrations of bending-torsion coupled beams. *Aerospace Science and Technology*, 4:41–55, 2000.

[8] D. H. Hodges, A. R. Atilgan, M. V. Fulton, and L. W. Rehfield. Free-vibration analysis of composite beams. *Journal of the American Helicopter Society*, 36(3):36–47, 1991.

[9] S. N. Jung, V. T. Nagaraj, and I. Chopra. Assessment of composite rotor blade modeling techniques. *Journal of the American Helicopter Society*, 44(3):188–205, 1999.

[10] C. Kim and S. R. White. Analysis of thick hollow composite beams under general loadings. *Composite Structures*, 34:263–277, 1996.

[11] C. Kim and S. R. White. Thick-walled composite beam theory including 3-d elastic effects and torsional warping. *International Journal of Solids and Structures*, 34(31-32):4237–59, 1997.

[12] L. Librescu, L. Meirovitch, and S. S. Na. Control of cantilevers vibration via structural tailoring and adaptive materials. *AIAA Journal*, 35(8):1309–1315, 1997.

[13] L. Librescu, L. Meirovitch, and O. Song. Integrated structural tailoring and control using adaptive materials for advanced aircraft wings. *Journal of Aircraft*, 33(1):1996, 1996.

[14] L. Librescu, L. Meirovitch, and O. Song. Refined structural modeling for enhancing vibrations and aeroelastic characteristics of composite aircraft wings. *La Recherche Aérospatiale*, (1):23–35, 1996.

[15] L. Librescu and S. S. Na. Dynamic response control of thin-walled beams to blast pulses using structural tailoring and piezoelectric actuation. *Journal of Applied Mechanics*, 65(2):497–504, 1998.

[16] L. Librescu and S. S. Na. Dynamic response of cantilevered thin-walled beams to blast and sonic-boom loadings. *Shock and Vibration*, 5:23–33, 1998.

[17] L. Librescu and O. Song. Behavior of thin-walled beams made of advanced composite materials and incorporating non-classical effects. *Applied Mechanics Reviews*, 44(11):S174–S180, 1991.

[18] L. Librescu and O. Song. On the static aeroelastic tailoring of composite aircraft swept wings modeled as thin-walled beam structures. *Composites Engineering*, 2:497–512, 1992.

[19] L. Librescu, O. Song, and C. A. Rogers. Adaptive vibrational behavior of cantilevered structures modeled as composite thin-walled beams. *International Journal of Engineering Science*, 31(5):775–792, 1993.

[20] L. Meirovitch. *Principles and Techniques of Vibrations.* Prentice Hall, Upper Saddle River, New Jersey, 1997.

[21] S. S. Na. *Control of Dynamic Response of Thin-Walled Composite Beams Using Structural Tailoring and Piezoelectric Actuation.* PhD thesis, Virginia Polytechnic Institute and State University, 1997.

[22] S. S. Na and L. Librescu. Oscillation control of cantilevers via smart materials technology and optimal feedback control: Actuator location and power consumption issues. *Smart Material and Structures*, 7:833–842, 1998.

[23] A. N. Palazotto and P. E. Linnemann. Vibration and buckling characteristics of composite cylindrical panels incorporating the effects of a higher order shear theory. *International Journal of Solids and Structures*, 28(3):341–361, 1991.

[24] L. W. Rehfield, A. R. Atilgan, and D. H. Hodges. Nonclassical behavior of thin-walled composite beams with closed cross sections. *Journal of the American Helicopter Society*, 35(2):42–51, 1990.

[25] M. H. Shirk, T. J. Hertz, and T. A. Weisshaar. Aeroelastic tailoring–theory, practice and promise. *Journal of Aircraft*, 23(1):6–18, 1986.

[26] E. C. Smith and I. Chopra. Formulation and evaluation of an analytical model for composite box-beams. *Journal of the American Helicopter Society*, 36(3):23–35, 1991.

[27] O. Song. *Modeling and Response Analysis of Thin-Walled Beam Structures Constructed of Advanced Composite Materials.* PhD thesis, Virginia Polytechnic Institute and State University, 1990.

[28] O. Song, J. S. Ju, and L. Librescu. Dynamic response of anisotropic thin-walled beams to blast and harmonically oscillating loads. *International Journal of Impact Engineering*, 21(8):663–682, 1998.

[29] O. Song and L. Librescu. Free vibration of anisotropic composite thin-walled beams of closed cross-section contour. *Journal of Sound and Vibration*, 167(1):129–147, 1993.

[30] O. Song, L. Librescu, and C. A. Rogers. Application of adaptive technology to static aeroelastic control of wing structures. *AIAA Journal*, 30(12):2882–2889, 1992.

[31] J. K. Suresh and V. T. Nagaraj. Higher-order shear deformation theory for thin-walled composite beams. *Journal of Aircraft*, 33(5):978–986, 1996.

[32] V. V. Volovoi, D. H. Hodges, C. E. S. Cesnik, and B. Popescu. Assessment of beam modeling methods for rotor blade applications. In *Journal of the American Helicopter Society, 55th Annual Forum*, Montreal, Quebec, Canada, May 25-27, 1999.

[33] X. X. Wu and C. T. Sun. Simplified theory for composite thin-walled beams. *AIAA Journal*, 30(12):2945–51, 1992.

1.12 Appendix A

The global stiffness quantities a_{ij} $(= a_{ji})$ and inertial terms I_i related to the problem are defined as:

$$a_{11} = \oint_C K_{11} ds \qquad a_{14} = \oint_C K_{12} \frac{dx}{ds} ds \qquad a_{15} = \oint_C K_{12} \frac{dz}{ds} ds$$

$$a_{17} = \oint_C K_{13} ds \qquad a_{22} = \oint_C [x^2 K_{11} - 2x \frac{dz}{ds} K_{14} + (\frac{dz}{ds})^2 K_{44}] ds$$

$$a_{25} = \oint_C [x \frac{dz}{ds} K_{12} - (\frac{dz}{ds})^2 K_{42}] ds \qquad a_{27} = \oint_C [x K_{13} - \frac{dz}{ds} K_{43}] ds$$

$$a_{33} = \oint_C [z^2 K_{11} + 2z \frac{dx}{ds} K_{14} + (\frac{dx}{ds})^2 K_{44}] ds \qquad a_{34} = \oint_C [z \frac{dx}{ds} K_{12} + (\frac{dx}{ds})^2 K_{42}] ds$$

$$a_{37} = \oint_C [z K_{13} + \frac{dx}{ds} K_{43}] ds \qquad a_{44} = \oint_C [(\frac{dx}{ds})^2 K_{22} + (\frac{dz}{ds})^2 \bar{A}_{44}] ds$$

$$a_{55} = \oint_C [(\frac{dz}{ds})^2 K_{22} + (\frac{dx}{ds})^2 \bar{A}_{44}] ds \qquad a_{66} = \oint_C [F_w^2 K_{11} + 2F_w a(s) K_{14} + a(s)^2 K_{44}] ds$$

$$a_{77} = \oint_C \psi(s) K_{23} ds$$

where $\bar{A}_{44} = A_{44} - \dfrac{A_{45}^2}{A_{55}}$.

The inertial terms are defined as:

$$I_1 = \oint_C m_0(\ddot{u}_0 + z\ddot{\phi})ds \qquad I_2 = \oint_C m_0[\ddot{v}_0 + x\ddot{\theta}_z + z\ddot{\theta}_x - F_w\ddot{\phi}']ds$$

$$I_3 = \oint_C m_0(\ddot{w}_0 - x\ddot{\phi})ds \qquad I_4 = \oint_C m_0[z\ddot{u}_0 + z^2\ddot{\phi} - x\ddot{w}_0 + x^2\ddot{\phi}]ds$$

$$I_5 = \oint_C m_0[z\ddot{v}_0 + zx\ddot{\theta}_z + z^2\ddot{\theta}_x - zF_w\ddot{\phi}']ds + \oint_C m_2[-\frac{dx}{ds}\frac{dz}{ds}\ddot{\theta}_z + (\frac{dx}{ds})^2\ddot{\theta}_x - a(s)\frac{dx}{ds}\ddot{\phi}']ds$$

$$I_6 = \oint_C m_0[x\ddot{v}_0 + x^2\ddot{\theta}_z + xz\ddot{\theta}_x - xF_w\ddot{\phi}']ds + \oint_C m_2[(\frac{dz}{ds})^2\ddot{\theta}_z - \frac{dx}{ds}\frac{dz}{ds}\ddot{\theta}_x + a(s)\frac{dz}{ds}\ddot{\phi}']ds$$

$$I_7 = \oint_C m_0[z\ddot{v}_0 - zx\ddot{u}_0' - z^2\ddot{w}_0' - zF_w\ddot{\phi}']ds + \oint_C m_2[\frac{dx}{ds}\frac{dz}{ds}\ddot{u}_0' - (\frac{dx}{ds})^2\ddot{w}_0' - a(s)\frac{dx}{ds}\ddot{\phi}']ds$$

$$I_8 = \oint_C m_0[x\ddot{v}_0 - x^2\ddot{u}_0' - xz\ddot{w}_0' - xF_w\ddot{\phi}']ds + \oint_C m_2[-(\frac{dz}{ds})^2\ddot{u}_0' + \frac{dx}{ds}\frac{dz}{ds}\ddot{w}_0' + a(s)\frac{dz}{ds}\ddot{\phi}']ds$$

$$I_9 = \oint_C m_0[-F_w\ddot{v}_0 - xF_w\ddot{\theta}_z - zF_w\ddot{\theta}_x + F_w^2\ddot{\phi}']ds + \oint_C m_2[a(s)\frac{dz}{ds}\ddot{\theta}_z - a(s)\frac{dx}{ds}\ddot{\theta}_x + a^2(s)\ddot{\phi}']ds$$

in which

$$(m_0, m_2) = \sum_{k=1}^{m_l} \int_{h_{(k^-)}}^{h_{(k^+)}} \rho_{(k)}(1, n^2)dn$$

The reduced stiffness coefficientK_{ij} (in Eq. 1.9) are defined as:

$$\begin{array}{lll}
K_{11} = A_{22} - \dfrac{A_{12}^2}{A_{11}} & K_{12} = A_{26} - \dfrac{A_{12}A_{16}}{A_{11}} = K_{21} & K_{13} = (A_{26} - \dfrac{A_{12}A_{16}}{A_{11}})\psi(s) \\
K_{14} = B_{22} - \dfrac{A_{12}B_{12}}{A_{11}} = K_{41} & K_{22} = A_{66} - \dfrac{A_{16}^2}{A_{11}} & K_{23} = (A_{66} - \dfrac{A_{16}^2}{A_{11}})\psi(s) \\
K_{24} = B_{26} - \dfrac{A_{16}B_{12}}{A_{11}} = K_{42} & K_{43} = (B_{26} - \dfrac{B_{12}A_{16}}{A_{11}})\psi(s) & K_{44} = D_{22} - \dfrac{B_{12}^2}{A_{11}} \\
K_{51} = B_{26} - \dfrac{B_{16}A_{12}}{A_{11}} & K_{52} = B_{66} - \dfrac{B_{16}A_{16}}{A_{11}} & K_{53} = (B_{66} - \dfrac{B_{16}A_{16}}{A_{11}})\psi(s) \\
K_{54} = D_{26} - \dfrac{B_{12}B_{16}}{A_{11}} & &
\end{array}$$

The inertial coefficients in Eq. 1.27c are defined as:

$$b_1 = \oint_C m_0 ds \qquad (b_4,\ b_5) = \oint_C (z^2, x^2)m_0 ds \quad b_{14} = \oint_C m_2(\frac{dx}{ds})^2 ds$$

$$b_{15} = \oint_C m_2(\frac{dz}{ds})^2 ds \quad (b_{10},\ b_{18}) = \oint_C (m_0F_w^2(s),\ m_2a^2(s))ds$$

Table 1.1: Convergence and accuracy test of the extended Galerkin's method (EGM)

	Eigenfrequencies ω_i unit:[rad/sec]						
Mode#	Exact[a]	DEF	$\|Err.^b\|$	FEM	$\|Err.^b\|$	Present	$\|Err.^b\|$
1	49.62	49.62	0.00(%)	49.56	0.12(%)	49.61	0.02(%)
2	97.04	97.05	0.01(%)	97.00	0.04(%)	97.04	0.00(%)
3	248.87	249.00	0.05(%)	248.61	0.11(%)	248.87	0.00(%)
4	355.59	357.54	0.55(%)	352.97	0.74(%)	355.59	0.00(%)
5	451.46	452.57	0.25(%)	450.89	0.13(%)	451.53	0.02(%)
6	610.32	610.63	0.05(%)	610.18	0.02(%)	613.48	0.52(%)

[a] The sources of these data are listed in the footnote of Table II in Ref. [7].
[b] Relative error.

Table 1.2: Comparison of EGM ($N = 7$) and the exact method on prediction of the non-dimensionalized natural frequencies $\Omega = \omega/\omega_h$ ($\mathcal{R} = 12$, $\theta = 90^0$)

Mode#	EGM	Exact	Error of EGM
1	3.465	3.465	0.0%
2	7.482	7.481	0.01%
3	20.063	20.047	0.08%
4	23.071	23.065	0.03%
5	40.433	40.418	0.04%
6	50.625	50.548	0.15%
7	60.560	60.477	0.14%

Table 1.3: Comparison of EGM ($N = 7$) and the exact method on prediction of the non-dimensionalized natural frequencies $\Omega = \omega/\omega_h$ ($A\!\!\!R = 3$, $\theta = 0^0$)

Mode#	EGM	Exact	Error of EGM
1	3.492	3.474	0.52%
2	11.556	11.518	0.33%
3	21.038	20.843	0.94%
4	35.064	35.023	0.12%
5	55.686	54.470	2.2%
6	59.03	59.573	0.22%
7	86.160	86.057	0.12%

Table 1.4: Comparison of EGM ($N = 7$) and the exact method on prediction of the non-dimensionalized natural frequencies $\Omega = \omega/\omega_h$ ($A\!\!\!R = 3$, $\theta = 45^0$)

Mode#	EGM	Exact	Error of EGM
1	3.061	3.053	0.26%
2	11.229	11.212	0.15%
3	18.429	18.246	1.0%
4	33.025	32.996	0.088%
5	48.319	47.776	1.1%
6	58.299	58.232	0.12%
7	83.003	81.486	1.9%

Table 1.5: Comparison of EGM ($N = 7$) and the exact method on prediction of the non-dimensionalized natural frequencies $\Omega = \omega/\omega_h$ ($A\!\!R = 3$, $\theta = 90^0$)

Mode#	EGM	Exact	Error of EGM
1	2.307	2.308	-0.04%
2	2.887	2.882	0.17%
3	8.383	8.383	0.0%
4	10.865	10.825	0.37%
5	18.590	18.584	0.032%
6	21.966	21.930	0.16%
7	32.503	32.275	0.71%

Table 1.6: Material properties of the test beams

$E_{11} = 141.96 \times 10^9\ N/m^2$	$E_{22} = E_{33} = 9.79 \times 10^9\ N/m^2$
$G_{12} = G_{13} = 6.0 \times 10^9\ N/m^2$	$G_{23} = 4.83 \times 10^9\ N/m^2$
$\mu_{12} = \mu_{13} = 0.42, \quad \mu_{23} = 0.25$	$\rho = 1.445 \times 10^3\ Kg/m^3$

Table 1.7: Geometric specification of the thin-walled box beams for the static validation [unit: in(mm)]

Parameters	Cross-ply	CAS	CUS
Length (L)	30(762)	30(762)	30(762)
Outer width ($2b$)	2.06(52.3)	0.953(24.2)	0.953(24.2)
Outer depth ($2d$)	1.03(26.0)	0.537(13.6)	0.537(13.6)
Slenderness ratio($L/2b$)	14.5	31.5	31.5
Wall thickness	0.030(0.762)	0.030(0.762)	0.030(0.762)
Number of layers (m_l)	6	6	6
Layer thickness	0.005(0.127)	0.005(0.127)	0.005(0.127)

Table 1.8: specification of the thin-walled box beam lay-ups for the static validation [unit:deg.[a]]

Lay-up	Flanges		Webs	
	Top	Bottom	Left	Right
CAS1	$[15]_6$	$[15]_6$	$[15/-15]_3$	$[15/-15]_3$
CAS2	$[30]_6$	$[30]_6$	$[30/-30]_3$	$[30/-30]_3$
CAS3	$[45]_6$	$[45]_6$	$[45/-45]_3$	$[45/-45]_3$
CUS1	$[15]_6$	$[-15]_6$	$[15]_6$	$[-15]_6$
CUS2	$[0/30]_3$	$[0/-30]_3$	$[0/30]_3$	$[0/-30]_3$
CUS3	$[0/45]_3$	$[0/-45]_3$	$[0/45]_3$	$[0/-45]_3$

[a] For the convenience of comparison, the definition of ply angle used in Refs. [10, 26] is adopted in this article

Table 1.9: Dynamic validation: comparison of the natural frequencies of different models against experimental data (unit: Hz)

Lay-up	Mode#	Exp.[a] Ref. [4]	Analytical Ref. [1]	Diff. with Exp. data	Present	Diff. with Exp. data
$[30]_6$ CAS	1	20.96	19.92	-4.96%	21.8	4.00%
	2	128.36	124.73	-2.83%	123.28	-3.96%
$[45]_6$ CAS	1	16.67	14.69	-11.88%	15.04	-9.78%
	2	96.15	92.02	-4.30%	92.39	-3.91%
$[15]_6$ CUS	1	28.66	28.67	0.03%	30.06	4.88%
$[0/30]_3$ CUS	1	30.66	34.23	11.7%	34.58	12.79%
$[0/45]_3$ CUS	1	30.0	32.75	9.1%	32.64	8.80%

[a] The data are obtained from Ref. [3] and are also listed in Ref. [1]

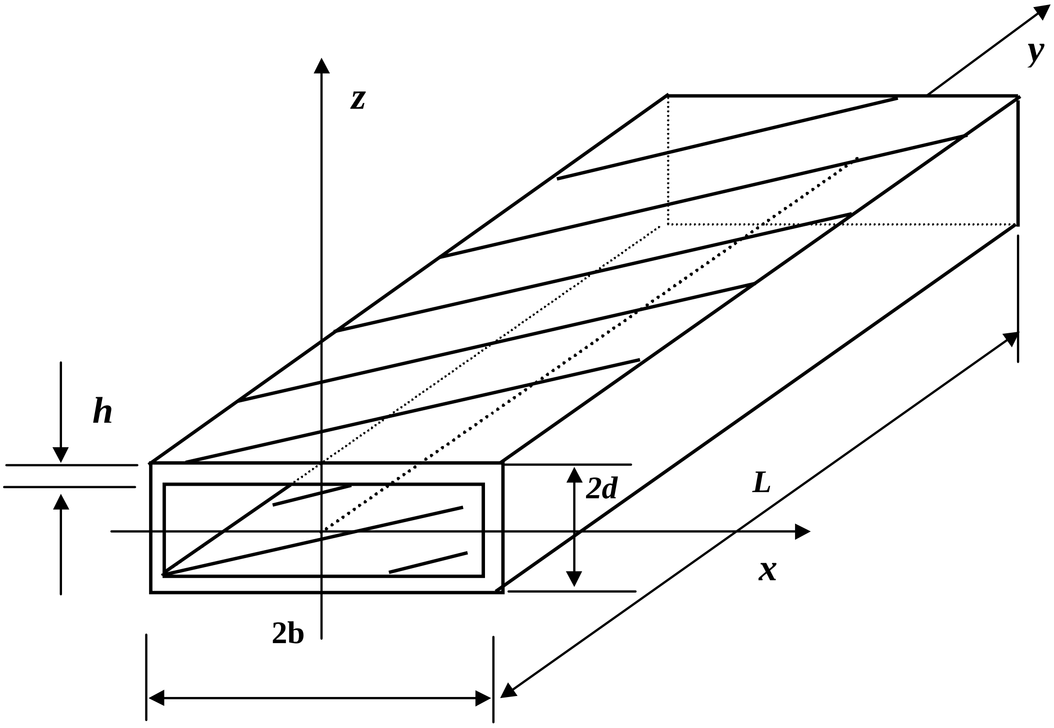

Figure 1.1: Geometric configuration of the box beam (CAS configuration).

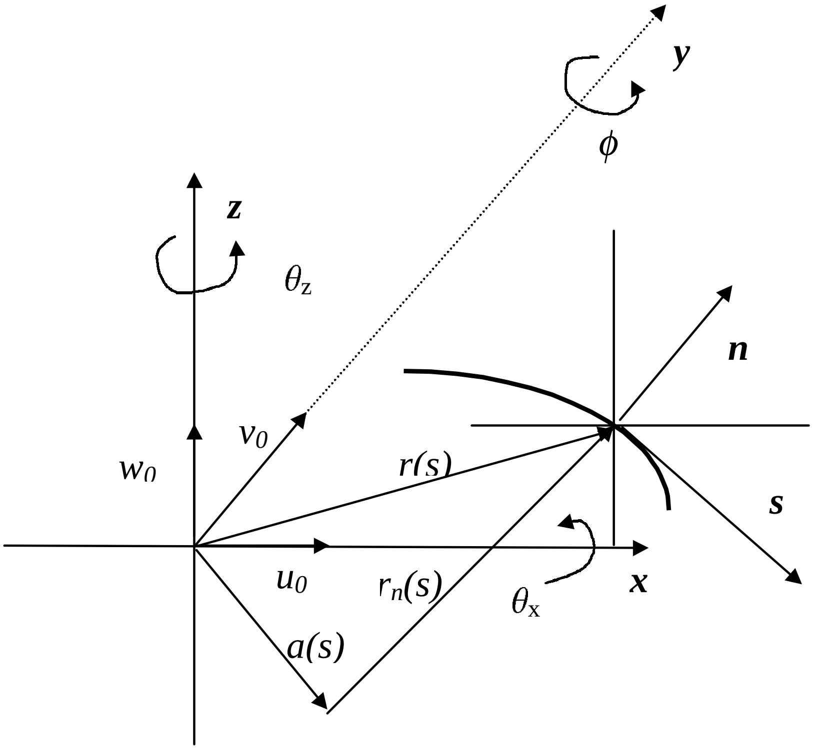

Figure 1.2: Coordinate system and displacement field for the beam model.

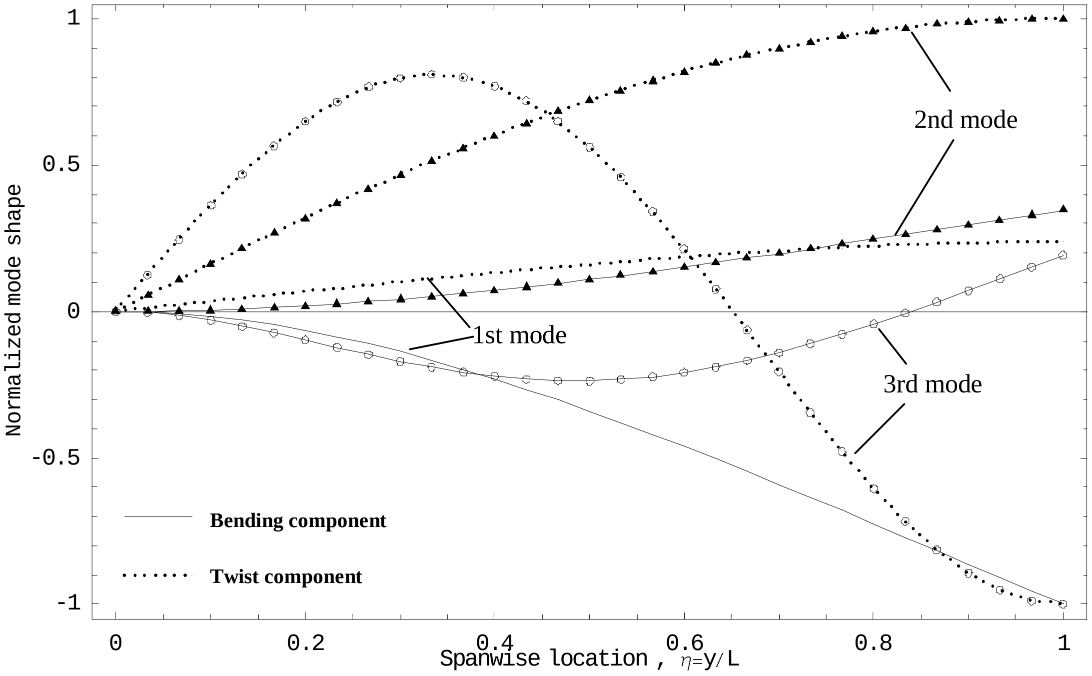

Figure 1.3: Mode shapes of the bending /twist components in the first three modes.

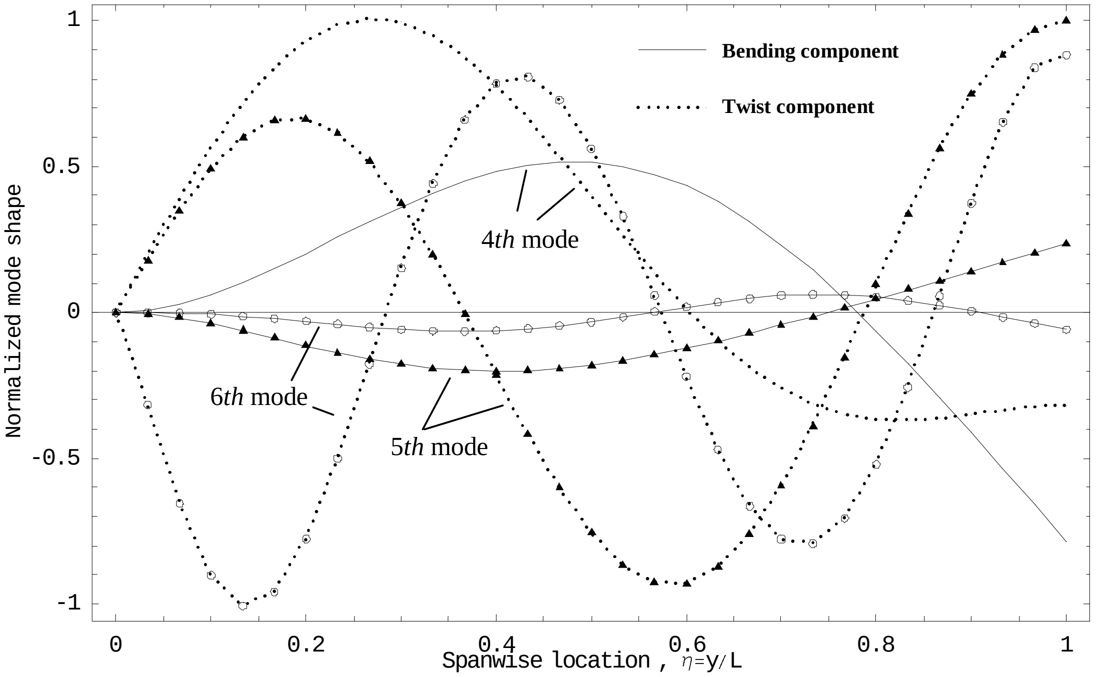

Figure 1.4: Mode shapes of the bending /twist components in the (4, 5, 6)th modes.

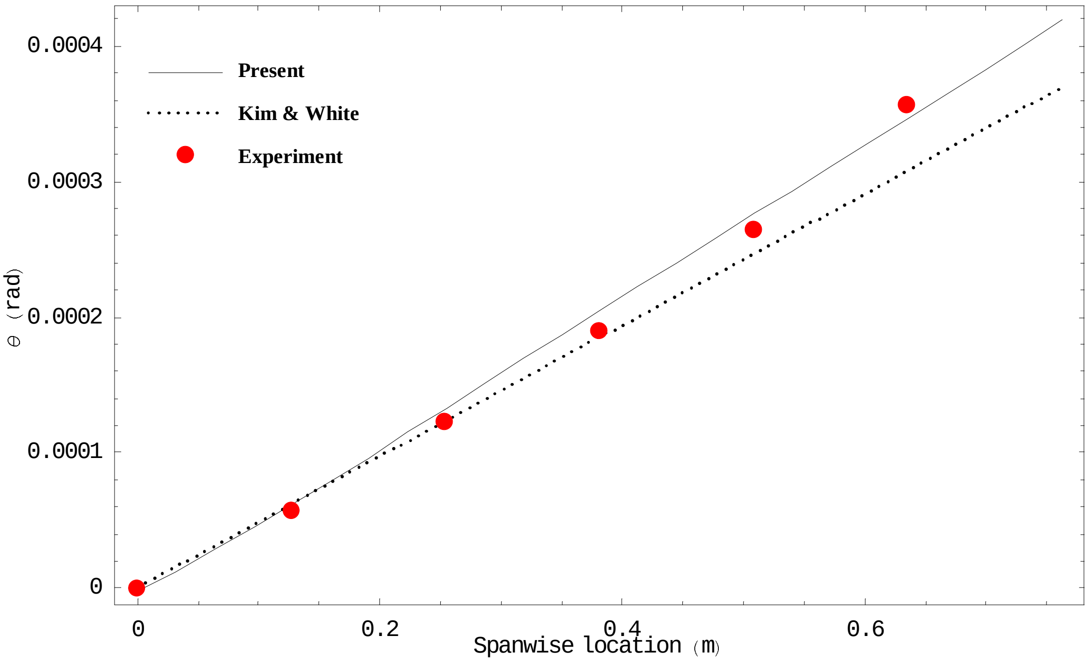

Figure 1.5: Twist angle of cross-ply test beam under 0.113 N-m tip torque.

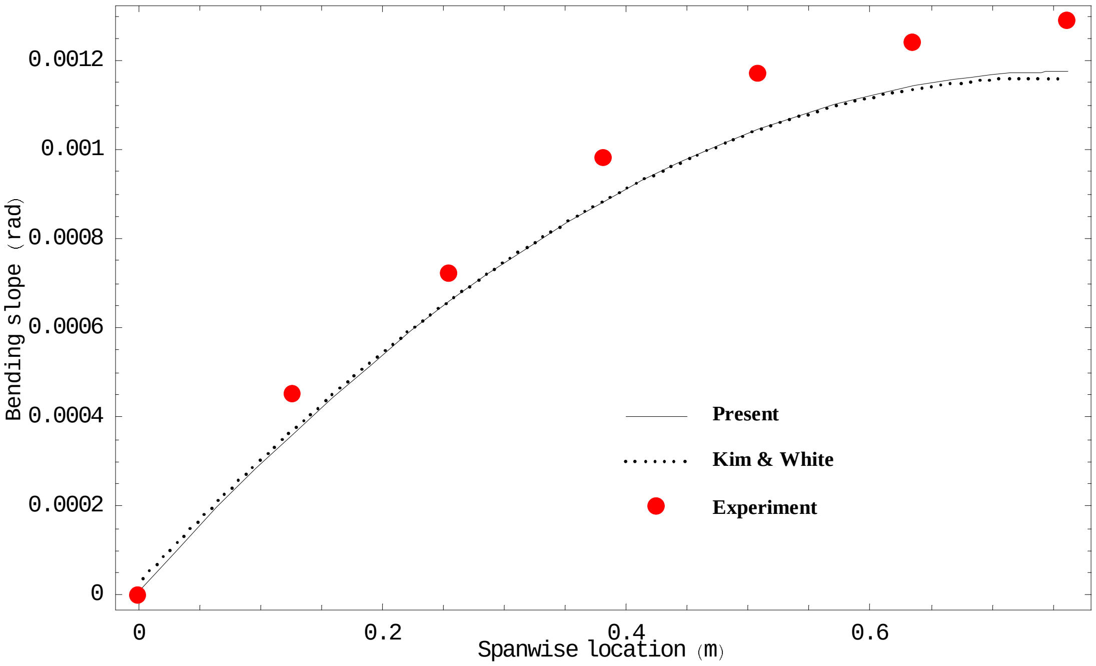

Figure 1.6: Bending slope of cross-ply test beam under 4.45 N tip shear load.

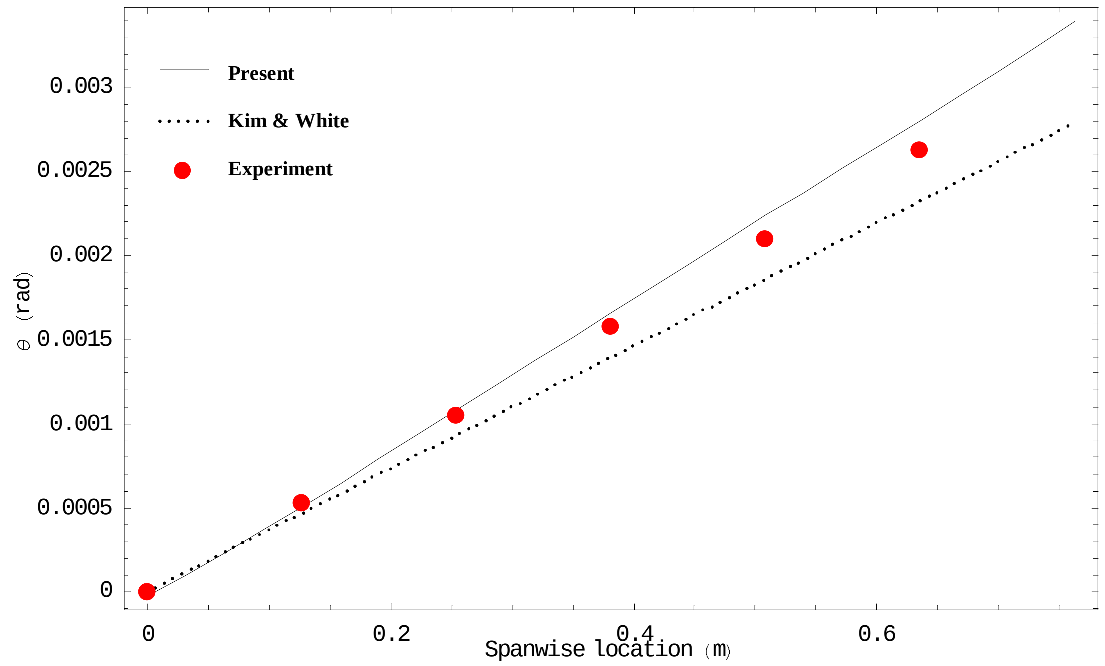

Figure 1.7: Twist angle of CUS1 beam by 0.113 N-m tip torque.

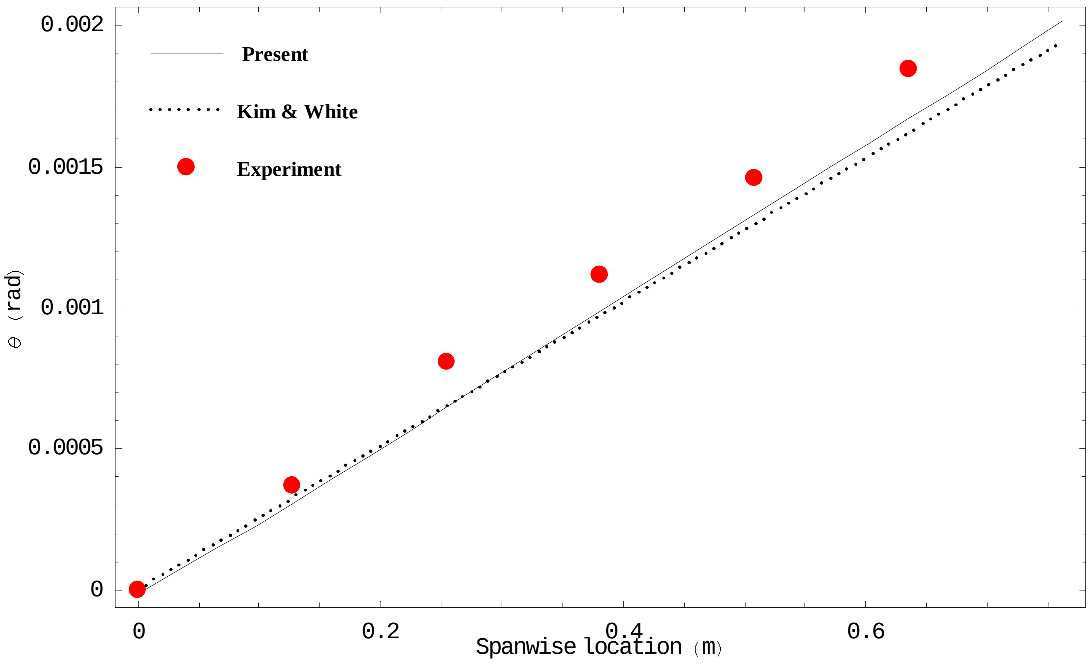

Figure 1.8: Twist angle of CUS2 beam by 0.113 N-m tip torque.

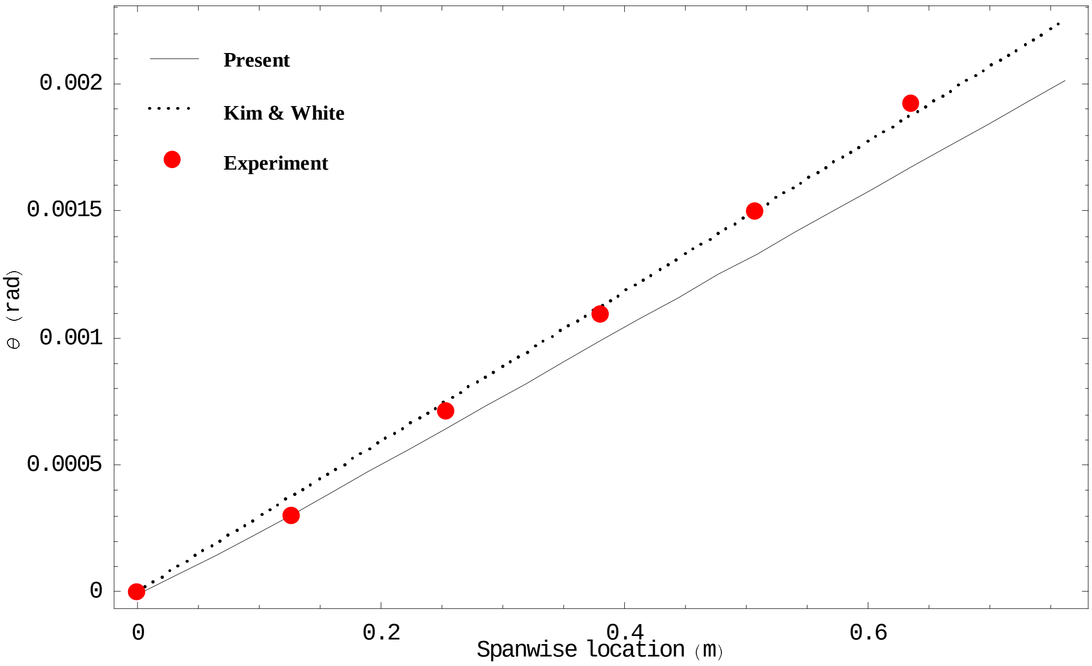

Figure 1.9: Twist angle of CUS3 beam by 0.113 N-m tip torque.

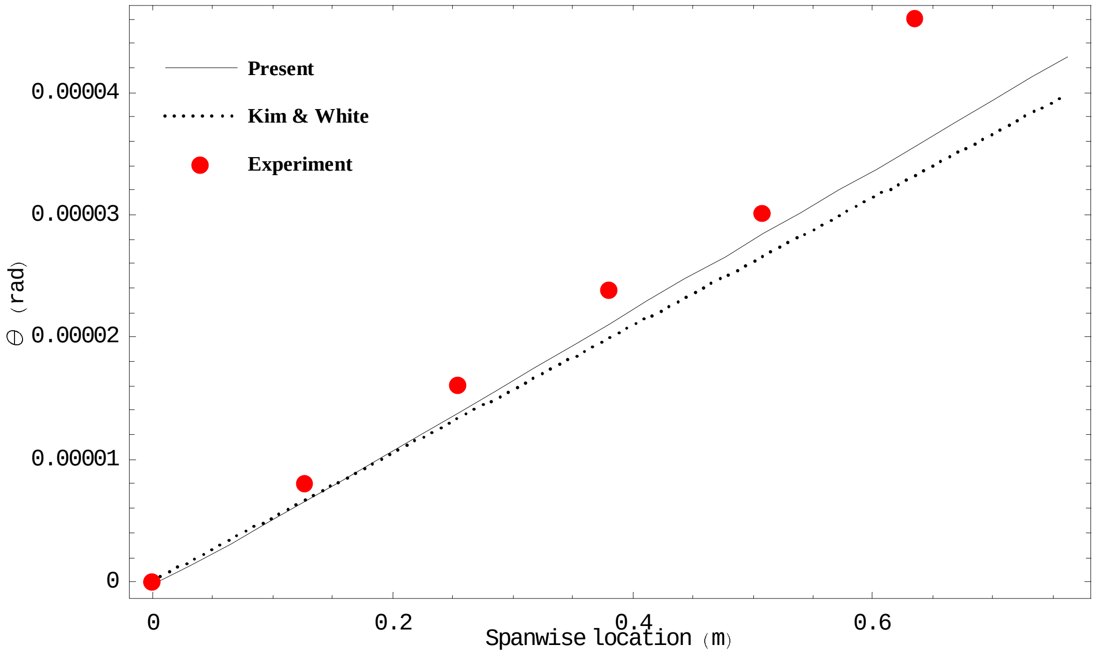

Figure 1.10: Induced twist angle of CUS3 beam by 4.45 N tip extension load.

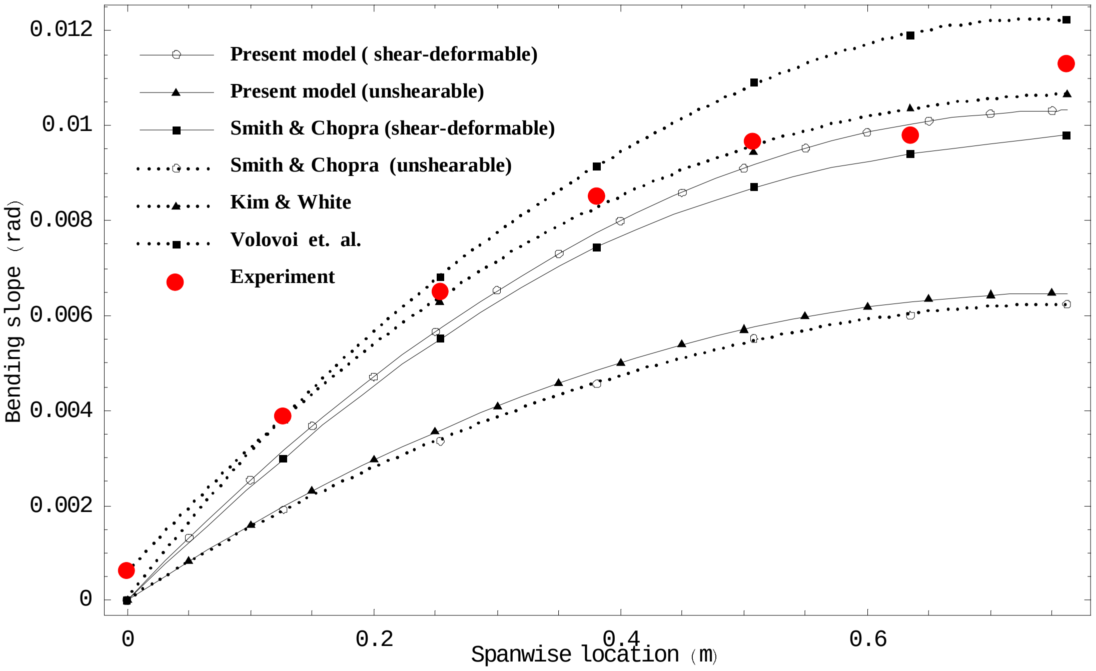

Figure 1.11: Bending slope of CUS1 beam by 4.45 N tip shear load.

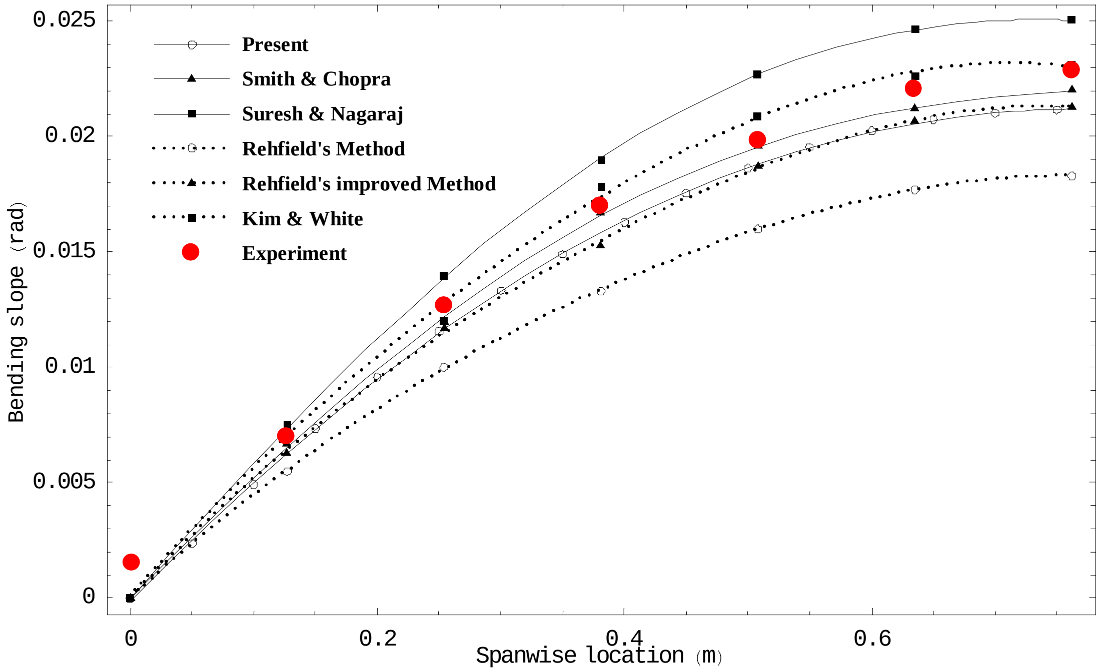

Figure 1.12: Bending Slope of CAS2 beam by 4.45 N tip shear load.

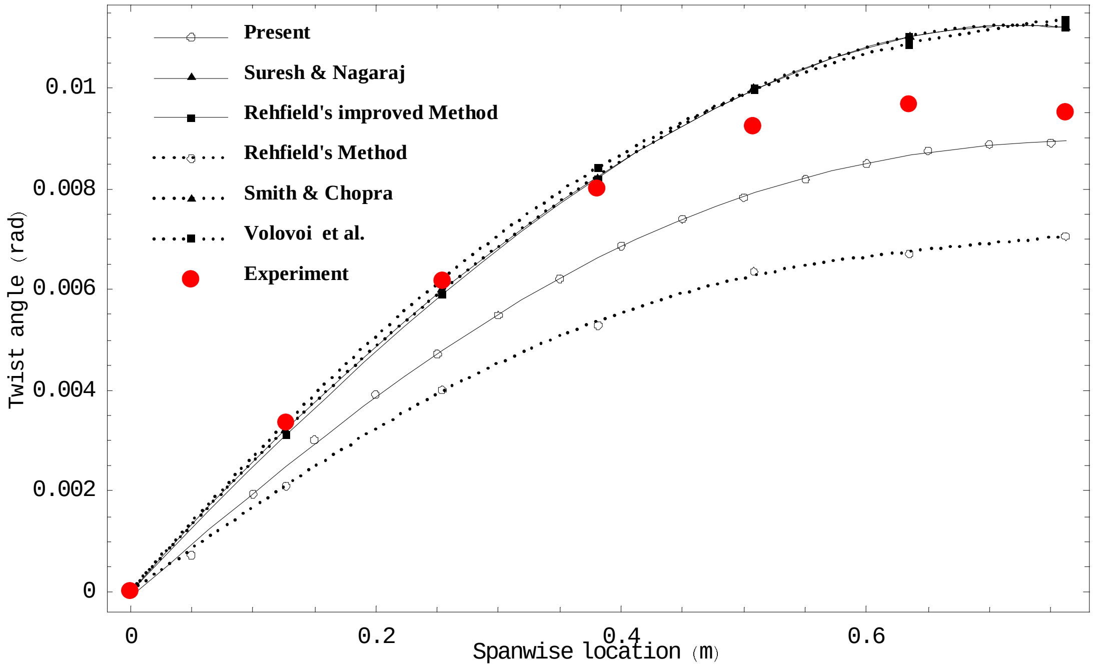

Figure 1.13: Twist angle of CAS1 beam by 4.45 N tip shear load.

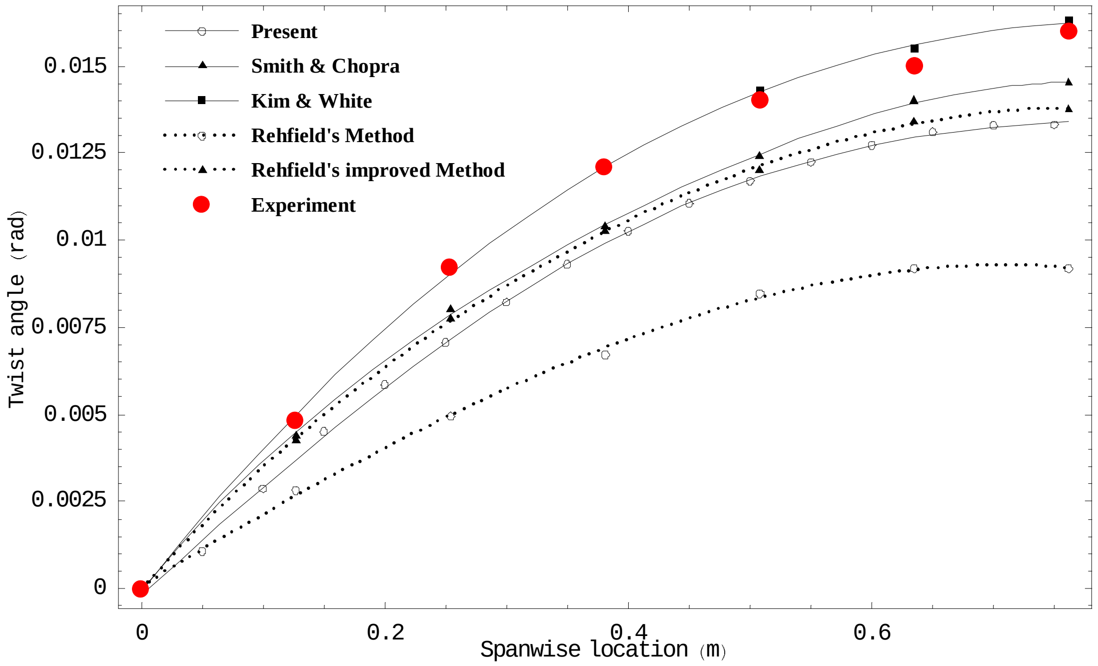

Figure 1.14: Twist angle of CAS2 beam by 4.45 N tip shear load.

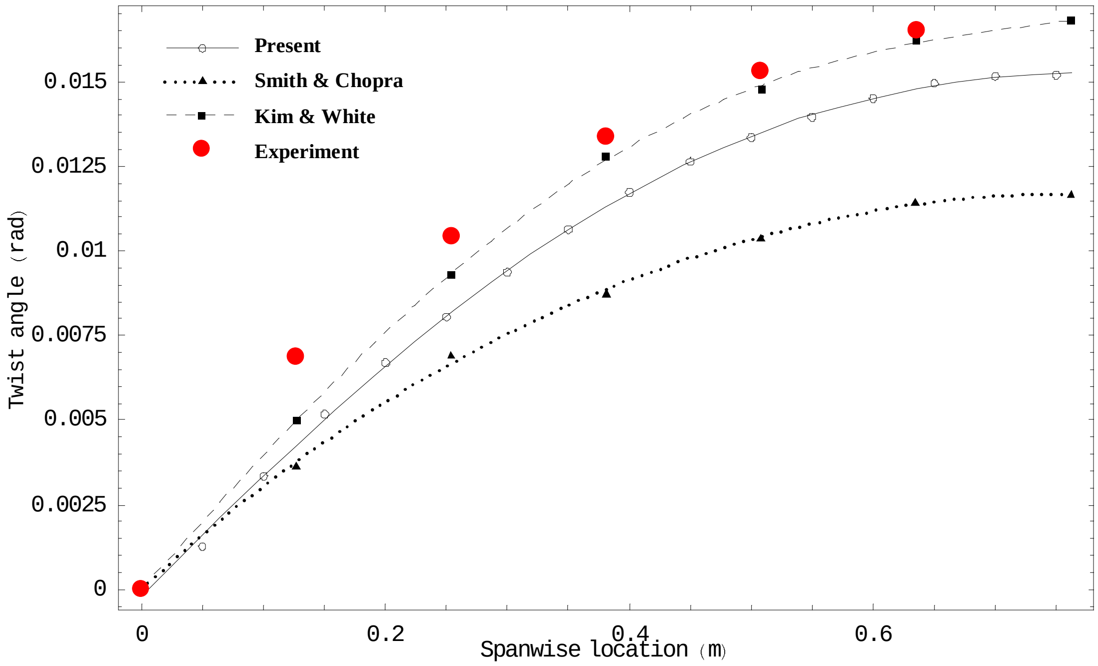

Figure 1.15: Twist angle of CAS3 beam by 4.45 N tip shear load.

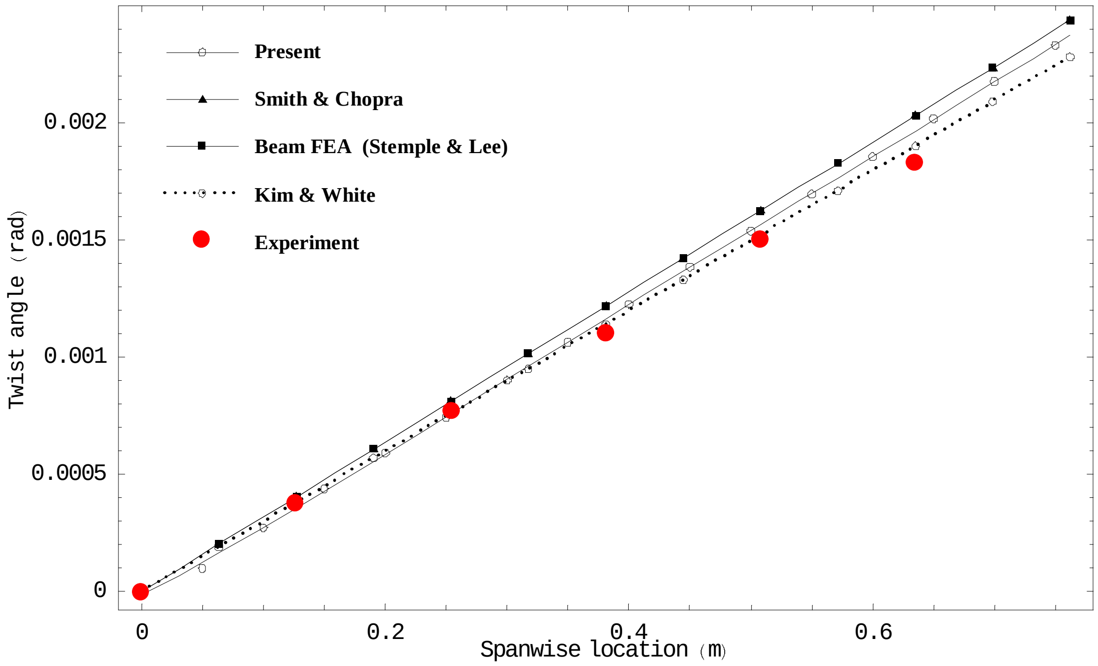

Figure 1.16: Twist angle of CAS1 beam by 0.113 N-m tip torque.

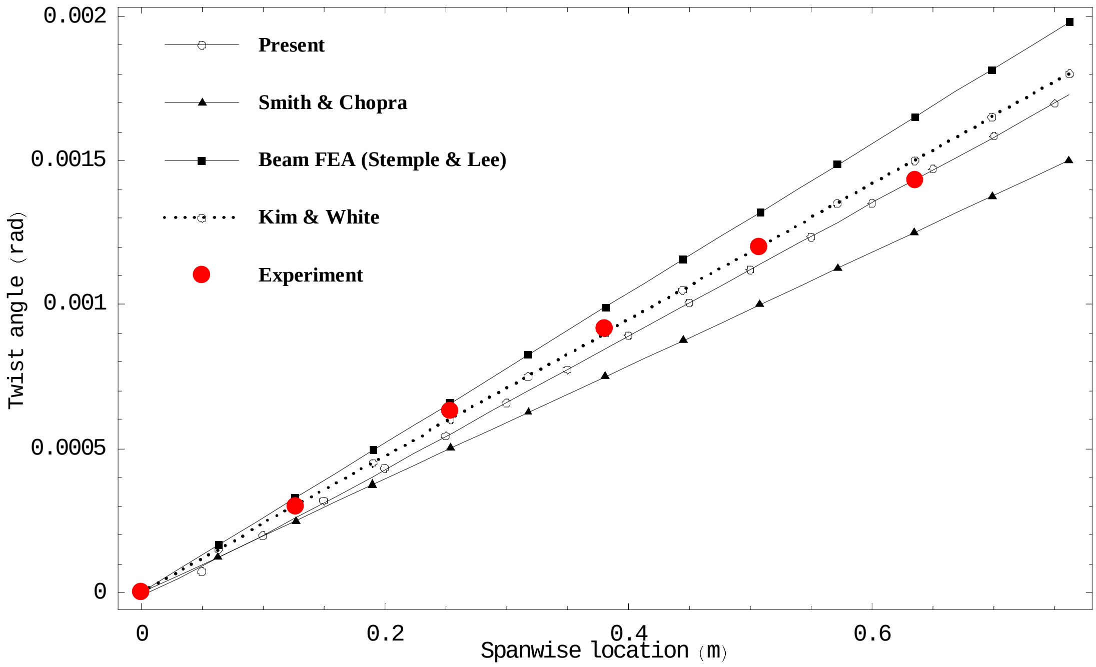

Figure 1.17: Twist angle of CAS2 beam by 0.113 N-m tip torque.

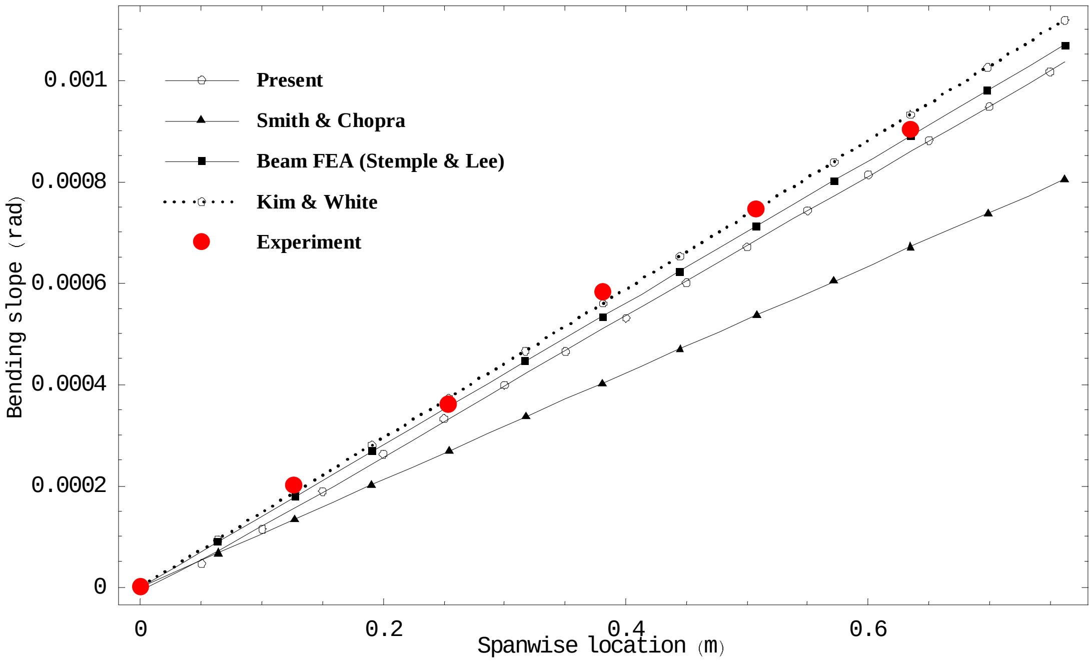

Figure 1.18: Bending slope of CAS3 beam by 0.113 N-m tip torque.

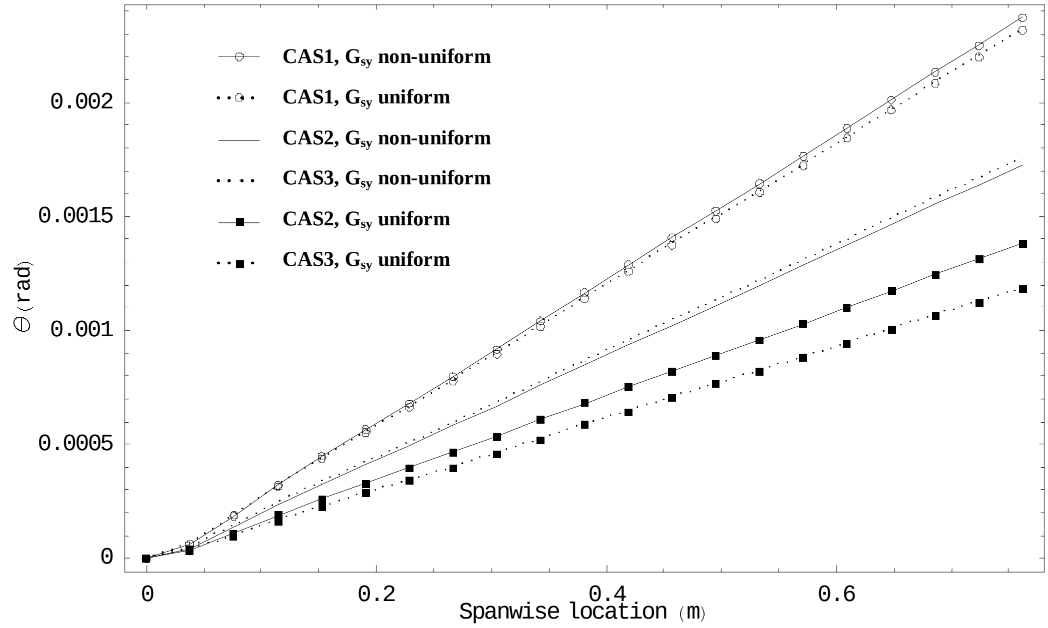

Figure 1.19: Influence of the tranverse shear non-uniformity on the twist deformation of CAS test beams by 0.113 N-m tip torque.

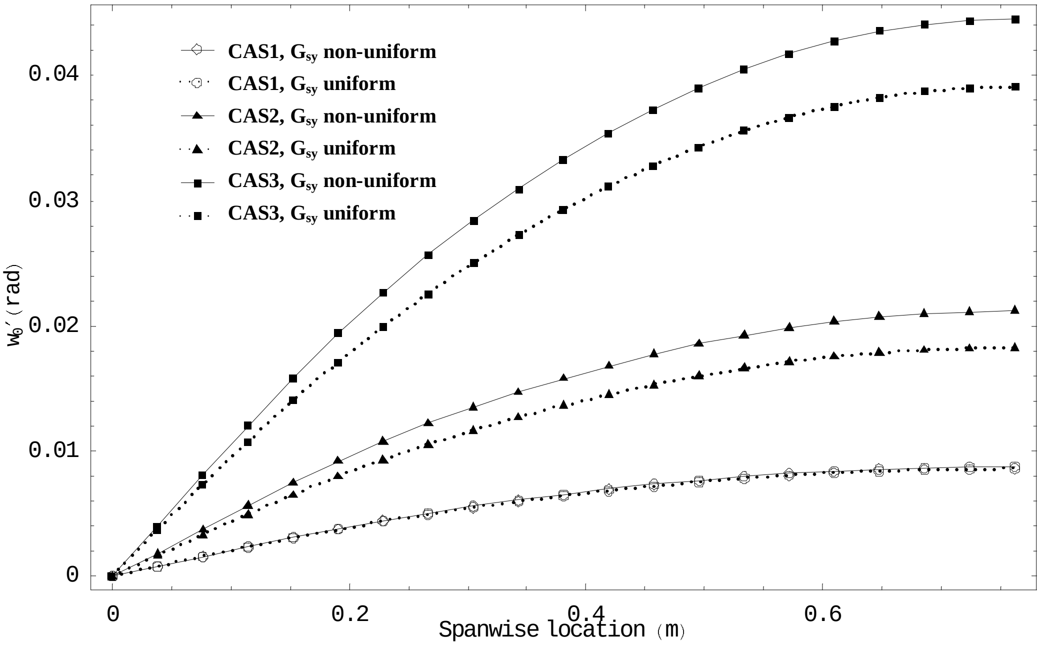

Figure 1.20: Influence of the tranverse shear non-uniformity on the bending slope of CAS test beams by 4.45 N tip shear load.

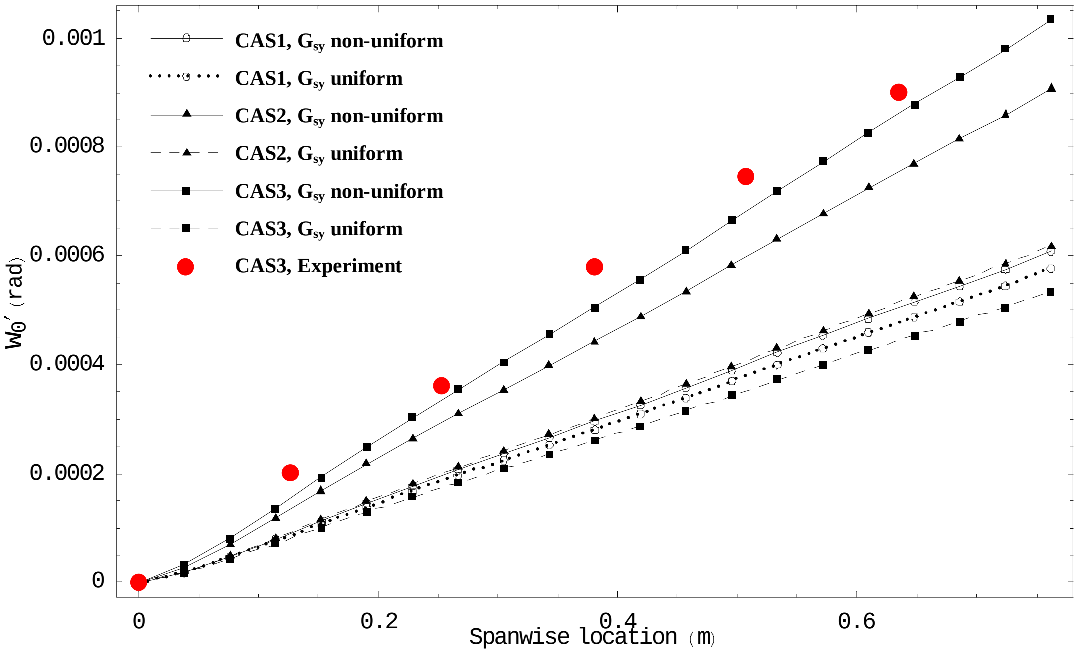

Figure 1.21: Influence of the tranverse shear non-uniformity on the bending slope of CAS test beams by 0.113 N-m tip torque.

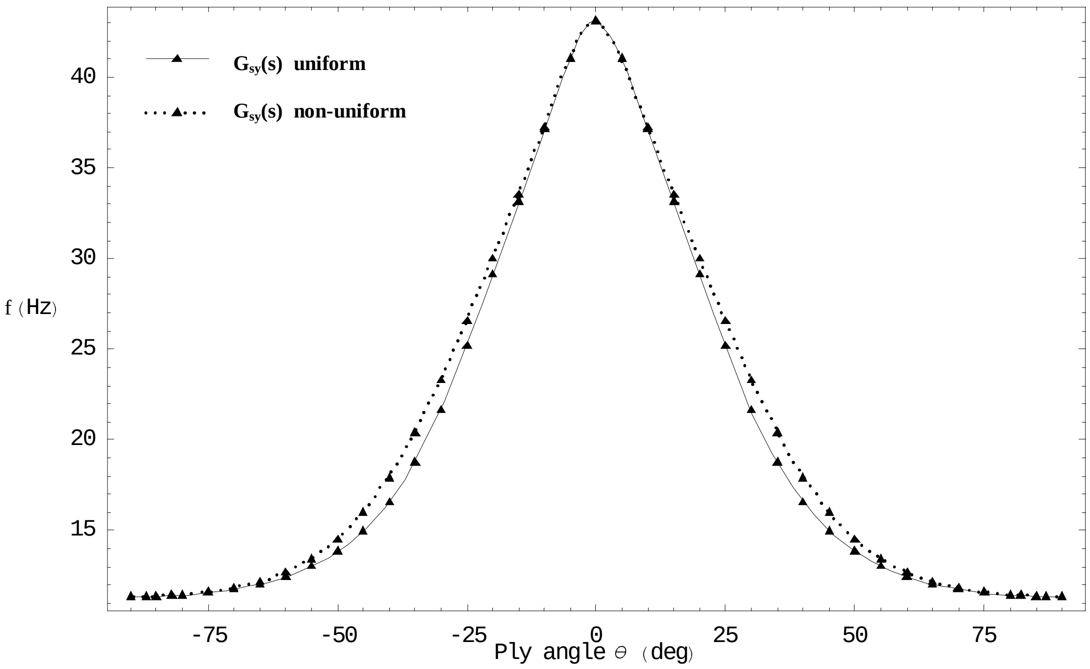

Figure 1.22: Natural frequency vs. ply angle of CAS beams (1st mode) (the material, geometric and lay-ups are listed in the Table 1 in Ref. [3]).

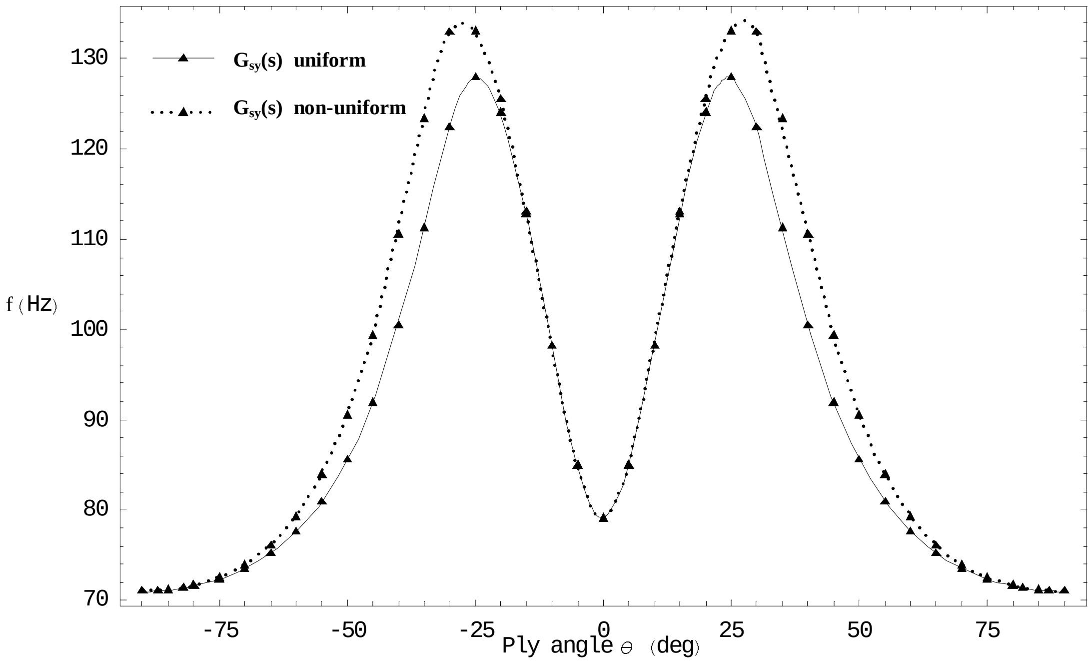

Figure 1.23: Natural frequency vs. ply angle of CAS beams (2nd mode) (the material, geometric and lay-ups are listed in the Table 1 in Ref. [3]).

Chapter 2

Dynamic Aeroelastic Response of Advanced Aircraft Wings Modeled as Thin-Walled Beams

Abstract

The dynamic aeroelastic response of aircraft wings modeled as anisotropic thin-walled beams in an incompressible flow and exposed to gust and blast loads is investigated. The structural model incorporates a number of non-classical effects, such as transverse shear, material anisotropy, warping inhibition, rotatory inertia, etc. The circumferentially asymmetric stiffness (CAS) lay-up configuration is used to generate preferred elastic couplings, and in this context the implication of elastic tailoring on the dynamic aeroelastic response is investigated. The unsteady incompressible aerodynamics for arbitrary small motion in the time domain is used and the finite span effect is included. Due to the non-conservative nature of the boundary value/eigenvalue problem and of the complexity of the structure, non-dimensionalization and spatial semi-discretization are adopted and the aeroelastic governing system is then cast into a state space form. The finite state space approximation of the unsteady aerodynamic loads is derived based on quasi-polynomial approximation of the Wagner's function and the spatial semi-discretization is based on the

---

[0] A slightly different version of this chapter has been submitted for publication to the *Journal of Aircraft*

extended Galerkin's method (EGM). The effects of elastic tailoring on the dynamic aeroelastic response under selected gust and blast loads are discussed and pertinent conclusions are outlined.

2.1 Introduction

It is a well-known fact that the next generation of advanced flight vehicles, in general, and the combat aircraft of the post-cold era, in particular, are likely to operate in more severe environmental conditions than in the past. In this connection, the dynamic aeroelastic response of advanced aircraft wings to time-dependent external loading, such as gust, sonic boom and explosive blast induced loads, is closely related to the level of the operational qualities of these flight vehicles. In spite of the evident practical importance of the problem involving the determination of the dynamic aeroelastic response of flight vehicles to time-dependent pressure pulses, there are very few works addressing this issue. To the best of the authors' knowledge, the literature devoted to the dynamic aeroelastic response is quite void of such works. A recent paper, (see Ref. 1), considers the problem in a comprehensive form, including the combination of various gusts and explosive blast loads. However, the structural model is still based on the 2-D cross-section. This article approaches the problem in an extended context in the sense that the aircraft wing is modeled as an anisotropic thin-walled beam and based on it, the elastic tailoring effects on the dynamic aeroelastic response are investigated. Special attention is given to the formulation of the problem and the solution methodology. It should be noted that due to the non-conservative nature of the problem, the classical modal analysis is not efficient for the solution. As emphasized in Ref. 2, the solution of a general non-conservative system requires a state space description. Correspondingly, the unsteady aerodynamic loads have to be cast into a compatible form, i.e., in a finite state form. Other advantages of using finite state space form of unsteady aerodynamic loads include the facts that the dynamic instability problem (flutter) can be solved in a usual way and the control can be incorporated very conveniently. Also to be noted here is that the structural model used in this paper was mainly developed in Refs. 3–6. However, in order to be reasonably self-contained, a number of basic ingredients related to the pertinent governing equations will be displayed.

2.2 Formulation of the Governing System

2.2.1 The Structural Model

A single-cell, closed cross-section, fiber-reinforced composite thin-walled beam is used in the modeling of advanced aircraft wings for the study of the dynamic subcritical aeroelastic response. Due to the importance demonstrated in Refs. 3–11, a number of non-classical effects have to be considered, which include transverse shear, anisotropy of the constituent material, warping inhibition [3–6]), 3-D strain effects [6, 7, 10, 11]. It should be noted that the original development of the beam theory in Refs. 3–5 does not consider the variation of contour-wise shear stiffness, which was later extended in Ref. 6. For its geometric configuration and the chosen coordinate system that is usually adopted in the analyses of aircraft wings, see Figs. 1a through 1d. Based on the basic assumptions stated in Refs. 3–5, the following representation of the 3-D displacement quantities is postulated:

$$u(x,y,z,t) = u_0(y,t) + z\phi(y,t); \quad w(x,y,z,t) = w_0(y,t) - x\phi(y,t); \tag{2.1a}$$

$$v(x,y,z,t) = v_0(y,t) + [x(s) - n\frac{dz}{ds}]\theta_z(y,t) + [z(s) + n\frac{dx}{ds}]\theta_x(y,t) - [F_w(s) + na(s)]\phi'(y,t) \tag{2.1b}$$

where

$$\theta_x(y,t) = \gamma_{yz}(y,t) - w_0'(y,t); \theta_z(y,t) = \gamma_{xy}(y,t) - u_0'(y,t); a(s) = -(z\frac{dz}{ds} + x\frac{dx}{ds}) \tag{2.2}$$

In the above expressions, $\theta_x(y,t)$, $\theta_z(y,t)$ and $\phi(y,t)$ denote the rotations of the cross-section about the axes x, z and the twist about the y axis, respectively, $\gamma_{yz}(y,t)$ and $\gamma_{xy}(y,t)$ denote the transverse shear strain measures.

The warping function in Eq.(2.1b) is expressed as

$$F_w(s) = \int_0^s [r_n(s) - \psi(s)]ds \tag{2.3}$$

in which the torsional function $\psi(s)$ and the quantity $r_n(s)$ are expressed as

$$\psi(s) = \frac{\oint_C r_n(\bar{s})d\bar{s}}{h(s)G_{sy}(s)\oint_C \frac{d\bar{s}}{h(\bar{s})G_{sy}(\bar{s})}}; \quad r_n(s) = z\frac{dx}{ds} - x\frac{dz}{ds} \tag{2.4}$$

where $G_{sy}(s)$ is the effective membrane shear stiffness, which is defined as [6]:

$$G_{sy}(s) = \frac{N_{sy}}{h(s)\gamma^0_{sy}(s)} \tag{2.5}$$

Notice that for the thin-walled beam theory considered herein, the six kinematic variables, $u_0(y,t),\ v_0(y,t),\ w_0(y,t),\ \theta_x(y,t),\ \theta_z(y,t),\ \phi(y,t)$, which represent 1-D displacement measures, constitute the basic unknowns of the problem. When the transverse shear effect is ignored, Eq. (2.2) degenerates to $\theta_x = -w_0'$, $\theta_z = -u_0'$, and as a result, the number of basic unknown quantities reduces to four. Such a case leads to the classical, unshearable beam model.

The strains contributing to the potential energy are:

Spanwise strain:

$$\varepsilon_{yy}(n,s,y,t) = \varepsilon^0_{yy}(s,y,t) + n\varepsilon^n_{yy}(s,y,t) \tag{2.6a}$$

where

$$\varepsilon^0_{yy}(s,y,t) = {v_0}'(y,t) + {\theta_z}'(y,t)x(y,t) - \phi''(y,t)F_w(s) \tag{2.6b}$$

$$\varepsilon^n_{yy}(s,y,t) = -{\theta_z}'(y,t)\frac{dz}{ds} + {\theta_x}'(y,t)\frac{dx}{ds} - a(s)\phi''(y,t) \tag{2.6c}$$

are the axial strain components associated with the primary and secondary warping, respectively.

Tangential shear strain:

$$\gamma_{sy}(s,y,t) = \gamma^0_{sy}(s,y,t) + \psi(s)\phi'(y,t) \tag{2.7a}$$

$$\textit{where } \gamma^0_{sy}(s,y,t) = \gamma_{xy}\frac{dx}{ds} + \gamma_{yz}\frac{dz}{ds} = [u_0' + \theta_z]\frac{dx}{ds} + [w_0' + \theta_x]\frac{dz}{ds} \tag{2.7b}$$

Transverse shear strain measure:

$$\gamma_{ny}(s,y,t) = -\gamma_{xy}\frac{dz}{ds} + \gamma_{yz}\frac{dx}{ds} = -[u_0' + \theta_z]\frac{dz}{ds} + [w_0' + \theta_x]\frac{dx}{ds} \tag{2.8}$$

The stress resultants and stress couples can be reduced to the following expressions:

$$\left\{ \begin{array}{c} N_{yy} \\ N_{sy} \\ L_{yy} \\ L_{sy} \end{array} \right\} = \left[\begin{array}{cccc} K_{11} & K_{12} & K_{13} & K_{14} \\ K_{21} & K_{22} & K_{23} & K_{24} \\ K_{41} & K_{42} & K_{43} & K_{44} \\ K_{51} & K_{52} & K_{53} & K_{54} \end{array} \right] \left\{ \begin{array}{c} \varepsilon_{yy}^0 \\ \gamma_{sy}^0 \\ \phi' \\ \varepsilon_{yy}^n \end{array} \right\} \tag{2.9a}$$

$$N_{ny} = [A_{44} - \frac{A_{45}^2}{A_{55}}]\gamma_{ny} \tag{2.9b}$$

in which the reduced stiffness coefficients K_{ij} are defined in Appendix A.

2.2.2 Unsteady Aerodynamic Loads for Arbitrary Small Motion in Incompressible Flow

Based on the strip theory and 2-D incompressible unsteady aerodynamics, the unsteady aerodynamic lift and aerodynamic twist moment about the reference axis (in this paper, the mid-chord locus is adopted as the reference axis) can be expressed as (see Fig. 2.3): [12]

$$L_{ae}(y,t) = \rho_\infty U_n \Gamma_0(y,t) - \rho_\infty \frac{d}{dt}\int_{-b}^{b} \gamma_0(x,y,t)x dx + \rho_\infty U_n \int_{-b}^{\infty} \frac{\gamma_w(x,y,t)}{\sqrt{x^2-b^2}} dx \tag{2.10a}$$

$$\begin{aligned} T_{ae}(y,t) = & -\rho_\infty U_n \int_{-b}^{b} \gamma_0(x,y,t)x\,dx + \frac{1}{2}\rho_\infty \frac{d}{dt}\int_{-b}^{b} \gamma_0(x,y,t)(x^2 - \frac{1}{2}b^2)dx \\ & + \frac{1}{2}\rho_\infty U_n b^2 \int_{-b}^{\infty} \frac{\gamma_w(x,y,t)}{\sqrt{x^2-b^2}} dx \end{aligned} \tag{2.10b}$$

where U_n is the free stream speed normal to the leading edge, $\gamma_0(x,y,t)$ is the quasi-steady distributed bound vortex intensity (on the wing), $\gamma_w(x,y,t)$ is the vortex intensity in the wake, and $\Gamma_0(y,t)$ is the quasi-steady circulation. From the potential aerodynamic theory, $\gamma_0(x,y,t)$, $\gamma_w(x,y,t)$ can be uniquely determined by the boundary (no-penetration) condition and the Kutta condition, as illustrated in the following.

Expressed in the body-fixed frame [13, 14] (see Fig. 2.3), the vertical position of any point in the wing cross-section can be expressed as:

$$z_a(x, y, t) = w_0(y, t) - \phi(y, t)x \tag{2.11}$$

where $w_0(y, t)$ and $\phi(y, t)$ denote the plunging displacement of the points belonging to the reference axis; and the twist about this axis, respectively. It should be noted that the rigid angle of attack is not considered in this article.

Denote $F(x, y, z, t) = z_a(x, y, t) - w_0(y, t) - \phi(y, t)x = 0$, then the no-penetration condition of the flow can be expressed as:

$$\frac{DF(x, y, t)}{Dt} = \frac{\partial F}{\partial t} + \mathbf{U} \cdot \nabla F = \frac{\partial F}{\partial t} + (U_n + u_b + u_w)\frac{\partial F}{\partial x} + v\frac{\partial F}{\partial y} + (w_b + w_w)\frac{\partial F}{\partial z} = 0 \tag{2.12}$$

where $u_b = \frac{\partial \Phi_b}{\partial x}, u_w = \frac{\partial \Phi_w}{\partial x}$, and $w_b = \frac{\partial \Phi_b}{\partial z}, w_w = \frac{\partial \Phi_w}{\partial z}$, in which Φ_b, Φ_w are potential functions of the bound vortex and the wake. Based on the thin-airfoil theory and small perturbation assumption [13], we get

$$w_b(x, y, z, t)|_{z \to 0} = \frac{\partial \Phi_b}{\partial z}|_{z \to 0} = -\frac{1}{2\pi} \int_{-b}^{b} \frac{\gamma_b(\xi, y, t) d\xi}{x - \xi} \tag{2.13a}$$

$$w_w(x, y, z, t)|_{z \to 0} = \frac{\partial \Phi_w}{\partial z}|_{z \to 0} = -\frac{1}{2\pi} \int_{b}^{\infty} \frac{\gamma_w(\xi, y, t) d\xi}{x - \xi} \tag{2.13b}$$

and the downwash:

$$\begin{aligned} w_a(x, y, t) &\equiv \frac{\partial z_a}{\partial t} + U_n \frac{\partial z_a}{\partial x} \\ &= \dot{w}_0 - x\dot{\phi} - U_n \phi = -\frac{1}{2\pi} \int_{-b}^{b} \frac{\gamma_b(\xi, y, t) d\xi}{x - \xi} - \frac{1}{2\pi} \int_{b}^{\infty} \frac{\gamma_w(\xi, y, t) d\xi}{x - \xi} \end{aligned} \tag{2.13c}$$

In Eqs. (2.13b and 2.13c), the wake is assumed to be in a flat plane. From Eq. (2.13c), the downwash quantities at the mid-chord and three quarter locations are:

$$w_{0.5c}(y, t) \equiv w_a(x, y, t)|_{x=0} = \dot{w}_0 - U_n \phi, \tag{2.14a}$$

$$w_{0.75c}(y, t) \equiv w_a(x, y, t)\Big|_{x=\frac{1}{2}b} = \dot{w}_0 - U_n \phi - \frac{1}{2} b\dot{\phi} \tag{2.14b}$$

Following the works by Theodorsen15, von Kármán and Sears12 (see also Bisplinghoff et al,

For the quasi-steady part of the solution,

$$w_a(x,y,t) \equiv \dot{w}_0 - x\dot{\phi} - U_n\phi = -\frac{1}{2\pi}\int_{-b}^{b}\frac{\gamma_0(\xi,y,t)d\xi}{x-\xi} \tag{2.15a}$$

$$\Gamma_0(y,t) = \int_{-b}^{b}\gamma_0(\xi,y,t)d\xi \tag{2.15b}$$

while for the influence of the wake,

$$0 = -\frac{1}{2\pi}\int_{-b}^{b}\frac{\gamma_1(\xi,y,t)d\xi}{x-\xi} - \frac{1}{2\pi}\int_{b}^{\infty}\frac{\gamma_w(\xi,y,t)d\xi}{x-\xi} \tag{2.16a}$$

$$\Gamma_1(y,t) = \int_{-b}^{b}\gamma_1(\xi,y,t)d\xi = \int_{b}^{\infty}[\sqrt{\frac{\xi+b}{\xi-b}} - 1]\gamma_w(\xi,y,t)d\xi \tag{2.16b}$$

Obviously, the total circulation on the airfoil is:

$$\Gamma_b(y,t) = \Gamma_0(y,t) + \Gamma_1(y,t) \tag{2.17}$$

The Kutta condition applied at the trailing edge is: [13]

$$\Gamma_0(y,t) + \int_{b}^{\infty}\sqrt{\frac{\xi+b}{\xi-b}}\gamma_w(\xi,y,t)d\xi = 0 \tag{2.18}$$

The procedure of the solution consists firstly, of solving the integral equation [Eq. (2.15a)] by using Söhngen's inverse formulas of integral equations [13], then getting the expression of $\gamma_0(x,y,t)$, and$\Gamma_0(y,t)$, and solving the integral equation [Eq. (2.18)] to get the expression of $\gamma_w(x,y,t)$. In his paper [16], Sears has shown that the spatial Laplace Transform technique can significantly reduce the complexity of the derivations. Finally, we get:

$$\begin{aligned}\Gamma_0(y,t) &= -2b\int_{-1}^{1}\sqrt{\frac{1+\hat{\xi}}{1-\hat{\xi}}}[\dot{w}_0 - U_n\phi - b\hat{\xi}\dot{\phi}]d\hat{\xi} \\ &= -2\pi b[\dot{w}_0 - U_n\phi - \frac{1}{2}b\dot{\phi}] \equiv -2\pi b w_{0.75c}(y,t)\end{aligned} \tag{2.19a}$$

$$\begin{aligned} L_{ae}(y,t) &= -\pi\rho_\infty b^2[\dot{w}_{0.5c}(y,t)] \\ &\quad \underline{-\,2\pi\rho_\infty U_n b\{w_{0.75c}(y,0)\phi_W(\frac{U_n t}{b}) + \int_0^t \frac{dw_{0.75c}(t_0)}{dt_0}\phi_W(\frac{U_n}{b}(t-t_0))dt_0\}} \end{aligned} \tag{2.19b}$$

$$\begin{aligned} T_{ae}(y,t) &= -\pi\rho_\infty b^3[\frac{1}{2}U_n\dot{\phi} + \frac{1}{8}b\ddot{\phi}] \\ &\quad \underline{-\,\pi\rho_\infty U_n b^2\{w_{0.75c}(y,0)\phi_W(\frac{U_n t}{b}) + \int_0^t \frac{dw_{0.75c}(t_0)}{dt_0}\phi_W(\frac{U_n}{b}(t-t_0))dt_0\}} \end{aligned} \tag{2.19c}$$

where ϕ_W is the Wagner's function fulfilling

$$\frac{d\phi_W(\tau)}{d\tau} = \mathcal{L}^{-1}[\frac{K_1(p)}{K_0(p)+K_1(p)}] \tag{2.20}$$

in which, $\tau = U_n t/b$ is the non-dimensional time, $\mathcal{L}^{-1}$ is the inverse Laplace Transform operator; p is the Laplace-transform variable (the counterpart of τ), while $K_0(p)$ and$K_1(p)$ are the modified Bessel functions of the $2nd$ kind [2, 16]). In Eqs. (2.19b, c), the terms underlined are associated with the *circulatory* part of the aerodynamic loads. The quantity $K_1(p)/(K_0(p)+K_1(p)) \equiv C(p)$ is identified as the generalized Theodorsen function in the Laplace transformed domain [17].

In order to cast L_{ae}, T_{ae} to state space form, the quasi-polynomial approximation of the lift deficiency function is used: [13, 17, 20]

$$\phi_W(\tau) = [1.0 - \sum_{i=1}^{n} \alpha_i \exp(-\beta_i\tau)]H(\tau) \tag{2.21}$$

where $H(\tau)$denotes the Heaviside's step function.

By denoting

$$D(y,t) \doteq \int_0^t \frac{\partial w_{0.75c}(y,t_0)}{\partial t_0}\phi_W(\frac{U_n(t-t_0)}{b})dt_0, \tag{2.22}$$

we get

$$D(y,t) = w_{0.75c}(y,t) - \sum_{i=1}^{n} \alpha_i B_i(y,t) \tag{2.23}$$

where $B_i(y,t)$ satisfies $\dot{B}_i + (\beta_i\frac{U_n}{b})B_i = \dot{w}_{0.75c}(y,t)$

In the following derivation, we assume that the wing starts from rest.

Compared with the methods based on the transfer function realization, the present method can easily model as many as necessary aerodynamic lag terms into the finite state space form. It should be noted that this method yields the same number of augmented states as those provided by the Roger's approximation method [18].

The above results are for 2-D cross-section wings. For a finite-span wing, the modified strip theory [13, 19] is used to extend the 2-D aerodynamics to the 3-D one. Firstly, in order to be able to approach also the case of swept aircraft wings, the reference coordinate system is being rotated with the wing by the sweep angle Λ [13]. Secondly, the lift curve slope 2π and the downwash boundary condition (i.e., three quarter rule for 2-D aerodynamics model) are modified to account for the finite span effects [13, 19, 20]:

$$2\pi \longrightarrow C_{L\phi} = \frac{dC_L}{d\phi} = \frac{\text{Æ}}{\text{Æ} + 2\cos\Lambda} 2\pi, \quad \frac{1}{2}b \rightarrow b[\frac{C_{L\phi}}{2\pi} - \frac{1}{2}] \tag{2.24}$$

It should be noted that only the *circulatory* terms in Eqs. (2.19b, c) will be modified [19, 20]. All the geometric measures are now taken in the rotated chordwise coordinate system (see Fig. 2.1).

As to the frame transformation, we follow the procedure in Ref. 13. After collecting the coefficients of the chordwise coordinate x, the downwash velocity in the rotated coordinate system is expressed as:

$$\begin{aligned} w_a(x, y, t) \tilde{=} \frac{\partial z_a}{\partial t} + \frac{\partial z_a}{\partial \bar{x}} &= \frac{\partial z_a}{\partial t} + U_\infty(\frac{\partial z_a}{\partial x} + \frac{\partial z_a}{\partial y}\sin\Lambda) \\ &= [\dot{w}_0 - U_\infty \phi\cos\Lambda + U_\infty \sin\Lambda \frac{\partial w_0}{\partial y}] - x[\dot{\phi} + U_\infty \frac{\partial \phi}{\partial y}\sin\Lambda] \end{aligned} \tag{2.25}$$

Replacing $\dot{w}_0 - U_n\phi$ by $\dot{w}_0 - U_\infty\phi\cos\Lambda + U_\infty \sin\Lambda\frac{\partial w_0}{\partial y}$; $\dot{\phi}$ by $\dot{\phi} + U_\infty\frac{\partial\phi}{\partial y}\sin\Lambda$ in the preceding formulas, and denoting $U_n \equiv U_\infty \cos\Lambda$, we get:

$$w_{0.75c}(y, t) = \dot{w}_0 - U_n\phi + U_n \tan\Lambda \frac{\partial w_0}{\partial y} - \frac{b}{2}[\dot{\phi} + U_n \frac{\partial \phi}{\partial y}\tan\Lambda][\frac{C_{L\phi}}{\pi} - 1] \tag{2.26a}$$

$$w_{0.5c}(y, t) = \dot{w}_0 - U_n\phi + U_n \tan\Lambda \frac{\partial w_0}{\partial y} \tag{2.26b}$$

Based on these equations, the explicit expressions of unsteady aerodynamic lift and moment will be given in the following sections.

2.2.3 Gust and blast loads

Based on the Duhamel's integral and the indicial function for an arbitrary gust $w_G(\tau)$, the induced aerodynamic lift is expressed as:

$$L_g(\tau) = C_{L\phi} b U_n [w_G(0)\psi_K(\tau) + \int_0^\tau \frac{\partial w_G(\tau_0)}{\partial \tau_0} \psi_K(\tau - \tau_0) d\tau_0] \tag{2.27}$$

where $\psi_K(\tau) = \mathcal{L}^{-1}[\frac{1}{pe^p}\frac{1}{K_0(p)+K_1(p)}]$ is the Küssner's function.[16] In the practical calculation, ψ_K can be approximated by the following quasi-polynomials [13]:

$$\psi_K(\tau) = 1 - 0.500e^{-0.130\tau} - 0.500e^{-1.00\tau}, \quad \tau > 0 \tag{2.28}$$

As proved by von Kármán and Sears [12], the gust embedded in the atmosphere and flowing with the atmosphere always acts at the quarter-chord position, even when the aerodynamic load is not completely circulatory. For simplicity, we assume that the gust is not affected by the penetration of the wing. Therefore, the aerodynamic moment about the reference axis due to the gust is

$$T_g(\tau) = \frac{1}{2} b L_g(\tau) = \frac{1}{2} C_{L\phi} b^2 U_n [w_G(0)\psi_K(\tau) + \int_0^\tau \frac{\partial w_G(\tau_0)}{\partial \tau_0} \psi_K(\tau - \tau_0) d\tau_0] \tag{2.29}$$

In general, a gust (discrete model, as considered in this paper) can be specified by the gust intensity, gradient and its profile [13]. In this article, the gust intensity is assumed to be uniformly distributed along the span. The following types of gust are used in the present study of aeroelastic response:

- Sharp-edged gust: $w_G(\tau) = H(\tau)V_G$
- 1-COSINE gust: $w_G(\tau) = \frac{1}{2}V_G(1 - \cos\frac{\pi\tau}{\tau_p})[H(\tau) - H(\tau - 2\tau_p)]$

where V_G is the peak gust velocity, τ_p is the gust gradient expressed in semichord length.[12] Other types of gusts are listed in Ref. 1.

The blast load due to a sonic boom signature can be modeled as an N-shaped pressure pulse [1, 7]:

$$L_b(\tau) = P_m(1 - \frac{\tau}{\tau_p})[H(\tau) - H(\tau - r\,\tau_p)] \tag{2.30}$$

in which, P_m is the peak reflected pressure in excess to the ambient pressure and τ_p is the positive phase duration of the pressure pulse, r is the pulse length factor [1, 7]. When $r = 1$, the N-shaped pulse degenerates into an explosive pulse (in triangular form) and when $r = 2$, a symmetric sonic-boom pulse is obtained [1]. For blast loads, we assume that these act throughout the wing.

2.2.4 The Governing System

The governing equations and boundary conditions can be systematically derived from the extended Hamilton's Principle,[2]which states that the true path of motion renders the following variational form stationary:

$$\int_{t_1}^{t_2} (\delta T - \delta V + \overline{\delta W_e})\, dt = 0 \tag{2.31a}$$

with

$$\delta u_0 = \delta v_0 = \delta w_0 = \delta\theta_x = \delta\theta_z = \delta\phi = 0 \quad \text{at } t = t_1,\, t_2 \tag{2.31b}$$

where T and V denote the kinetic energy and strain energy, respectively, while $\overline{\delta W_e}$ denotes the virtual work due to external forces. These are defined as:

Kinetic energy

$$T = \frac{1}{2}\int_0^L \oint_C \sum_{k=1}^{m_l} \int_{h_{(k)}} \rho_{(k)}[(\frac{\partial u}{\partial t})^2 + (\frac{\partial w}{\partial t})^2 + (\frac{\partial v}{\partial t})^2] dndsdy, \tag{2.32}$$

Strain energy

$$\begin{aligned} V &= \frac{1}{2}\int_{\tau} \sigma_{ij}\varepsilon_{ij}\, d\tau \\ &= \frac{1}{2}\int_0^L \oint_C \sum_{k=1}^{m_l} \int_{h_{(k)}} [\sigma_{yy}\varepsilon_{yy} + \sigma_{sy}\gamma_{sy} + \sigma_{ny}\gamma_{ny}]_{h_{(k)}}\, dndsdy \end{aligned} \tag{2.33}$$

Virtual work due to unsteady aerodynamic, gust and blast loads:

$$\overline{\delta W_e} = \int_0^L (p_z(y,t)\delta w_0(y,t) + m_y(y,t)\delta\phi(y,t))\, dy \tag{2.34}$$

where $p_z = L_{ae} + L_g + L_b$ (positive upwards) is the combined aerodynamic lift per unit span length and $m_y = T_{ae} + T_g$ (positive nose-up) aerodynamic twist moments about the reference axis.

In order to study the dynamic aeroelastic response featuring bending-twist cross-coupling, the beams featuring circumferentially asymmetric stiffness (CAS) lay-up configuration (see Ref. [9]) and with the biconvex cross-section are considered. As demonstrated in Refs. [4, 5], this type of beams feature the following two sets of completely independent elastic couplings:

- vertical bending/twist/vertical transverse shear (w_0, ϕ, θ_x)
- extension/lateral bending/lateral transverse shear (u_0, v_0, θ_z)

Also, the aerodynamic loads and the inertia forces of the beams are completely split into the above two groups, hence the total equations of motion and the boundary conditions are completely decoupled. Therefore, the second group in the above mentioned sets can be safely discarded. The equations of motion of the first group that are of interest for the present problem are:

$$\delta w_0: \quad Q_z' + L_{ae} + L_g + L_b - b_1\ddot{w}_0 = 0 \tag{2.35a}$$

$$\delta\phi: \quad M_y' - B_w'' + T_{ae} + T_g - (b_4 + b_5)\ddot{\phi} + (b_{10} + b_{18})\ddot{\phi}'' = 0 \tag{2.35b}$$

$$\delta\theta_x : \quad M_x' - Q_z - (b_4 + b_{14})\ddot{\theta}_x = 0 \tag{2.35c}$$

Boundary conditions:

$$\begin{aligned}
&\text{At } y = 0,\ w_0 = 0, \quad \phi = 0, \quad \phi' = 0, \quad \theta_x = 0 \\
&\text{At } y = L, Q_z = 0, \quad -B_w' + M_y + (b_{10} + b_{18})\ddot{\phi}' = 0, \\
&\qquad B_w = 0, \quad M_x = 0
\end{aligned} \tag{2.36}$$

In the above equations, M_x, Q_z, B_w, M_y are the 1-D stress resultant and stress couple measures that are defined as:

$$\begin{aligned}
M_x(y,t) &= \oint_C (zN_{yy} + L_{yy}\frac{dx}{ds})ds & Q_z(y,t) &= \oint_C (N_{sy}\frac{dz}{ds} + N_{ny}\frac{dx}{ds})ds \\
B_w(y,t) &= -\oint_C [F_w(s)N_{yy} + a(s)L_{yy}]ds & M_y(y,t) &= \oint_C N_{sy}\psi(s)ds
\end{aligned} \tag{2.37}$$

The inertia coefficients b_1, b_4, b_5, b_{10}, b_{14}, b_{15}, b_{18} are defined in Appendix A.

For biconvex cross-section thin-walled beams with CAS lay-up configuration, the force-displacement relations are:

$$\begin{Bmatrix} M_x \\ Q_z \\ B_w \\ M_y \end{Bmatrix} = \begin{bmatrix} a_{33} & 0 & 0 & a_{37} \\ 0 & a_{55} & a_{56} & 0 \\ 0 & a_{56} & a_{66} & 0 \\ a_{37} & 0 & 0 & a_{77} \end{bmatrix} \begin{Bmatrix} \theta_x' \\ (w_0' + \theta_x) \\ \phi'' \\ \phi' \end{Bmatrix} \tag{2.38}$$

For the free warping model (see Refs. [4, 5, 8]), the force-displacement relations are:

$$\begin{Bmatrix} M_x \\ Q_z \\ B_w \\ M_y \end{Bmatrix} = \begin{bmatrix} a_{33} & 0 & a_{37} \\ 0 & a_{55} & 0 \\ 0 & a_{56} & 0 \\ a_{37} & 0 & a_{77} \end{bmatrix} \begin{Bmatrix} \theta_x' \\ (w_0' + \theta_x) \\ \phi' \end{Bmatrix} \tag{2.39}$$

In terms of the basic unknowns, the governing equations that include all the above mentioned effects are:

$$\delta w_0 \ : \quad a_{55}(w_0'' + \theta_x') + \underline{\underline{a_{56}\phi'''}} + L_{ae} + L_g + L_b - b_1\ddot{w}_0 = 0 \tag{2.40a}$$

$$\delta\phi \ : \quad a_{37}\theta_x'' + a_{77}\phi'' - a_{56}(w_0''' + \theta_x'') - \underline{\underline{a_{66}\phi^{(IV)}}} + T_{ae} + T_g - (b_4 + b_5)\ddot{\phi} + \underline{\underline{(b_{10} + b_{18})\ddot{\phi}''}} = 0 \tag{2.40b}$$

$$\delta\theta_x \ : \quad a_{33}\theta_x'' + a_{37}\phi'' - a_{55}(w_0' + \theta_x) - \underline{\underline{a_{56}\phi''}} - \underline{(b_4 + b_{14})\ddot{\theta}_x} = 0 \tag{2.40c}$$

Boundary conditions:

$$\text{At } y = 0, \quad w_0 = 0, \quad \phi = 0, \quad \underline{\underline{\phi' = 0}}, \quad \theta_x = 0 \tag{2.41a}$$

At $y = L$,

$$\begin{aligned}
\delta w_0 \quad &: \quad a_{55}(w_0' + \theta_x) + \underline{\underline{a_{56}\phi''}} = 0, \\
\delta\phi \quad &: \quad -a_{56}(w_0'' + \theta_x') - \underline{\underline{a_{66}\phi'''}} + a_{37}\theta_x' + a_{77}\phi' = -(b_{10} + b_{18})\ddot{\phi}', \\
\delta\phi' \quad &: \quad -a_{56}(w_0' + \theta_x) - \underline{\underline{a_{66}\phi''}} = 0, \\
\delta\theta_x \quad &: \quad a_{33}\theta_x' + a_{37}\phi' = 0
\end{aligned} \tag{2.41b}$$

In the above equations, the terms underscored by double solid lines are associated with the warping inhibition effect, whereas the term underscored by single solid line identifies the rotatory inertia effect (see Refs. [3–5]).

The unsteady aerodynamic lift and twist moment are expressed as:

$$\begin{aligned}
L_{ae}(y,t) &= -\pi\rho_\infty b^2[\dot{w}_{0.5c}(y,t)] - C_{L\phi}\rho_\infty U_n b[w_{0.75c}(y,t) - \sum_{i=1}^{n}\alpha_i B_i] \\
&= -\pi\rho_\infty b^2[\ddot{w}_0 + U_n\frac{\partial^2 w_0}{\partial y \partial t}\tan\Lambda - U_n\dot{\phi}] \\
&\quad - C_{L\phi}\rho_\infty U_n b[\dot{w}_0 - U_n\phi + U_n\frac{\partial w_0}{\partial y}\tan\Lambda - \frac{b}{2}(\frac{C_{L\phi}}{\pi} - 1)(\dot{\phi} + U_n\frac{\partial\phi}{\partial y}\tan\Lambda) - \sum_{i=1}^{n}\alpha_i B_i]
\end{aligned} \tag{2.42a}$$

$$\begin{aligned}
T_{ae}(y,t) &= -\pi\rho_\infty b^3[\frac{1}{2}U_n\dot{\phi} + \frac{1}{8}b\ddot{\phi}] - \frac{1}{2}C_{L\phi}\rho_\infty U_n b^2[w_{0.75c}(y,t) - \sum_{i=1}^{n}\alpha_i B_i] \\
&= -\pi\rho_\infty b^3\{[\frac{1}{2}(\frac{C_{L\phi}}{\pi} - 1)(U_n\dot{\phi} + U_n^2\frac{\partial\phi}{\partial y}\tan\Lambda)] + \frac{1}{8}b[\ddot{\phi} + U_n\frac{\partial^2\phi}{\partial y \partial t}\tan\Lambda]\} \\
&\quad - \frac{1}{2}C_{L\phi}\rho_\infty U_n b^2\{\dot{w}_0 - U_n\phi + U_n\frac{\partial w_0}{\partial y}\tan\Lambda - \frac{b}{2}(\frac{C_{L\phi}}{\pi} - 1)(\dot{\phi} + U_n\frac{\partial\phi}{\partial y}\tan\Lambda) - \sum_{i=1}^{n}\alpha_i B_i\}
\end{aligned} \tag{2.42b}$$

In Eqs. (2.42a, b), B_i fulfil Eq. (2.23). The expressions of the gust and blast loads have been provided in Eqs. (2.27, 2.29, 2.30).

2.3 Solution Methodology

Due to the non-conservative nature of the boundary value/eigenvalue problems and the high complexity arising from the anisotropy of the constituent materials and the boundary conditions, we apply the non-dimensionalization, spatial semi-discretization and then cast the governing equations into state space form. The spatial semi-discretization is based on the extended Galerkin's method (EGM) (see Refs. 7, 21). The conversion of governing equations into state space form is prompted by the facts that on one hand, for a general non-conservative system, the solution requires a state space description [2] and, on the other hand, the classical modal analysis based on complex eigensystem does not yield efficient solution. In addition, for the purpose of treating various gust and blast loads in a unified way, the temporal discretization is also implemented. It should be noted that the Laplace transform method (LTM) can only be efficiently applied to sufficiently low order systems. For the problem being addressed here, this methodology does not constitute the most appropriate one.

2.3.1 Non-Dimensionalization and Spatial Semi-Discretization

Introduce the following basic non-dimensional parameters:

$$\eta \equiv y/L, \quad \tau \equiv U_n t/b, \quad AR \equiv L/b, \quad \hat{w}_0(\eta,\tau) \equiv w_0/2b, \quad \hat{\phi}(\eta,\tau) \equiv \phi(\eta,\tau),$$
$$\hat{\theta}_x(\eta,\tau) \equiv \theta_x(\eta,\tau), \quad d()/d\tau = (b/U_n)d()/dt$$

and for spatial semi-discretization,

$$\hat{w}_0(\eta,\tau) = \hat{\mathbf{\Psi}}_w^T(\eta)\hat{\mathbf{q}}_w(\tau) \quad \hat{\phi}(\eta,\tau) = \hat{\mathbf{\Psi}}_\phi^T(\eta)\hat{\mathbf{q}}_\phi(\tau) \quad \hat{\theta}_x(\eta,\tau) = \hat{\mathbf{\Psi}}_x^T(\eta)\hat{\mathbf{q}}_x(\tau)$$

where the shape functions $\hat{\mathbf{\Psi}}_w(\eta)$,$\hat{\mathbf{\Psi}}_\phi(\eta)$,and $\hat{\mathbf{\Psi}}_x(\eta)$ are only required to fulfil the geometric boundary conditions.

In terms of the above basic non-dimensional parameters, the downwash quantities at the mid-chord and three-quarter locations are:

$$w_{0.75c}(\eta,\tau) = U_n[2\dot{\hat{w}}_0 - \frac{1}{2}(\frac{C_{L\phi}}{\pi} - 1)\dot{\hat{\phi}} - \hat{\phi} + \frac{2}{\mathit{AR}}\frac{\partial \hat{w}_0}{\partial \eta}\tan\Lambda - \frac{1}{2\mathit{AR}}(\frac{C_{L\phi}}{\pi} - 1)\frac{\partial \hat{\phi}}{\partial \eta}\tan\Lambda] \tag{2.43a}$$

$$w_{0.5c}(\eta,\tau) = U_n[\dot{\hat{w}}_0 - \hat{\phi} + \frac{\partial \hat{w}_0}{\partial \eta}\tan\Lambda] \tag{2.43b}$$

As a result, the unsteady aerodynamic loads are expressed as:

$$\begin{aligned} L_{ae}(\eta,\tau) = &-\pi\rho_\infty b^2 U_n^2[2\ddot{\hat{w}}_0 + \frac{2}{\mathit{AR}}\frac{\partial^2 \hat{w}_0}{\partial\eta\partial\tau}\tan\Lambda - \dot{\hat{\phi}}] \\ &- C_{L\phi}\rho_\infty U_n^2 b[2\dot{\hat{w}}_0 - \hat{\phi} + \frac{2}{\mathit{AR}}\frac{\partial \hat{w}_0}{\partial \eta}\tan\Lambda - \frac{1}{2}(\frac{C_{L\phi}}{\pi} - 1)(\dot{\hat{\phi}} + \frac{1}{\mathit{AR}}\frac{\partial \hat{\phi}}{\partial \eta}\tan\Lambda) - \sum_{i=1}^{n}\alpha_i B_i/U_n] \end{aligned} \tag{2.44a}$$

$$\begin{aligned} T_{ae}(\eta,\tau) = &-\pi\rho_\infty b^2 U_n^2\{[\frac{1}{2}(\frac{C_{L\phi}}{\pi} - 1)(\dot{\hat{\phi}} + \frac{1}{\mathit{AR}}\frac{\partial \hat{\phi}}{\partial \eta}\tan\Lambda)] + \frac{1}{8}[\ddot{\hat{\phi}} + \frac{1}{\mathit{AR}}\frac{\partial^2 \hat{\phi}}{\partial\eta\partial\tau}\tan\Lambda]\} \\ &- \frac{1}{2}C_{L\phi}\rho_\infty U_n^2 b^2\{2\dot{\hat{w}}_0 - \hat{\phi} + \frac{2}{\mathit{AR}}\frac{\partial \hat{w}_0}{\partial \eta}\tan\Lambda - \frac{1}{2}(\frac{C_{L\phi}}{\pi} - 1)(\dot{\hat{\phi}} + \frac{1}{\mathit{AR}}\frac{\partial \hat{\phi}}{\partial \eta}\tan\Lambda) - \sum_{i=1}^{n}\alpha_i B_i/U_n\} \end{aligned} \tag{2.44b}$$

After spatial semi-discretization, the following equations are derived:

$$\begin{aligned} (\bar{\mathbf{M}}_s + \frac{1}{8\mu_0}\bar{\mathbf{M}}_{ae})\ddot{\hat{\mathbf{q}}} + (\frac{1}{8\mu_0}\bar{\mathbf{C}}_{ae})\dot{\hat{\mathbf{q}}} + (k_r\bar{\mathbf{K}}_s + \frac{1}{8\mu_0}\bar{\mathbf{K}}_{ae})\hat{\mathbf{q}} = \frac{1}{8\mu_0}\left\{ \begin{array}{c} \mathbf{z}_1 \\ \mathbf{z}_2 \\ 0 \end{array} \right\} \\ + \frac{1}{4b_1 U_n^2}\left\{ \begin{array}{l} 2b\int_0^1 \hat{\mathbf{\Psi}}_w(L_g + L_b)d\eta \\ \int_0^1 \hat{\mathbf{\Psi}}_\phi T_g d\eta \\ 0 \end{array} \right\} \end{aligned} \tag{2.45a}$$

where

$$\bar{\mathbf{M}}_s = \int_0^1 \left[\begin{array}{ccc} \hat{\mathbf{\Psi}}_w\hat{\mathbf{\Psi}}_w^{\mathrm{T}} & \mathbf{0} & \mathbf{0} \\ \mathbf{0} & \hat{I}_t\hat{\mathbf{\Psi}}_\phi\mathbf{\Psi}_\phi^{\mathrm{T}} + \hat{I}_w\hat{\mathbf{\Psi}}'_\phi\hat{\mathbf{\Psi}}'^{\mathrm{T}}_\phi & \mathbf{0} \\ \mathbf{0} & \mathbf{0} & \hat{r}^2\hat{\mathbf{\Psi}}_x\hat{\mathbf{\Psi}}_x^{\mathrm{T}} \end{array} \right] d\,\eta \tag{2.45b}$$

$$\bar{\mathbf{K}}_s = \int_0^1 \begin{bmatrix} \frac{4}{\text{Æ}^2}\hat{\boldsymbol{\Psi}}'_w\hat{\boldsymbol{\Psi}}'^{T}_w & \frac{2}{\text{Æ}}\mu_1 c_{14}\hat{\boldsymbol{\Psi}}'_w\hat{\boldsymbol{\Psi}}''^{T}_\phi & \frac{2}{\text{Æ}}\hat{\boldsymbol{\Psi}}'_w\hat{\boldsymbol{\Psi}}^T_x \\ & \frac{4}{\text{Æ}^2}\mu_1\mu_2\hat{\boldsymbol{\Psi}}''_\phi\hat{\boldsymbol{\Psi}}''^{T}_\phi + \mu_1 c_{12}\hat{\boldsymbol{\Psi}}'_\phi\hat{\boldsymbol{\Psi}}'^{T}_\phi & \mu_1 c_{14}\hat{\boldsymbol{\Psi}}''_\phi\hat{\boldsymbol{\Psi}}^T_x + \mu_1 c_{13}\hat{\boldsymbol{\Psi}}'_\phi\hat{\boldsymbol{\Psi}}'^{T}_x \\ \textbf{symm} & & (\mu_1\hat{\boldsymbol{\Psi}}'_x\hat{\boldsymbol{\Psi}}'^{T}_x + \hat{\boldsymbol{\Psi}}_x\hat{\boldsymbol{\Psi}}^T_x) \end{bmatrix} d\eta \tag{2.45c}$$

$$\bar{\mathbf{M}}_{ae} = \int_0^1 \begin{bmatrix} 2\hat{\boldsymbol{\Psi}}_w\hat{\boldsymbol{\Psi}}^T_w & \mathbf{0} & \mathbf{0} \\ \mathbf{0} & \frac{1}{16}\hat{\boldsymbol{\Psi}}_\phi\hat{\boldsymbol{\Psi}}^T_\phi & \mathbf{0} \\ \mathbf{0} & \mathbf{0} & \mathbf{0} \end{bmatrix} d\eta \tag{2.45d}$$

$$\bar{\mathbf{C}}_{ae} = \int_0^1 \begin{bmatrix} \frac{2}{\text{Æ}}\tan\Lambda\hat{\boldsymbol{\Psi}}_w\hat{\boldsymbol{\Psi}}'^{T}_w + \frac{2C_{L\phi}}{\pi}\hat{\boldsymbol{\Psi}}_w\hat{\boldsymbol{\Psi}}^T_w & -[1 + \frac{C_{L\phi}}{2\pi}(\frac{C_{L\phi}}{\pi} - 1)]\hat{\boldsymbol{\Psi}}_w\hat{\boldsymbol{\Psi}}^T_\phi & \mathbf{0} \\ \frac{C_{L\phi}}{2\pi}\hat{\boldsymbol{\Psi}}_\phi\hat{\boldsymbol{\Psi}}^T_w & \begin{array}{l} \dfrac{1}{16\text{Æ}}\tan\Lambda\hat{\boldsymbol{\Psi}}_\phi\hat{\boldsymbol{\Psi}}'^{T}_\phi \\ +\dfrac{1}{4}(\dfrac{C_{L\phi}}{\pi} - 1)(1 - \dfrac{C_{L\phi}}{2\pi})\hat{\boldsymbol{\Psi}}_\phi\hat{\boldsymbol{\Psi}}^T_\phi \end{array} & \mathbf{0} \\ \mathbf{0} & \mathbf{0} & \mathbf{0} \end{bmatrix} d\eta \tag{2.45e}$$

$$\bar{\mathbf{K}}_{ae} = \int_0^1 \begin{bmatrix} \frac{2C_{L\phi}}{\pi\text{Æ}}\tan\Lambda\hat{\boldsymbol{\Psi}}_w\hat{\boldsymbol{\Psi}}'^{T}_w & -\frac{C_{L\phi}}{\pi}\hat{\boldsymbol{\Psi}}_w\hat{\boldsymbol{\Psi}}^T_\phi - \frac{C_{L\phi}}{2\pi\text{Æ}}(\frac{C_{L\phi}}{\pi} - 1)\tan\Lambda\hat{\boldsymbol{\Psi}}_w\hat{\boldsymbol{\Psi}}'^{T}_\phi & \mathbf{0} \\ \frac{C_{L\phi}}{2\pi\text{Æ}}\tan\Lambda\hat{\boldsymbol{\Psi}}_\phi\hat{\boldsymbol{\Psi}}'^{T}_w & -\frac{C_{L\phi}}{4\pi}\hat{\boldsymbol{\Psi}}_\phi\hat{\boldsymbol{\Psi}}^T_\phi + (1 - \frac{C_{L\phi}}{2\pi})(\frac{C_{L\phi}}{\pi} - 1)\frac{\tan\Lambda}{4\text{Æ}}\hat{\boldsymbol{\Psi}}_\phi\hat{\boldsymbol{\Psi}}'^{T}_\phi & \mathbf{0} \\ \mathbf{0} & \mathbf{0} & \mathbf{0} \end{bmatrix} d\eta \tag{2.45f}$$

$$\mathbf{z}_1 = \sum_{i=1}^{n}\alpha_i\int_0^1 \frac{C_{L\phi}}{\pi}\hat{\boldsymbol{\Psi}}_w\hat{B}_i d\eta \quad \mathbf{z}_2 = \sum_{i=1}^{n}\alpha_i\int_0^1 \frac{C_{L\phi}}{4\pi}\hat{\boldsymbol{\Psi}}_\phi\hat{B}_i d\eta \quad \hat{B}_i = B_i/U_n \tag{2.45g}$$

$$\mathbf{q} = [\ \hat{\boldsymbol{\Psi}}^T_w \quad \hat{\boldsymbol{\Psi}}^T_\phi \quad \hat{\boldsymbol{\Psi}}^T_x\ ]^T. \tag{2.45h}$$

The related non-dimensional parameters in the above equations are listed in Appendix B.

By using the mode expansion theorem, [2]

$$\hat{\mathbf{q}}_w = \boldsymbol{\Theta}_w\hat{\xi}_s, \quad \hat{\mathbf{q}}_\phi = \boldsymbol{\Theta}_\phi\hat{\xi}_s, \quad \hat{\mathbf{q}}_x = \boldsymbol{\Theta}_x\hat{\xi}_s$$

where $\boldsymbol{\Theta}_w$, $\boldsymbol{\Theta}_\phi$, $\boldsymbol{\Theta}_x$ are $N \times m$ eigenvector matrices for the $\hat{w}_0$,$\hat{\phi}$,$\hat{\theta}_x$, respectively, and $\hat{\xi}_s$ is the vector consisting of the first m generalized mode coordinates, we have,

$$\begin{aligned} \bar{\mathbf{M}}_n\ddot{\hat{\xi}}_s + \bar{\mathbf{C}}_n\dot{\hat{\xi}}_s + \bar{\mathbf{K}}_n\hat{\xi}_s &= \frac{1}{8\mu_0}\{\boldsymbol{\Theta}^T_w\mathbf{z}_1 + \boldsymbol{\Theta}^T_\phi\mathbf{z}_2\} \\ &+ \frac{1}{4b_1U_n^2}\Big\{2b\boldsymbol{\Theta}^T_w\int_0^1 \hat{\boldsymbol{\Psi}}_w(L_g + L_b)d\eta + \boldsymbol{\Theta}^T_\phi\int_0^1 \hat{\boldsymbol{\Psi}}_\phi T_g d\eta\Big\} \end{aligned} \tag{2.46}$$

On the left hand side of Eq. (2.46),

$$\bar{\mathbf{M}}_n = \boldsymbol{\Theta}^T[\bar{\mathbf{M}}_s + \frac{1}{8\mu_0}\bar{\mathbf{M}}_{ae}]\boldsymbol{\Theta} \quad \bar{\mathbf{C}}_n = \boldsymbol{\Theta}^T[\frac{1}{8\mu_0}\bar{\mathbf{C}}_{ae}]\boldsymbol{\Theta} \quad \bar{\mathbf{K}}_n = \boldsymbol{\Theta}^T[k_r\bar{\mathbf{K}}_s + \frac{1}{8\mu_0}\bar{\mathbf{K}}_{ae}]\boldsymbol{\Theta}$$

$$\mathbf{\Theta}\overset{-}{=}\left[\begin{array}{ccc} \mathbf{\Theta}_w^T & \mathbf{\Theta}_\phi^T & \mathbf{\Theta}_x^T \end{array}\right]^T$$

On its right hand side,

$$\mathbf{\Theta}_w^T\mathbf{z}_1+\mathbf{\Theta}_\phi^T\mathbf{z}_2=\left[\begin{array}{ccc} \alpha_1\mathbf{I}_{m\times m} & \ldots & \alpha_n\mathbf{I}_{m\times m} \end{array}\right]\left\{\begin{array}{c} \hat{\mathbf{x}}_{a1} \\ \vdots \\ \hat{\mathbf{x}}_{an} \end{array}\right\} \tag{2.47}$$

In Eq. (2.47), the augmented state vector $\hat{\mathbf{x}}_{ai}$fulfils the following equation:

$$\dot{\hat{\mathbf{x}}}_{ai}+\beta_i\hat{\mathbf{x}}_{ai}=\mathbf{D}_1\dot{\hat{\xi}}_s+\mathbf{D}_2\ddot{\hat{\xi}}_s \tag{2.48}$$

where

$$\begin{aligned}\mathbf{D}_1=&\frac{C_{L\phi}}{\pi}\mathbf{\Theta}_w^{\mathrm{T}}\{\frac{2}{A\!\!\!R}\tan\Lambda\int_0^1\hat{\mathbf{\Psi}}_w\mathbf{\Psi}'^{\mathrm{T}}_w d\,\eta\mathbf{\Theta}_w-\int_0^1[\hat{\mathbf{\Psi}}_w\hat{\mathbf{\Psi}}_\phi^{\mathrm{T}}+(\frac{C_{L\phi}}{\pi}-1)\frac{\tan\Lambda}{2A\!\!\!R}\hat{\mathbf{\Psi}}_w\hat{\mathbf{\Psi}}'^{\mathrm{T}}_\phi d\,\eta\mathbf{\Theta}_\phi]\}\\&+\frac{C_{L\phi}}{2\pi}\mathbf{\Theta}_\phi^{\mathrm{T}}\{\frac{1}{A\!\!\!R}\tan\Lambda\int_0^1\hat{\mathbf{\Psi}}_\phi\hat{\mathbf{\Psi}}'^{\mathrm{T}}_w d\,\eta\mathbf{\Theta}_w-\frac{1}{2}\int_0^1[\hat{\mathbf{\Psi}}_\phi\hat{\mathbf{\Psi}}_\phi^{\mathrm{T}}+(\frac{C_{L\phi}}{\pi}-1)\frac{\tan\Lambda}{2A\!\!\!R}\hat{\mathbf{\Psi}}_\phi\hat{\mathbf{\Psi}}'^{\mathrm{T}}_\phi]d\,\eta\mathbf{\Theta}_\phi\}\end{aligned} \tag{2.49a}$$

$$\begin{aligned}\mathbf{D}_2=&\frac{C_{L\phi}}{\pi}\mathbf{\Theta}_w^T\{2\int_0^1\hat{\mathbf{\Psi}}_w\hat{\mathbf{\Psi}}_w^T d\eta\mathbf{\Theta}_w-\frac{1}{2}(\frac{C_{L\phi}}{\pi}-1)\int_0^1\hat{\mathbf{\Psi}}_w\hat{\mathbf{\Psi}}_\phi^T d\eta\mathbf{\Theta}_\phi\}\\&+\frac{C_{L\phi}}{2\pi}\mathbf{\Theta}_\phi^T\{\int_0^1\hat{\mathbf{\Psi}}_\phi\hat{\mathbf{\Psi}}_w^T d\eta\mathbf{\Theta}_w-\frac{1}{4}(\frac{C_{L\phi}}{\pi}-1)\int_0^1\hat{\mathbf{\Psi}}_\phi\hat{\mathbf{\Psi}}_\phi^T d\eta\mathbf{\Theta}_\phi\}\end{aligned} \tag{2.49b}$$

2.3.2 State Space Form of the Governing System

By denoting

$$\hat{\mathbf{x}}_s\equiv\left\{\begin{array}{c} \hat{\xi}_s \\ \dot{\hat{\xi}}_s \end{array}\right\}_{2m\times1},\quad \hat{\mathbf{x}}_a\equiv\left\{\begin{array}{c} \mathbf{x}_{a1} \\ \vdots \\ \mathbf{x}_{an} \end{array}\right\}_{nm\times1},\quad \{\hat{\mathbf{X}}\}\equiv\left\{\begin{array}{c} \hat{\mathbf{x}}_s \\ \hat{\mathbf{x}}_a \end{array}\right\}_{(2+n)m\times1} \tag{2.50}$$

we get the state space form of the above aeroelastic governing equations and the augmented state equations:

$$\left\{ \begin{array}{c} \dot{\hat{\mathbf{x}}}_s \\ \dot{\hat{\mathbf{x}}}_a \end{array} \right\} = \left[\begin{array}{cc} \mathbf{A}_s & \mathbf{B}_s \\ \mathbf{B}_a\mathbf{A}_s & \mathbf{A}_a + \mathbf{B}_a\mathbf{B}_s \end{array} \right] \left\{ \begin{array}{c} \hat{\mathbf{x}}_s \\ \hat{\mathbf{x}}_a \end{array} \right\} + \left[\begin{array}{l} \mathbf{0}_{m\times 1} \\ \bar{\mathbf{M}}_n^{-1} \\ \mathbf{D}_2\bar{\mathbf{M}}_n^{-1} \\ \vdots \\ \mathbf{D}_2\bar{\mathbf{M}}_n^{-1} \end{array} \right] \{\mathbf{Q}_g + \mathbf{Q}_b\} \tag{2.51}$$

or in a more compact form, as

$$\{\dot{\hat{\mathbf{X}}}\} = [\mathbf{A}]\{\hat{\mathbf{X}}\} + [\mathbf{B}_e]\{\mathbf{Q}_g\} + [\mathbf{B}_e]\{\mathbf{Q}_b\} \tag{2.52}$$

In Eq. (2.52),

$$[\mathbf{A}] = \left[\begin{array}{cc} \mathbf{A}_s & \mathbf{B}_s \\ \mathbf{B}_a\mathbf{A}_s & \mathbf{A}_a + \mathbf{B}_a\mathbf{B}_s \end{array} \right], \qquad [\mathbf{B}_e] = \left[\begin{array}{l} \mathbf{0}_{m\times 1} \\ \bar{\mathbf{M}}_n^{-1} \\ \mathbf{D}_2\bar{\mathbf{M}}_n^{-1} \\ \vdots \\ \mathbf{D}_2\bar{\mathbf{M}}_n^{-1} \end{array} \right]$$

$$\begin{aligned} \mathbf{Q}_g = {} & \frac{1}{8\mu_0}\left\{ \frac{C_{L\phi}}{\pi}\mathbf{\Theta}_w^T \int_0^1 \hat{\mathbf{\Psi}}_w d\eta + \frac{C_{L\phi}}{4\pi}\mathbf{\Theta}_\phi^T \int_0^1 \hat{\mathbf{\Psi}}_\phi d\eta \right\} \\ & \times \frac{1}{U_n}\left\{ w_G(0)\psi_K(\tau) + \int_0^\tau \frac{\partial w_G(\tau_0)}{\partial \tau_0}\psi_K(\tau - \tau_0)d\tau_0 \right\} \end{aligned}$$

$$\mathbf{Q}_b = \frac{1}{4b_1U_n^2}\left\{ 2b\mathbf{\Theta}_w^T \int_0^1 \hat{\mathbf{\Psi}}_w d\eta \right\} L_b, \quad [\mathbf{A}_s]_{2m\times 2m} = \left[\begin{array}{cc} 0_{m\times m} & \mathbf{I}_{m\times m} \\ -\bar{\mathbf{M}}_n^{-1}\bar{\mathbf{K}}_n & -\bar{\mathbf{M}}_n^{-1}\bar{\mathbf{C}}_n \end{array} \right]$$

$$[\mathbf{B}_s]_{2m\times nm} = \left[\begin{array}{l} \mathbf{0}_{m\times nm} \\ \frac{1}{8\mu_0}\bar{\mathbf{M}}_n^{-1} \left[\begin{array}{ccc} \alpha_1\mathbf{I}_{m\times m} & \cdots & \alpha_1\mathbf{I}_{m\times m} \end{array} \right]_{m\times nm} \end{array} \right],$$

$$[\mathbf{A}_a]_{nm\times nm} = \left[\begin{array}{ccc} -\beta_1\mathbf{I}_{m\times m} & & \\ & \ddots & \\ & & -\beta_n\mathbf{I}_{m\times m} \end{array} \right], \quad [\mathbf{B}_a]_{nm\times 2m} = \left[\begin{array}{c} \mathbf{I}_{m\times m} \\ \vdots \\ \mathbf{I}_{m\times m} \end{array} \right]_{nm\times m} \left[\begin{array}{cc} \mathbf{D}_1 & \mathbf{D}_2 \end{array} \right]_{m\times 2m}$$

The remaining matrices and vectors have been defined in the preceding section.

2.3.3 Temporal Discretization of the Governing System

The general solution of Eq. (2.52) can be expressed as: [2]

$$\{\hat{\mathbf{X}}(\tau)\} = [e^{\mathbf{A}\tau}]\{\hat{\mathbf{X}}(0)\} + \int_0^\tau [e^{\mathbf{A}(\tau-\tau_0)}][\mathbf{B}_e]\{\mathbf{Q}_g(\tau_0) + \{\mathbf{Q}_b(\tau_0)\}d\tau_0 \tag{2.53}$$

where the transition matrix $[e^{\mathbf{A}\tau}] = \mathcal{L}^{-1}[(p\mathbf{I} - \mathbf{A})^{-1}] = \sum_{i=0}^{\infty} \mathbf{A}^i/i!\, \tau^i$.

For a general non-conservative system, the eigenvalues and eigenvectors are complex valued quantities. Although the system matrix $\mathbf{A}$ can be orthogonalized in terms of its left and right eigenvectors [2], for large order of $\mathbf{A}$, the actual implementation is not efficient [2]. Moreover, the Laplace transform method is almost impractical for systems featuring large orders. So the above equation is directly discretized in the time domain.

With the fixed sampling step $\Delta\tau$, the following discretized equation is derived: [2]

$$\{\hat{\mathbf{X}}(k+1)\} = [e^{\mathbf{A}\Delta\tau}]\{\hat{\mathbf{X}}(k)\} + [\mathbf{A}]^{-1}[e^{\mathbf{A}\Delta\tau} - \mathbf{I}][\mathbf{B}_e]\{\mathbf{Q}_g(k) + \mathbf{Q}_b(k)\} \tag{2.54}$$

where the discretized transition matrix

$$[e^{\mathbf{A}\Delta\tau}] = \sum_{i=0}^{\infty} \frac{\mathbf{A}^i}{i!}(\Delta\tau)^i \tag{2.55}$$

Given the maximum amplitude of the eigenvalues of $\mathbf{A}$ and the sampling step $\Delta\tau$, the numerical convergence requirement of the above equation and the prescribed computation accuracy determines the number of truncated terms in Eq. (2.55) for the approximation of $[e^{\mathbf{A}\Delta\tau}]$ [2]. In this paper, the accuracy order of 10^{-5} is prescribed.

Once the solution of $\{\hat{\mathbf{X}}(k)\}$ is known, the generalized coordinate $\hat{\xi}_s(k)$ can be extracted, and then the aeroelastic response can be reconstructed as follows:

$$\hat{w}_0(\eta, k) = \hat{\mathbf{\Psi}}_w^T(\eta)\mathbf{\Theta}_w\hat{\xi}_s(k), \quad \hat{\phi}(\eta, k) = \hat{\mathbf{\Psi}}_\phi^T(\eta)\mathbf{\Theta}_\phi\hat{\xi}_s(k), \quad \hat{\theta}_x(\eta, k) = \hat{\mathbf{\Psi}}_x^T(\eta)\mathbf{\Theta}_x\hat{\xi}_s(k) \tag{2.56}$$

2.4 Simulation Results and Discussions

In this section, the dynamic aeroelastic response of anisotropic thin-walled beams exposed to selected gust and blast loads is investigated. Also investigated are the influences of lay-ups and flight speed on the response. It should be noted that, depending on the design objectives and model/tools to be used, there are many other design parameters for investigating the broad range effects of the aeroelastic tailoring [22]. The geometric and material specifications of the beams with CAS lay-up configuration are listed in Table 2.1, 2.2. In Table 2.2, two sets of geometric specifications are adopted, with the second set (type B) dealing with the onset of the dynamic flutter instability. It should be noted that in the actual calculation, the first 5 structural modes and 2 aerodynamic lag terms (see Eq. 2.21) are used, i.e., $m = 5, n = 2$, the Wagner's function is approximated by the Jones' quasi-polynomial formulas [13], and all the response components (bending, twist and transverse) are measured at the beam tip ($\eta = 1$).

Figures 2.4, 2.5, 2.6 display the response of the wing (type A) featuring various ply angles exposed to a sharp-edged gust. Other related parameters are: $U_n = 150m/s$, $V_G = 15m/s$, and $[\theta_6]$ lay-up of the walls. It can be seen that the directionality property of the structure has a dramatic influence on the response amplitudes of all the bending, twist and transverse shear. The bending, twist and shear stiffness of the wing monotonically increases from ply angle $\theta = 0^0$ to 90^0. It should be noted that no structural damping is considered. The damping is entirely of aerodynamic nature and in the cases considered in this paper, it is mainly from the feedback mechanism of the unsteady aerodynamic loads (see Eqs. 2.19b, c).

Figures 2.7 and 2.8 display the response of a type A wing featuring two lay-ups. The lay-up of Fig. 2.7 is $[75_6]$, while in Fig. 2.8 is $[75_2/-75_2/75_2]$. Other related parameters are $U_n = 150m/s$, $V_G/U_n = 0.1$. It is quite remarkable that for the bending response, both the peak value of the transient oscillation and steady response amplitude of the former case are almost 3 times that of the latter case. This reveals that the structural stiffness has been dramatically changed due to the change of only two out of 6 constituent ply orientations.

Figures 2.9, 2.10, 2.11 and Fig. 2.7 display the influence of the flight speed on the response. The wing (type A) is subject to a sharp-edged gust. The related parameters are:$V_G =$

$15m/s$, the lay-up is $[75_6]$, $U_n = 75, 150, 200, 250m/s$. With the increase of the flight speed, the amplitudes of the response increase in an accelerating rate. For some wings, a higher flight speed may induce flutter, as shown in Figs. 2.12 -2.14, the related parameters are: a type B wing, $V_G = 15m/s$, the lay-up is $[-75_6]$. As discussed before, the damping for the dynamic aeroelastic system considered here is mainly from the feedback mechanism of the unsteady aerodynamic loads. In some flight speed range, this feedback yields the positive damping on the structure, but for other ranges, usually in a high flight speed one, the feedback may yield negative damping on the structure, i.e., the aerodynamic loads act as an energy source [23], thus providing infinite energy to the structure, and leading to structural failure. From Figs. 2.12, 2.13, it can be seen that a flutter speed is between $U_n = 235m/s$ and $U_n = 236m/s$. In fact, by tracing the eigenvalues of the system matrix $[\boldsymbol{A}]$, the most critical flutter speed can be determined, as shown in Fig. 2.14, from which, the dimensional flutter speed is measured as $U_n = 235.05m/s$. Figure 2.15 shows the frequency coalescence phenomenon, which is a typical characteristic of the coupling-driven flutter. Figure 2.16 reveals the flutter intensity. The eigenvalues of the system matrix $[\mathbf{A}]$ for the above two flight conditions are listed in Table 2.3, wherefrom the roots with positive real part explain the occurrence of divergent oscillations. It is interesting to note that the above flutter speed and flutter frequency have an excellent correlation with those by the V-g method. Table 2.4 shows the comparison of flutter results by these two different methods. It should be noted that the Theodorsen function used in the V-g method is approximated by [24]:

$$\begin{aligned} C(k) &= F(k) + jG(k) \\ &= \frac{0.021573 + 0.210400k + 0.512607k^2 + 0.500502k^3}{0.021508 + 0.251239k + 1.035378k^2 + k^3} \\ &- j\frac{0.001995 + 0.327214k + 0.122397k^2 + 0.000146k^3}{0.089318 + 0.934530k + 2.481481k^2 + k^3} \end{aligned} \tag{2.57}$$

Here, k is the reduced frequency. The difference of the flutter predictions by the two methods is well within the approximation accuracy of the Wagner's function (in the time domain) and the Theodorsen function (in the frequency domain). It is also interesting to note that in Figs. 2.9, 2.10, 2.11, the higher the flight speed, the quicker the response goes to its steady solution with less transient oscillations.

Figures 2.17, 2.18, 2.19, 2.20, 2.21, 2.22 display the influence of the 1-COSINE gust gradient τ_p on the response. The related parameters are: a type A wing, $U_n = 150m/s$, $V_G = 15m/s$, the lay-up is $[\theta_6]$. It is interesting to note that for the wing with $\theta = 90^0$, larger τ_p results in smaller peak amplitudes of the response, while for wing with $\theta = 45^0$, larger τ_p yields larger peak amplitudes of the response.

Figures 2.23, 2.24 display the influence of explosive blast and sonic boom on the response. The related parameters are: a type A wing, $[75_6]$ lay-up, $U_n = 150m/s$, $\hat{P}_m = 0.001$ and $r = 2$. The maximum amplitude of the response occurs in the free motion region, i.e., when the explosive or sonic boom has left the wing.

Figures 2.25, 2.26 display the combined effect of sonic boom /sharp-edged gust and sonic boom/1-COSINE gust on the response. The related parameters are: a type A wing, $[75_6]$ lay-up, $U_n = 150m/s$, $V_G = 15m/s$, $\hat{P}_m = 0.001$, $\tau_p = 20$, and$r = 2$. The maximum amplitude of the response (bending component) still occurs when the sonic boom has left the wing ($\tau = 40$).

2.5 Conclusions

The dynamic aeroelastic response of advanced aircraft wings modeled as anisotropic composite thin-walled beams in an incompressible flow and exposed to selected gust and blast loads is investigated. The 2-D unsteady aerodynamics is extended to account for the effect of the finite wing span. Due to the non-conservative nature of the dynamic aeroelastic system and the high complexity of the boundary value/eigenvalue problem arising from advanced structural system considered in this article, the techniques of non-dimensionalization, spatial semi-discretization are applied to the governing equations, which are then cast into state space form. Finally, temporal discretization of the governing equations is used in the actual computation. The significant influence of the lay-ups on the response is highlighted. The potential advantage of exploiting elastic tailoring is vast, but the complete understanding of the elastic tailoring is a prerequisite for a reliable use of these exotic advanced composite materials. The flight speed can also dramatically modify the dynamic response behavior of the subcritical aeroelastic system, and its increase may result in the onset of flutter instability.

Acknowledgement

The authors of this paper wish to express their indebtedness to Dr. Piergiovanni Marzocca for helpful discussions and comments.

2.6 References

[1] Marzocca, P., Librescu, L., and Chiocchia, G., "Aeroelastic Response of 2-D Lifting Surfaces to Gust and Arbitrary Explosive Loading Signatures," *International Journal of Impact Engineering*, Vol. 25, 2001, pp. 41–65.

[2] Meirovitch, L., *Principles and Techniques of Vibrations*, Prentice Hall, Upper Saddle River, New Jersey, 1997, pp. 189-194, 206-210.

[3] Song, O., *Modeling and Response Analysis of Thin-Walled Beam Structures Constructed of Advanced Composite Materials*, Ph.D. thesis, Virginia Polytechnic Institute and State University, 1990.

[4] Librescu, L. and Song, O., "Behavior of Thin-Walled Beams Made of Advanced Composite Materials and Incorporating Non-Classical Effects," *Applied Mechanics Reviews*, Vol. 44, No. 11, part 2, 1991, pp. S174–S180.

[5] Song, O. and Librescu, L., “Free Vibration of Anisotropic Composite Thin-Walled Beams of Closed Cross-Section Contour,” *Journal of Sound and Vibration*, Vol. 167, No. 1, 1993, pp. 129–147.

[6] Bhaskar, K. and Librescu, L., “A Geometrically Non-Linear Theory for Laminated Anisotropic Thin-Walled Beams,” *International Journal of Engineering Science*, Vol. 33, No. 9, 1995, pp. 1331–1344.

[7] Librescu, L. and Na, S. S., “Dynamic Response of Cantilevered Thin-Walled Beams to Blast and Sonic-Boom Loadings,” *Shock and Vibration*, , No. 5, 1998, pp. 23–33.

[8] Na, S. S., *Control of Dynamic Response of Thin-Walled Composite Beams Using Structural Tailoring and Piezoelectric Actuation*, Ph.D. thesis, Virginia Polytechnic Institute and State University, 1997.

[9] Rehfield, L. W., Atilgan, A. R., and Hodges, D. H., “Nonclassical Behavior of Thin-Walled Composite Beams with Closed Cross Sections,” *Journal of the American Helicopter Society*, Vol. 35, No. 2, 1990, pp. 42–51.

[10] Smith, E. C. and Chopra, I., “Formulation and Evaluation of an Analytical Model for Composite Box-Beams,” *Journal of American Helicopter Society*, Vol. 36, No. 3, 1991, pp. 23–35.

[11] Kim, C. and White, S. R., “Thick-Walled Composite Beam Theory Including 3-D Elastic Effects and Torsional Warping,” *International Journal of Solids and Structures*, Vol. 34, No. 31-32, 1997, pp. 4237–59.

[12] von Kármán, T. and Sears, W. R., “Airfoil Theory for Non-Uniform Motion,” *Journal of the aeronautical Sciences*, Vol. 5, No. 10, 1938, pp. 379–390.

[13] Bisplinghoff, R. L., Ashley, H., and Halfman, R. L., *Aeroelasticity*, Dover Publications, New York, 1996.

[14] Katz, J. and Plotkin, A., *Low-Speed Aerodynamics: From Wing Theory to Panels Methods*, McGraw-Hill, New York, 1991, pp. 451-457.

[15] Theodorsen, T., "General Theory of Aerodynamic Instability and the Mechanism of Flutter," NACA Report 496, NACA, 1935.

[16] Sears, W. R., "Operational Methods in the Theory of Airfoils in Non-Uniform Motion," *Journal of the Franklin Institute*, Vol. 230, 1940, pp. 94–111.

[17] Venkatesan, C. and Friedmann, P. P., "New Approach to Finite-State Modeling of Unsteady Aerodynamics," *AIAA Journal*, Vol. 24, No. 12, 1986, pp. 1889–1897.

[18] karpel, M., "Design of Active Flutter Suppression and Gust Alleviation Using State-Space Aeroelastic Modeling," *Journal of Aircraft*, Vol. 19, No. 3, 1982, pp. 221–227.

[19] E. C. Yates, J., "Calculation of Flutter Characteristics for Finite-Span Swept or Unswept Wings at Subsonic and Supersonic Speeds by a Modified Strip Analysis," RM L57L10, NACA, 1958.

[20] Rodden, W. P. and Stahl, B., "A Strip Method for Prediction of Damping in Subsonic Wind Tunnel and Flight Flutter Tests," *Journal of Aircraft*, Vol. 6, No. 1, 1969, pp. 9–17.

[21] Palazotto, A. N. and Linnemann, P. E., "Vibration and Buckling Characteristics of Composite Cylindrical Panels Incorporating the Effects of a Higher Order Shear Theory," *International Journal of Solids and Structures*, Vol. 28, No. 3, 1991, pp. 341–361.

[22] Shirk, M. H., Hertz, T. J., and Weisshaar, T. A., "Aeroelastic Tailoring– Theory, Practice and Promise," *Journal of Aircraft*, Vol. 23, No. 1, 1986, pp. 6–18.

[23] Preidikman, S. and Mook, D. T., "A New Method for Actively Suppressing Flutter of Suspension Bridges," *Journal of Wind Engineering and Industrial Aerodynamics*, Vol. 69-71, 1997, pp. 955–974.

[24] Gern, F. and Librescu, L., "Static and Dynamic Aeroelasticity of Advanced Aircraft Wings Carrying External Stores," *AIAA Journal*, Vol. 36, No. 7, 1998, pp. 1121–1129.

Appendix A

The global stiffness quantities a_{ij} $(= a_{ji})$ and inertial terms I_i related to the problem are defined as:

$$\begin{array}{ll}
a_{33} = \oint_C [z^2 K_{11} + 2z\frac{dx}{ds}K_{14} + (\frac{dx}{ds})^2 K_{44}]ds & a_{37} = \oint_C [zK_{13} + \frac{dx}{ds}K_{43}]ds \\
a_{55} = \oint_C [(\frac{dz}{ds})^2 K_{22} + (\frac{dx}{ds})^2 \bar{A}_{44}]ds & a_{56} = -\oint_C [F_w \frac{dz}{ds}K_{21} + a(s)\frac{dz}{ds}K_{24}]ds \\
a_{66} = \oint_C [F_w^2 K_{11} + 2F_w a(s)K_{14} + a(s)^2 K_{44}]ds & a_{77} = \oint_C \psi(s)K_{23}ds
\end{array}$$

where $\bar{A}_{44} = A_{44} - \dfrac{A_{45}^2}{A_{55}}$.

The reduced stiffness coefficientK_{ij} (in Eq. 2.9) are defined as:

$$\begin{array}{lll}
K_{11} = A_{22} - \dfrac{A_{12}^2}{A_{11}} & K_{12} = A_{26} - \dfrac{A_{12}A_{16}}{A_{11}} = K_{21} & K_{13} = (A_{26} - \dfrac{A_{12}A_{16}}{A_{11}})\psi(s) \\
K_{14} = B_{22} - \dfrac{A_{12}B_{12}}{A_{11}} = K_{41} & K_{22} = A_{66} - \dfrac{A_{16}^2}{A_{11}} & K_{23} = (A_{66} - \dfrac{A_{16}^2}{A_{11}})\psi(s) \\
K_{24} = B_{26} - \dfrac{A_{16}B_{12}}{A_{11}} = K_{42} & K_{43} = (B_{26} - \dfrac{B_{12}A_{16}}{A_{11}})\psi(s) & K_{44} = D_{22} - \dfrac{B_{12}^2}{A_{11}} \\
K_{51} = B_{26} - \dfrac{B_{16}A_{12}}{A_{11}} & K_{52} = B_{66} - \dfrac{B_{16}A_{16}}{A_{11}} & K_{53} = (B_{66} - \dfrac{B_{16}A_{16}}{A_{11}})\psi(s) \\
K_{54} = D_{26} - \dfrac{B_{12}B_{16}}{A_{11}} & &
\end{array}$$

The inertial coefficients in the Eqs. 2.35 are defined as:

$$\begin{array}{lll}
b_1 = \oint_C m_0 ds & (b_4,\ b_5) = \oint_C (z^2, x^2)m_0 ds & b_{14} = \oint_C m_2(\frac{dx}{ds})^2 ds \\
b_{15} = \oint_C m_2(\frac{dz}{ds})^2 ds & (b_{10},\ b_{18}) = \oint_C (m_0 F_w^2(s),\ m_2 a^2(s))ds &
\end{array}$$

in which

$$(m_0, m_2) = \sum_{k=1}^{m_l} \int_{h_{(k^-)}}^{h_{(k^+)}} \rho_{(k)}(1, n^2)dn$$

Appendix B

Non-dimensional parameters used in Eq. (2.45) and section 4:

$$\mu_0 = \frac{b_1}{\pi\rho(2b)^2} \qquad \mu_1 = \frac{a_{33}}{a_{55}L^2} \quad \mu_2 = \frac{a_{66}}{a_{33}(2b)^2} \quad \omega_h^2 = \frac{a_{33}}{b_1 L^4} \quad \omega_{hr} = \omega_h \big|_{\theta=\pi/2}$$

$$\hat{r} = \sqrt{\frac{(b_4 + b_{14})}{b_1 L^2}} \quad c_{12} = \frac{a_{77}}{a_{33}} \quad c_{13} = \frac{a_{37}}{a_{33}} \qquad c_{14} = \frac{a_{56}}{a_{33}} \quad \hat{I}_t = \frac{(b_4 + b_5)}{(2b)^2 b_1}$$

$$\hat{I}_w = \frac{(b_{10} + b_{18})}{L^2(2b)^2 b_1} \quad k_r = \frac{a_{55}}{4b_1 U_n^2} \quad \hat{P}_m = \frac{bP_m}{2b_1 U_n^2}$$

Table 2.1: Material properties of the thin-walled beams with CAS lay-up and biconvex cross-section

$E_{11} = 206.8 \times 10^9\ N/m^2$	$E_{22} = E_{33} = 5.17 \times 10^9\ N/m^2$
$G_{13} = G_{23} = 2.55 \times 10^9\ N/m^2$	$G_{12} = 3.10 \times 10^9\ N/m^2$
$\mu_{12} = \mu_{13} = \mu_{23} = 0.25$	$\rho = 1.528 \times 10^3\ Kg/m^3$

Table 2.2: Geometric specifications of the wings with CAS lay-up and biconvex cross-section

Parameters	Type A	Type B
Length ($L:\ m$)	2.032	6.058
Width ($2b:\ m$)	0.254	0.757
Depth ($2d^a:\ m$)	0.06807	0.100
Aspect ratio	16	16
Wall thickness ($h:\ m$)	0.0102	0.010
Number of layers	6	6
Layer thisckness (: m)	0.0017	0.0017
Sweep angle (Λ : deg.)	0	0

[a] the length is measured on the contour line

Table 2.3: Eigenvalues ($\sigma + jk$) of the system matrix [**A**] near the onset of flutter

$U_n = 235\ m/s$ (subcritical response)	$U_n = 236\ m/s$ (supercritical response)
$-0.0104 \pm 1.052j$	$-0.0104 \pm 1.05j$
$-0.0120 \pm 0.5510j$	$-0.0120 \pm 0.549j$
$-0.0169 \pm 0.3352j$	$-0.0169 \pm 0.333j$
$-0.0358 \pm 0.1577j$	$-0.0380 \pm 0.157j$
$-0.000201 \pm 0.1429j$	$0.00185 \pm 0.143j$
$-0.295 \pm 0.00454j$	-0.295±0.00457j
-0.0478±0.00117j	$-0.0478 \pm 0.00119j$
$-0.0456 \pm 0.000318j$	$-0.0456 \pm 0.000320j$
$-0.300 \pm 0.000297j$	$-0.300 \pm 0.000299j$
-0.0455	-0.0455
-0.253	-0.253

Table 2.4: Comparison of the flutter results by the transient method and V-g method

Method	$\lambda_F = V_F/b\omega_{hr}$	$\Omega_F = \omega_F/\omega_{hr}$	$V_F\ (m/s)$	$\omega_F(rad/s)$
Transient method	53.75	7.53	235.05	87.12
V-g method	53.74	7.57	235.00	87.58

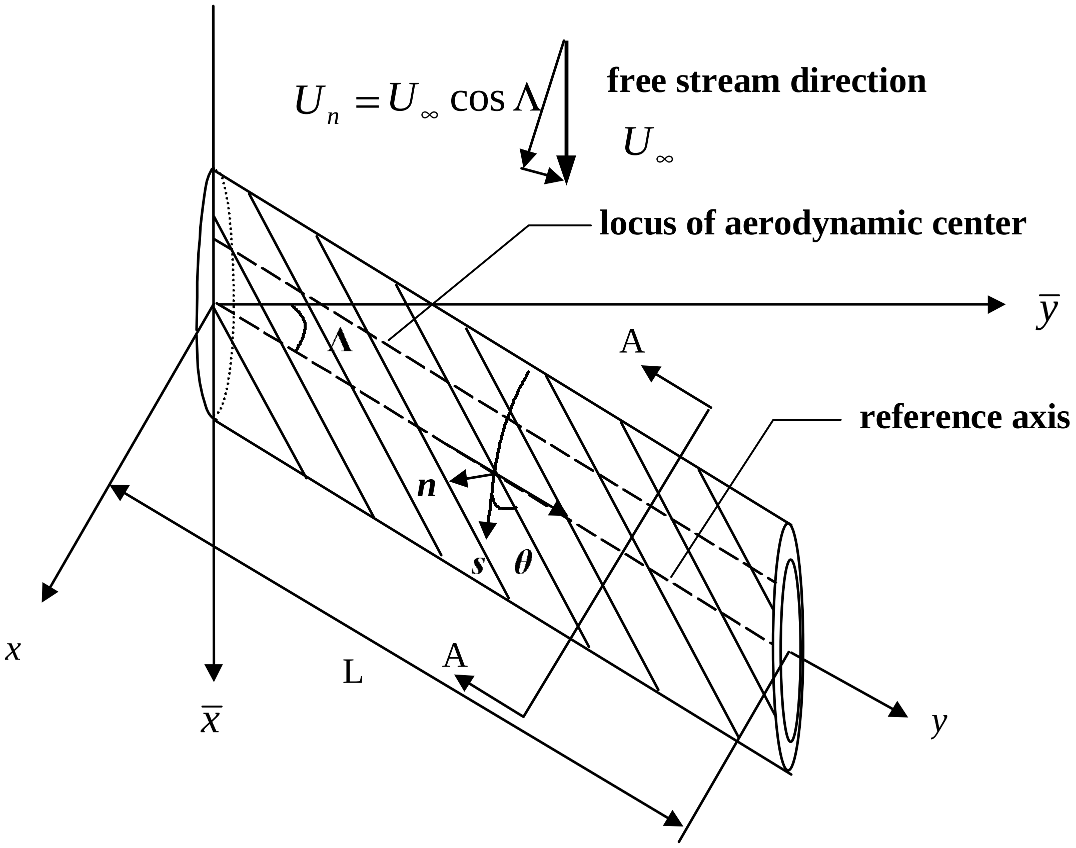

Figure 2.1: Geometric configuration of the aircraft wing modeled as a thin-walled beam model.

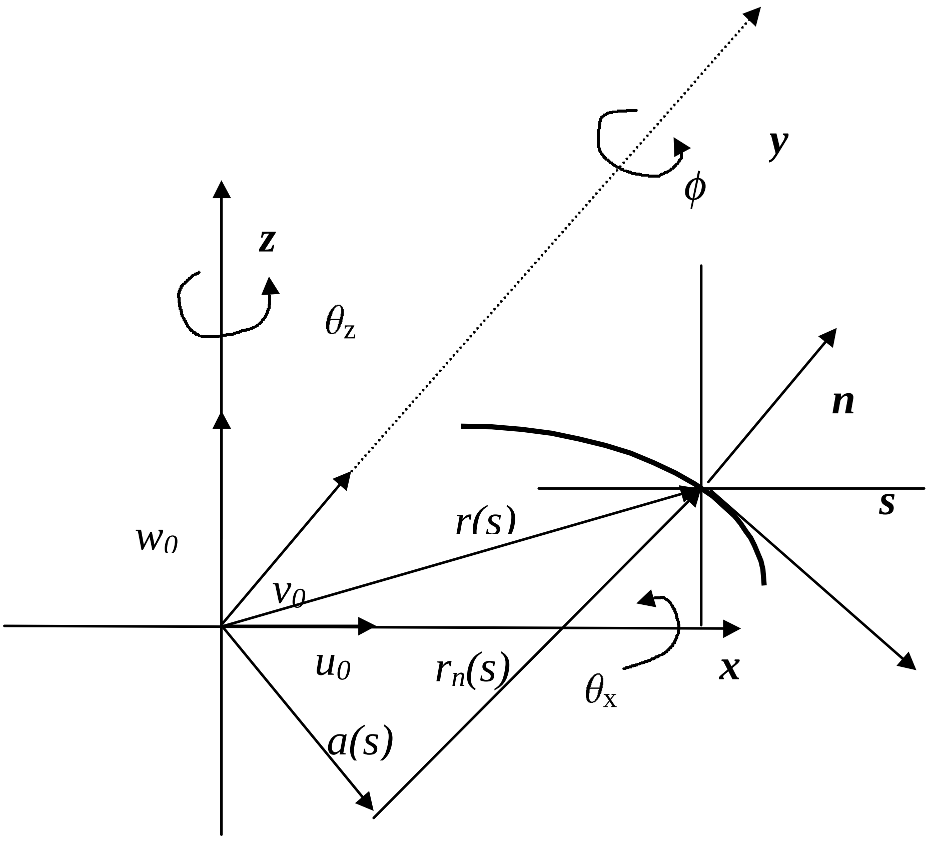

Figure 2.2: Displacement field for the beam model.

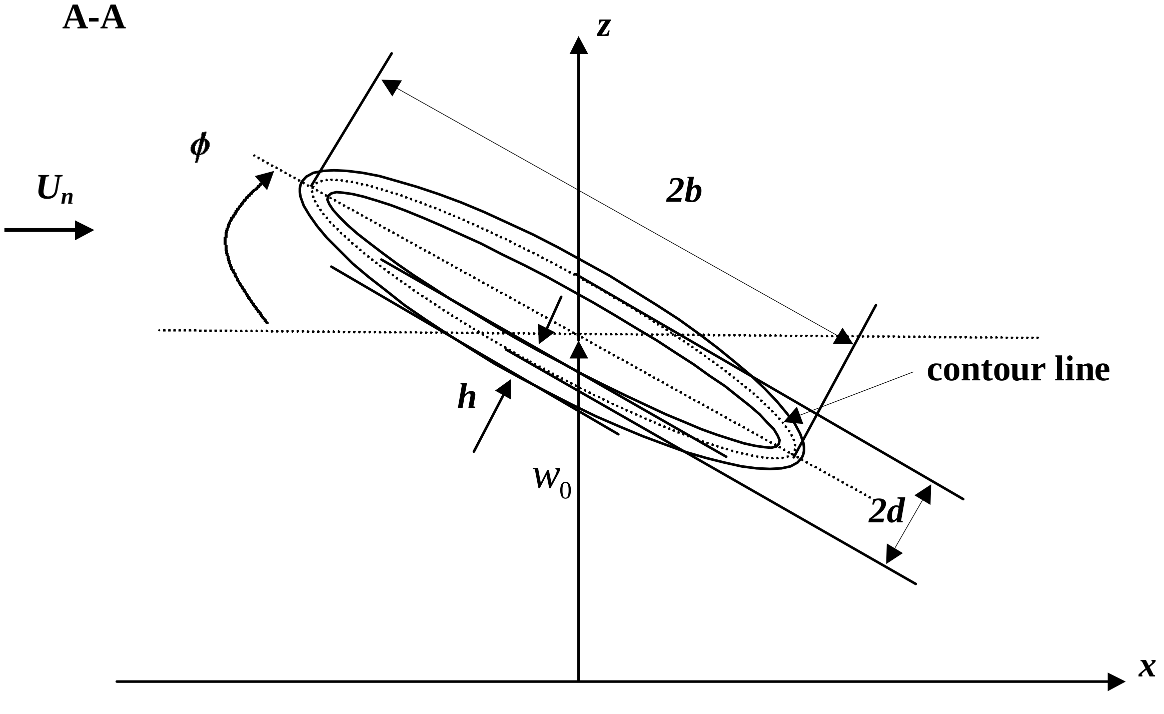

Figure 2.3: Geometric specification of the normal cross-section.

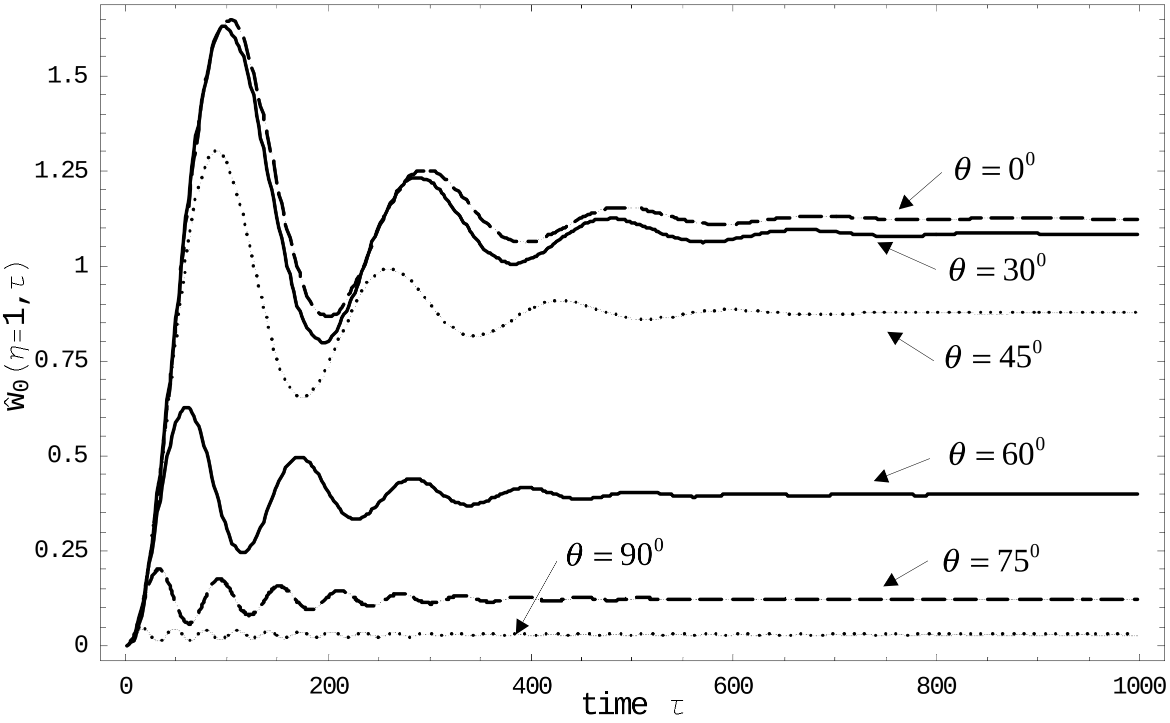

Figure 2.4: The response $\hat{w}_0(\eta = 1,\, \tau)$ of the wings (type A, $[\theta_6]$) subject to a sharp-edged gust with parameters ($U_n = 150\ m/s$, $V_G = 15\ m/s$).

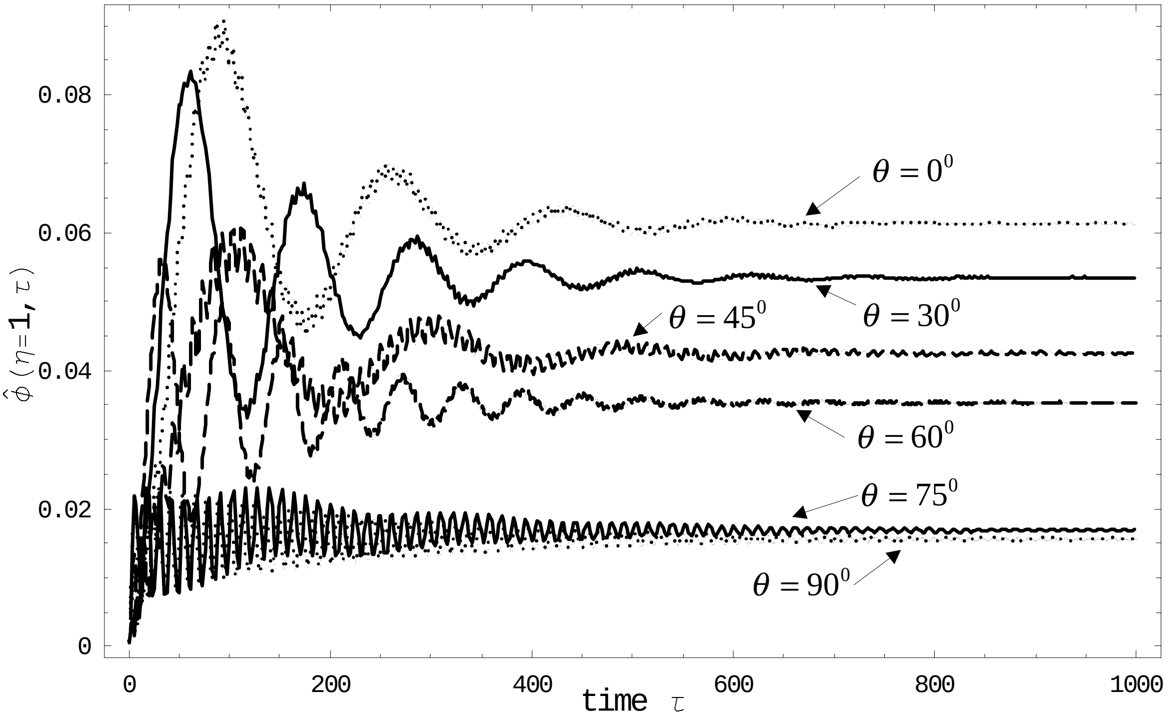

Figure 2.5: The response $\hat{\phi}(\eta = 1,\, \tau)$ of the wings (type A, $[\theta_6]$) subject to a sharp-edged gust with parameters ($U_n = 150\ m/s$, $V_G = 15\ m/s$).

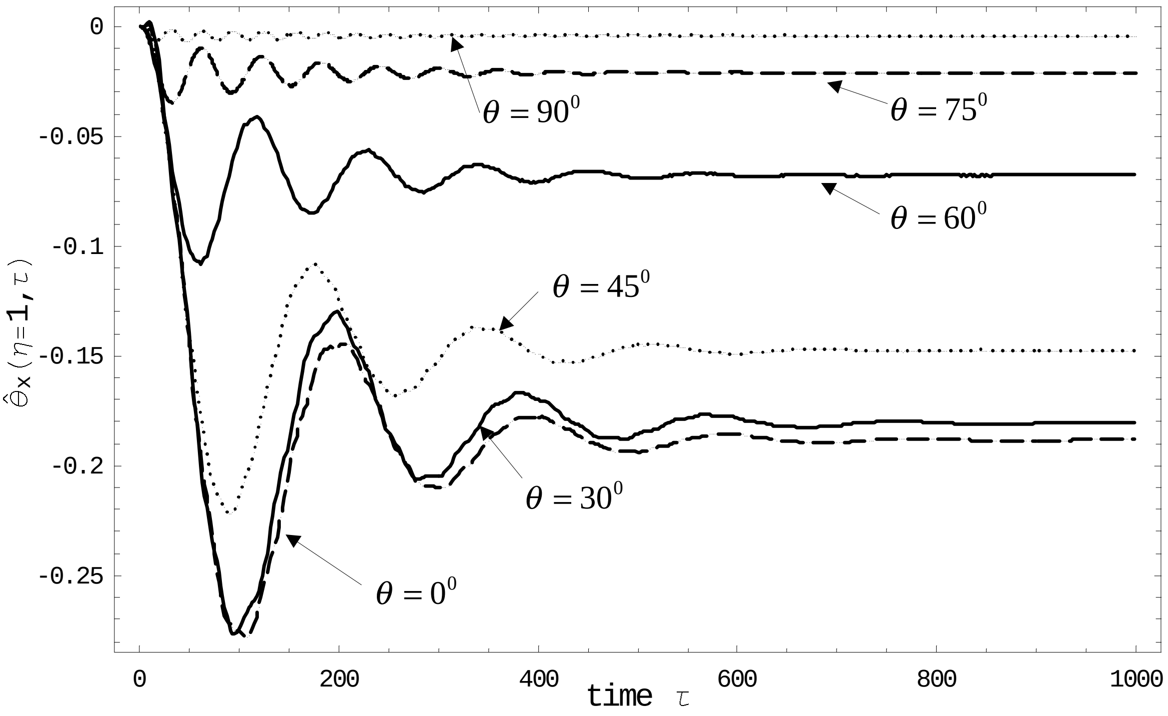

Figure 2.6: The response $\hat{\theta}_x(\eta = 1,\, \tau)$ of the wings (type A, $[\theta_6]$) subject to a sharp-edged gust with parameters ($U_n = 150\ m/s$, $V_G = 15\ m/s$).

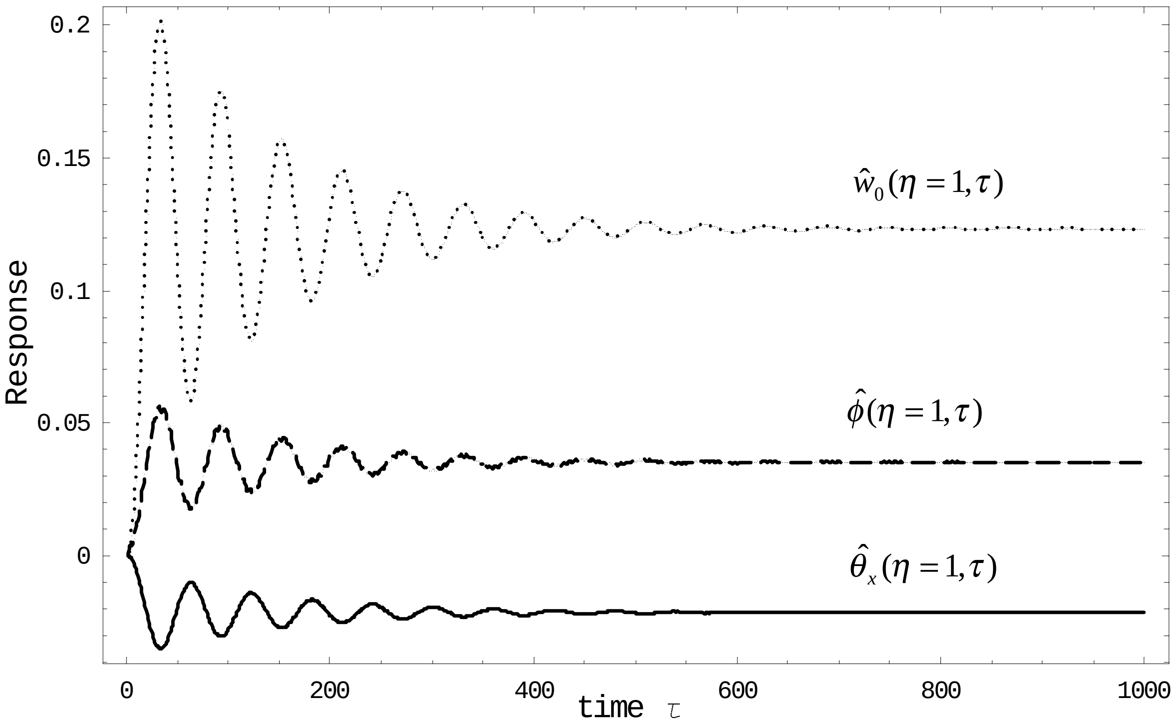

Figure 2.7: Dynamic aeroelastic response of a wing (type A, $[75_6]$) subject to a sharp-edged gust with parameters ($U_n = 150$ m/s, $V_G = 15$ m/s).

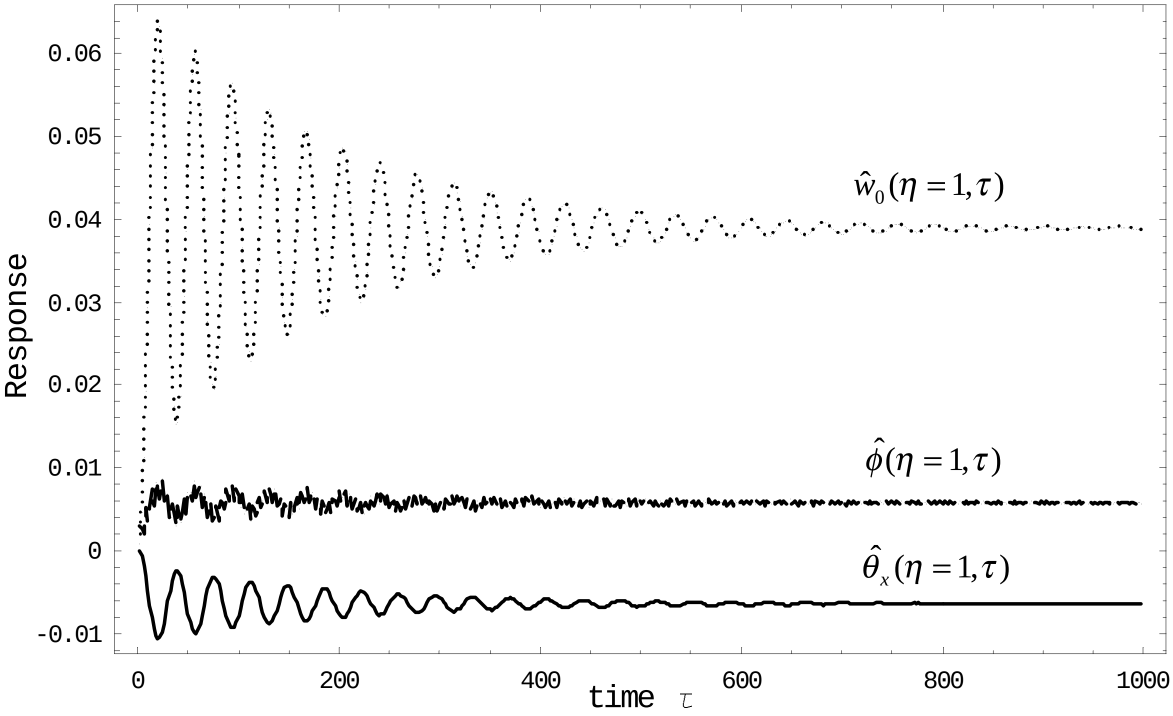

Figure 2.8: Dynamic aeroelastic response of a wing (type A, $[75_2/-75_2/75_2]$) subject to a sharp-edged gust with parameters($U_n = 150\ m/s$, $V_G = 15\ m/s$).

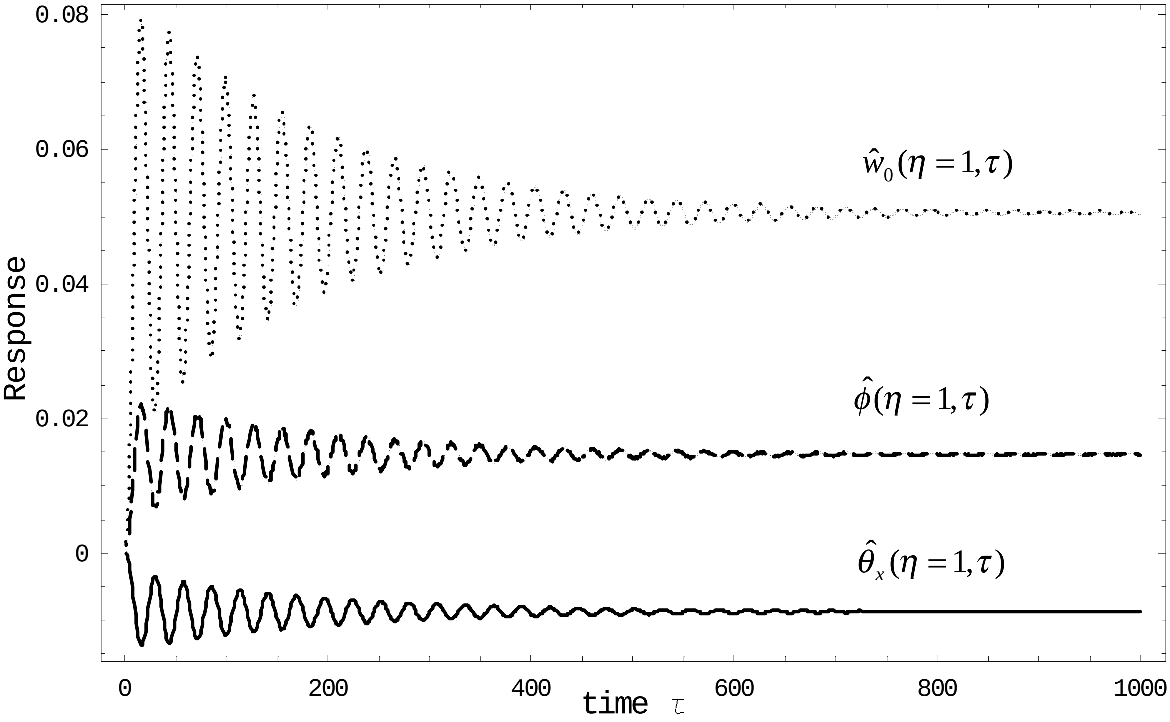

Figure 2.9: Dynamic aeroelastic response of a wing (type A, $[75_6]$) subject to a sharp-edged gust with parameters($U_n = 75\ m/s$, $V_G = 15\ m/s$).

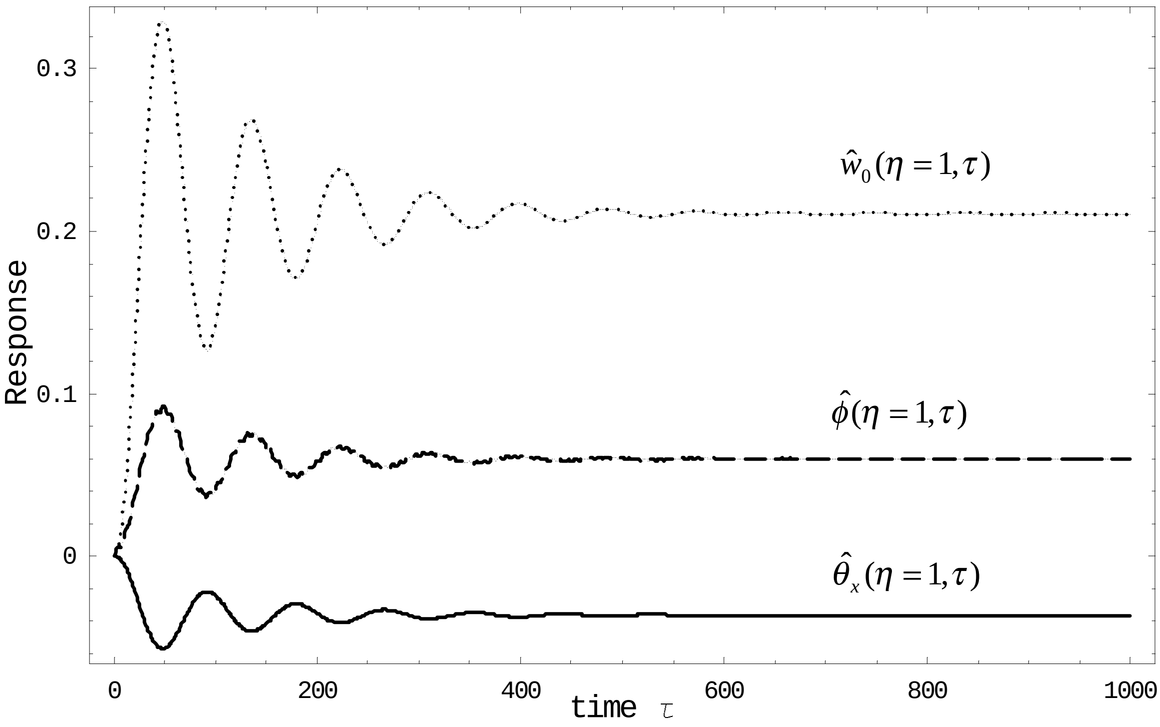

Figure 2.10: Dynamic aeroelastic response of a wing (type A, [75_6]) subject to a sharp-edged gust with parameters($U_n = 200\ m/s$, $V_G = 15\ m/s$).

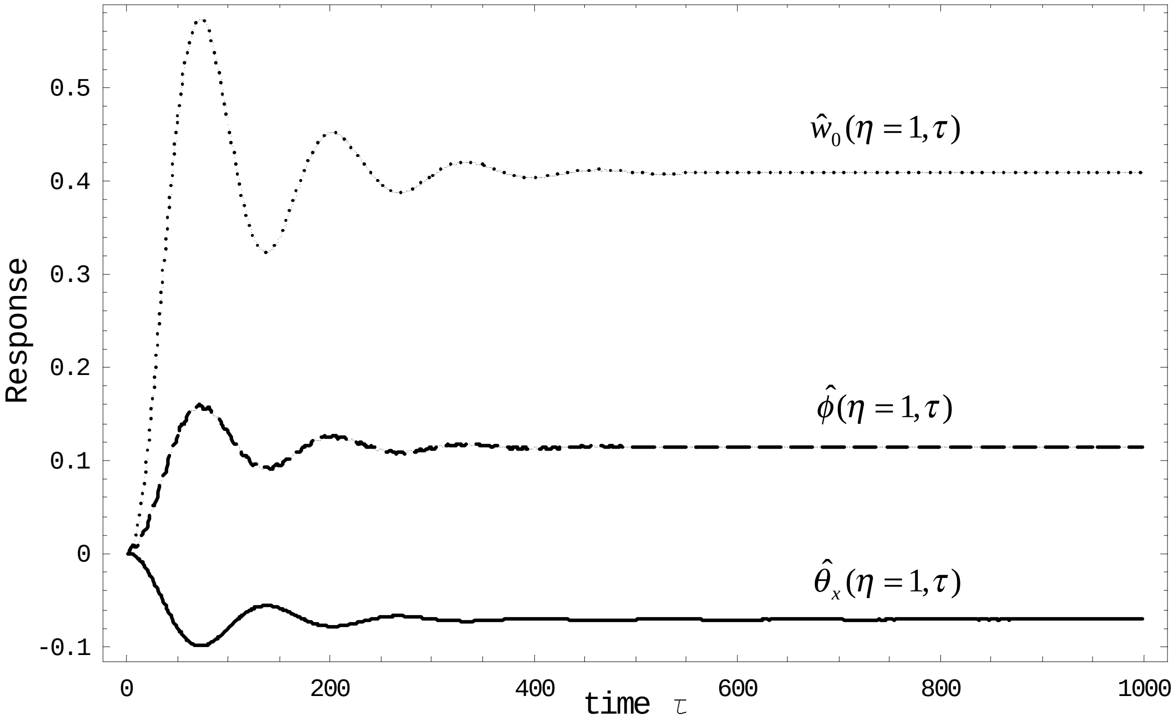

Figure 2.11: Dynamic aeroelastic response of a wing (type A, $[75_6]$) subject to a sharp-edged gust with parameters($U_n = 250\ m/s$, $V_G = 15\ m/s$).

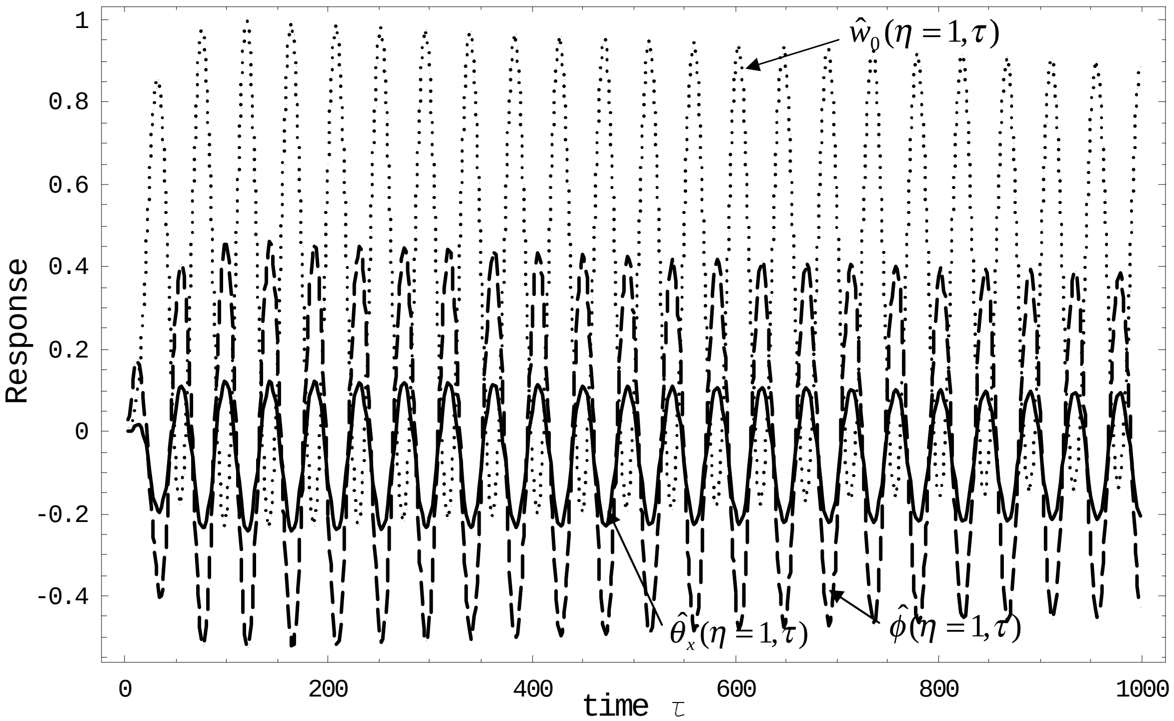

Figure 2.12: Dynamic aeroelastic response of a wing (type B, $[-75_6]$) subject to a sharp-edged gust near the onset of flutter with parameters ($U_n = 235$ m/s, $V_G = 15$ m/s).

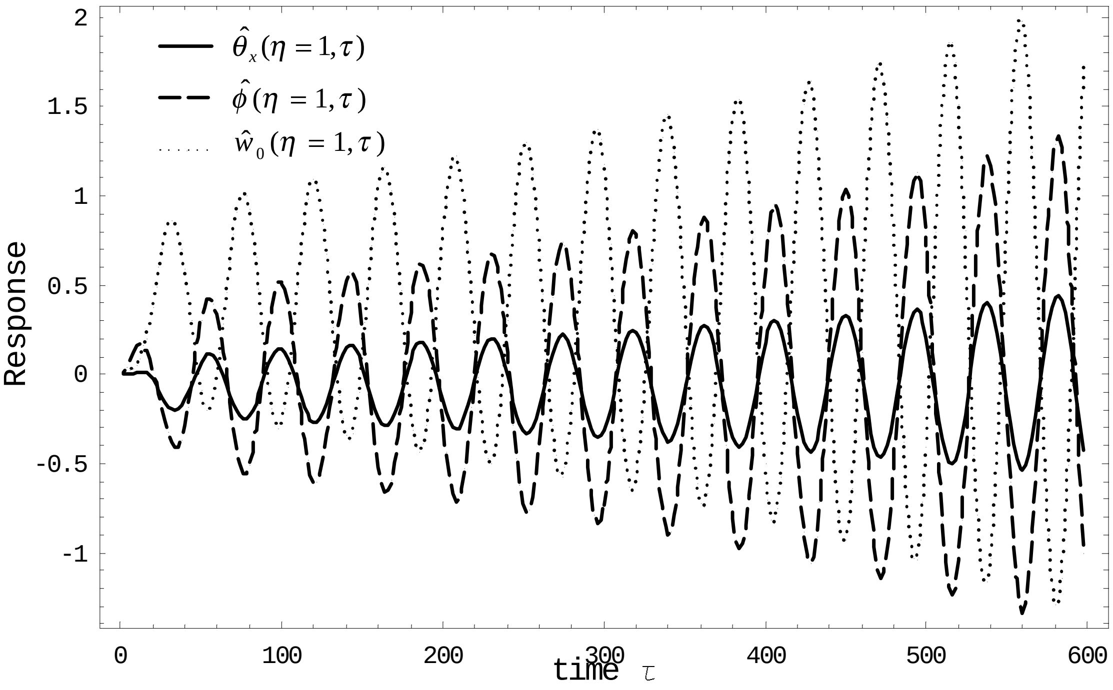

Figure 2.13: Dynamic aeroelastic response of a wing (type B, $[-75_6]$) subject to a sharp-edged gust near the onset of flutter with parameters ($U_n = 236\ m/s$, $V_G = 15\ m/s$).

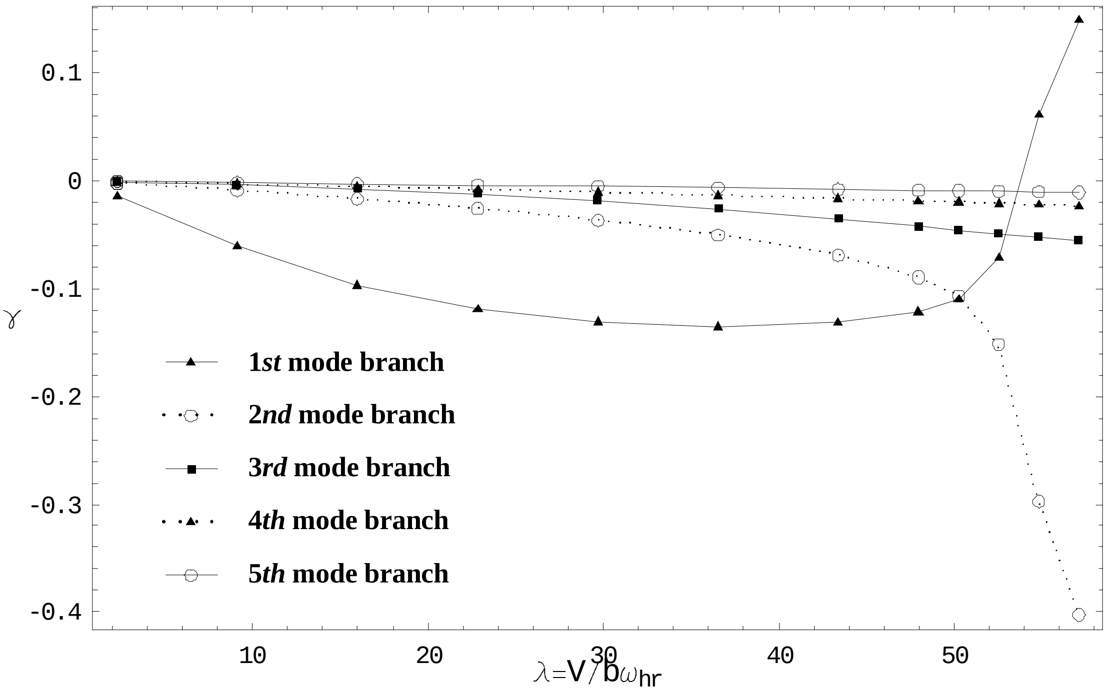

Figure 2.14: Flutter analysis of a wing (type B, $[-75_6]$) by the transient method ($\lambda - \gamma$ Plot).

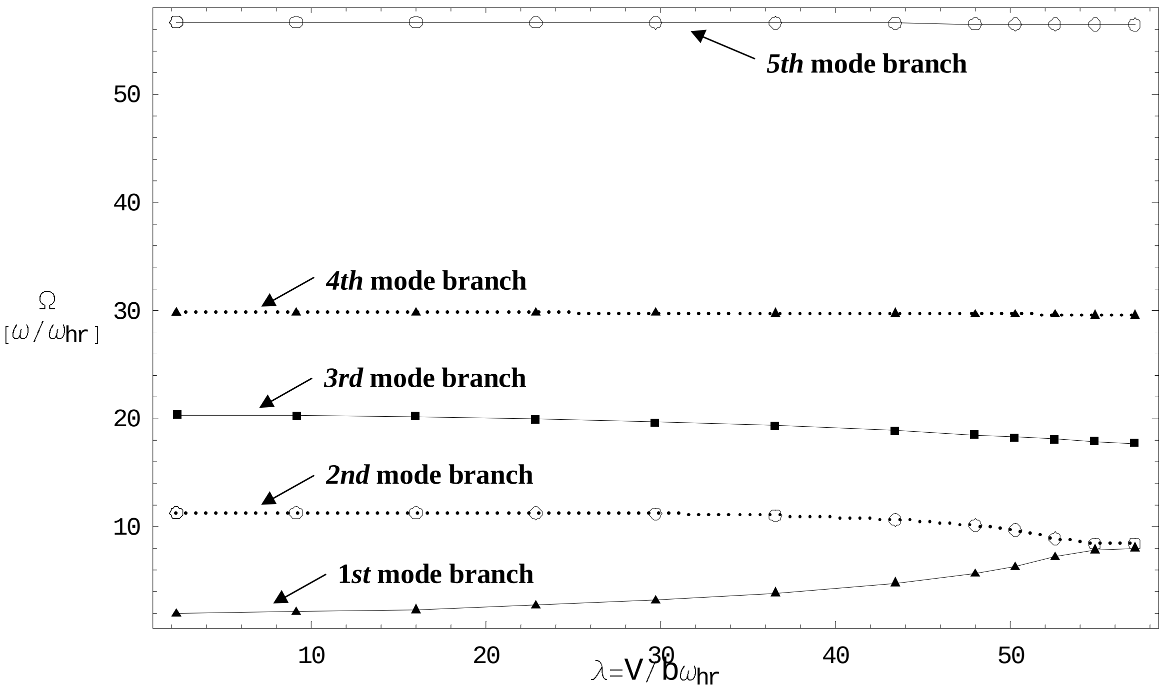

Figure 2.15: Flutter analysis of a wing (type B, $[-75_6]$) by the transient method ($\lambda - \Omega$ Plot).

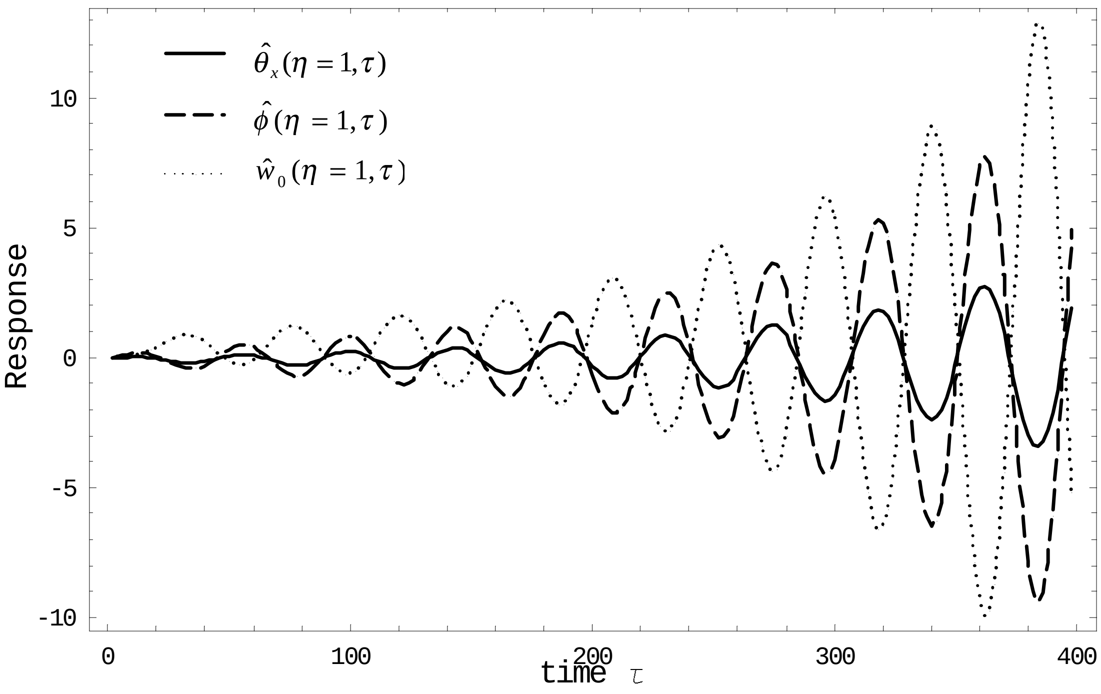

Figure 2.16: Dynamic aeroelastic response prediction of a wing (type B, $[-75_6]$) subject to a sharp-edged gust beyond the onset of flutter with parameters ($U_n = 240\ m/s$, $V_G = 15\ m/s$).

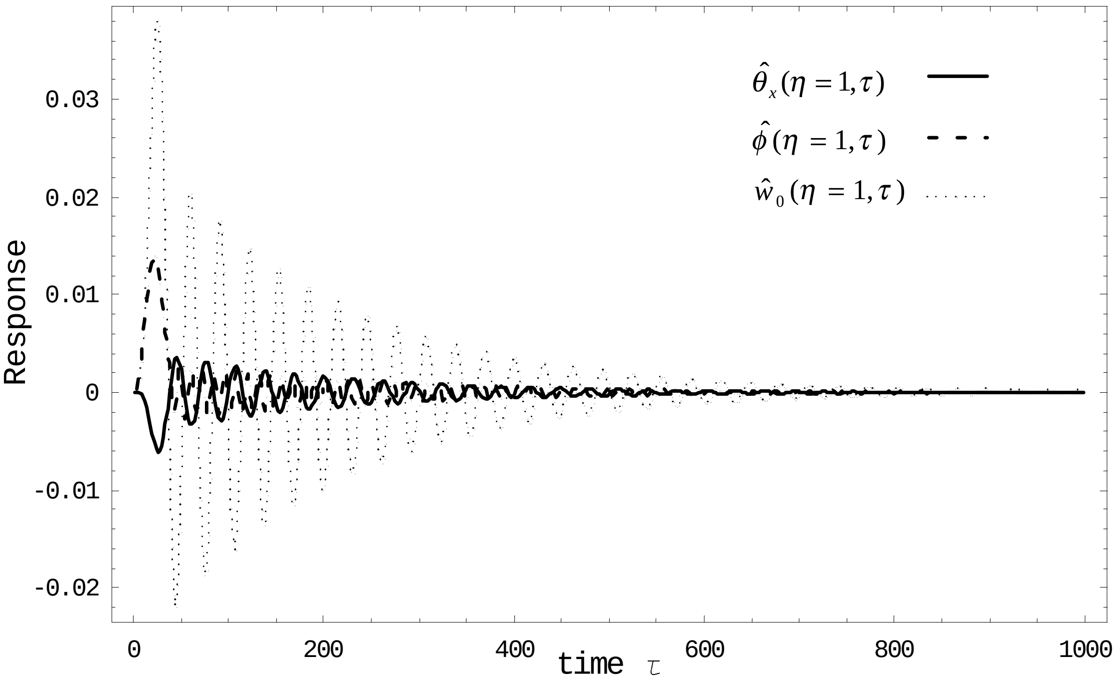

Figure 2.17: Dynamic aeroelastic response of a wing (type A, $[90_6]$) subject to a 1-COSINE gust with parameters($U_n = 150\ m/s$, $V_G = 15\ m/s$, $\tau_p = 20$).

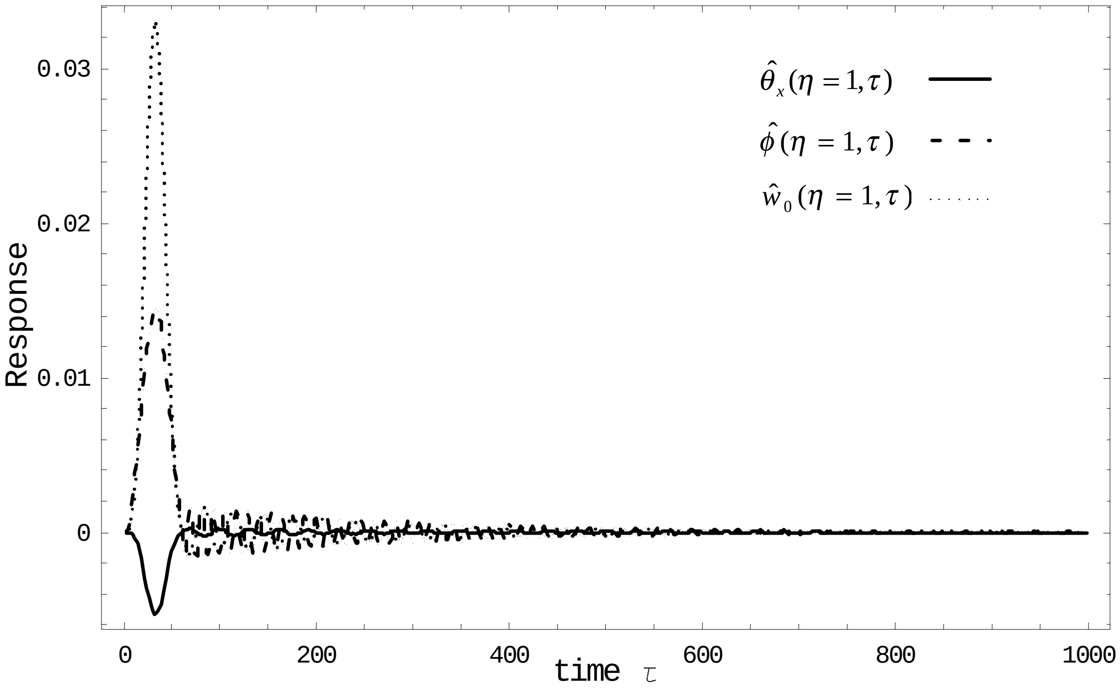

Figure 2.18: Dynamic aeroelastic response of a wing (type A, $[90_6]$) subject to a 1-COSINE gust with parameters($U_n = 150\ m/s$, $V_G = 15\ m/s$, $\tau_p = 30$).

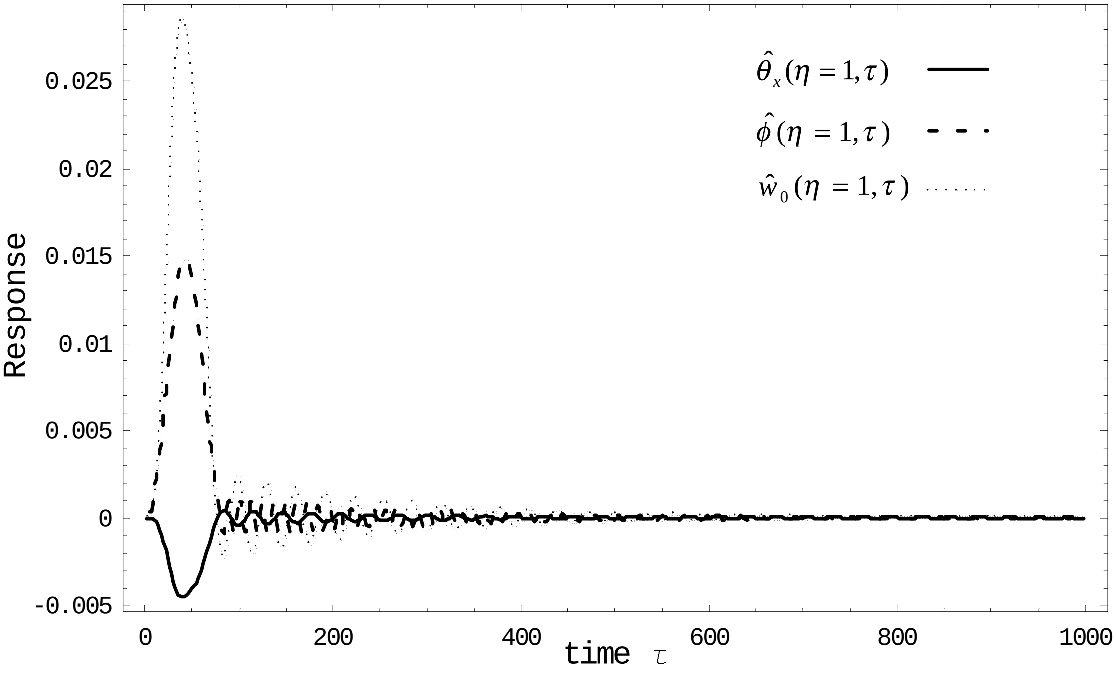

Figure 2.19: Dynamic aeroelastic response of a wing (type A, $[90_6]$) subject to a 1-COSINE gust with parameters($U_n = 150\ m/s$, $V_G = 15\ m/s$, $\tau_p = 40$).

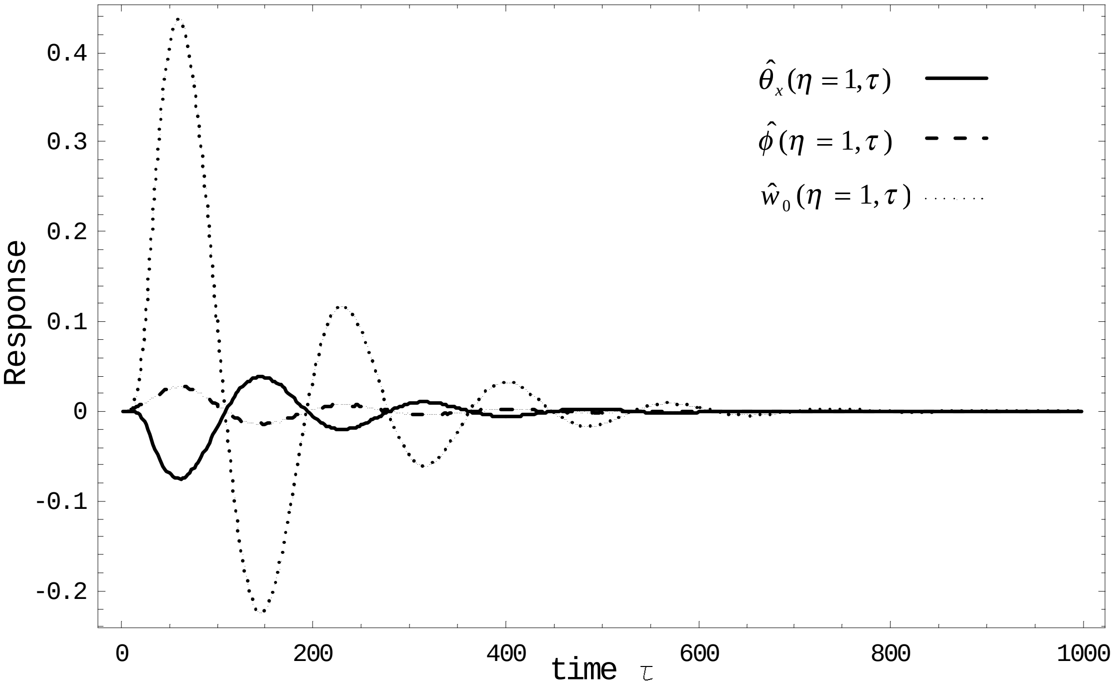

Figure 2.20: Dynamic aeroelastic response of a wing (type A, [45_6]) subject to a 1-COSINE gust with parameters($U_n = 150\ m/s$, $V_G = 15\ m/s$, $\tau_p = 20$).

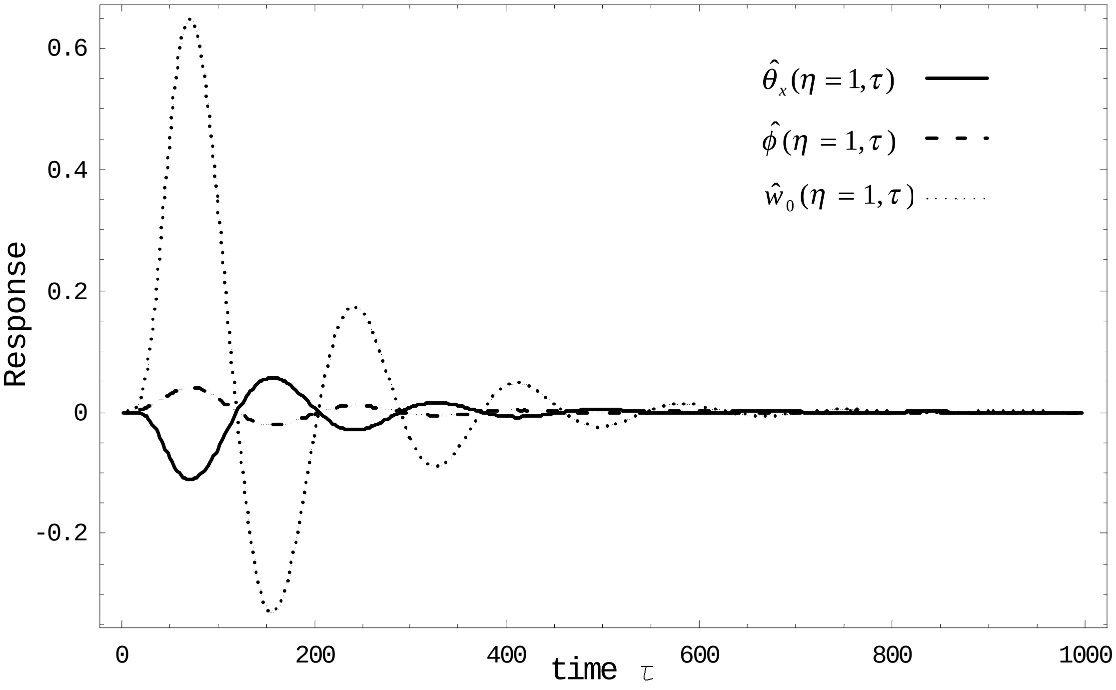

Figure 2.21: Dynamic aeroelastic response of a wing (type A, $[45_6]$) subject to a 1-COSINE gust with parameters($U_n = 150\ m/s$, $V_G = 15\ m/s$, $\tau_p = 30$).

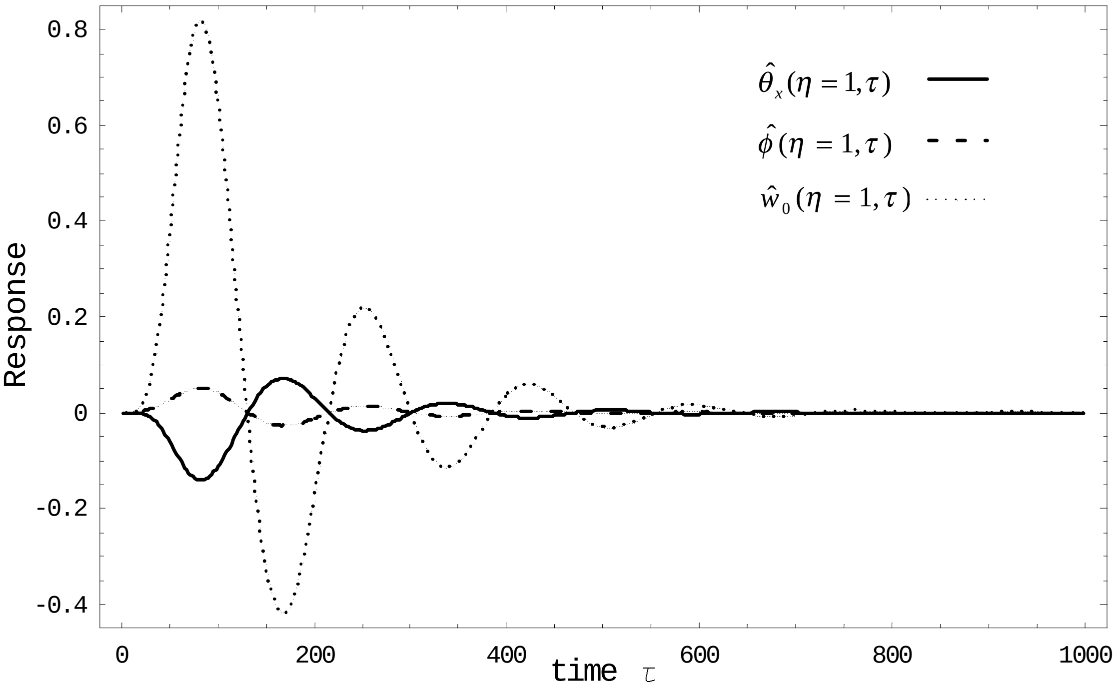

Figure 2.22: Dynamic aeroelastic response of a wing (type A, [45_6]) subject to a 1-COSINE gust with parameters($U_n = 150\ m/s$, $V_G = 15\ m/s$, $\tau_p = 40$).

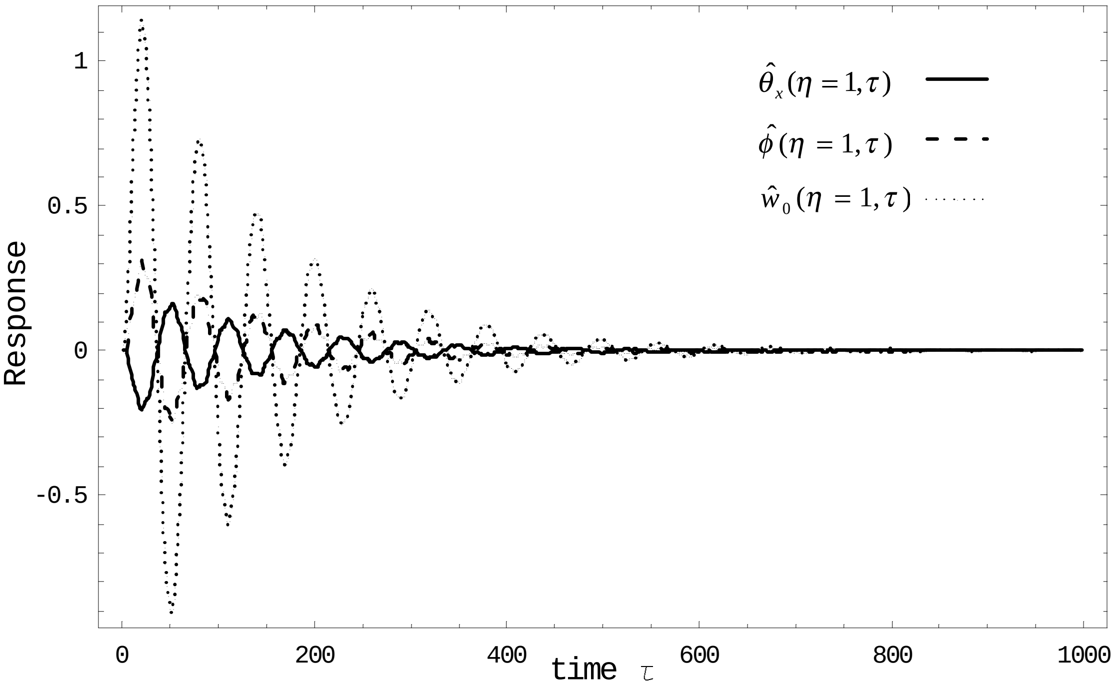

Figure 2.23: Dynamic aeroelastic response of a wing (type A, [75_6]) subject to an explosive blast load with parameters ($U_n = 150\ m/s$, $\hat{P}_m = 0.001$, $\tau_p = 20$).

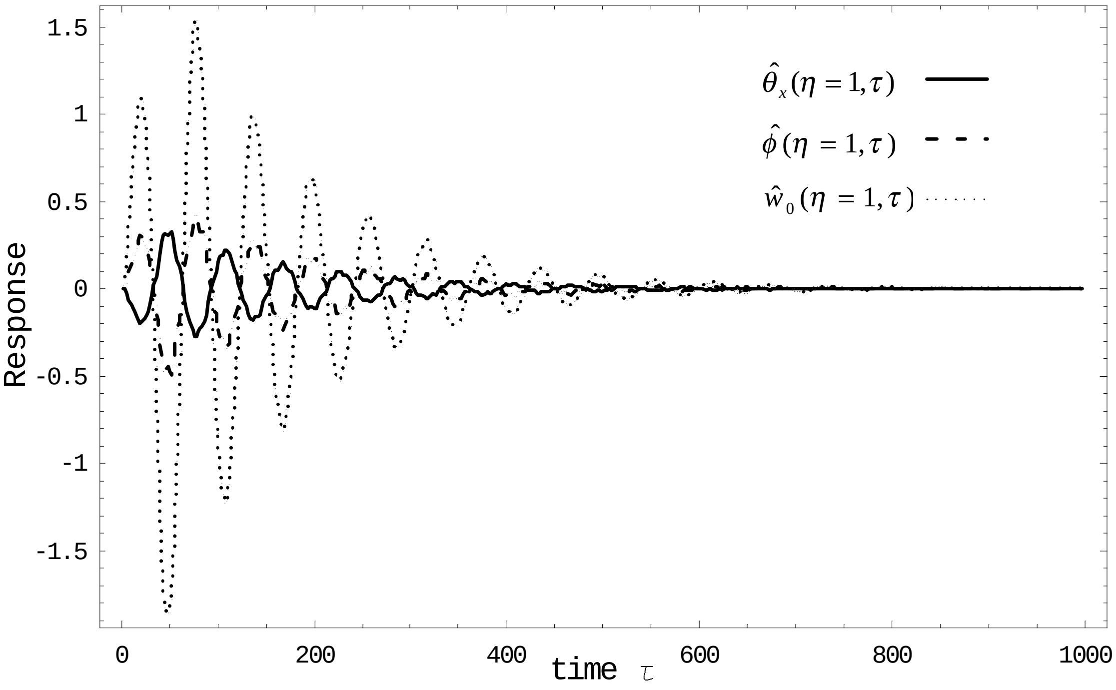

Figure 2.24: Dynamic aeroelastic response of a wing (type A, [75_6]) subject to a sonic-boom pressure signature with parameters ($U_n = 150\ m/s$, $\hat{P}_m = 0.001$, $\tau_p = 20$).

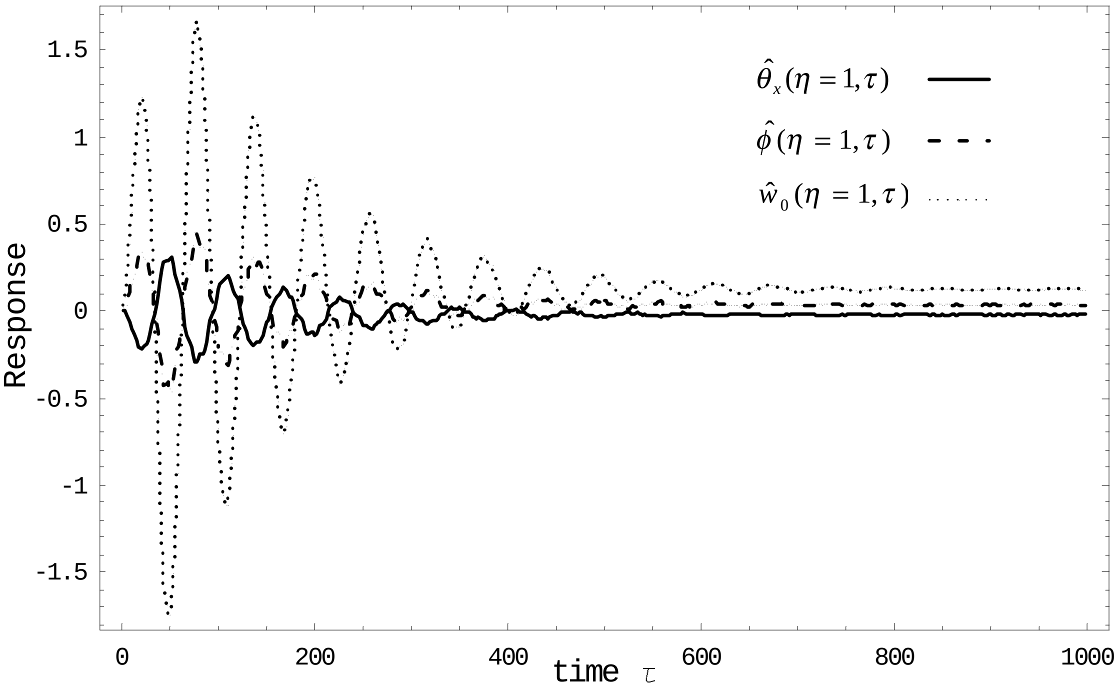

Figure 2.25: Dynamic aeroelastic response of a wing (type A, [75_6]) subject to a sonic-boom pressure signature and a sharp-edged gust with parameters ($U_n = 150\ m/s$, $V_G = 15\ m/s$, $\hat{P}_m = 0.001$, $\tau_p = 20$).

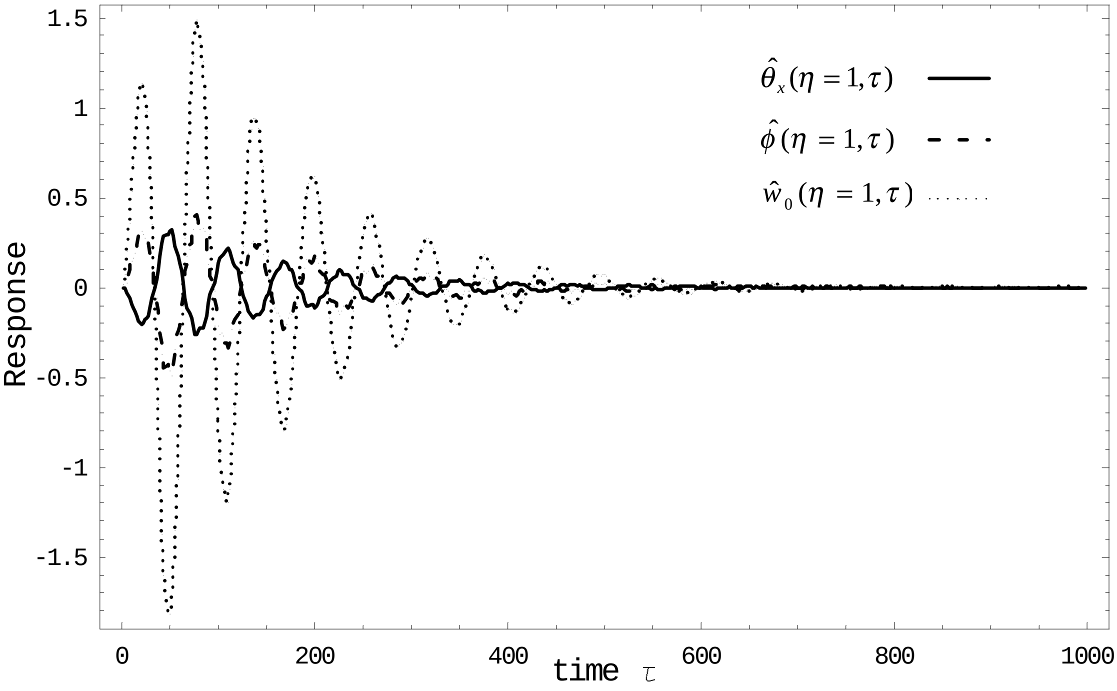

Figure 2.26: Dynamic aeroelastic response of a wing (type A, with $[75_6]$) subject to a sonic-boom pressure signature and a 1-COSINE gust with parameters ($U_n = 150\ m/s$, $V_G = 15\ m/s$, $\hat{P}_m = 0.001$, $\tau_p = 20$).

Chapter 3

Aeroelastic Instability and Response of Advanced Aircraft Wings at Subsonic Flight Speeds

Abstract

A unified aeroelastic model developed towards investigating the flutter instability and subcritical dynamic aeroelastic response to selected gust loads in the subsonic flight speed range is presented. The aircraft wing is modeled as an anisotropic composite thin-walled beam featuring circumferentially asymmetric stiffness (CAS) lay-up configuration that generates preferred elastic couplings. A number of non-classical effects such as transverse shear, warping restraint, and the 3-D strain effects are incorporated in the structural model. The unsteady aerodynamic loads in subsonic flow are based on 2-D indicial functions in conjunction with aerodynamic strip theory extended to 3-D wing model. The numerical results reveal that the compressibility, elastic tailoring and warping restraint have substantial influence on the flutter instability and dynamic response of selected wing configurations.

---

[0] A slightly different version of this chapter with the exception of Section 3.8 has been submitted for publication to the *Journal of Aerospace Science and Technology*;

Section 3.8 is adopted from another paper: "Aeroelasticity of Advanced Aircraft Wings in Supersonic-Hypersonic Flows", which has been submitted for publication to the *Journal of Spacecraft and Rockets.*

Keywords: flutter / subcrticial dynamic aeroelastic response / indicial function / subsonic flow / thin-walled beam

3.1 Introduction

Driven by their high structural efficiency and tremendous potential advantages, thin-walled beam structures made of anisotropic composite materials are likely to be widely used in the design of new generation of flight vehicles [6, 20, 26]. The potential advantages come from the proper exploitation of the material's directionality property, which, in the context of aeroelasticity, has generated a new technology referred to as the aeroelastic tailoring [23]. However, compared with the metallic thin-walled beams, the composite ones are much more complex in the sense that these involve a number of important non-classical effects such as transverse shear, warping inhibition (or warping restraint), non-uniformity of shear stiffness [2, 6, 8, 13, 14, 18, 21, 25, 27, 28], and 3-D strain effects [2, 8, 29]. It is well known that within the classical Euler-Bernoulli beam model, the ratio of Young's modulus to transverse shearing modulus is assumed to be zero, implying that the transverse shear stiffness is infinite. However, for anisotropic composite material, this ratio can be of the order $\mathbf{O}(100)$. For finite span aircraft wings featuring non-uniform distribution of the aerodynamic twist moment, the classical St. Venant twist model has to be discarded in favor of the restrained twist model. In addition, as revealed in [25], the non-uniform distribution of shear stiffness has a significant influence on the warping and twist, and as a result, its effect has to be considered. Towards a reliable aircraft wing design, it is of vital importance to use a structural model that effectively captures these effects and based on it, to investigate the aeroelastic instability and the aeroelastic response. In fact, during the last two decades, a number of analytical thin-walled beam models have been proposed [1, 2, 4, 8, 13, 21, 25, 28, 29]. It should be noted that most of the available work has focused on the modeling and validation (especially static validation) [1, 4, 8, 21, 25, 28, 29], and that very few ones have applied the concept of thin-walled beam models on the aeroelastic problems (on the static divergence and free vibration analyses, see [13, 14, 26, 27]). It is interesting to note that a plate-beam model has been used for investigating the warping restraint and transverse shear on the static divergence, and flutter [7]. Since the aircraft design is primarily based on the principle of thin-walled beams, it is desirable to investigate the aeroelastic instability and aeroelastic response directly within the framework of thin-walled beams. To the best of the authors' knowledge, investigation of flutter instability and dynamic aeroelastic response of advanced aircraft wings modeled as anisotropic thin-walled beams in subsonic flow is quite void in the open literature. In the following section, a refined thin-walled beam model that incorporates all the above mentioned major non-classical effects will be adopted. It should be noted that the basic assumptions underlying this model are proposed in [2, 21, 26].

3.2 Kinematics

A single-cell, closed cross-section, fiber-reinforced composite thin-walled beam will be used in the modeling of advanced aircraft wings in this paper. As stated in the previous section, the major non-classical effects have to be considered, which include transverse shear, anisotropy of the constituent material, warping restraint, and 3-D strain effects. It should be noted that in the original formulation of the beam theory [13, 26, 27], the variation of contour-wise shear stiffness was not included. However, the theory was later extended to account for these effects in a nonlinear theory [2]. For the geometric configuration and the chosen coordinate system that is usually adopted in the analyses of aircraft wings, see *figures 1a* through 1*c*. Based on the basic assumptions stated in [2, 13, 26, 27], the following representation of the 3-D displacement quantities is postulated:

$$u(x,y,z,t) = u_0(y,t) + z\phi(y,t); \quad w(x,y,z,t) = w_0(y,t) - x\phi(y,t); \tag{3.1a}$$

$$v(x,y,z,t) = v_0(y,t) + [x(s) - n\frac{dz}{ds}]\theta_z(y,t) + [z(s) + n\frac{dx}{ds}]\theta_x(y,t) - [F_w(s) + na(s)]\phi'(y,t) \tag{3.1b}$$

where

$$\theta_x(y,t) = \gamma_{yz}(y,t) - w_0'(y,t); \theta_z(y,t) = \gamma_{xy}(y,t) - u_0'(y,t); a(s) = -(z\frac{dz}{ds} + x\frac{dx}{ds}) \quad (3.2)$$

In the above expressions, $\theta_x(y,t)$, $\theta_z(y,t)$ and $\phi(y,t)$ denote rotations of the plane of the cross-section about the axes x, z and the twist about the$y$axis, respectively. $\gamma_{yz}(y,t)$ and $\gamma_{xy}(y,t)$ denote the transverse shear strain measures.

The warping function in Eq.(3.1b) is expressed as

$$F_w(s) = \int_0^s [r_n(s) - \psi(s)]ds \quad (3.3)$$

in which the torsional function $\psi(s)$ and the quantity $r_n(s)$ are expressed as

$$\psi(s) = \frac{\oint_C r_n(\bar{s})d\bar{s}}{h(s)G_{sy}(s)\oint_C \frac{d\bar{s}}{h(\bar{s})G_{sy}(\bar{s})}}; \quad r_n(s) = z\frac{dx}{ds} - x\frac{dz}{ds} \quad (3.4)$$

where $G_{sy}(s)$ is the effective membrane shear stiffness, which is defined as [2]:

$$G_{sy}(s) = \frac{N_{sy}}{h(s)\gamma_{sy}^0(s)} \quad (3.5)$$

Notice that for the thin-walled beam theory considered herein, the six kinematic variables, i.e., $u_0(y,t),\ v_0(y,t),\ w_0(y,t),\ \theta_x(y,t),\ \theta_z(y,t),\ \phi(y,t)$, which represent 1-D displacement measures, constitute the basic unknowns of the problem. When the transverse shear effect is discarded, Eq. (3.2) degenerates to $\theta_x = -w_0'$, $\theta_z = -u_0'$, and as a result, the number of basic unknown quantities reduces to four. Such a case leads to the classical, unshearable beam model.

The strains that contribute to the potential energy are:

Spanwise strain:

$$\varepsilon_{yy}(n,s,y,t) = \varepsilon_{yy}^0(s,y,t) + n\varepsilon_{yy}^n(s,y,t) \quad (3.6a)$$

where

$$\varepsilon_{yy}^0(s,y,t) = {v_0}'(y,t,) + {\theta_z}'(y,t)x(y,t) - \phi''(y,t)F_w(s) \quad (3.6b)$$

$$\varepsilon_{yy}^n(s,y,t) = -{\theta_z}'\frac{dz}{ds} + {\theta_x}'(y,t)\frac{dx}{ds} - a(s)\phi''(y,t) \quad (3.6c)$$

are the axial strain components associated with the primary and secondary warping, respectively.

Tangential shear strain:

$$\gamma_{sy}(s,y,t) = \gamma^0_{sy}(s,y,t) + \psi(s)\phi'(y,t) \tag{3.7a}$$

$$\text{where } \gamma^0_{sy}(s,y,t) = \gamma_{xy}\frac{dx}{ds} + \gamma_{yz}\frac{dz}{ds} = [u'_0 + \theta_z]\frac{dx}{ds} + [w'_0 + \theta_x]\frac{dz}{ds} \tag{3.7b}$$

Transverse shear strain measure:

$$\gamma_{ny}(s,y,t) = -\gamma_{xy}\frac{dz}{ds} + \gamma_{yz}\frac{dx}{ds} = -[u'_0 + \theta_z]\frac{dz}{ds} + [w'_0 + \theta_x]\frac{dx}{ds} \tag{3.8}$$

3.3 Subsonic Aerodynamic Loads, an Indicial Function Approach

The indicial function based aerodynamic models provide an efficient, general, and convenient approach to describe the compressible unsteady flow. This stems from the facts that: i) wherever the linear theory is valid, when the proper indicial functions are available, the unsteady aerodynamic loads to arbitrary small motion can be derived through Duhamel's convolution integral; ii)the indicial functions involved can be derived/approximated by various approaches, such as computational fluid dynamics (CFD) [24], or with the aid of experiments [10]; iii)derivation of indicial functions via CFD can be several orders faster than the direct CFD simulations [24].

However, even in 2-D domain, in contrast to the incompressible case, the indicial functions in subsonic compressible flow are not analytic, except for very limited durations of time [3]. Therefore, in this chapter, in conjunction with the aerodynamic strip theory, a set of empirical 2-D indicial functions developed in [10] are adopted towards the investigation of the aeroelastic behavior of 3-D advanced wings. As to the basic elements and validation of 2-D subsonic indicial functions, the reader is referred to [3, 10, 16, 24].

The downwash velocity can be expressed in a non-dimensional form as

$$w_a(\hat{x},\eta,\tau)=U_n\left\{[2\dot{\hat{w}}_0-\hat{\phi}+\frac{2}{\mathit{AR}}\frac{\partial\hat{w}_0}{\partial\eta}\tan\Lambda_e]-\hat{x}[\dot{\hat{\phi}}+\frac{1}{\mathit{AR}}\frac{\partial\hat{\phi}}{\partial\eta}\tan\Lambda_e]\right\}\triangleq U_n\{\hat{w}_{aT}-\hat{x}\dot{\hat{\phi}}_{aP}\} \tag{3.9a}$$

where we define:

$$\hat{w}_{aT}(\eta,\tau)\equiv U_n[2\dot{\hat{w}}_0-\hat{\phi}+\frac{2}{\mathit{AR}}\frac{\partial\hat{w}_0}{\partial\eta}\tan\Lambda_e];\quad \dot{\hat{\phi}}_{aP}(\eta,\tau)\equiv[\dot{\hat{\phi}}+\frac{1}{\mathit{AR}}\frac{\partial\hat{\phi}}{\partial\eta}\tan\Lambda_e] \tag{3.9b}$$

Denote $(\Phi_c)_0(\tau)$,$(\Phi_{cM})_0(\tau)$ as the indicial lift and moment functions (about the leading edge) due to the unit step change of the vertical translation velocity at the leading edge. As a result, the indicial lift and aerodynamic moment about the *mid-chord* (taken as the reference axis, see *figure 3.3*) are:

$$\begin{aligned}L_T^*(\eta,\tau)&=-\pi\rho_\infty U_n^2(2b)\\&\left\{[\hat{w}_{aT}(\eta,0)+\dot{\hat{\phi}}_{aP}(\eta,0)](\Phi_c)_0(\tau)+\int_0^\tau\frac{\partial(\hat{w}_{aT}(\eta,\sigma)+\dot{\hat{\phi}}_{aP}(\eta,\sigma))}{\partial\sigma}(\Phi_c)_0(\tau-\sigma)d\sigma\right\}\end{aligned} \tag{3.10a}$$

$$\begin{aligned}T_{yT}^*(\eta,\tau)&=-\pi\rho_\infty U_n^2(2b)^2\\&\left\{[\hat{w}_{aT}(\eta,0)+\dot{\hat{\phi}}_{aP}(\eta,0)](\Phi_{cM})_0(\tau)+\int_0^\tau\frac{\partial(\hat{w}_{aT}(\eta,\sigma)+\dot{\hat{\phi}}_{aP}(\eta,\sigma))}{\partial\sigma}(\Phi_{cM})_0(\tau-\sigma)d\sigma\right\}\\&+bL_T^*(\eta,\tau)\end{aligned} \tag{3.10b}$$

where the ratio $(\Phi_{cM})_0(\tau)/(\Phi_c)_0(\tau)$measures the location of the aerodynamic center (fraction of the whole chord length from the leading edge). Upon denoting $(\Phi_{qc})_0(\tau)$,$(\Phi_{cMq})_0(\tau)$ as the indicial lift and moment functions (about the leading edge) due to the unit step change of the pitching rate at the leading edge, the corresponding indicial lift and aerodynamic moment about the *mid-chord* are:

$$L_q^*(\eta,\tau)=2\pi\rho_\infty U_n^2(2b)\left\{[\dot{\hat{\phi}}_{aP}(\eta,0)](\Phi_{cq})_0(\tau)+\int_0^\tau\frac{\partial\dot{\hat{\phi}}_{aP}(\eta,\sigma)}{\partial\sigma}(\Phi_{cq})_0(\tau-\sigma)d\sigma\right\} \tag{3.11a}$$

$$\begin{aligned}T^*_{yq}(\eta,\tau) = {} & 2\pi\rho_\infty U_n^2(2b)^2\left\{\dot{\hat{\phi}}_{aP}(\eta,0)(\Phi_{cMq})_0(\tau) + \int_0^\tau \frac{\partial\dot{\hat{\phi}}_{aP}(\eta,\sigma)}{\partial\sigma}(\Phi_{cMq})_0(\tau-\sigma)d\sigma\right\}\\ & + bL^*_q(\eta,\tau)\end{aligned}\tag{3.11b}$$

Similarly, the ratio $(\Phi_{cMq})_0(\tau)/(\Phi_{cq})_0(\tau)$ measures the location of the aerodynamic center (fraction of the whole chord length from the leading edge).

Therefore, the total aerodynamic lift L_{ae} (positive upwards) and moment about the *mid-chord* T_{ae} (positive nose-up) are:

$$\begin{aligned}L_{ae}(\eta,\tau) &= L^*_T(\eta,\tau) + L^*_q(\eta,\tau)\\ &= -\pi\rho_\infty U_n^2(2b)\left\{\hat{w}_{aT}(\eta,0)(\Phi_c)_{c/2}(\tau) + \int_0^\tau \frac{\partial\hat{w}_{aT}(\eta,\sigma)}{\partial\sigma}(\Phi_c)_{c/2}(\tau-\sigma)d\sigma\right\}\\ &\quad + 2\pi\rho_\infty U_n^2(2b)\left\{\dot{\hat{\phi}}_{aP}(\eta,0)(\Phi_{cq})_{c/2}(\tau) + \int_0^\tau \frac{\partial\dot{\hat{\phi}}_{aP}(\eta,\sigma)}{\partial\sigma}(\Phi_{cq})_{c/2}(\tau-\sigma)d\sigma\right\}\end{aligned}\tag{3.12a}$$

$$\begin{aligned}T_{ae}(\eta,\tau) &= T^*_{yT}(\eta,\tau) + T^*_{yq}(\eta,\tau)\\ &= -\pi\rho_\infty U_n^2(2b)^2\left\{\hat{w}_{aT}(\eta,0)(\Phi_{cM})_{c/2}(\tau) + \int_0^\tau \frac{\partial\hat{w}_{aT}(\eta,\sigma)}{\partial\sigma}(\Phi_{cM})_{c/2}(\tau-\sigma)d\sigma\right\}\\ &\quad + 2\pi\rho_\infty U_n^2(2b)\left\{\dot{\hat{\phi}}_{aP}(\eta,0)(\Phi_{cMq})_{c/2}(\tau) + \int_0^\tau \frac{\partial\dot{\hat{\phi}}_{aP}(\eta,\sigma)}{\partial\sigma}(\Phi_{cMq})_{c/2}(\tau)d\sigma\right\}\end{aligned}\tag{3.12b}$$

where

$$(\Phi_c)_{c/2}(\tau) = (\Phi_c)_0(\tau);\quad (\Phi_{cM})_{c/2}(\tau) = (\Phi_{cM})_0(\tau) + \frac{1}{2}(\Phi_c)_0(\tau);\tag{3.13a}$$

$$(\Phi_{cMq})_{c/2}(\tau) = (\Phi_{cMq})_0(\tau) - \frac{1}{2}(\Phi_{cM})_0(\tau) + \frac{1}{2}(\Phi_{cq})_0(\tau) - \frac{1}{4}(\Phi_c)_0(\tau);\tag{3.13b}$$

$$(\Phi_{cq})_{c/2}(\tau) = (\Phi_{cq})_0(\tau) - \frac{1}{2}(\Phi_c)_0(\tau).\tag{3.13c}$$

In order to expedite the solution of the aeroelastic system, the analytical indicial functions

[3] are approximated by quasi-polynomials:

$$(\Phi_c)_{c/2}(\tau) = A_0^c + \sum_{i=1}^{l} A_i^c \exp[-\beta_i^c \tau]; \quad (\Phi_{cM})_{c/2}(\tau) = A_0^{cM} + \sum_{i=1}^{l} A_i^{cM} \exp[-\beta_i^{cM} \tau]; \tag{3.14a}$$

$$(\Phi_{cq})_{c/2}(\tau) = A_0^{cq} + \sum_{i=1}^{l} A_i^{cq} \exp[-\beta_i^{cq} \tau]; \quad (\Phi_{cMq})_{c/2}(\tau) = A_0^{cMq} + \sum_{i=1}^{l} A_i^{cMq} \exp[-\beta_i^{cMq} \tau] \tag{3.14b}$$

Herein, three aerodynamic lag terms are used for each indicial function, i.e., $l = 3$, as a result, totally 12 aerodynamic lag terms are involved in the description of the 2-D unsteady aerodynamic loads in the subsonic compressible flow. Notice that the above indicial functions are dependent on the flight Mach number. The implementation of the approximation is based on the non-linear curve fitting functions provided by Mathematica®. Comparison of the approximation against the Leishman's indicial functions [10] is displayed in *figure 3.4*.

3.4 Aeroelastic Governing Equations and Solution Methodology

3.4.1 Aeroelastic Governing Equations and Boundary Conditions

The extended Hamilton's Principle [17] provides a convenient way to systematically derive the aeroelastic governing equations and the boundary conditions. This principle states that the true path of motion renders the following variational form stationary:

$$\int_{t_1}^{t_2} (\delta T - \delta V + \overline{\delta W_e})\, dt = 0 \tag{3.15a}$$

with

$$\delta u_0 = \delta v_0 = \delta w_0 = \delta\theta_x = \delta\theta_z = \delta\phi = 0 \quad \text{at } t = t_1,\, t_2 \tag{3.15b}$$

where, δ is the variation operator, T and V denote the kinetic energy and strain energy, respectively, while $\overline{\delta W_e}$ denotes the virtual work due to external forces. These terms are defined as:

Kinetic energy

$$T = \frac{1}{2}\int_0^L \oint_C \sum_{k=1}^{m_l} \int_{h_{(k)}} \rho_{(k)}[(\frac{\partial u}{\partial t})^2 + (\frac{\partial w}{\partial t})^2 + (\frac{\partial v}{\partial t})^2] dndsdy, \tag{3.16}$$

Strain energy

$$\begin{aligned} V &= \frac{1}{2}\int_\tau \sigma_{ij}\varepsilon_{ij}\, d\tau \\ &= \frac{1}{2}\int_0^L \oint_C \sum_{k=1}^{m_l} \int_{h_{(k)}} [\sigma_{yy}\varepsilon_{yy} + \sigma_{sy}\gamma_{sy} + \sigma_{ny}\gamma_{ny}]_{h_{(k)}}\, dndsdy \end{aligned} \tag{3.17}$$

Virtual work due to unsteady aerodynamic, gust and blast loads:

$$\overline{\delta W_e} = \int_0^L (p_z(y,t)\delta w_0(y,t) + m_y(y,t)\delta\phi(y,t))\, dy \tag{3.18}$$

In equation (3.18), the total lift density $p_z(y,t) = L_{ae} + L_g + L_b$and total twist moment density $m_y(y,t) = T_{ae} + T_g + T_b$. It should be noted here that the conjugate pairs $(\sigma_{ss}, \varepsilon_{ss})$ and $(\sigma_{sn}, \gamma_{sn})$ do not contribute to the total strain energy V, hence do not appear in equation (3.18). In order to study the aeroelastic problems featuring bending-twist cross-coupling, a beam featuring circumferentially asymmetric stiffness (CAS) lay-up configuration [21, 25, 27] and characterized by a biconvex cross-section is considered. As demonstrated in [13, 27], this type of beam features two separate sets of elastic couplings, vertical bending/twist/vertical transverse shear (w_0, ϕ, θ_x) and extension/lateral bending/ lateral transverse shear (u_0, v_0, θ_z). Moreover, the aerodynamic loads and the inertia forces of the beam are completely split into the above two groups, hence the total equations of motion and the boundary conditions are completely decoupled. Therefore, the second group in the above mentioned sets can be safely discarded.

In terms of the basic unknowns, the governing equations that account for warping inhibition and transverse shear are:

$$\delta w_0 \ : \quad a_{55}(w_0'' + \theta_x') + \underline{\underline{a_{56}\phi'''}} + L_{ae} + L_g + L_b - b_1\ddot{w}_0 = 0 \tag{3.19a}$$

$$\delta\phi \ : \quad a_{37}\theta_x'' + a_{77}\phi'' - a_{56}(w_0''' + \theta_x'') - \underline{\underline{a_{66}\phi^{(IV)}}} + T_{ae} + T_g - (b_4 + b_5)\ddot{\phi} + \underline{\underline{(b_{10} + b_{18})\ddot{\phi}''}} = 0 \tag{3.19b}$$

$$\delta\theta_x \ : \quad a_{33}\theta_x'' + a_{37}\phi'' - a_{55}(w_0' + \theta_x) - \underline{\underline{a_{56}\phi''}} - \underline{(b_4 + b_{14})\ddot{\theta}_x} = 0 \tag{3.19c}$$

Boundary conditions:

$$\text{At } y = 0, \quad w_0 = 0, \quad \phi = 0, \quad \underline{\underline{\phi' = 0}}, \quad \theta_x = 0 \tag{3.20a}$$

At $y = L$,

$$\begin{aligned}
\delta w_0 \quad &: \quad a_{55}(w_0' + \theta_x) + \underline{\underline{a_{56}\phi''}} = 0,\\
\delta\phi \quad &: \quad -a_{56}(w_0'' + \theta_x') - \underline{\underline{a_{66}\phi'''}} + a_{37}\theta_x' + a_{77}\phi' = -(b_{10} + b_{18})\ddot{\phi}',\\
\delta\phi' \quad &: \quad -a_{56}(w_0' + \theta_x) - \underline{\underline{a_{66}\phi''}} = 0,\\
\delta\theta_x \quad &: \quad a_{33}\theta_x' + a_{37}\phi' = 0
\end{aligned} \tag{3.20b}$$

In the above equations, the terms underscored by double solid lines are associated with the warping inhibition effect, whereas the term underscored by a single solid line identifies the rotatory inertia effect [13, 18, 26, 27].

For the unshearable beam model, the governing equations reduce to:

$$\delta w_0 \ : \quad -a_{33}w_0^{(IV)} + a_{37}\phi''' + L_{ae} + L_g + L_b - b_1\ddot{w}_0 + (b_4 + b_{14})\ddot{w}_0'' = 0 \tag{3.21a}$$

$$\delta\phi \ : \quad -a_{37}w_0''' + a_{77}\phi'' - a_{66}\phi^{(IV)} + T_{ae} + T_g - (b_4 + b_5)\ddot{\phi} + (b_{10} + b_{18})\ddot{\phi}'' = 0 \tag{3.21b}$$

and the boundary conditions are:

$$\text{At } y = 0; \quad w_0 = 0;\ w_0' = 0;\ \phi = 0;\ \phi' = 0; \tag{3.22a}$$

At $y = L$

$$
\begin{aligned}
\delta w_0 &: \quad a_{33} w_0''' - a_{37} \phi'' - (b_4 + b_{14}) \ddot{w}_0' = 0; \\
\delta w_0' &: \quad -a_{33} w_0'' + a_{37} \phi' = 0; \\
\delta \phi &: \quad a_{66} \phi''' + a_{37} w_0'' - a_{77} \phi' - (b_{10} + b_{18}) \ddot{\phi}' = 0; \\
\delta \phi' &: \quad a_{66} \phi'' = 0
\end{aligned}
\tag{3.22b}
$$

3.4.2 State Space Solution

In conjunction with the extended Galerkin's method (EGM) [11, 19], we cast the approximated solution of the aeroelastic system into the following state space form:

$$
\left\{ \begin{array}{c} \dot{\hat{\mathbf{x}}}_s \\ \dot{\hat{\mathbf{x}}}_a \end{array} \right\} = \left[\begin{array}{cc} \mathbf{A}_s & \mathbf{B}_s \\ \mathbf{B}_a \mathbf{A}_s & \mathbf{A}_a + \mathbf{B}_a \mathbf{B}_s \end{array} \right] \left\{ \begin{array}{c} \hat{\mathbf{x}}_s \\ \hat{\mathbf{x}}_a \end{array} \right\} + \left[\begin{array}{c} \mathbf{0}_{m \times 1} \\ \bar{\mathbf{M}}_n^{-1} \\ \mathbf{D}_2 \bar{\mathbf{M}}_n^{-1} \\ \vdots \\ \mathbf{D}_2 \bar{\mathbf{M}}_n^{-1} \end{array} \right] \{ \mathbf{Q}_g + \mathbf{Q}_b \}
\tag{3.23}
$$

or in a more compact form, as

$$
\{\dot{\hat{\mathbf{X}}}\} = [\mathbf{A}]\{\hat{\mathbf{X}}\} + [\mathbf{B}_e]\{\mathbf{Q}_g\} + [\mathbf{B}_e]\{\mathbf{Q}_b\}
\tag{3.24}
$$

where $\hat{\mathbf{x}}_s$ and $\hat{\mathbf{x}}_a$ are $2m \times 1$, $lm \times 1$ vectors, which describing the motion of the wing and unsteady aerodynamic loads on the wing, respectively. $\mathbf{Q}_g$ and $\mathbf{Q}_b$ are the generalized gust and blast loads, respectively. The details of the matrices and vectors in equations (3.23, 3.24) are listed in Appendix B. For an analytical description of the gust and blast loads, see e.g. [3, 12, 15]. Notice that for blast loads, we assume that they are uniform throughout the wing.

3.5 Validation

In order to validate the accuracy of the model developed so far, Goland's wing [5] is used. The flutter result in incompressible flow by using the transient method [22] is calculated, which is compared against the exact one [5]. Notice that in the above transient method, Jones' quasi-polynomial approximation of Wagner's function is used. It can be seen in *Table 3.1* that the correlation is excellent and the offfset of flutter speed and flutter frequency by the transient method is well within the approximation accuracy of Wagner's function. Followed by the first step, compressibility effect on Goland's wing is investigated and the comparison results are also displayed in *Table 3.1*. It can be seen that the compressibility only causes about 5.0% decrease of the flutter speed and 2.2% decrease of the flutter frequency compared with the predictions by the incompressible model. This is consistent with the well-known fact that at the lower range of the compressible subsonic speeds, the effect of compressibility on flutter is quite small.

3.6 Numerical Results and Discussion

In this section, the effect of the flow compressibility on flutter instability of advanced aircraft wings modeled as anisotropic thin-walled beams is first investigated. This will be followed by the investigation of the influences of ply orientation, sweep angle, and aspect ratio on the dynamic aeroelastic response of aircraft wings exposed to selected gust and blast loads. The implication of warping restraint and transverse shear effects on the response is also investigated. The geometric and material specifications of the beams with CAS lay-up configuration are listed in *Table 3.2*, and *3.3*. Notice that in the actual implementation, the first 5 structural modes and 3 aerodynamic lag terms for each indicial function (see equations (3.14a-d)) are used, i.e., $m = 5,\ l = 3$, all the response components (bending, twist and transverse) are measured at the beam tip ($\eta = 1$), and the gust intensity is specified to be $V_G = 15m/s$ for the all test cases.

Figures 3.6, 3.7, 3.8, 3.9 display the flutter results by using the incompressible and compressible unsteady aerodynamic models, respectively. Notice that Jones' quasi-polynomial approximation of Wagner's function is used in the incompressible model while Leishman's indicial functions are used in the compressible model. The related parameters are: $[105_6]$ lay-up,$\mathcal{R} = 12$, $\Lambda_g = 0^0$. From these figures, it results $M_{Flutter} = 1.18$ and $f_{Flutter} = 18.89Hz$ for the incompressible aerodynamic model while $M_{Flutter} = 0.69$ and $f_{Flutter} = 10.57Hz$ for the compressible aerodynamic model. The big difference of the flutter results (41.8% drop of the flutter speed and 44.1% drop of the flutter frequency compared with the incompressible results) between these two models reveals the significant role played by the compressibility on the flutter. Paralleling the explanation in [9] of the transonic dip, it can be conjectured that also in this case, the same mechanism yielding the big drop both in the flutter speed and flutter frequency can be invoked. Another interesting phenomenon from *figures 3.7* and *3.8* is that the frequency coalescence featuring the flutter onset predicted by the incompressible model almost vanishes in the compressible case, implying the possible dramatic change of flutter type induced by compressibility.

Figures 3.10 displays the influence of sweep angle on the response of a selected wing to a sharp-edged gust. The related parameters are: $[120_6]$ lay-up, $\mathcal{R} = 12$,$M_{Flight} = 0.5$, $\tau_p = 40$. It is noted that the sweep angle can be effectively used to reduce the deflection amplitude.

Figure 3.11 displays the sensitivity of the wing response to subsonic flight speeds. The related parameters are: $[120_6]$ lay-up, $\mathcal{R} = 12$, $\Lambda_g = 0^0$. Notice that the unsteadiness of the subsonic aerodynamic loads played a significant role on the response behavior.

Figure 3.12 displays the influence of ply orientation on the dynamic aeroelastic response to a sharp-edged gust. The related parameters are: $[\theta_6]$ lay-up, $\mathcal{R} = 12$, $\Lambda = 0^0$, $M_{Flight} = 0.7$. Two interesting observations can be reached: 1) ply orientation can be effectively used to postpone the occurrence of the flutter instability; 2) this postponement of flutter instability may be at the cost of introducing large amplitudes of the dynamic aeroelastic response, implying the complex influences by elastic tailoring on the aeroelastic behavior and optimization techniques may become a necessity.

Figures 3.13, 3.14 display the effect of warping restraint and transverse shear on the dynamic aeroelastic response subject to a sharp-edged gust. The related parameters are: $[75_6]$ lay-up, $\Lambda = 30^0$, $M_{Flight} = 0.7$, $\mathit{AR} = 10$ in *figure 3.13* and $\mathit{AR} = 8$ in *figure 3.14*. It can be seen that the warping restraint has significant influence on the response even for large aspect ratio wings. In contrast, transverse shear has a negligible influence on the response of the large aspect ratio wings. *Figure 3.15* displays the shape of the wing predicted by warping restraint, free warping and unshearable models at the fixed time $\tau = 1000$. It can be seen that the maximum amplitudes of the response occur at the wing tip.

Figure 3.16 displays one remarkable result related to warping restraint, i.e., warping restraint model may yield larger amplitudes of the response than the free warping model counterpart. The related parameters are: $[135_6]$ lay-up, $\Lambda = 0^0$, $\mathit{AR} = 12$ and $M_{Flight} = 0.7$. This is due to the complex interaction of warping restraint effect and the elastic coupling: warping restraint tends to increase the twist stiffness, which is outweighed by the decrease of the twist stiffness induced by elastic coupling for $[135_6]$ lay-up.

3.7 Conclusion

The problems of flutter and dynamic aeroelastic response of advanced aircraft wings modeled as anisotropic composite thin-walled beams in subsonic flow and exposed to selected gust and blast loads are approached in a unified framework. Based on the model developed herein, the effect of aerodynamic compressibility on flutter and the implications of ply orientation, sweep angle, aspect ratio, warping restraint, and transverse shear on the dynamic aeroelastic response are investigated. For the wings selected in the test cases, the non-uniformity of the contour-wise shear stiffness becomes immaterial. The major conclusions are:

- Compressibility at high subsonic speeds has a significant influence on flutter of the advanced aircraft wings: the compressibility can yield a drop of the flutter speed and flutter frequency by about 41% as compared to the incompressible counterpart. In addition, the mechanism of flutter may be dramatically changed by compressibility.

- Elastic tailoring can be effectively used to suppress the onset of flutter. However, this may be achieved at the cost of dramatically increasing the response intensity.
- Warping restraint has a significant influence on the dynamic response on the selected wings in subsonic flow, even for large aspect ratio wings. Therefore, warping restraint effect has to be considered in the structural model. Compared with the warping restraint effect on the response, the influence of transverse shear is much smaller.
- The interaction of warping restraint effect and the elastic coupling complicates the aeroelastic response behavior.

3.8 Time-Domain Unsteady Aerodynamic Loads in Supersonic-Hypersonic Flows

As formerly mentioned, within linear theory, the indicial function based aerodynamic model provides a general and convenient approach to describe the compressible unsteady flows. For the case of compressible subsonic flow, a set of empirical 2-D indicial functions are adopted in conjunction with the aerodynamic strip theory; for the case of supersonic or hypersonic flow, a set of exact Lomax's indicial functions (2-D, Ref. [3], pp. 371-372) are adopted in conjunction with the strip theory. The approximation of these exact indicial functions by quasi-polynomials and the conversion to state-space form is similar to the case of subsonic flow. Comparisons of the approximation against the exact solution are displayed in Fig. 3.5. Tables 3.4, 3.5, 3.6, and 3.7 list the coefficients of each unsteady aerodynamic indicial function for the selected Mach numbers.

3.9 References

[1] Badir A. Berdichevski V. L., Armanios E. Theory of anisotropic thin-walled closed cross-section beams. *Composite Engineering*, 2(5-7):411–432, 1992.

[2] K. Bhaskar and L. Librescu. A Geometrically Non-Linear Theory for Laminated Anisotropic Thin-Walled Beams. *International Journal of Engineering Science*, 33(9):1331–1344, 1995.

[3] R. L. Bisplinghoff, H. Ashley, and R. L. Halfman. *Aeroelasticity.* Dover Publications, New York, 1996.

[4] R. Chandra and I. Chopra. Structural response of composite beams and blades with elastic couplings. *Composites Engineering*, 2(5-7):347–374, 1992.

[5] M. Goland and Y. Luke. The flutter of a uniform cantilever wing with tip weights. *Journal of Applied Mechanics*, 15(1):13–20, 1948.

[6] S. N. Jung, V. T. Nagaraj, and I. Chopra. Assessment of composite rotor blade modeling techniques. *Journal of the American Helicopter Society*, 44(3):188–205, 1999.

[7] G. Karpouzion and L. Librescu. Nonclassical effects on divergence and flutter of anisotropic swept aircraft wings. *AIAA Journal*, 34(4):786–794, 1996.

[8] C. Kim and S. R. White. Thick-Walled Composite Beam Theory Including 3-D Elastic Effects and Torsional Warping. *International Journal of Solids and Structures*, 34(31-32):4237–59, 1997.

[9] Isogai Koji. On the transonic-dip mechanism of flutter of a sweptback wing. *AIAA Journal*, 17(7):793–795, 1979.

[10] J. Leishman. Indicial lift approximations for two-dimensional subsonic flow as obtained from oscillatory measurements. *Journal of Aircraft*, 30(3):340–351, 1993.

[11] L. Librescu, L. Meirovitch, and S. S. Na. Control of cantilevers vibration via structural tailoring and adaptive materials. *AIAA Journal*, 35(8):1309–1315, 1997.

[12] L. Librescu and S. S. Na. Dynamic response of cantilevered thin-walled beams to blast and sonic-boom loadings. *Shock and Vibration*, (5):23–33, 1998.

[13] L. Librescu and O. Song. Behavior of Thin-Walled Beams Made of Advanced Composite Materials and Incorporating Non-Classical Effects. *Applied Mechanics Reviews*, 44(11, part 2):S174–S180, 1991.

[14] L. Librescu and O. Song. On the static aeroelastic tailoring of composite aircraft swept wings modeled as thin-walled beam structures. *Composites Engineering*, 2:497–512, 1992.

[15] P. Marzocca, L. Librescu, and G. Chiocchia. Aeroelastic response of 2-d lifting surfaces to gust and arbitrary explosive loading signatures. *International Journal of Impact Engineering*, 25:41–65, 2001.

[16] P. Marzocca, L. Librescu, and G. Chiocchia. Unsteady aerodynamics in various flight speed regimes for flutter/dynamic response analyses. In *Proceeding of the 18th AIAA Applied Aerodynamic Conference*, Denver, CO., Aug. 14-17, 2000. AIAA-2000-4229.

[17] L. Meirovitch. *Principles and Techniques of Vibrations.* Prentice Hall, Upper Saddle River, New Jersey, 1997. pp. 189-194, 206-210.

[18] S. S. Na. *Control of Dynamic Response of Thin-Walled Composite Beams Using Structural Tailoring and Piezoelectric Actuation.* PhD thesis, Virginia Polytechnic Institute and State University, 1997.

[19] A. N. Palazotto and P. E. Linnemann. Vibration and buckling characteristics of composite cylindrical panels incorporating the effects of a higher order shear theory. *International Journal of Solids and Structures*, 28(3):341–361, 1991.

[20] M. J. Patil and D. H. Hodges. Nonlinear aeroelastic analysis of complete aircraft in subsonic flow, journal of aircraft. *Journal of Aircraft*, 37(5):751–760, 2000.

[21] L. W. Rehfield, A. R. Atilgan, and D. H. Hodges. Nonclassical behavior of thin-walled composite beams with closed cross sections. *Journal of the American Helicopter Society*, 35(2):42–51, 1990.

[22] W. P. Rodden and B. Stahl. A strip method for prediction of damping in subsonic wind tunnel and flight flutter tests. *Journal of Aircraft*, 6(1):9–17, 1969.

[23] M. H. Shirk, T. J. Hertz, and T. A. Weisshaar. Aeroelastic tailoring theory, practice and promise. *Journal of Aircraft*, 23(1):6–18, 1986.

[24] R. Singh and J. D. Baeder. Direct calculation of three-dimensional indicial lift response using computational fluid dynamics. *Journal of Aircraft*, 34(4):465–471, 1997.

[25] E. C. Smith and I. Chopra. Formulation and Evaluation of an Analytical Model for Composite Box-Beams. *Journal of American Helicopter Society*, 36(3):23–35, 1991.

[26] O. Song. *Modeling and Response Analysis of Thin-Walled Beam Structures Constructed of Advanced Composite Materials*. PhD thesis, Virginia Polytechnic Institute and State University, 1990.

[27] O. Song and L. Librescu. Free vibration of anisotropic composite thin-walled beams of closed cross-section contour. *Journal of Sound and Vibration*, 167(1):129–147, 1993.

[28] J. K. Suresh and V. T. Nagaraj. Higher-order shear deformation theory for thin-walled composite beams. *Journal of Aircraft*, 33(5):978–986, 1996.

[29] X. X. Wu and C. T. Sun. Vibration analysis of laminated composite thin-walled beams using finite elements. *AIAA Journal*, 29(5):736–742, 1991.

Appendix A

Listed below are the global stiffness quantities $a_{ij}(= a_{ji})$ related to the problem addressed in this paper:

$$\begin{array}{ll}
a_{33} = \oint_C [z^2 K_{11} + 2z\frac{dx}{ds}K_{14} + (\frac{dx}{ds})^2 K_{44}]ds & a_{37} = \oint_C [zK_{13} + \frac{dx}{ds}K_{43}]ds \\
a_{55} = \oint_C [(\frac{dz}{ds})^2 K_{22} + (\frac{dx}{ds})^2 \bar{A}_{44}]ds & a_{56} = -\oint_C [F_w\frac{dz}{ds}K_{21} + a(s)\frac{dz}{ds}K_{24}]ds \\
a_{66} = \oint_C [F_w^2 K_{11} + 2F_w a(s)K_{14} + a(s)^2 K_{44}]ds & a_{77} = \oint_C \psi(s)K_{23}ds
\end{array}$$

where $\bar{A}_{44} = A_{44} - \frac{A_{45}^2}{A_{55}}$. K_{ij} are the reduced stiffness coefficient defined as:

$$\begin{array}{lll}
K_{11} = A_{22} - \dfrac{A_{12}^2}{A_{11}} & K_{12} = A_{26} - \dfrac{A_{12}A_{16}}{A_{11}} = K_{21} & K_{13} = (A_{26} - \dfrac{A_{12}A_{16}}{A_{11}})\psi(s) \\
K_{14} = B_{22} - \dfrac{A_{12}B_{12}}{A_{11}} = K_{41} & K_{22} = A_{66} - \dfrac{A_{16}^2}{A_{11}} & K_{23} = (A_{66} - \dfrac{A_{16}^2}{A_{11}})\psi(s) \\
K_{24} = B_{26} - \dfrac{A_{16}B_{12}}{A_{11}} = K_{42} & K_{43} = (B_{26} - \dfrac{B_{12}A_{16}}{A_{11}})\psi(s) & K_{44} = D_{22} - \dfrac{B_{12}^2}{A_{11}} \\
K_{51} = B_{26} - \dfrac{B_{16}A_{12}}{A_{11}} & K_{52} = B_{66} - \dfrac{B_{16}A_{16}}{A_{11}} & K_{53} = (B_{66} - \dfrac{B_{16}A_{16}}{A_{11}})\psi(s) \\
K_{54} = D_{26} - \dfrac{B_{12}B_{16}}{A_{11}} & &
\end{array}$$

The inertial coefficients in the Eqs. (3.19, 3.20, 3.21, 3.22) are defined as:

$$\begin{array}{lll}
b_1 = \oint_C m_0 ds & (b_4,\ b_5) = \oint_C (z^2, x^2)m_0 ds & b_{14} = \oint_C m_2(\frac{dx}{ds})^2 ds \\
b_{15} = \oint_C m_2(\frac{dz}{ds})^2 ds & (b_{10},\ b_{18}) = \oint_C (m_0 F_w^2(s),\ m_2 a^2(s))ds &
\end{array}$$

in which

$$(m_0, m_2) = \sum_{k=1}^{m_l} \int_{h_{(k^-)}}^{h_{(k^+)}} \rho_{(k)}(1, n^2)dn$$

Appendix B

Matrices in equations (3.23, 3.24) are defined as:

$$[\mathbf{A}] = \begin{bmatrix} \mathbf{A}_s & \mathbf{B}_s \\ \mathbf{B}_d\mathbf{A}_s & \mathbf{A}_a + \mathbf{B}_a\mathbf{B}_s \end{bmatrix}; \quad [\mathbf{A}_s]_{2m\times 2m} = \begin{bmatrix} \mathbf{0}_{m\times m} & \mathbf{I}_{m\times m}; \\ -\bar{\mathbf{M}}_n^{-1}\bar{\mathbf{K}}_n & -\bar{\mathbf{M}}_n^{-1}\bar{\mathbf{C}}_n \end{bmatrix};$$

$$[\mathbf{B}_s]_{2m\times 4lm} = \begin{bmatrix} \mathbf{0}_{m\times 4lm} \\ \frac{1}{8\mu_0}\bar{\mathbf{M}}_n^{-1}[-A_1^c\mathbf{I}_{m\times m}\cdots A_l^{cMq}\mathbf{I}_{m\times m}]_{m\times 4lm} \end{bmatrix}; \bar{\mathbf{M}}_n = \mathbf{\Theta}^{\mathrm{T}}\bar{\mathbf{M}}_s\mathbf{\Theta};$$

$$\bar{\mathbf{C}}_n = \frac{1}{8\mu_0}\mathbf{\Theta}^{\mathrm{T}}\bar{\mathbf{C}}_{ae}\mathbf{\Theta}; \qquad \bar{\mathbf{K}}_n = \mathbf{\Theta}^{\mathrm{T}}[k_r\bar{\mathbf{K}}_s + \frac{1}{8\mu_0}\bar{\mathbf{K}}_{ae}]\mathbf{\Theta};$$

$$[\mathbf{A}_a]_{4lm\times 4lm} = \begin{bmatrix} -\beta_1^c\mathbf{I}_{m\times m} & & \\ & \ddots & \\ & & -\beta_l^{cMq}\mathbf{I}_{m\times m} \end{bmatrix};$$

$$[\mathbf{B}_a]_{4lm\times 2m} = \begin{bmatrix} \begin{bmatrix} \mathbf{I}_{m\times m} \\ \vdots \\ \mathbf{I}_{m\times m} \end{bmatrix}_{lm\times m} \begin{bmatrix} \mathbf{D}R_1^c & \mathbf{D}R_2^c \end{bmatrix}_{m\times 2m} \\ \begin{bmatrix} \mathbf{I}_{m\times m} \\ \vdots \\ \mathbf{I}_{m\times m} \end{bmatrix}_{lm\times m} \begin{bmatrix} \mathbf{D}R_1^{cq} & \mathbf{D}R_2^{cq} \end{bmatrix}_{m\times 2m} \\ \begin{bmatrix} \mathbf{I}_{m\times m} \\ \vdots \\ \mathbf{I}_{m\times m} \end{bmatrix}_{lm\times m} \begin{bmatrix} \mathbf{D}R_1^{cM} & \mathbf{D}R_2^{cM} \end{bmatrix}_{m\times 2m} \\ \begin{bmatrix} \mathbf{I}_{m\times m} \\ \vdots \\ \mathbf{I}_{m\times m} \end{bmatrix}_{lm\times m} \begin{bmatrix} \mathbf{D}R_1^{cMq} & \mathbf{D}R_2^{cMq} \end{bmatrix}_{m\times 2m} \end{bmatrix}$$

$$\mathbf{D}R_1^c = \mathbf{\Theta}_w^T\left[\frac{4\tan\Lambda_e}{A\!\!\!R}\int_0^1 \hat{\mathbf{\Psi}}_w\hat{\mathbf{\Psi}}_w^{\mathrm{T}}d\,\eta\mathbf{\Theta}_w - 2\int_0^1 \hat{\mathbf{\Psi}}_w\hat{\mathbf{\Psi}}_\phi^T d\,\eta\mathbf{\Theta}_\phi\right];$$

$$\mathbf{D}R_2^c = 4\Theta_w^T\int_0^1 \hat{\mathbf{\Psi}}_w\hat{\mathbf{\Psi}}_w^T d\,\eta\mathbf{\Theta}_w; \quad \mathbf{D}R_1^{cq} = \mathbf{\Theta}_w^T\left[\frac{4\tan\Lambda_e}{A\!\!\!R}\int_0^1 \hat{\mathbf{\Psi}}_w\hat{\mathbf{\Psi}}'^{\mathrm{T}}d\,\eta\mathbf{\Theta}_\phi\right];$$

$$\mathbf{D}R_2^{cq} = 4\mathbf{\Theta}_w^T\int_0^1 \hat{\mathbf{\Psi}}_w\hat{\mathbf{\Psi}}_\phi^T d\,\eta\mathbf{\Theta}_\phi; \quad \mathbf{D}S_1^{cM} = \mathbf{\Theta}_\phi^T\left[\frac{4\tan\Lambda_e}{A\!\!\!R}\int_0^1 \hat{\mathbf{\Psi}}_\phi\hat{\mathbf{\Psi}}'^{\mathrm{T}}_\phi d\,\eta\mathbf{\Theta}_w - 2\int_0^1 \hat{\mathbf{\Psi}}_\phi\hat{\mathbf{\Psi}}_\phi^T d\,\eta\mathbf{\Theta}_\phi\right];$$

$$\mathbf{D}S_2^{cM} = 4\mathbf{\Theta}_\phi^T\int_0^1 \hat{\mathbf{\Psi}}_\phi\hat{\mathbf{\Psi}}_w^T d\,\eta\mathbf{\Theta}_w;$$

$$\mathbf{D}S_1^{cMq} = \mathbf{\Theta}_\phi^T\left[\frac{4\tan\Lambda_e}{A\!\!\!R}\int_0^1 \hat{\mathbf{\Psi}}_\phi\hat{\mathbf{\Psi}}'^{\mathrm{T}}_\phi d\,\eta\mathbf{\Theta}_\phi\right]; \qquad \mathbf{D}R_2^{cMq} = 4\mathbf{\Theta}_\phi^T\int_0^1 \hat{\mathbf{\Psi}}_\phi\hat{\mathbf{\Psi}}_\phi^T d\,\eta\mathbf{\Theta}_\phi;$$

$$\bar{\mathbf{M}}_s = \int_0^1 \begin{bmatrix} \hat{\mathbf{\Psi}}_w\hat{\mathbf{\Psi}}_w^{\mathrm{T}} & \mathbf{0} & \mathbf{0} \\ \mathbf{0} & \hat{I}_t\hat{\mathbf{\Psi}}_\phi\mathbf{\Psi}_\phi^{\mathrm{T}} + \hat{I}_w\hat{\mathbf{\Psi}'}_\phi\hat{\mathbf{\Psi}'}_\phi^{\mathrm{T}} & \mathbf{0} \\ \mathbf{0} & \mathbf{0} & \hat{r}^2\hat{\mathbf{\Psi}}_x\hat{\mathbf{\Psi}}_x^{\mathrm{T}} \end{bmatrix} d\,\eta$$

$$\bar{\mathbf{K}}_s = \int_0^1 \begin{bmatrix} \frac{4}{A\!\!\!R^2}\hat{\mathbf{\Psi}'}_w\hat{\mathbf{\Psi}'}_w{}^T & \frac{2}{A\!\!\!R}\mu_1 c_{14}\underline{\underline{\hat{\mathbf{\Psi}'}_w\hat{\mathbf{\Psi}''}_\phi^T}} & \frac{2}{A\!\!\!R}\hat{\mathbf{\Psi}'}_w\Psi_x^T \\ & \frac{4}{A\!\!\!R^2}\mu_1\mu_2\underline{\underline{\hat{\mathbf{\Psi}''}_\phi\hat{\mathbf{\Psi}''}_\phi^T}} + \mu_1 c_{12}\hat{\mathbf{\Psi}'}_\phi\hat{\mathbf{\Psi}'}_\phi{}^T & \mu_1 c_{14}\underline{\underline{\hat{\mathbf{\Psi}''}_\phi\hat{\mathbf{\Psi}}_x^T}} + \mu_1 c_{13}\hat{\mathbf{\Psi}'}_\phi\hat{\mathbf{\Psi}'}_x{}^T \\ \textbf{symm} & & (\mu_1\hat{\mathbf{\Psi}'}_x\hat{\mathbf{\Psi}'}_x{}^T + \hat{\mathbf{\Psi}}_x\hat{\mathbf{\Psi}}_x^T) \end{bmatrix} d\eta$$

$$\mathbf{Q}_g = \frac{1}{4b_1U_n^2}\{2b\mathbf{\Theta}_w^T\int_0^1 \hat{\mathbf{\Psi}}_w L_g(\tau)d\,\eta + \mathbf{\Theta}_\phi^T\int_0^1 \hat{\mathbf{\Psi}}_\phi T_g(\tau)d\,\eta\};$$

$$\mathbf{Q}_b = \frac{1}{4b_1U_n^2}\{2b\mathbf{\Theta}_w^T\int_0^1 \hat{\mathbf{\Psi}}_w L_b(\tau)d\,\eta + \mathbf{\Theta}_\phi^T\int_0^1 \hat{\mathbf{\Psi}}_\phi T_b(\tau)d\,\eta\};$$

in which, the gust loads $L_g(\tau)$ and $T_g(\tau)$ are defined as

$$L_g(\tau) = 2\pi\rho_\infty bU_n^2\int_0^\tau \frac{w_G(\tau_0)}{U_n}\frac{\partial(\psi_c)_{c/2}(\tau-\tau_0)}{\partial\tau}d\,\tau_0;$$

$$T_g(\tau) = 2\pi\rho_\infty(2b^2)U_n^2\int_0^\tau \frac{w_G(\tau_0)}{U_n}\frac{\partial(\psi_{cM})_{c/2}(\tau-\tau_0)}{\partial\tau}d\,\tau_0$$

Non-dimensional parameters used in the above equations are:

$$\mu_0 = \frac{b_1}{\pi\rho(2b)^2}; \quad \mu_1 = \frac{a_{33}}{a_{55}L^2}; \quad \mu_2 = \frac{a_{66}}{a_{33}(2b)^2}; \quad \hat{r} = \sqrt{\frac{(b_4 + b_{14})}{b_1 L^2}}; \quad c_{12} = \frac{a_{77}}{a_{33}};$$

$$c_{13} = \frac{a_{37}}{a_{33}}; \quad c_{14} = \frac{a_{56}}{a_{33}}; \quad \hat{I}_t = \frac{(b_4 + b_5)}{(2b)^2 b_1}; \quad \hat{I}_w = \frac{(b_{10} + b_{18})}{L^2(2b)^2 b_1}; \quad k_r = \frac{a_{55}}{4b_1 U_n^2};$$

$$\hat{P}_m = \frac{bP_m}{2b_1 U_n^2};$$

Table 3.1: Comparison of the calculated flutter results of Goland's Wing

Method	Description	Flutter speed (Mach#)	Flutter frequency (Hz)
Exact	2-D incompressible flow	$M_{Flutter} = 0.40$	$f_{Flutter} = 11.25$
EGM[a]	$N = 7$, 2-D incompressible flow, transient method[b]	$M_{Flutter} = 0.40$	$f_{Flutter} = 11.15$
EGM	$N = 7$, 2-D compressible flow, transient method[c]	$M_{Flutter} = 0.38$	$f_{Flutter} = 10.90$

[a] Extended Galerkin's method
[b] Jones' approximation of Wagner's function is used [3]
[c] Leishman's indicial functions are used [10]

Table 3.2: Material properties of the test thin-walled beams

$E_{11} = 206.8 \times 10^9 \ N/m^2$	$E_{22} = E_{33} = 5.17 \times 10^9 \ N/m^2$
$G_{13} = G_{23} = 2.55 \times 10^9 \ N/m^2$	$G_{12} = 3.10 \times 10^9 \ N/m^2$
$\mu_{12} = \mu_{13} = \mu_{23} = 0.25$	$\rho = 1.528 \times 10^3 \ Kg/m^3$

Table 3.3: Geometric specifications of the test wings

Parameters	Values
Width ($2b^a : \ m$)	0.757
Depth ($2d^a : \ m$)	0.0997
Wall thickness ($h : \ m$)	0.0203
Number of layers	6
Layer thisckness (: m)	0.0034
Lay-up of the walls	$[\theta_6]$

[a] the length is measured on the contour line

Table 3.4: Approximation of the 2-D indicial function $(\Phi_c)_0(\tau)$ at a set of selected Mach#

		$(\Phi_c)_0(\tau) = A_0^c + A_1^c e^{-\beta_1^c \tau} + A_2^c e^{-\beta_2^c \tau} + A_3^c e^{-\beta_3^c \tau}$					
Mach#	A_0^c	A_1^c	A_2^c	A_3^c	β_1^c	β_2^c	β_3^c
1.2	0.960	2.254	1.809	-4.479	0.470	0.468	0.411
1.3	0.766	1.218	1.389	-2.866	0.648	0.644	0.553
1.5	0.569	0.554	0.808	-1.501	0.874	0.868	0.733
2.0	0.368	0.592	0.374	-1.012	1.104	1.100	1.000
3.0	0.225	21.300	-42.441	21.131	0.857	0.838	0.820
4.0	0.164	0.179	0.450	-0.633	1.330	1.330	1.305

Table 3.5: Approximation of the 2-D indicial function $(\Phi_{cq})_0(\tau)$ at a set of selected Mach#

	$(\Phi_{cq})_0(\tau) = A_0^{cq} + A_1^{cq} e^{-\beta_1^{cq} \tau} + A_2^{cq} e^{-\beta_2^{cq} \tau} + A_3^{cq} e^{-\beta_3^{cq} \tau}$						
Mach#	A_0^{cq}	A_1^{cq}	A_2^{cq}	A_3^{cq}	β_1^{cq}	β_2^{cq}	β_3^{cq}
1.2	0.480	1.459	1.026	2.703	0.596	0.595	0.550
1.3	0.383	0.743	-0.910	0.029	0.794	0.646	0.271
1.5	0.285	2.596	-3.549	0.883	0.882	0.808	0.679
2.0	0.184	7.188	-13.771	6.560	1.043	1.001	0.961
3.0	0.113	-0.881	1.951	-1.076	2.769	2.530	2.327
4.0	0.082	0.578	-0.927	0.347	1.247	1.189	1.109

Table 3.6: Approximation of the 2-D indicial function $(\Phi_{cM})_0(\tau)$ at a set of selected Mach#

	$(\Phi_{cM})_0(\tau) = A_0^{cM} + A_1^{cM} e^{-\beta_1^{cM}\tau} + A_2^{cM} e^{-\beta_2^{cM}\tau} + A_3^{cM} e^{-\beta_3^{cM}\tau}$						
Mach#	A_0^{cM}	A_1^{cM}	A_2^{cM}	A_3^{cM}	β_1^{cM}	β_2^{cM}	β_3^{cM}
1.2	-0.480	-0.579	-1.104	1.880	0.463	0.455	0.362
1.3	-0.383	-2.191	-0.875	3.183	0.577	0.575	0.522
1.5	-0.285	-1.494	0.839	0.708	0.799	6.707	6.704
2.0	-0.184	-1.201	-0.434	1.651	1.015	1.014	0.971
3.0	-0.113	-16.897	32.098	-15.197	0.785	0.768	0.751
4.0	-0.082	-4.020	7.569	-3.548	0.825	0.802	0.778

Table 3.7: Approximation of the 2-D indicial function $(\Phi_{cMq})_0(\tau)$ at a set of selected Mach#

	$(\Phi_{cMq})_0(\tau) = A_0^{cMq} + A_1^{cMq} e^{-\beta_1^{cMq}\tau} + A_2^{cMq} e^{-\beta_2^{cMq}\tau} + A_3^{cMq} e^{-\beta_3^{cMq}\tau}$						
Mach#	A_0^{cMq}	A_1^{cMq}	A_2^{cMq}	A_3^{cMq}	β_1^{cMq}	β_2^{cMq}	β_3^{cMq}
1.2	-0.320	-1.821	0.965	0.999	0.568	0.522	0.522
1.3	-0.255	-2.711	1.342	1.458	0.770	0.736	0.736
1.5	-0.190	2.545	-5.217	2.720	1.627	1.458	2.720
2.0	-0.123	-3.698	6.676	-2.963	0.985	0.937	0.887
3.0	-0.075	-4.218	7.720	-3.499	1.094	1.067	1.037
4.0	-0.055	-0.331	0.962	-0.630	1.176	1.094	1.058

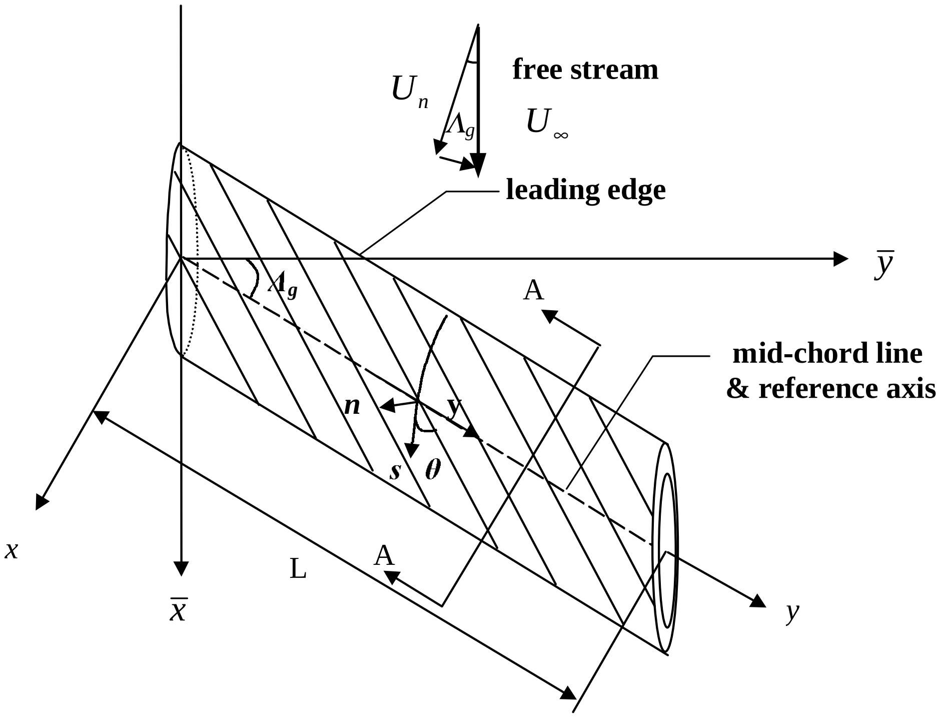

Figure 3.1: Geometric configuration of the aircraft wing modeled as a thin-walled beam model.

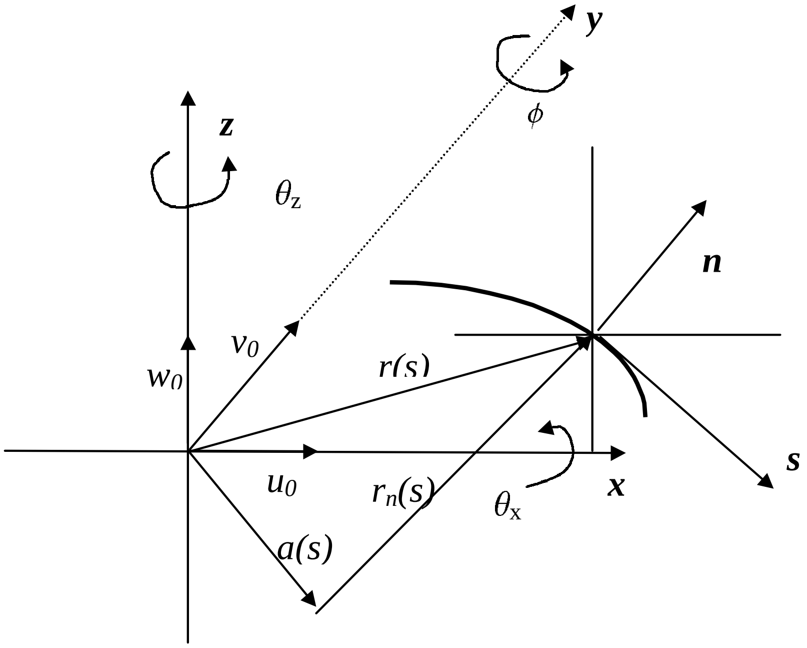

Figure 3.2: Displacement field for the beam model.

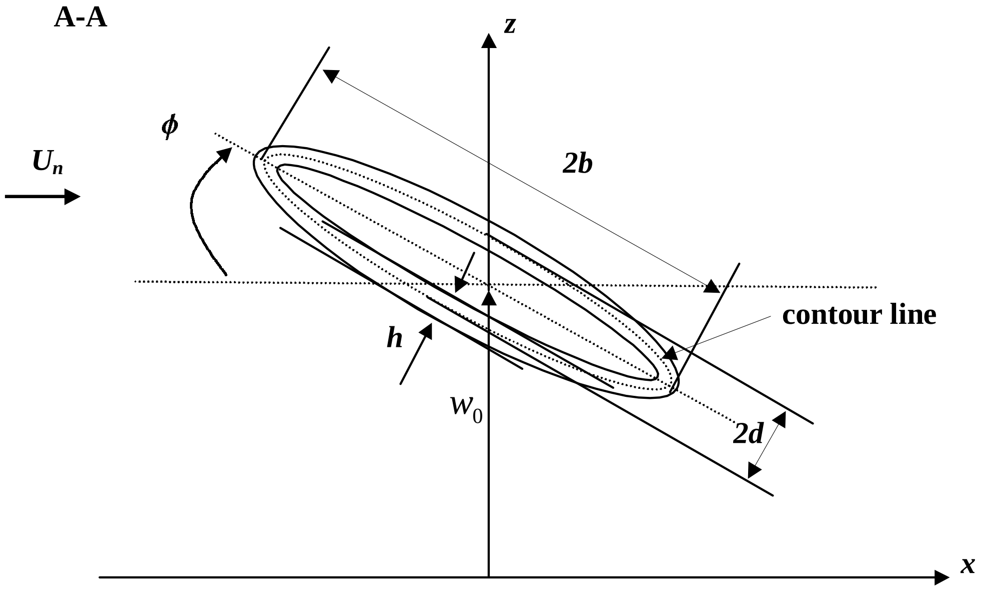

Figure 3.3: Geometric specification of the normal cross-section.

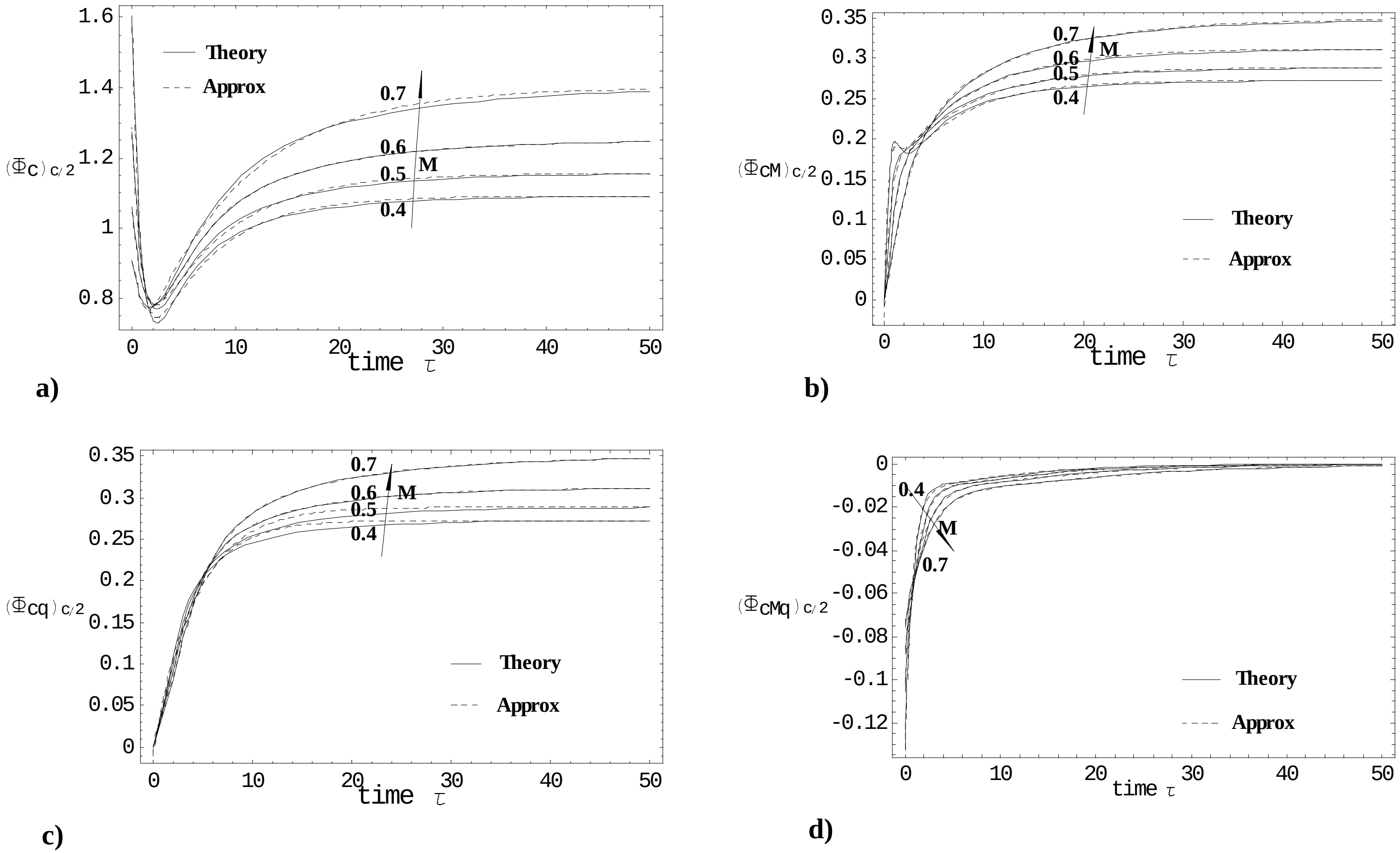

Figure 3.4: Nonlinear curve fitting of the unsteady 2-D subsonic aerodynamic indicial functions.

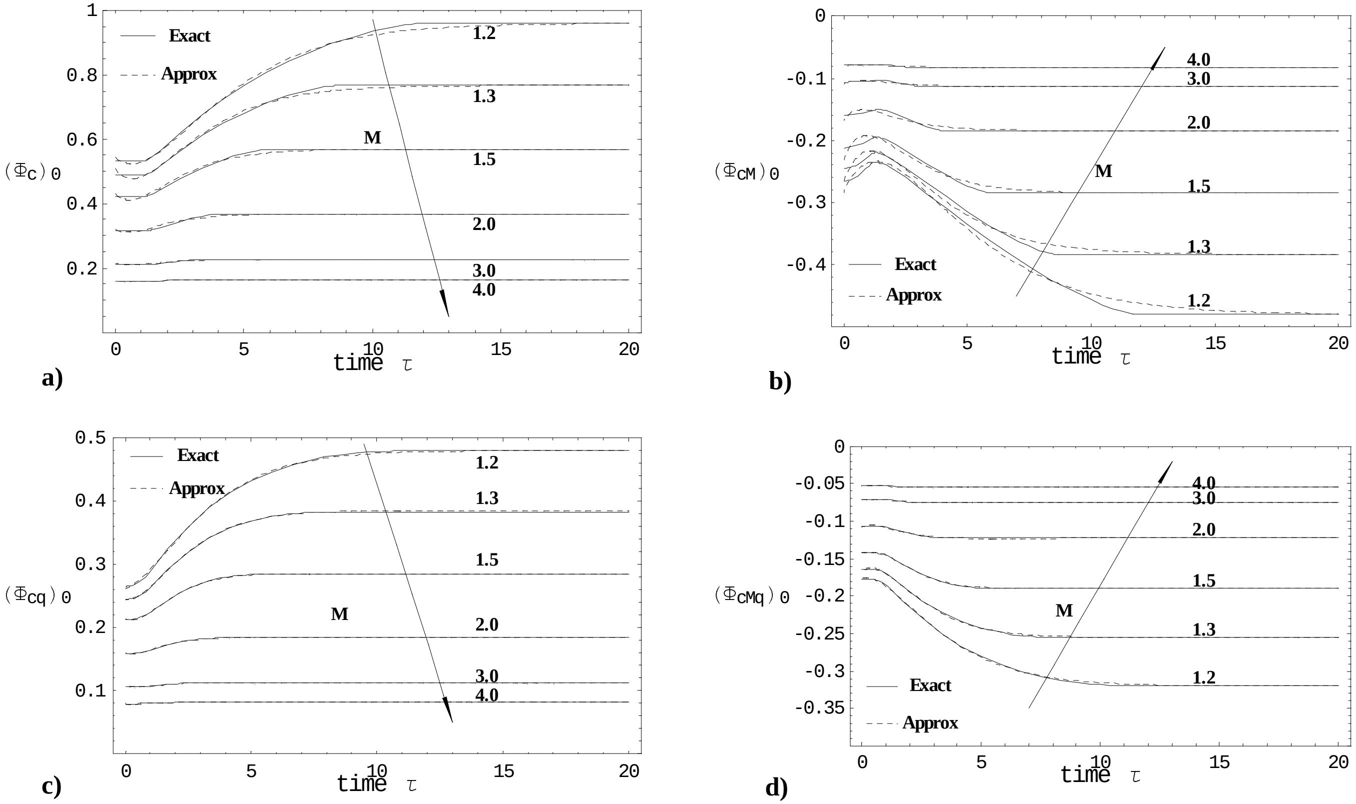

Figure 3.5: Nonlinear curve fitting of the unsteady 2-D supersonic/hypersonic aerodynamic indicial functions.

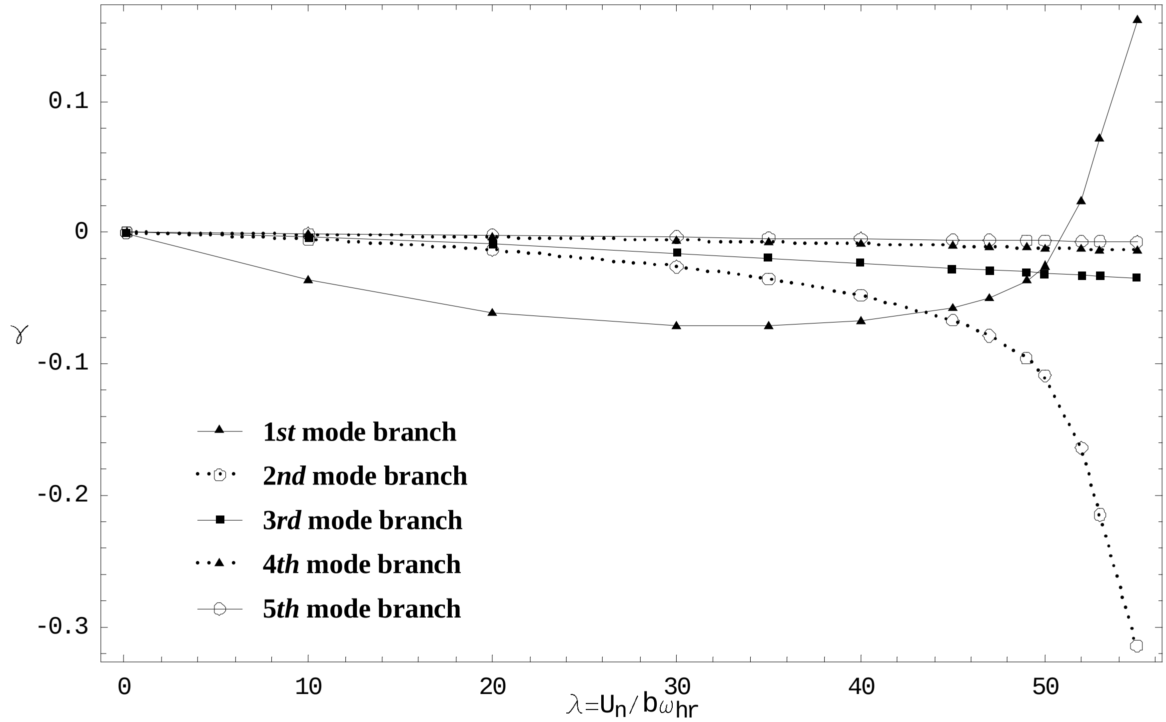

Figure 3.6: Flutter analysis of a wing ($[105_6]$, $\mathcal{R} = 12$, $\Lambda_g = 0^0$) by the transient method ($\lambda - \gamma$ Plot), incompressible aerodynamic model (Jones' approximation of Wagner's function is used).

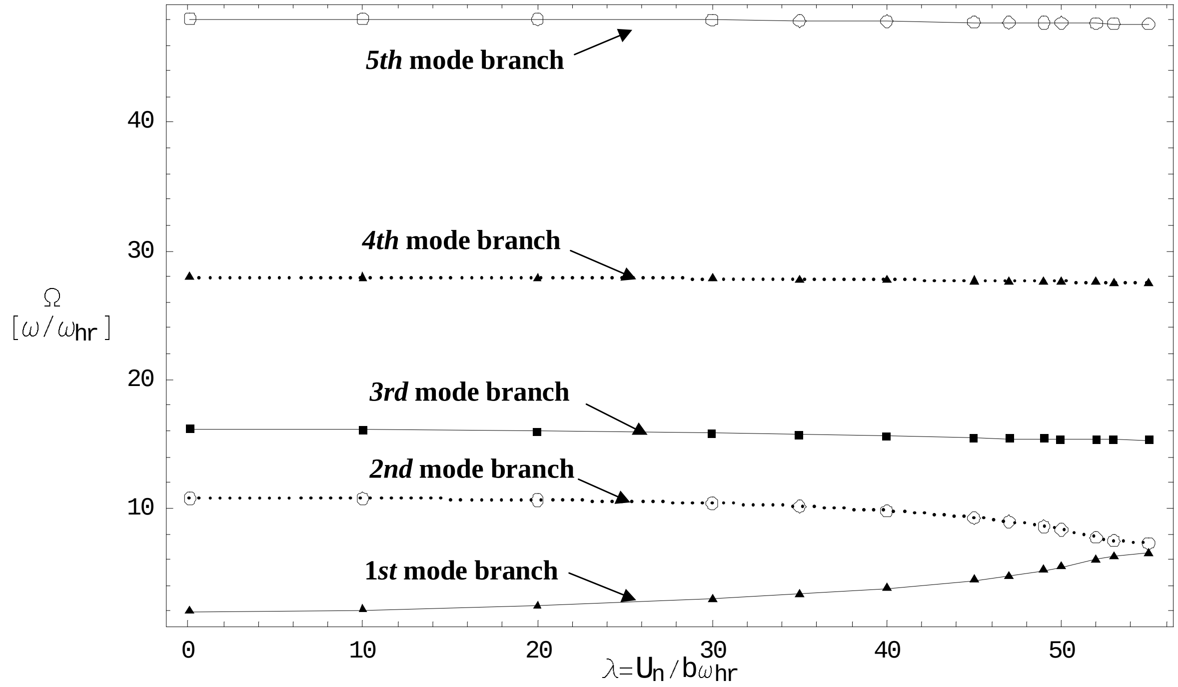

Figure 3.7: Flutter analysis of a wing ($[105_6]$, $\text{Æ} = 12$, $\Lambda_g = 0^0$) by the transient method ($\lambda - \Omega$ Plot), incompressible aerodynamic model (Jones' approximation of Wagner's function is used).

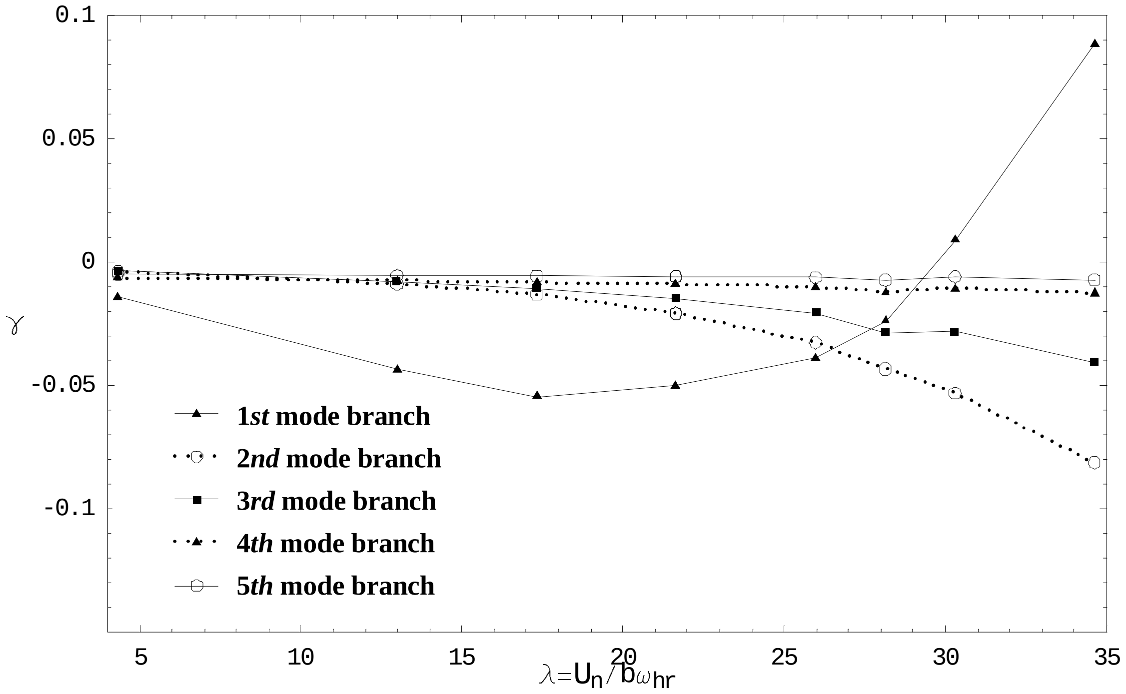

Figure 3.8: Flutter analysis of a wing ($[105_6]$, $\text{Æ} = 12$, $\Lambda_g = 0^0$) by the transient method ($\lambda - \gamma$ Plot), compressible aerodynamic model (Leishman's indicial functions are used).

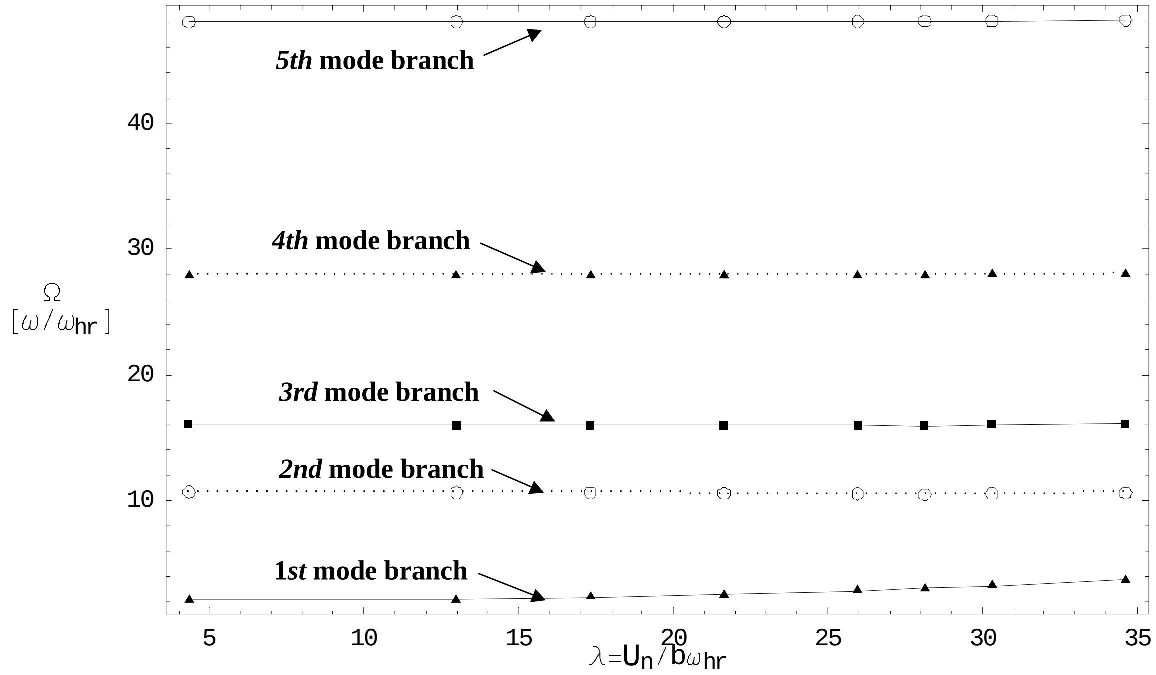

Figure 3.9: Flutter analysis of a wing ($[105_6]$, $\text{Æ} = 12$, $\Lambda_g = 0^0$) by the transient method ($\lambda - \Omega$ Plot), compressible aerodynamic model (Leishman's indicial functions are used).

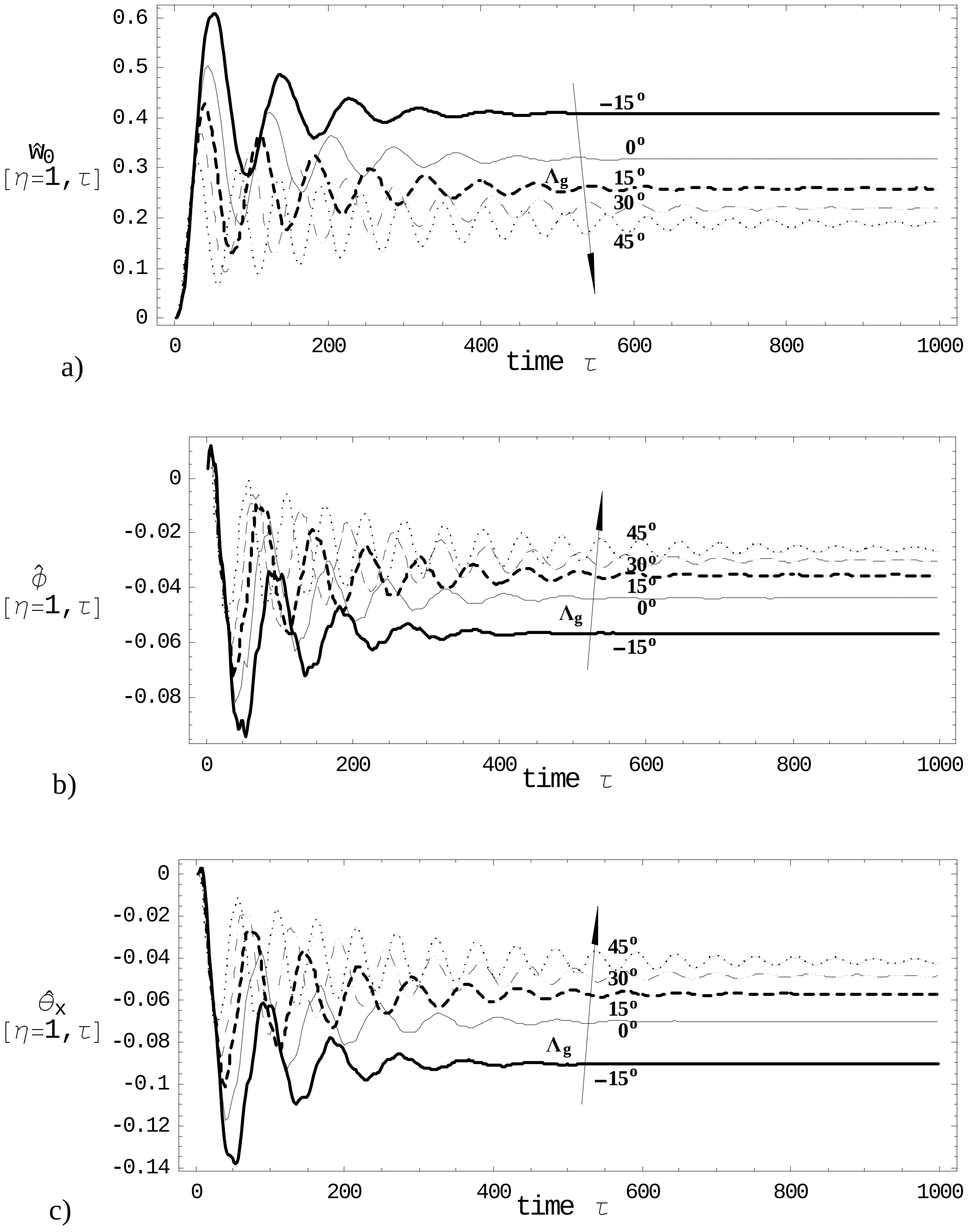

Figure 3.10: Influence of sweep angle on the dynamic aeroelastic response (deflection) of a wing to a sharp-edged gust ($[120_6]$, $\mathcal{A}\!\!R = 12$, $M_{Flight} = 0.5$).

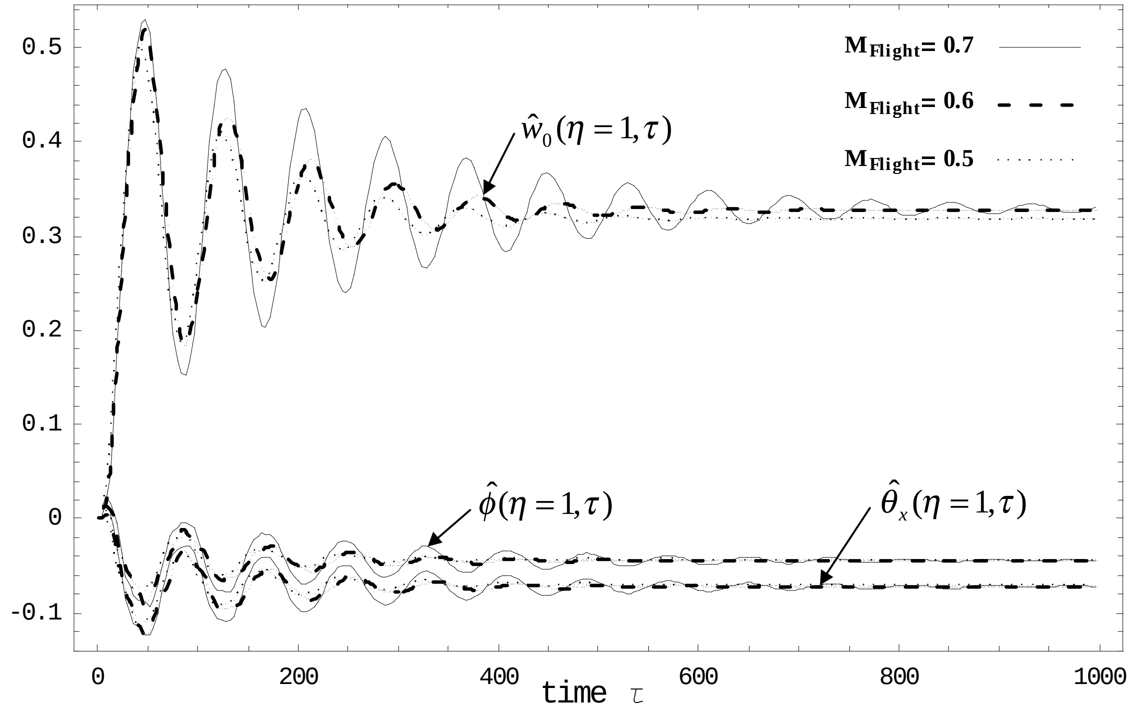

Figure 3.11: Wing response subject to a sharp-edged gust at different subsonic flight speeds ($[120_6]$, $\text{Æ} = 12$, $\Lambda_g = 0^0$).

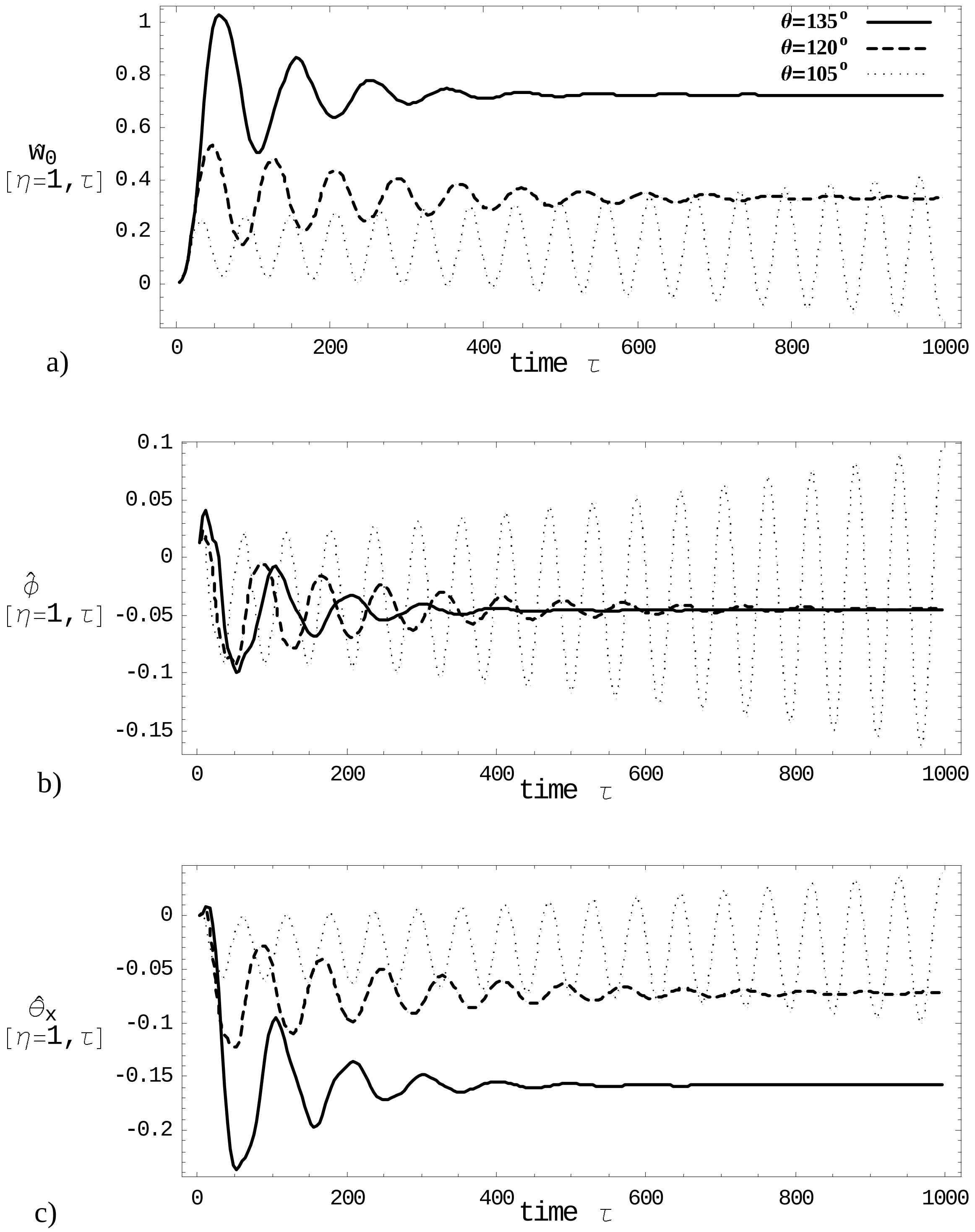

Figure 3.12: Elastic tailoring on the suppression of flutter of a wing ($[\theta_6]$ lay-up, $\mathit{AR} = 12$, $\Lambda_g = 0^0$, $M_{Flight} = 0.7$, sharp-edged gust).

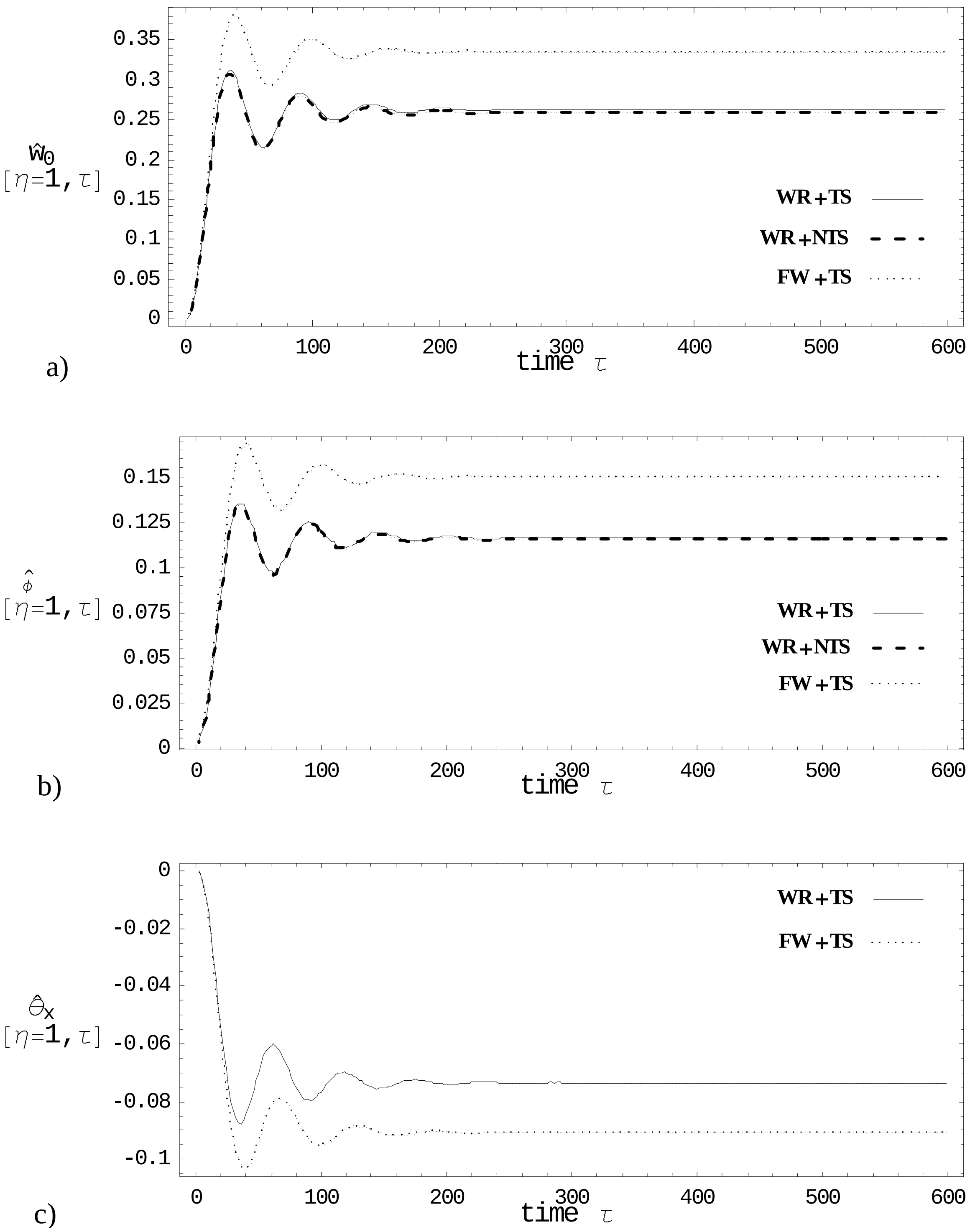

Figure 3.13: Effect of warping restraint and transverse shear on the dynmaic aeroelastic response of a wing subject to a sharp-edged gust ($[75_6]$, $A\!\!R = 10$, $\Lambda_g = 30^0$, $M_{Flight} = 0.7$).

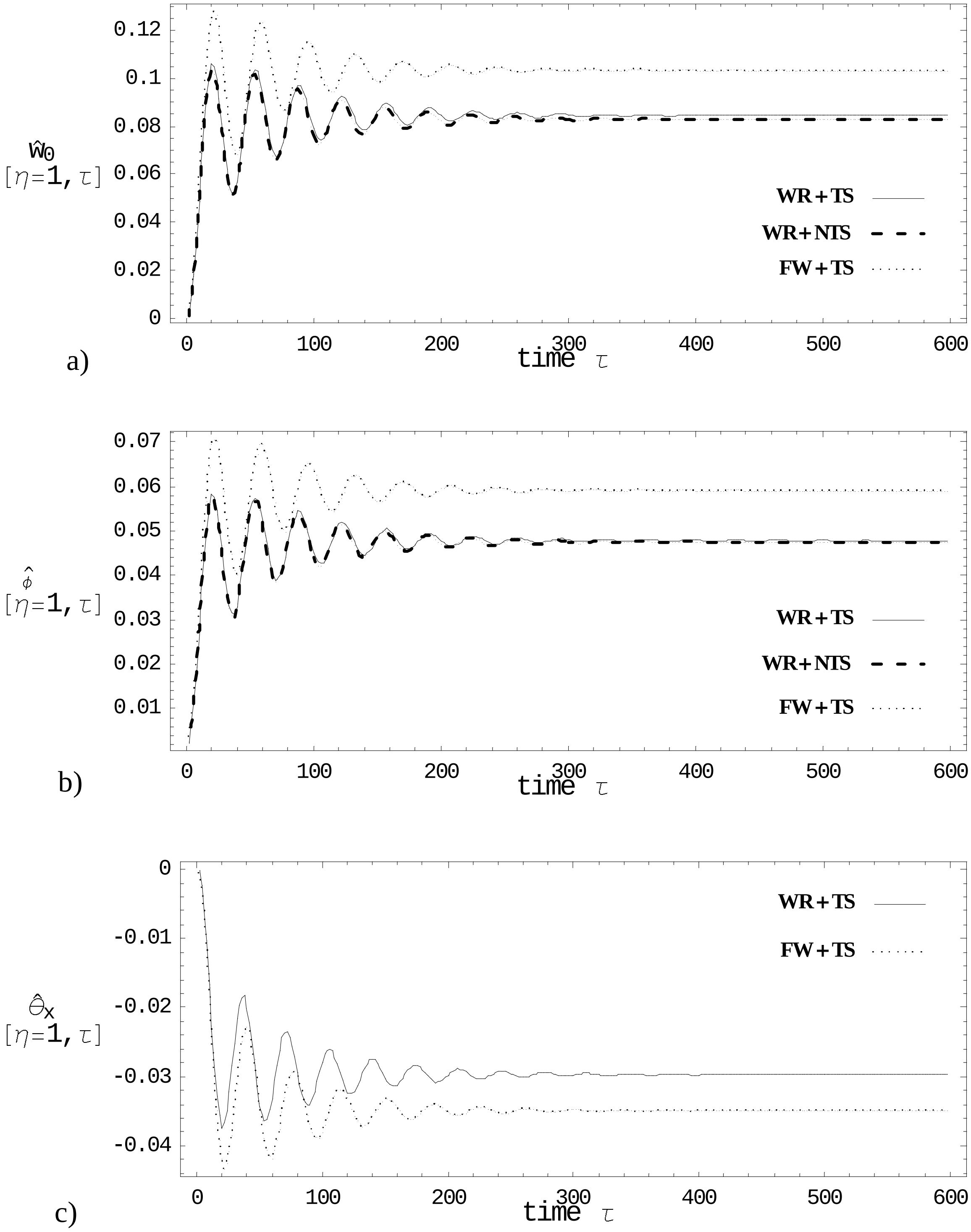

Figure 3.14: Effect of warping restraint and transverse shear on the dynmaic aeroelastic response of a wing subject to a sharp-edged gust ([75_6], $\text{Æ} = 8$, $\Lambda_g = 30^0$, $M_{Flight} = 0.7$).

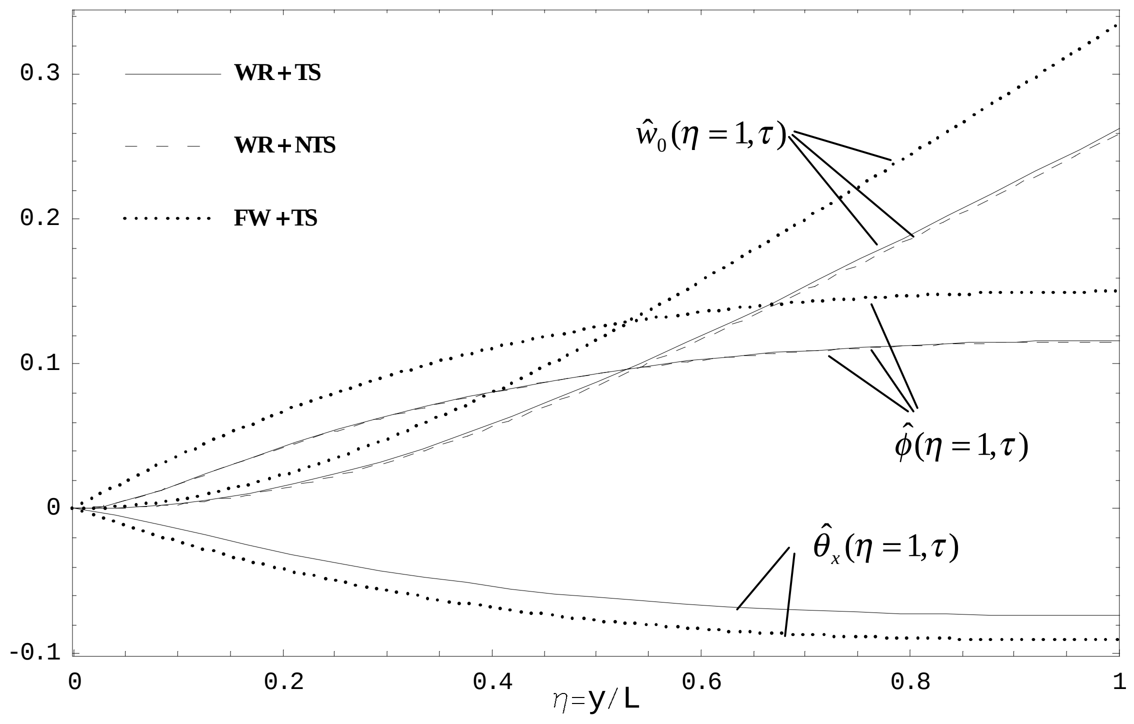

Figure 3.15: Influence of warping restraint and transverse shear on the dynmaic aeroelastic response of a wing subject to a sharp-edged gust at the fixed time $\tau = 1000$ ([75_6], $\mathcal{A}\!R = 10$, $\Lambda_g = 30^0$, $M_{Flight} = 0.7$).

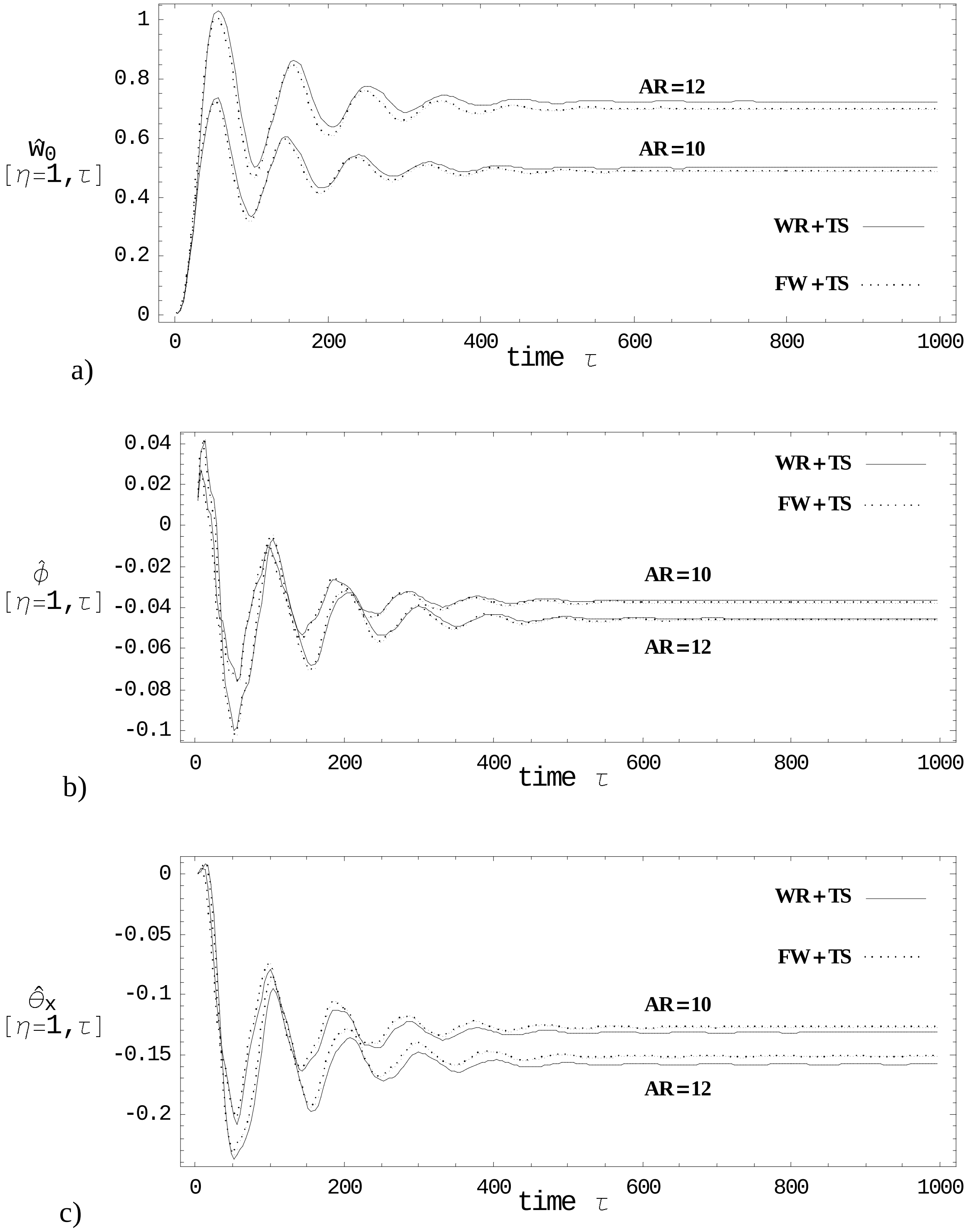

Figure 3.16: Effect of warping restraint on the dynmaic aeroelastic response of a wing subject to a sharp-edged gust ([135_6], $\Lambda_g = 0^0$, $M_{Flight} = 0.7$).

Chapter 4

Minimax Aeroelastic Control of Smart Aircraft Wings Exposed to Gust/Blast Loads

Abstract

A worst case control design based on the game theory aimed at augmenting the flutter envelope and enhancing the dynamic aeroelastic response of a smart aircraft wing subject to gust/balst loads is formulated. The smart aircraft wing is modeled as anisotropic thin-walled beam featuring circumferentially asymmetric stiffness (CAS) lay-up and a number of non-classical effects such as transverse shear, warping restraint and 3-D strain effects. Adaptive materials technology is used for implementing the active control via the boundary bending moment feedback mechanism. The unsteady aerodynamic loads in subsonic compressible flows are based on 2-D indicial functions considered in conjunction with aerodynamic strip theory extended to 3-D wing model. The capability of the control on flutter suppression and dynamic response enhancement are investigated, and the corresponding applied voltage requirement and power consumption are addressed.

4.1 Introduction

The emergence of the new composite materials and their incorporation in the design of advanced space vehicle structures has generated not only new hopes, but also many challenges to the aeroelasticity discipline. In this sense, a new technology, known as the *aeroelastic tailoring* (see e.g., [1]) and its unique advantages have been demonstrated, among others, by the successful construction and test of the Grumman's X-29 swept-forward wing aircraft. In the last decade, due to their inherent, material-level coupling between mechanical and electrical properties, piezoelectric materials (see [2] for a comprehensive review of its application), especially piezoceramic materials have been extended to address problems of the flutter suppression and dynamic aeroelastic response enhancement (see, e.g., [3–7]). At the same time, due to the increased importance of composite materials in the design of aerospace vehicles, the concept of *thin-walled anisotropic beam model* has reached special prominence in the last years (see, e.g., [8]). In this context, a comprehensive review [9] provides the state-of-the-art of the problem and several non-classical effects have been identified to have non-negligible influence on the accuracy and validity of the various theories of this type of structures. The major non-classical effects concern among others, transverse shear, warping restraint, 3-D strain effect, contour-wise non-uniform distribution of transverse shear stiffness and the exotic elastic/structural couplings induced by the anisotropy and stacking sequence of the structure. It is emphasized here that due to complex influence of these non-classical effects, thin-walled beam models should be carefully validated, especially against experimental evidence.

The objective of this chapter is to study the active control effect on flutter suppression and dynamic aeroelastic response enhancement of a smart aircraft wing modeled as thin-walled beams. The major features of this article include: (1)The integrated aeroelastic model is rigorously and consistently derived from a thin-walled beam model, which has been validated [10]; (2)An indicial function based unsteady subsonic aerodynamic model that is valid for medium to large aspect ratio wings is proposed; (3)Due to the potential catastrophic outcome of flutter, the worst case control design paradigm is adopted for the investigation of flutter suppression. The capability of the designed control laws towards the dynamic enhancement of aeroelastic response is also investigated and the voltage/power requirements addressed.

Throughout this article, variational principles provide a uniform tool to derive not only the mechanical/electrical governing system, but also the control laws. Due to the fact that the augmented states (related to the unsteady aerodynamic loads) are initially prescribed and the integrated aeroelastic system are not totally controllable, the existing minimax control theories (see, e.g., [11]) are not suitable for the control design. Therefore, a new worst case control design is proposed, in which, the constraints on the initial conditions and on the disturbance can be separately treated.

4.2 Structural modeling

4.2.1 Basic Assumptions and Kinematics

The wing is modeled as a single-cell, closed cross-section, fiber-reinforced composite thin-walled beam. Its geometric configuration and specification are shown in Figs. 4.1 and 4.2. The major difference of the basic assumptions adopted in this article [12] from those used in [8, 13, 14] is that the 3-D strain effect of the cross section is consistently accounted for on both the host structure and active layers, namely, $\sigma_{nn} = 0$, $N_{sn} = 0$, $N_{ss} = 0$ while in [8, 13], it is assumed that $\varepsilon_{nn} = 0$, $\gamma_{sn} = 0$, $N_{ss} = 0$.

Based on the basic assumptions, and consistent with the wing geometry as depicted in Fig. 4.1, the following representation of the 3-D displacement quantities is postulated:

$$u(x, y, z, t) = u_0(y, t) + z\phi(y, t); \quad w(x, y, z, t) = w_0(y, t) - x\phi(y, t); \tag{4.1a}$$

$$v(x, y, z, t) = v_0(y, t) + [x(s) - n\frac{dz}{ds}]\theta_z(y, t) + [z(s) + n\frac{dx}{ds}]\theta_x(y, t) - [F_w(s) + na(s)]\phi'(y, t) \tag{4.1b}$$

where

$$\theta_x(y,t) = \gamma_{yz}(y,t) - w_0'(y,t); \theta_z(y,t) = \gamma_{xy}(y,t) - u_0'(y,t); a(s) = -(z\frac{dz}{ds} + x\frac{dx}{ds}) \quad (4.2)$$

In the above expressions, $\theta_x(y,t)$, $\theta_z(y,t)$ and $\phi(y,t)$ denote the rotations of the cross-section about the axes x, z and the twist about the y axis, respectively, $\gamma_{yz}(y,t)$ and $\gamma_{xy}(y,t)$ denote the transverse shear strain measures.

The warping function in Eq.(4.1b) is expressed as

$$F_w(s) = \int_0^s [r_n(s) - \psi(s)]ds \quad (4.3)$$

in which the torsional function $\psi(s)$ and the quantity $r_n(s)$ are expressed as

$$\psi(s) = \frac{\oint_C r_n(\bar{s})d\bar{s}}{h(s)G_{sy}(s)\oint_C \frac{d\bar{s}}{h(\bar{s})G_{sy}(\bar{s})}}; \quad r_n(s) = z\frac{dx}{ds} - x\frac{dz}{ds} \quad (4.4)$$

where $G_{sy}(s)$ is the effective membrane shear stiffness, which is defined as [12]:

$$G_{sy}(s) = \frac{N_{sy}}{h(s)\gamma_{sy}^0(s)} \quad (4.5)$$

Notice that for the thin-walled beam theory considered herein, the six kinematic variables, i.e., $u_0(y,t)$, $v_0(y,t)$, $w_0(y,t)$, $\theta_x(y,t)$, $\theta_z(y,t)$, $\phi(y,t)$, which represent 1-D displacement measures, constitute the basic unknowns of the problem. When the transverse shear effect is discarded, Eq. (4.2) degenerates to $\theta_x = -w_0'$, $\theta_z = -u_0'$, and as a result, the number of basic unknown quantities reduces to four. Such a case leads to the classical, unshearable beam model.

The strains contributing to the potential energy are:

Spanwise strain:

$$\varepsilon_{yy}(n,s,y,t) = \varepsilon_{yy}^0(s,y,t) + n\varepsilon_{yy}^n(s,y,t) \quad (4.6a)$$

where

$$\varepsilon_{yy}^0(s,y,t) = v_0{}'(y,t,) + \theta_z{}'(y,t)x(y,t) - \phi''(y,t)F_w(s) \quad (4.6b)$$

$$\varepsilon_{yy}^n(s,y,t) = -\theta_z{}'\frac{dz}{ds} + \theta_x{}'(y,t)\frac{dx}{ds} - a(s)\phi''(y,t) \quad (4.6c)$$

are the axial strain components associated with the primary and secondary warping, respectively.

Tangential shear strain:

$$\gamma_{sy}(s,y,t) = \gamma_{sy}^0(s,y,t) + \psi(s)\phi'(y,t) \tag{4.7a}$$

$$\textit{where } \gamma_{sy}^0(s,y,t) = \gamma_{xy}\frac{dx}{ds} + \gamma_{yz}\frac{dz}{ds} = [u_0' + \theta_z]\frac{dx}{ds} + [w_0' + \theta_x]\frac{dz}{ds} \tag{4.7b}$$

Transverse shear strain measure:

$$\gamma_{ny}(s,y,t) = -\gamma_{xy}\frac{dz}{ds} + \gamma_{yz}\frac{dx}{ds} = -[u_0' + \theta_z]\frac{dz}{ds} + [w_0' + \theta_x]\frac{dx}{ds} \tag{4.8}$$

4.2.2 Constitutive Equations

The host structure of the smart aircraft wing is assumed to consist of m_s layers of (Graphite/ Epoxy) laminates and on the upper and lower surfaces of the host structure 2 piezoceramic patches each with m_p layers symmetrically are mounted (see Figs. 4.1, 4.2). For piezoelectric materials and within linear theory, considering the strain S_i $(i = \overline{1,\ 6})$ (in Voigt contract notation) and electric field intensity E_r $(r = \overline{1,\ 3})$ as the independent unknowns, we get the following constitutive equations:

$$\sigma_i = C_{ij}^E S_j - e_{ri}E_r; \qquad D_r = e_{rj}S_j + \epsilon_{rl}^S E_l. \qquad (i,j = \overline{1,6}; \quad r,l = \overline{1,3}) \tag{4.9}$$

where the first expression describes the *converse* piezoelectric effect, and the second one describes the *direct* piezoelectric effect. σ_i are the *Cauchy* stress components([15], pp. 30), and D_r electric displacements. C_{ij}^E are the elastic moduli measured in condition of constant, preferably zero electric intensity field; ϵ_{ij}^S are the electric permittivity coefficients, measured under a constant, preferably zero strain field; and e_{ij} are piezoelectric coupling coefficients. Due to physical constraints, $C_{ij}^E = C_{ji}^E$, $\epsilon_{rl}^S = \epsilon_{lr}^S$ and $[C_{ij}^E] > 0$, $[\epsilon_{rl}^S] > 0$ (from the first law of thermodynamics). To facilitate the following derivation, we also assume that the poling direction is along the normal of the mounted surface, i.e., along n

(thickness) direction (see Fig. 4.1). Since piezoceramic materials (transversely isotropic) is a special case of othotropic materials, the stress-strain relation for both the host structure and piezoelectric layers can be written in a unified way as (in the principal *material* coordinates)

$$\left\{\begin{array}{c}\sigma_{11}\\ \sigma_{22}\\ \sigma_{33}\\ \sigma_{23}\\ \sigma_{13}\\ \sigma_{12}\end{array}\right\}^{(k)} = \left[\begin{array}{cccccc} C_{11} & C_{12} & C_{13} & 0 & 0 & 0\\ C_{12} & C_{22} & C_{23} & 0 & 0 & 0\\ C_{13} & C_{23} & C_{33} & 0 & 0 & 0\\ 0 & 0 & 0 & C_{44} & 0 & 0\\ 0 & 0 & 0 & 0 & C_{55} & 0\\ 0 & 0 & 0 & 0 & 0 & C_{66}\end{array}\right]\left\{\begin{array}{c}\varepsilon_{11}\\ \varepsilon_{22}\\ \varepsilon_{33}\\ \varepsilon_{23}\\ \varepsilon_{13}\\ \varepsilon_{12}\end{array}\right\}^{(k)} - \left\{\begin{array}{c}e_{31}\\ e_{31}\\ e_{33}\\ 0\\ 0\\ 0\end{array}\right\} E_3 R^{(k)}(s,y,n) \tag{4.10}$$

For the piezoceramic patches, since the isotropic plane is the 1-2 plane, we further have

$$C_{22} = C_{11}; \quad C_{23} = C_{13}; \quad C_{55} = C_{44}; \quad C_{66} = (C_{11} - C_{12})/2 \tag{4.11}$$

Transforming from the principal *material* coordinates to the *local* coordinates (s, y, n) of the wing, we get the constitutive relations between (σ_{ss}, σ_{yy}, σ_{nn}, σ_{yn}, σ_{sn}, σ_{sy}) and (ε_{ss}, ε_{yy}, ε_{nn}, ε_{yn}, ε_{sn}, ε_{sy}), which are not listed in this chapter. In the following derivation, $\bar{C}_{ij}$ is denoted as the corresponding transformed elastic moduli. Since the direction of the n axis remains invariant during the transformation and the plane of isotropy of the piezo. patches is $s-y$ plane (perpendicular to n axis), e_{31}, e_{32} remain the same during the transformation. For brevity of notations, e_{31} and e_{32} are still used for the corresponding transformed quantities.

Define the stress resultant and stress couples as:

$$\begin{gathered}\{N_{ss},\ N_{yy},\ N_{sy},\ N_{ny},\ N_{sn},\ L_{yy},\ N_{sy}\} = \\ \sum_{k=1}^{m_s+m_p} \int_{h_{(k)}} \{\sigma_{ss},\ \sigma_{yy},\ \sigma_{sy},\ \sigma_{ny},\ \sigma_{sn},\ \sigma_{yy}n,\ \sigma_{sy}n\}^{(k)}\, dn\end{gathered} \tag{4.12}$$

Invoking the basic assumptions [10, 12], the stress resultants and stress couples are reduced to:

$$\left\{\begin{array}{l} N_{yy} \\ N_{sy} \\ L_{yy} \\ L_{sy} \end{array}\right\} = \left[\begin{array}{llll} K_{11} & K_{12} & K_{13} & K_{14} \\ K_{21} & K_{22} & K_{23} & K_{24} \\ K_{31} & K_{32} & K_{33} & K_{43} \\ K_{51} & K_{52} & K_{53} & K_{54} \end{array}\right] \left\{\begin{array}{l} \varepsilon^0_{yy} \\ \gamma^0_{yy} \\ \phi' \\ \varepsilon^n_{yy} \end{array}\right\} - \left\{\begin{array}{l} N^a_{yy} \\ 0 \\ L^a_{yy} \\ 0 \end{array}\right\} \tag{4.13}$$

and

$$N_{ny} = [A_{44} - \frac{A_{45}^2}{A_{55}}]\gamma_{ny} \tag{4.14}$$

In Eq. 4.13,

$$N^a_{yy} = [1 - \frac{A_{12}}{A_{11}}] \sum_{k=m_p}^{m_s+m_p} \int_{h_{(k)}} \left\{[e_{31} - \frac{\bar{C}_{13}}{\bar{C}_{33}} e_{33}] E_3 R(s,y,n)\right\}^{(k)} dn \tag{4.15a}$$

$$L^a_{yy} = \sum_{k=m_p}^{m_s+m_p} \left\{[e_{31} - \frac{\bar{C}_{13}}{\bar{C}_{33}} e_{33}] E_3 R(s,y) [n_{k^+} - n_{k^-}][\frac{1}{2}(n^2_{k^+} - n^2_{k^-}) - \frac{B_{12}}{A_{11}}]\right\}^{(k)} \tag{4.15b}$$

and

$$\begin{aligned} R^{(k)}(s,y) &= [H(y - y_{k^-}) - H(y - y_{k^+})] \cdot [H(y - y_{k^-}) - H(y - y_{k^+})] \\ &\quad \cdot [H(s - s_{k^-}) - H(s - s_{k^+})]; \qquad (4.16a) \\ R^{(k)}(s,y,n) &= [H(n - n_{k^-}) - H(n - n_{k^+})] \cdot [H(y - y_{k^-}) - H(y - y_{k^+})] \\ &\quad \cdot [H(y - y_{k^-}) - H(y - y_{k^+})] \cdot [H(s - s_{k^-}) - H(s - s_{k^+})]; \qquad (4.16b) \\ R^{(k)}(y) &= [H(y - y_{k^-}) - H(y - y_{k^+})]. \qquad (4.16c) \end{aligned}$$

where $R^{(k)}(.)$ is the spatial Heaviside function.

In Eqs. (4.13, 4.14, and 4.15a, b), K_{ij} are the reduced stiffness coefficients, A_{ij}, B_{ij} are the stretching, stretching-bending coupling coefficients, respectively.

4.3 Subsonic Aerodynamic Loads, an Indicial Function Approach

Compared with the mature oscillatory compressible unsteady aerodynamic models, the indicial function based aerodynamic models provide a very efficient approach to describe the compressible unsteady flow. This is mainly due to the fact that once the proper indicial functions are available, which can be obtained via the aid of experiments and computational fluid dynamics (CFD) (see e.g., [16]), the linearized unsteady aerodynamic loads to arbitrary small motion can be derived through Duhamel's convolution.

However, even in 2-D domain, in contrast to the incompressible case, the indicial functions in subsonic compressible flow are not analytic, except for very limited durations of time [17]. Therefore, in this article, in conjunction with the aerodynamic strip theory, a set of empirical 2-D indicial functions developed in [18] are adopted on the aeroelastic analysis of 3-D advanced wings. As to the basic elements and validation of 2-D subsonic indicial functions, the reader is referred to [16–19].

The downwash velocity can be expressed in a non-dimensional form as

$$w_a(\hat{x},\eta,\tau) = U_n\left\{[2\dot{\hat{w}}_0 - \hat{\phi} + \frac{2}{\mathit{AR}}\frac{\partial \hat{w}_0}{\partial \eta}\tan\Lambda_e] - \hat{x}[\dot{\hat{\phi}} + \frac{1}{\mathit{AR}}\frac{\partial \hat{\phi}}{\partial \eta}\tan\Lambda_e]\right\} \triangleq U_n\{\hat{w}_{aT} - \hat{x}\dot{\hat{\phi}}_{aP}\} \tag{4.17a}$$

where we define:

$$\hat{w}_{aT}(\eta,\tau) \equiv U_n[2\dot{\hat{w}}_0 - \hat{\phi} + \frac{2}{\mathit{AR}}\frac{\partial \hat{w}_0}{\partial \eta}\tan\Lambda_e]; \quad \dot{\hat{\phi}}_{aP}(\eta,\tau) \equiv [\dot{\hat{\phi}} + \frac{1}{\mathit{AR}}\frac{\partial \hat{\phi}}{\partial \eta}\tan\Lambda_e] \tag{4.17b}$$

Denote $(\Phi_c)_0(\tau)$, $(\Phi_{cM})_0(\tau)$ as the indicial lift and moment functions (about the leading edge) due to the unit step change of the vertical translation velocity at the leading edge. As a result, the indicial lift and aerodynamic moment about the *mid-chord* (taken as the reference axis, see Fig. 4.1) are:

$$\begin{aligned} L_T^*(\eta,\tau) &= -\pi\rho_\infty U_n^2(2b) \\ &\left\{[\hat{w}_{aT}(\eta,0) + \dot{\hat{\phi}}_{aP}(\eta,0)](\Phi_c)_0(\tau) + \int_0^\tau \frac{\partial(\hat{w}_{aT}(\eta,\sigma) + \dot{\hat{\phi}}_{aP}(\eta,\sigma))}{\partial\sigma}(\Phi_c)_0(\tau-\sigma)d\sigma\right\} \end{aligned} \tag{4.18a}$$

$$
\begin{aligned}
T^*_{yT}(\eta,\tau) &= -\pi\rho_\infty U_n^2(2b)^2 \\
&\left\{[\hat{w}_{aT}(\eta,0)+\dot{\hat{\phi}}_{aP}(\eta,0)](\Phi_{cM})_0(\tau)+\int_0^\tau \frac{\partial(\hat{w}_{aT}(\eta,\sigma)+\dot{\hat{\phi}}_{aP}(\eta,\sigma))}{\partial\sigma}(\Phi_{cM})_0(\tau-\sigma)d\sigma\right\} \\
&+ bL^*_T(\eta,\tau)
\end{aligned}
\tag{4.18b}
$$

where the ratio $(\Phi_{cM})_0(\tau)/(\Phi_c)_0(\tau)$ measures the location of the aerodynamic center (fraction of the whole chord length from the leading edge). Upon denoting $(\Phi_{qc})_0(\tau)$, $(\Phi_{cMq})_0(\tau)$ as the indicial lift and moment functions (about the leading edge) due to the unit step change of the pitching rate at the leading edge, the corresponding indicial lift and aerodynamic moment about the *mid-chord* are:

$$
L^*_q(\eta,\tau) = 2\pi\rho_\infty U_n^2(2b)\left\{[\dot{\hat{\phi}}_{aP}(\eta,0)](\Phi_{cq})_0(\tau)+\int_0^\tau \frac{\partial\dot{\hat{\phi}}_{aP}(\eta,\sigma)}{\partial\sigma}(\Phi_{cq})_0(\tau-\sigma)d\sigma\right\}
\tag{4.19a}
$$

$$
\begin{aligned}
T^*_{yq}(\eta,\tau) &= 2\pi\rho_\infty U_n^2(2b)^2\left\{\dot{\hat{\phi}}_{aP}(\eta,0)(\Phi_{cMq})_0(\tau)+\int_0^\tau \frac{\partial\dot{\hat{\phi}}_{aP}(\eta,\sigma)}{\partial\sigma}(\Phi_{cMq})_0(\tau-\sigma)d\sigma\right\} \\
&+ bL^*_q(\eta,\tau)
\end{aligned}
\tag{4.19b}
$$

Similarly, the ratio $(\Phi_{cMq})_0(\tau)/(\Phi_{cq})_0(\tau)$ measures the location of the aerodynamic center (fraction of the whole chord length from the leading edge).

Therefore, the total unsteady aerodynamic lift L_{ae} (positive upwards) and moment about the *mid-chord* T_{ae} (positive nose-up) are:

$$
\begin{aligned}
L_{ae}(\eta,\tau) &= L^*_T(\eta,\tau)+L^*_q(\eta,\tau) \\
&= -\pi\rho_\infty U_n^2(2b)\left\{\hat{w}_{aT}(\eta,0)(\Phi_c)_{c/2}(\tau)+\int_0^\tau \frac{\partial\hat{w}_{aT}(\eta,\sigma)}{\partial\sigma}(\Phi_c)_{c/2}(\tau-\sigma)d\sigma\right\} \\
&+ 2\pi\rho_\infty U_n^2(2b)\left\{\dot{\hat{\phi}}_{aP}(\eta,0)(\Phi_{cq})_{c/2}(\tau)+\int_0^\tau \frac{\partial\dot{\hat{\phi}}_{aP}(\eta,\sigma)}{\partial\sigma}(\Phi_{cq})_{c/2}(\tau-\sigma)d\sigma\right\}
\end{aligned}
\tag{4.20a}
$$

$$
\begin{aligned}
T_{ae}(\eta,\tau) &= T^*_{yT}(\eta,\tau)+T^*_{yq}(\eta,\tau) \\
&= -\pi\rho_\infty U_n^2(2b)^2\left\{\hat{w}_{aT}(\eta,0)(\Phi_{cM})_{c/2}(\tau)+\int_0^\tau \frac{\partial\hat{w}_{aT}(\eta,\sigma)}{\partial\sigma}(\Phi_{cM})_{c/2}(\tau-\sigma)d\sigma\right\} \\
&+ 2\pi\rho_\infty U_n^2(2b)\left\{\dot{\hat{\phi}}_{aP}(\eta,0)(\Phi_{cMq})_{c/2}(\tau)+\int_0^\tau \frac{\partial\dot{\hat{\phi}}_{aP}(\eta,\sigma)}{\partial\sigma}(\Phi_{cMq})_{c/2}(\tau)d\sigma\right\}
\end{aligned}
\tag{4.20b}
$$

where

$$(\Phi_c)_{c/2}(\tau) = (\Phi_c)_0(\tau); \quad (\Phi_{cM})_{c/2}(\tau) = (\Phi_{cM})_0(\tau) + \frac{1}{2}(\Phi_c)_0(\tau); \tag{4.21a}$$

$$(\Phi_{cMq})_{c/2}(\tau) = (\Phi_{cMq})_0(\tau) - \frac{1}{2}(\Phi_{cM})_0(\tau) + \frac{1}{2}(\Phi_{cq})_0(\tau) - \frac{1}{4}(\Phi_c)_0(\tau); \tag{4.21b}$$

$$(\Phi_{cq})_{c/2}(\tau) = (\Phi_{cq})_0(\tau) - \frac{1}{2}(\Phi_c)_0(\tau). \tag{4.21c}$$

In order to cast the aeroelastic system into state-space form, the analytical indicial functions (see [18]) are approximated by quasi-polynomials:

$$(\Phi_c)_{c/2}(\tau) = A_0^c + \sum_{i=1}^{l} A_i^c \exp[-\beta_i^c \tau]; \quad (\Phi_{cM})_{c/2}(\tau) = A_0^{cM} + \sum_{i=1}^{l} A_i^{cM} \exp[-\beta_i^{cM} \tau]; \tag{4.22a}$$

$$(\Phi_{cq})_{c/2}(\tau) = A_0^{cq} + \sum_{i=1}^{l} A_i^{cq} \exp[-\beta_i^{cq} \tau]; \quad (\Phi_{cMq})_{c/2}(\tau) = A_0^{cMq} + \sum_{i=1}^{l} A_i^{cMq} \exp[-\beta_i^{cMq} \tau] \tag{4.22b}$$

Herein, three aerodynamic lag terms are used for each indicial function, i.e., totally 12 aerodynamic lag terms are needed to describe the 2-D unsteady aerodynamic loads in the subsonic compressible flow. Notice that the above indicial functions are dependent on the flight Mach number. The implementation of the approximation is based on the non-linear curve fitting functions provided by Mathematica®. The comparison of the approximation against the Leishman's indicial functions [18] is displayed in Fig. 4.3.

4.4 Integrated Aeroelastic Governing System in State-Space Form

4.4.1 General Theory

Stemming from the analytical mechanics, variational principles provide a very powerful approach in a particularly compact mathematical form [20] to conveniently derive the governing system of complex systems, especially with high degree of coupling. In this section, the modified extended Hamilton's principle [21, 22] is used to derive the governing system of the aeroelastic system considered in this study. Here, the term *extended* implies that the non-conservative forces can only be derived from the virtual work of external forces, instead of the potential energy; while the term *modified* implies that the potential functional adopted accounts for the piezoelectric effect. In the following section,another variational principle is used to derive the worst case optimal control which is based on the game theory.

The modified extended Hamilton's principle states that the true path of motion renders the following variational form stationary:

$$\int_{t_1}^{t_2} \left[\delta T - \delta\tilde{H} + \overline{\delta W}\right] dt = 0 \tag{4.23}$$

with $\delta u_0 = \delta v_0 = \delta w_0 = \delta\theta_x = \delta\theta_z = \delta\phi = 0 \;\; at \quad t = t_1,\, t_2.$

where T denotes the system's kinetic energy; $\tilde{H}$ denotes the thermodynamic potential (or the electric enthalpy density); $\overline{\delta W}$ denotes the virtual work due to external forces; and $t_1,\ t_2$ as two arbitrary instances of time. It should be reminded that other variational principles [23, 24] can be used to derive the governing system, provided that the strong form of the governing system can be reduced from the corresponding variational form. The terms in Eq. 4.23 are defined as:

$$T = \frac{1}{2}\int_0^L \oint_c \left\{ \sum_{k=1}^{m_s+m_p} \int_{h(k)} \rho^{(k)} \left[\left\{\frac{\partial u}{\partial t}\right\}^2 + \left\{\frac{\partial v}{\partial t}\right\}^2 + \left\{\frac{\partial w}{\partial t}\right\}^2 \right] dn\, ds \right\} dy \tag{4.24a}$$

$$\tilde{H} = \int_\Omega \left\{ \frac{1}{2}\sigma_i S_i - \frac{1}{2} D_i E_i \right\} dn\, ds\, dy \tag{4.24b}$$

$$\overline{\delta W} = \int_0^L \left\{ (L_{ae} + L_g + L_b + L_c)\delta w_0 + (T_{ae} + T_g + T_c)\delta\theta_x \right\} dy \tag{4.24c}$$

where $L_{ae},\ T_{ae}$ are unsteady aerodynamic lift and moment,respectively; $L_g,\ L_b$ are aerodynamic lift due to gust and blast; $T_g,\ T_b$ are aerodynamic moment due to gust and blast; and $L_c,\ T_c$ are the control force and control moment. It is straightforward to verify that the strong form of the governing system can exactly be derived from the above variational form. Define the following generalized beam forces:

$$\tilde{T}_y = \oint_C N_{yy}\, ds \triangleq T_y - T_y^a \tag{4.25a}$$

$$\tilde{M}_z = \oint_C [xN_{yy} - L_{yy}\frac{dz}{ds}]\, ds \triangleq M_z - M_z^a \tag{4.25b}$$

$$\tilde{M}_x = \oint_C [zN_{yy} + L_{yy}\frac{dx}{ds}]\, ds \triangleq M_x - M_x^a \tag{4.25c}$$

$$\tilde{Q}_x = \oint_C [N_{sy}\frac{dx}{ds} - N_{ny}\frac{dz}{ds}]\, ds \triangleq Q_x \tag{4.25d}$$

$$\tilde{Q}_z = \oint_C [N_{sy}\frac{dz}{ds} + N_{ny}\frac{dx}{ds}]\, ds \triangleq Q_z \tag{4.25e}$$

$$\tilde{B}_w = -\oint_C [F_w(s)N_{yy} + a(s)L_{yy}]\, ds \triangleq B_w - B_w^a \tag{4.25f}$$

$$\tilde{M}_y = \oint_C [N_{sy}\psi(s)]\, ds \triangleq M_y \tag{4.25g}$$

On the right hand side of each equation in Eqs. (4.25a, b, c, f, g), the first term corresponds to the forces contributed from the host structure, while the second term corresponds to the forces from piezo-actuators. Then the governing system in the most general form can be expressed in terms of the above generalized forces. However, for CAS lay-ups [25, 26] and for the case of fully-spanned piezo-actuators, i.e., extending from the wing root to its tip and the electric field intensity is distributed such that $E_3(x, -z) = -E_3(x, z)$ (*out-of phase* actuation, see [27, 28]), we get $T_y^a(y,t) = 0,\ M_z^a(y,t) = 0,\ B_w^a(y,t) = 0$ and

$$M_x^a(y,t) = \oint_C [zN_{yy}^a + L_{yy}^a\frac{dx}{ds}]\, ds \triangleq M_x^a(t) \tag{4.26}$$

As a result, from the governing equations (not displayed in this article), the piezoelectric effect is present only in the boundary condition:

$$\delta\theta_x: \qquad \tilde{M}_x(L,t) = M_x(L,t) - M_x^a(L,t) = 0 \tag{4.27}$$

The implementation of the control based on the above formulation is referred to as the *boundary (bending) moment control* [28–30].

Based on Eqs.(4.26 and 4.27), $M_x^a(t)$ has the following form:

$$M_x^a = (G_{p1} + G_{p2})(\hat{V}(\tau)) \triangleq G_p \hat{V}(\tau) \tag{4.28a}$$

where

$$\begin{aligned} G_{p1} &= \left[1 - \frac{A_{12}}{A_{11}}\right]\left[e_{31} - \frac{\bar{C}_{13}e_{33}}{\bar{C}_{33}}\right]\Delta b_p(2z)\hat{V}(\tau) && \text{(4.28b)} \\ G_{p2} &= \left[e_{31} - \frac{\bar{C}_{13}e_{33}}{\bar{C}_{33}}\right]\left[\frac{\Delta h_p}{2} - \frac{B_{12}}{A_{11}}\right](2\Delta b_p)\hat{V}(\tau) && \text{(4.28c)} \end{aligned}$$

in which, Δh_p is the thickness of the piezoceramic patch, Δb_p is the width of the piezoactuator patch, and $\hat{V}(\tau)$ is the applied voltage. Notice that in the derivation of Eqs. (4.28a, b, c), it is assumed that the piezo-actuator layers are materially uniform and the electric field intensity is uniformly distributed within the piezo-actuator patch.

It should be noted that the introduction of piezoactuator patches in the above specified way does not change the CAS elastic coupling mechanism, since the $s - y$ plane is the plane of isotropy.

4.4.2 State-Space Form

Define the following non-dimensional parameters:

$$\begin{gathered} \eta \equiv y/L; \quad \tau \equiv U_n t/b; \quad \text{Æ} \equiv L/b; \quad \hat{w}_0(\eta, \tau) \equiv w_0/2b; \\ \hat{\phi}(\eta, \tau) \equiv \phi(\eta, \tau); \ \hat{\theta}_x(\eta, \tau) \equiv \theta_x(\eta, \tau); \quad d()/d\tau = (b/U_n)d()/dt \end{gathered}$$

and perform the spatial semi-discretization:

$$\hat{w}_0(\eta, \tau) = \hat{\mathbf{\Psi}}_w^T(\eta)\hat{\mathbf{q}}_w(\tau); \quad \hat{\phi}(\eta, \tau) = \hat{\mathbf{\Psi}}_\phi^T(\eta)\hat{\mathbf{q}}_\phi(\tau); \quad \hat{\theta}_x(\eta, \tau) = \hat{\mathbf{\Psi}}_x^T(\eta)\hat{\mathbf{q}}_x(\tau)$$

where $\hat{\mathbf{\Psi}}_w(\eta)$, $\hat{\mathbf{\Psi}}_\phi(\eta)$, $\hat{\mathbf{\Psi}}_x(\eta)$ are the $N \times 1$ shape function vectors, which are required to fulfill only the geometric boundary conditions, $\hat{\mathbf{q}}_w(\tau)$, $\hat{\mathbf{q}}_\phi(\tau)$ and $\hat{\mathbf{q}}_x(\tau)$ are N-dimensional generalized displacement vectors, which, by the mode expansion theorem ([31], pp. 171-178), can be further expressed as:

$$\hat{\mathbf{q}}_w(\tau) = \mathbf{\Theta}_w \hat{\xi}_s(\tau); \quad \hat{\mathbf{q}}_\phi(\tau) = \mathbf{\Theta}_\phi \hat{\xi}_s(\tau); \quad \hat{\mathbf{q}}_x(\tau) = \mathbf{\Theta}_x \hat{\xi}_s(\tau) \tag{4.29}$$

where, $\mathbf{\Theta}_w$, $\mathbf{\Theta}_\phi$, and $\mathbf{\Theta}_x$ are $N \times m$ matrices consisting of the first m eigenmodes, $\hat{\xi}_s$ is the modal coordinates ([31], pp. 199). After casting the governing equations into state space form, we get:

$$\left\{\begin{array}{c}\dot{\hat{\mathbf{x}}}_s\\ \dot{\hat{\mathbf{x}}}_a\end{array}\right\} = \underbrace{\left[\begin{array}{cc}\mathcal{A}_s & \mathcal{B}_d\\ \mathcal{B}_a\mathcal{A}_s & \mathcal{A}_a+\mathcal{B}_a\mathcal{B}_s\end{array}\right]}_{\mathcal{A}} \left\{\begin{array}{c}\hat{\mathbf{x}}_s\\ \hat{\mathbf{x}}_a\end{array}\right\} + \underbrace{\left[\begin{array}{c}\mathbf{0}_{m\times m}\\ \mathcal{M}_n^{-1}\\ \mathcal{B}_a\left[\begin{array}{c}\mathbf{0}_{m\times m}\\ \mathcal{M}_n^{-1}\end{array}\right]\end{array}\right]}_{\mathcal{B}_e} \{\mathbf{Q}_g+\mathbf{Q}_b+\mathbf{Q}_c\} + \mathcal{B}_d^0(\tau)\left\{\begin{array}{c}\hat{\mathbf{x}}_s(0)\\ \hat{\mathbf{x}}_a(0)\end{array}\right\} \tag{4.30}$$

or in a more compact form as

$$\dot{\hat{\mathbf{x}}} = \mathcal{A}\hat{\mathbf{x}} + \mathcal{B}_d\hat{\mathbf{w}}_d(\tau) + \mathcal{B}_c\hat{\mathbf{u}}_c(\tau) + \mathcal{B}_d^0(\tau)\hat{\mathbf{x}}(0) \tag{4.31a}$$

The boundary conditions are:

$$\hat{\mathbf{x}}(0) = \hat{\mathbf{x}}_0 \tag{4.31b}$$

where $\hat{\mathbf{x}}_s = \left\{\hat{\xi}_s^{\mathrm{T}} \quad \dot{\hat{\xi}}_s^{\mathrm{T}}\right\}^{\mathrm{T}}$ is a $2m \times 1$ vector related to the structural modes, $\hat{\mathbf{x}}_a$ is a $4lm \times 1$ vector related to the augmented state which describes the unsteady aerodynamic loads, and $\hat{\mathbf{x}} = \left\{\hat{\mathbf{x}}_s^{\mathrm{T}} \quad \hat{\mathbf{x}}_a^{\mathrm{T}}\right\}^{\mathrm{T}}$ is a $(2+4l)m \times 1$ state vector. $\mathbf{Q}_g$, $\mathbf{Q}_b$ and $\mathbf{Q}_c$ are the generalized forces of related gust, blast and control forces, respectively. $\mathcal{B}_d = \mathcal{B}_e$, $\hat{\mathbf{w}}_d = \mathbf{Q}_g + \mathbf{Q}_b$, $\mathcal{B}_c = G_p/(4b_1U_n^2)\mathcal{B}_e \cdot \mathbf{\Theta}_x^{\mathrm{T}} \cdot \hat{\mathbf{\Psi}}_x(1)$, and $\hat{\mathbf{u}}_c(\tau) = \hat{V}(\tau)$. Due to the limited space, the details in Eq. 4.30 are not listed in this chapter.

4.4.3 Electric Power Consumption

Starting with the direct piezoelectric effect in Eq. (4.9), and keeping in mind that the poling direction is along the normal of the mounted surface, we get:

$$D_3 = \{e_{31}\varepsilon_{ss} + e_{32}\varepsilon_{yy} + e_{33}\varepsilon_{nn} + \epsilon_{33}^S E_3\}R(s,y,n) \tag{4.32}$$

At the upper surface $z = h_s/2 + \Delta h_p$,

$$\begin{aligned} D_3(t) = &(1 - \frac{A_{12}}{A_{11}})\bar{e}_{31}\varepsilon_{yy}^0 - \frac{A_{16}}{A_{11}}\bar{e}_{31}\gamma_{sy}^0 - \frac{A_{16}}{A_{11}}\bar{e}_{31}\psi(s)\phi' \\ &+ (\frac{h_s}{2} + \Delta h_p - \frac{B_{12}}{A_{11}})\bar{e}_{31}\varepsilon_{yy}^n + [\epsilon_{33}^S + \frac{e_{33}^2}{\bar{C}_{33}} + \frac{\bar{e}_{31}^2\Delta h_p}{A_{11}}]E_3 R(s,y) \end{aligned} \tag{4.33}$$

where

$$\bar{e}_{31} = e_{31} - \frac{\bar{C}_{13}}{\bar{C}_{33}}e_{33}$$

In the derivation of Eq.(4.33), it is assumed that the electric intensity E_3 is uniform throughout the thickness of piezoelectric layers.

Hence, the quantity of charges outflowed across the upper electrode of the patch mounted on the upper surface is:

$$\hat{Q}(\tau) = \int_{Upper\ electrode} D_3(s,y,t)\, dS \tag{4.34}$$

Therefore, the rate of change of this quantity, i.e., the electric current is as follows:

$$\hat{I}_c(\tau) = \left(\frac{U_n}{b}\right)\frac{d}{d\tau}\hat{Q}(\tau) \tag{4.35}$$

and electric power supplied from the electric source is:

$$\hat{P}_{applied}(\tau) = \hat{V}(\tau)\cdot\hat{I}_c(\tau) \tag{4.36}$$

4.5 Minimax Control Design

The worst case full-state control design paradigm based on the game theory is applied towards the flutter suppression and dynamic aeroelastic response enhancement.

Define the following game strategy:

$$\min_{\hat{\mathbf{u}}_c}\max_{\hat{\mathbf{w}}_d} J_1 \equiv \frac{1}{2}\hat{\mathbf{x}}^{\mathrm{T}}(\tau_f)\mathcal{T}\hat{\mathbf{x}}(\tau_f) + \frac{1}{2}\int_{\tau_0}^{\tau_f}\left\{\hat{\mathbf{x}}^{\mathrm{T}}\mathcal{Z}\hat{\mathbf{x}} + \hat{\mathbf{u}}_c^{\mathrm{T}}\mathcal{R}_c\hat{\mathbf{u}}_c\right\}\, d\tau \tag{4.37a}$$

$$subject\,to \qquad W_d = \frac{1}{2}\int_{\tau_0}^{\tau_f}\hat{\mathbf{w}}_d^{\mathrm{T}}\hat{\mathbf{w}}_d\, d\tau \tag{4.37b}$$

In Eqs. (4.37a, b), $\hat{\mathbf{x}}$, $\hat{\mathbf{u}}_c$ and $\hat{\mathbf{w}}_d$ fulfill Eq. (4.31) and the weight matrices fulfill $\mathcal{T}^{\mathrm{T}} = \mathcal{T} > 0$, $\mathcal{R}_c^{\mathrm{T}} = \mathcal{R}_c > 0$. W_d is a measure of the intensity of the gust load. The weight matrix $\mathcal{Z}$ is selected such that $\hat{\mathbf{x}}^{\mathrm{T}}\mathcal{Z}\hat{\mathbf{x}}$ represents the sum of the total structural kinetic and potential energy, namely,

$$\mathcal{Z} = \begin{bmatrix} \hat{\mathcal{K}}_s & \mathbf{0} & \mathbf{0} \\ \mathbf{0} & \hat{\mathcal{M}}_s & \mathbf{0} \\ \mathbf{0} & \mathbf{0} & \mathbf{0}_{4lm\times 4lm} \end{bmatrix} \tag{4.38}$$

where $\hat{\mathcal{K}}_s$ and $\hat{\mathcal{M}}_s$ are $m \times m$ non-dimensional stiffness and mass matrices, which,due to the space limitation, are not displayed in this article. Other zero matrices are dimension-compatible entities.

By introducing the Lagrangian multipliers μ and $\hat{\lambda}$, we convert the above constrained optimization problem to an unconditional one.

Constructing the following Lagrangian:

$$J_2 = \frac{1}{2}\hat{\mathbf{x}}^{\mathrm{T}}(\tau_f)\mathcal{T}\hat{\mathbf{x}}(\tau_f) + \mu W_d + \int_{\tau_0}^{\tau_f} \mathcal{H} d\tau \tag{4.39a}$$

where $\mathcal{H}$ is the Hamiltonian functional:

$$\mathcal{H} \equiv \frac{1}{2}\left[\hat{\mathbf{x}}^{\mathrm{T}}\mathcal{Z}\hat{\mathbf{x}} + \hat{\mathbf{u}}_c^{\mathrm{T}}\mathcal{R}_c\hat{\mathbf{u}}_c - \mu\hat{\mathbf{w}}_d^{\mathrm{T}}\hat{\mathbf{w}}_d\right] + \hat{\lambda}^{\mathrm{T}}[\mathcal{A}\hat{\mathbf{x}} + \mathcal{B}_d\hat{\mathbf{w}}_d + \mathcal{B}_c\hat{\mathbf{u}}_c + \mathcal{B}_d^0\hat{\mathbf{x}}_0 - \dot{\hat{\mathbf{x}}}] \tag{4.39b}$$

Following the rules of conventional variational operations, we get the *necessary* conditions of the control strategy (Eq. 4.37a):

$$\begin{aligned} \delta\hat{\mathbf{x}} \quad &: \quad \dot{\hat{\lambda}} + \mathcal{Z}\hat{\mathbf{x}} + \mathcal{A}^{\mathrm{T}}\hat{\lambda} = 0; && (4.40a) \\ \delta\hat{\mathbf{w}}_d \quad &: \quad \hat{\mathbf{w}}_d = \frac{1}{\mu}\mathcal{B}_d{}^{\mathrm{T}}\hat{\lambda}; && (4.40b) \\ \delta\hat{\mathbf{u}}_c \quad &: \quad \hat{\mathbf{u}}_c = -\mathcal{R}_c^{-1}\mathcal{B}_c{}^{\mathrm{T}}\hat{\lambda}; && (4.40c) \\ \delta\hat{\lambda} \quad &: \quad \dot{\hat{\mathbf{x}}} = \mathcal{A}\hat{\mathbf{x}} + \mathcal{B}_d\hat{\mathbf{w}}_d + \mathcal{B}_c\hat{\mathbf{u}}_c + \mathcal{B}_d^0\hat{\mathbf{x}}_0; && (4.40d) \\ \delta\mu \quad &: \quad W_d = \frac{1}{2}\int_{\tau_0}^{\tau_f} \hat{\mathbf{w}}_d^{\mathrm{T}}\hat{\mathbf{w}}_d d\tau && (4.40e) \end{aligned}$$

It then follows:

$$\left\{ \begin{array}{c} \dot{\hat{\mathbf{x}}} \\ \dot{\hat{\lambda}} \end{array} \right\} = \underbrace{\left[\begin{array}{cc} \mathcal{A} & -(\mathcal{B}_c\mathcal{R}_c^{-1}B_c^{\mathrm{T}} - \frac{1}{\mu}\mathcal{B}_d{\mathcal{B}_d}^{\mathrm{T}}) \\ -\mathcal{Z} & -\mathcal{A}^{\mathrm{T}} \end{array} \right]}_{system \quad matrix} \left\{ \begin{array}{c} \hat{\mathbf{x}} \\ \hat{\lambda} \end{array} \right\} + \left\{ \begin{array}{c} \mathcal{B}_d^0\hat{\mathbf{x}}_0 \\ \mathbf{0} \end{array} \right\} \tag{4.41a}$$

With boundary conditions:

$$\mathcal{T}\hat{\mathbf{x}}(\tau_f) = \hat{\lambda}(\tau_f); \qquad \hat{\mathbf{x}}(\tau_0) = \hat{\mathbf{x}}_0 \tag{4.41b}$$

Eqs. (4.41a, b) constitute the solution of the worst case control design (Eqs. 4.37a, b). Due to the unique characteristics of the boundary conditions , problems corresponding to Eqs. (4.41a, b) is also referred to as *two-point* boundary value problem [32].

In Eq. 4.41a, the system matrix is also referred to as the *Hamiltonian* matrix, which plays a pivoting role in the modern linear control theory and in the numerical implementation of various types of Riccati equations [33, 34].

The solution of Eq. (4.41a) is:

$$\left\{ \begin{array}{c} \hat{\mathbf{x}}(\tau) \\ \hat{\lambda}(\tau) \end{array} \right\} = \left[\begin{array}{cc} \Phi_{11}(\tau-\tau_f) & \Phi_{12}(\tau-\tau_f) \\ \Phi_{21}(\tau-\tau_f) & \Phi_{22}(\tau-\tau_f) \end{array} \right] \left\{ \begin{array}{c} \hat{\mathbf{x}}(\tau_f) \\ \hat{\lambda}(\tau_f) \end{array} \right\} + \int_{\tau_f}^{\tau} \left[\begin{array}{c} \Phi_{11}(\tau-\sigma) \\ \Phi_{21}(\tau-\sigma) \end{array} \right] \hat{\mathbf{B}}_d^0(\sigma)\hat{\mathbf{x}}_0 d\,\sigma \tag{4.42}$$

Combined with the two-point boundary conditions (Eq. 4.41b), it follows:

$$\begin{aligned} \hat{\mathbf{x}}(\tau) &= [\Phi_{11}(\tau-\tau_f) + \Phi_{12}(\tau-\tau_f)\mathcal{T}]\hat{\mathbf{x}}(\tau_f) + \int_{\tau_f}^{\tau} \Phi_{11}(\tau-\sigma)\mathcal{B}_d^0(\sigma)d\,\sigma\,\hat{\mathbf{x}}_0 && \text{(4.43a)} \\ \hat{\lambda}(\tau) &= \hat{\mathcal{S}}(\tau)\hat{\mathbf{x}}(\tau) - \hat{\mathbf{d}}(\tau) && \text{(4.43b)} \end{aligned}$$

where

$$\begin{aligned} \hat{\mathcal{S}}(\tau) &= [\Phi_{21}(\tau-\tau_f) + \Phi_{22}(\tau-\tau_f)\mathcal{T}][\Phi_{11}(\tau-\tau_f) + \Phi_{12}(\tau-\tau_f)\mathcal{T}]^{-1} && \text{(4.43c)} \\ \hat{\mathbf{d}}(\tau) &= [\hat{\mathcal{S}}(\tau)\int_{\tau_f}^{\tau} \Phi_{11}(\tau-\sigma)\mathcal{B}_d^0(\sigma)d\,\sigma - \int_{\tau_f}^{\tau} \Phi_{21}(\tau-\sigma)\mathcal{B}_d^0(\sigma)d\,\sigma]\hat{\mathbf{x}}_0 && \text{(4.43d)} \end{aligned}$$

Thus, the optimal control input $\hat{\mathbf{u}}_c^\star$ is:

$$\hat{\mathbf{u}}_c^\star(\tau) = -\mathcal{R}_c^{-1}{\mathcal{B}_c}^{\mathrm{T}}[\hat{\mathcal{S}}(\tau)\hat{\mathbf{x}}(\tau) - \hat{\mathbf{d}}(\tau)] \tag{4.44}$$

and the worst case disturbance (gust or blast loads constrained by Eq. (4.37b)) is (substituting Eq. (4.43a) into Eq. (4.40b)):

$$\hat{\mathbf{w}}_d^{\star}(\tau) = \frac{1}{\mu}\mathcal{B}_d{}^{\mathrm{T}}[\hat{\mathcal{S}}(\tau)\hat{\mathbf{x}}(\tau) - \hat{\mathbf{d}}(\tau)] \tag{4.45}$$

which plays, in essence, a positive feedback influence. Notice that the solution in Eq. (4.43) starts from $\hat{\mathbf{x}}(\tau_f)$, which is derived from Eqs. (4.43a, and 4.41b). This yields:

$$\hat{\mathbf{x}}(\tau_f) = [\Phi_{11}(\tau_0 - \tau_f) + \Phi_{12}(\tau_0 - \tau_f)\mathcal{T}]^{-1}\left[\mathbf{I} - \int_{\tau_f}^{\tau_0} \Phi_{11}(\tau - \sigma)\mathcal{B}_d^0(\sigma)\, d\sigma\right]\hat{\mathbf{x}}_0 \tag{4.46}$$

In the modern control theory, design of control laws is largely based on some form of Riccati equations. In fact, it is straightforward to verify that the symmetric matrix $\hat{\mathcal{S}}$ fulfills the following Riccati equation:

$$-\dot{\hat{\mathcal{S}}} = \mathcal{Z} + \mathcal{A}^{\mathrm{T}}\hat{\mathcal{S}} + \hat{\mathcal{S}}\mathcal{A} - \hat{\mathcal{S}}[\mathcal{B}_c\mathcal{R}_c^{-1}\mathcal{B}_c{}^{\mathrm{T}} - \frac{1}{\mu}\mathcal{B}_d\mathcal{B}_d{}^{\mathrm{T}}]\hat{\mathcal{S}} \tag{4.47a}$$

$$\hat{\mathcal{S}}(\tau_f) = \mathcal{T} \tag{4.47b}$$

while vector $\hat{\mathbf{d}}$ fulfills:

$$\dot{\hat{\mathbf{d}}} = -[\mathcal{A}^{\mathrm{T}} - \hat{\mathcal{S}}(\mathcal{B}_c\mathcal{R}_c^{-1}\mathcal{B}_c{}^{\mathrm{T}} - \frac{1}{\mu}\mathcal{B}_d\mathcal{B}_d{}^{\mathrm{T}})]\hat{\mathbf{d}} + \hat{\mathcal{S}}\mathcal{B}_d^0(\tau)\hat{\mathbf{x}}_0 \tag{4.48a}$$

$$\hat{\mathbf{d}}(\tau_f) = \mathbf{0} \tag{4.48b}$$

In connnection with Eqs. (4.47, 4.48), the following points should be outlined:

(a) Lagrangian multiplier μ should be determined from Eqs. (4.40b, e). However, its analytical determination does not constitute generally an easy task. In some special case, the solution is formulated in the following.

(b) The influence of the disturbance may lead the matrix $(\mathcal{B}_c\mathcal{R}_c^{-1}\mathcal{B}_c{}^{\mathrm{T}} - \frac{1}{\mu}\mathcal{B}_d\mathcal{B}_d{}^{\mathrm{T}})$ not to fulfill the semi-positive definiteness condition. If this is the case, Eq.(4.47) is referred to as the *non-standard* Riccati equation [35] and properties, such as the existence, uniqueness of its solution becomes critical to the success of a control design. As to the properties of such Riccati equation, the readers is referred to [11]

When $\tau_f \to \infty$, if we focus on the steady-state solution $\bar{\mathcal{S}}$ of Eq. 4.47a, we get the following algebraic Riccati equation:

$$\mathcal{Z} + \mathcal{A}^{\mathrm{T}}\bar{\mathcal{S}} + \bar{\mathcal{S}}\mathcal{A} - \bar{\mathcal{S}}[\mathcal{B}_c\mathcal{R}_c^{-1}\mathcal{B}_c{}^{\mathrm{T}} - \frac{1}{\mu}\mathcal{B}_d\mathcal{B}_d{}^{\mathrm{T}}]\bar{\mathcal{S}} = 0 \tag{4.49}$$

In literature, control syntheses based on Eq.(4.49) are referred to as the *sub-optimal* control design.

In the remaining part of this section, the worst-case μ, J_1 and their upper bounds based on the steady-state $\bar{\mathcal{S}}$ will be derived.

For unsteady aerodynamic loads, since the coefficient matrix $\mathcal{B}_d^0(\tau)$ decays much faster than the response $\hat{\mathbf{x}}(\tau)$, especially near the flutter boundary, the $\mathcal{B}_d^0(\tau)$-related terms can be discarded. In this case, from Eq. (4.48a, b), and $\tau_f \to \infty$, we get: $\hat{\mathbf{d}}(\tau) = \mathbf{0}$. Therefore,

$$\hat{\mathbf{u}}_c^\star(\tau) = -\mathcal{R}_c^{-1}\mathcal{B}_c^{\mathrm{T}}\bar{\mathcal{S}}\hat{\mathbf{x}}(\tau); \qquad \hat{\mathbf{w}}_d^\star(\tau) = \frac{1}{\mu}\mathcal{B}_d^{\mathrm{T}}\bar{\mathcal{S}}\hat{\mathbf{x}}(\tau) \tag{4.50}$$

Denoting the worst-case closed-loop system matrix $\left[\mathcal{A} + \frac{1}{\mu}\mathcal{B}_d\mathcal{B}_d^{\mathrm{T}}\bar{\mathcal{S}} - \mathcal{R}_c^{-1}\mathcal{B}_c^{\mathrm{T}}\bar{\mathcal{S}}\right] \triangleq \mathcal{A}_c$, we get

$$W_d = \frac{1}{2\mu^2}\hat{\mathbf{x}}_0^{\mathrm{T}}\bar{\mathcal{P}}_\mu\hat{\mathbf{x}}_0 \tag{4.51}$$

where the $(2+4l)m \times (2+4l)m$ matrix $\bar{\mathcal{P}}_\mu$ is defined as:

$$\bar{\mathcal{P}}_\mu = \int_0^\infty e^{\mathcal{A}_c^{\mathrm{T}}\tau}\left[\bar{\mathcal{S}}\mathcal{B}_d\mathcal{B}_d^{\mathrm{T}}\bar{\mathcal{S}}\right]e^{\mathcal{A}_c\tau}d\tau \ \geq 0 \tag{4.52}$$

Reminding that $\mathcal{P}e^{\mathcal{P}\tau} \equiv e^{\mathcal{P}\tau}\mathcal{P}, \ \forall\, \mathcal{P}$, it is quite straightforward to verify that $\bar{\mathcal{P}}_\mu$ satisfies the following Lyapunov equation:

$$\mathcal{A}_c^{\mathrm{T}}\bar{\mathcal{P}}_\mu + \bar{\mathcal{P}}_\mu\mathcal{A}_c + \bar{\mathcal{S}}\mathcal{B}_d\mathcal{B}_d^{\mathrm{T}}\bar{\mathcal{S}} = 0 \tag{4.53}$$

Denoting the norm $\hat{\mathbf{x}}_0^{\mathrm{T}} \cdot \hat{\mathbf{x}}_0 = W_{\hat{\mathbf{x}}_0}$, and invoking the stationarity properties of Rayleigh's quotient ([31], pp. 237-239, extended to arbitrary real symmetric matrices), we get the upper bound of μ:

$$2\mu^2 = \frac{W_{\hat{\mathbf{x}}_0}}{W_d}\frac{\hat{\mathbf{x}}_0^{\mathrm{T}}\bar{\mathcal{P}}_\mu\hat{\mathbf{x}}_0}{\hat{\mathbf{x}}_0^{\mathrm{T}}\hat{\mathbf{x}}_0} \leq \frac{W_{\hat{\mathbf{x}}_0}}{W_d}\lambda_m(\bar{\mathcal{P}}_\mu) \tag{4.54}$$

where $\lambda_m(\bar{\mathcal{P}}_\mu)$ denotes the maximum eigenvalue of the corresponding matrix.

Similarly, in the worst case, the performance index satisfies:

$$J_1 = \frac{1}{2}\int_0^\infty \left\{\hat{\mathbf{x}}^{\mathrm{T}}\mathcal{Z}\hat{\mathbf{x}} + \hat{\mathbf{u}}^{\star\mathrm{T}}_c\mathcal{R}_c\hat{\mathbf{u}}^{\star}_c\right\} d\,\tau = \frac{1}{2}\hat{\mathbf{x}}_0^{\mathrm{T}}\bar{\mathcal{P}}_{J_1}\hat{\mathbf{x}}_0 \tag{4.55}$$

where

$$\bar{\mathcal{P}}_{J_1} = \int_0^\infty e^{\mathcal{A}_c^{\mathrm{T}}\tau}\left[\mathcal{Z} + \bar{\mathcal{S}}\mathcal{B}_c\mathcal{R}_c^{-1}\mathcal{B}_c^{\mathrm{T}}\bar{\mathcal{S}}\right]e^{\mathcal{A}_c\tau}d\,\tau \ \geq 0 \tag{4.56}$$

Paralleling $\bar{\mathcal{P}}_\mu$, $\bar{\mathcal{P}}_{J_1}$ fulfills the following Lyapunov equation:

$$\mathcal{A}_c^{\mathrm{T}}\bar{\mathcal{P}}_{J_1} + \bar{\mathcal{P}}_{J_1}\mathcal{A}_c + \left[\mathcal{Z} + \bar{\mathcal{S}}\mathcal{B}_c\mathcal{R}_c^{-1}\mathcal{B}_c^{\mathrm{T}}\bar{\mathcal{S}}\right] = 0 \tag{4.57}$$

and the upper bound is:

$$J_1 = \frac{1}{2}W_{\hat{\mathbf{x}}_0}\frac{\hat{\mathbf{x}}_0^{\mathrm{T}}\bar{\mathcal{P}}_{J_1}\hat{\mathbf{x}}_0}{\hat{\mathbf{x}}_0^{\mathrm{T}}\hat{\mathbf{x}}_0} \leq \frac{1}{2}W_{\hat{\mathbf{x}}_0}\lambda_m(\bar{\mathcal{P}}_{J_1}) \tag{4.58}$$

4.6 Numerical Illustrations and Discussion

Design of sub-optimal control laws based on Eq. 4.49 is adopted in this section. The capabilities of the designed control laws for flutter suppression and dynamic aeroelastic response enhancement are investigated for the case of a smart aircraft wing. Its material and geometric properties (with biconvex cross section) are listed in Tables 4.1, 4.2. Notice that in the actual simulation, the first 3 structural modes are incorporated into the model and for each aerodynamic indicial function, 3 lag terms are used, i.e., $m = 3$, $l = 3$. All the response components (bending, twist and transverse shear) are measured at the wing tip (i.e., $\eta = 1$). Denote the control gain matrix $\mathcal{R}_c^{-1}\mathcal{B}_c^{\mathrm{T}}\bar{\mathcal{S}} \triangleq \mathbf{G}_c$, and weight matrix $\mathcal{R}_c = r_c\mathbf{I}$.

Figures 4.4, 4.5 and 4.6 display the control capability on the flutter suppression. $\mathbf{G}_c$ is designed at ($M_{design} = 0.7$, $\theta_{design} = 105^0$, $r_c = 10^{-9}$, $\mu = 10^{10}$). Compared with the open-loop flutter instability (Fig. 4.4), the incorporation of the control law successfully stabilizes the aeroelastic system. Figure 4.5 also demonstrates that the sub-optimal control law can stabilize the sharp-edged gust, although the sharp-edged gust does not fulfill Eq. 4.37b.

The required control voltage and power input for the case of sharp-edged gust are displayed in Figs. 4.7, 4.8 and for the case of 1-COSINE gust, in Figs. 4.9 and 4.10. Noticeably, the non-symmetric distribution of the power input amplitude in Fig. 4.8 reveals that the controlled aeroelastic wing absorbs the electric energy (positive) to counteract the effect of unsteady aerodynamic loads.

Table 4.3 reveals the relocation of structure-related eigenvalues of the aeroelastic system via the active control. It is observed that, a), for all the three control laws, only the open-loop unstable eigenvalue is shifted but the open-loop stable eigenvalues almost remain at the same positions; b), in the case $r_c = 10^{-9}$, the control law maps the unstable eigenvalue into its mirror position in terms of the imaginary axis in the s-plane, and c) for all the three cases, lower weight r_c, hence cheaper control effort, shifts the eigenvalues farther to the left. This is consistent with the intuition.

Table 4.4 displays the influence of parameter variation on the stability of controlled aeroelastic system. $\mathbf{G}_c$ is designed at ($M_{design} = 0.75$, $\theta_{design} = 105^0$, $r_c = 10^{-10}$, $\mu = 10^{10}$). Since for the investigated aircraft wing, ply angle θ_{flight} and flight speed M_{flight} and hence aerodynamic compressibility, are among the major parameters, they are used for the flutter robustness investigation.

It should be remarked that although the control law displays robustness over a relatively large range of the parameter variations, other issues, such as the allowable voltage limitation of the piezo-actuator, concerns for power consumption, may become a serious constraint on the actual implementation of the control, as displayed in Figs. 4.11 and 4.12. In this case, the required voltage is far beyond the physical allowable voltage of the piezoceramic actuator. Furthermore, the electric power consumption may become a serious concern.

Figures 4.13, 4.14 and 4.15 demonstrate the enhancement of control on the subcritical aeroelastic response to a blast load. $\mathbf{G}_c$ is still designed at ($M_{design} = 0.75$, $\theta_{design} = 105^0$, $r_c = 10^{-10}$, $\mu = 10^{10}$) but applied at $M_{flight} = 0.6$. Two observations should be provided: (a), all the three controlled vibration components (bending, twist, transverse shear-related quantity) are damped out in a rather shorter time as compared to the uncontrolled counterparts, implying that the boundary bending moment feedback control is a viable control mechanism for the vibration control of the aeroelastic system; (b), the maximum peak value of $\hat{w}_0(\eta = 1, \tau)$ is reduced by 35% and the maximum peak value of $\hat{\theta}_x(\eta = 1, \tau)$ is reduced by 21%, however, for the twist vibration component, only a slight reduction is achieved. This implies that the boundary bending moment feedback control is more suitable for bending vibration control. Figs. 4.16 and 4.17 display the required voltage input and power consumption. The big jumps of applied voltage and electric power are due to the sudden loading of the blast on the wing.

4.7 Concluding Remarks

A new minimax aeroelastic control on a smart aircraft wing is proposed and its capability on the flutter suppression and enhancement of dynamic aeroelastic response via the boundary bending moment feedback control is investigated. At high subsonic flight speed, the designed control law not only displays promising capability to augment the flutter speed, reduce the dynamic aeroelastic response amplitudes, but also demonstrates robustness over a relatively large range of variations of the major parameters. However, other issues such as the limitation of allowable voltage on the piezoelectric actuators, electric power consumption may become serious constraints towards the actual implementation of the control laws.

4.8 References

[1] Shirk, M. H., Hertz, T. J., and Weisshaar, T. A., "Aeroelastic Tailoring– Theory, Practice and Promise," *Journal of Aircraft*, Vol. 23, No. 1, 1986, pp. 6–18.

[2] Sunar, M. and Rao, S. S., "Recent Advances in Sensing and Control of Flexible Structures via Piezoelectric Materials Technology," *Applied Mechanics Reviews*, Vol. 52, No. 1, 1999, pp. 1–16.

[3] Nam, C. and Kim, J. S., "Robust Controller Design of a Wing with Piezoelectric Materials for Flutter Suppression," *The* 10^{th} *VPI SU Symposium on Structural Dynamics and COntrol*, Blacksburg, VA, May 8-10 1995.

[4] Lin, C. Y. and Crawley, E. F., "Open- and Closed-Loop Results of a Strain-Actuated Active Aeroelastic Wing," *Journal of Aircraft*, Vol. 33, No. 5, 1996, pp. 987–994.

[5] Loewy, R. G., "Recent Developments in Smart Structures with Aeronautical Applications," *Journal of Smart Materials and Structures*, Vol. 5, 1997, pp. 11–41.

[6] Crawley, E. F., "Intelligent Structures for Aerospace: A Technology Overview and Assessment," *AIAA Journal*, Vol. 32, No. 8, 1994, pp. 1689–99.

[7] Chopra, I., "Review of Current Status of Smart Structures and Integrated Systems," *SPIE Proceedings of Smart Structures and Integrated Systems*, Vol. 2717, San Diego, CA, 1996.

[8] Librescu, L. and Song, O., "Behavior of Thin-Walled Beams Made of Advanced Composite Materials and Incorporating Non-Classical Effects," *Applied Mechanics Reviews*, Vol. 44, No. 11, part 2, 1991, pp. S174–S180.

[9] Jung, S. N., Nagaraj, V. T., and Chopra, I., "Assessment of Composite Rotor Blade Modeling Techniques," *Journal of the American Helicopter Society*, Vol. 44, No. 3, 1999, pp. 188–205.

[10] Qin, Z. and Librescu, L., "Static and Dynamic Validations of a Refined Thin-Walled Composite Beam Model," *AIAA Journal*, in press.

[11] Lu, W. W., Balas, G. J., and Lee, E. B., "A Variational Approach to H^{∞} Control with Transients," *IEEE Transactions on Automatic Control*, Vol. 44, No. 10, 1999, pp. 1875–79.

[12] Bhaskar, K. and Librescu, L., "A Geometrically Non-Linear Theory for Laminated Anisotropic Thin-Walled Beams," *International Journal of Engineering Science*, Vol. 33, No. 9, 1995, pp. 1331–1344.

[13] Song, O., *Modeling and Response Analysis of Thin-Walled Beam Structures Constructed of Advanced Composite Materials*, Ph.D. thesis, Virginia Polytechnic Institute and State University, 1990.

[14] Na, S. S., *Control of Dynamic Response of Thin-Walled Composite Beams Using Structural Tailoring and Piezoelectric Actuation*, Ph.D. thesis, Virginia Polytechnic Institute and State University, 1997.

[15] Reddy, J. N., *Theory and Analysis of Elastic Plates*, Taylor Francis, Philadelphia, 1999.

[16] Singh, R. and Baeder, J. D., "Direct Calculation of Three-Dimensional Indicial Lift Response Using Computational Fluid Dynamics," *Journal of Aircraft*, Vol. 34, No. 4, 1997, pp. 465–471.

[17] Bisplinghoff, R. L., Ashley, H., and Halfman, R. L., *Aeroelasticity*, Dover Publications, New York, 1996.

[18] Leishman, J., "Indicial Lift Approximations for Two-Dimensional Subsonic Flow as Obtained from Oscillatory Measurements," *Journal of Aircraft*, Vol. 30, No. 3, 1993, pp. 340–351.

[19] Marzocca, P., Librescu, L., and Chiocchia, G., "Unsteady Aerodynamics in Various Flight Speed Regimes for Flutter/Dynamic Response Analyses," *Proceeding of the 18th AIAA Applied Aerodynamic Conference*, Denver, CO, August 14-17 2000, AIAA-2000-4229.

[20] Mingori, D. L., "Lagrange's Equations, Hamilton's Equations, and Kane's Equations: Interrelations, Energy Integrals, and a Variational Principle," *Journal of Applied Mechanics*, Vol. 62, June 1995, pp. 505–510.

[21] Tiersten, H. F., *Linear Piezoelectric Plate Vibations*, Plenum Press, New York, 1969.

[22] Librescu, L., Song, O., and Rogers, R. A., "Adaptive Vibational Behavior of Cantilevered Strctures Modeled as Composite Thin-Walled Beams," *International Journal of Engineering Science*, Vol. 31, No. 5, 1993, pp. 775–792.

[23] Yang, J. S., "Mixed Variational Principles for Piezoelectric Elasticity," *Developments in Theoretical and Applied Mechanics*, edited by B. Antar, R. Engels, A. A. Prinaris, and T. H. Moulden, The University of Tennessee Space Institute, 1992, pp. 31–38.

[24] Ghandi, K. and Hagood, N. W., "A Hybrid Finite Element Model for Phase Transitions in Nonlinear Electro-Mechanically Coupled Material," *Proceedings of the SPIE Smart Structures and Materials Conference*, Vol. 3039, 1997, pp. 97–112.

[25] Rehfield, L. W. and Atilgan, A. R., "Towards Understanding the Tailoring Mechanisms for Thin-Walled Composite Tubular Beams," *Proceedings of the First USSR-US Symposium on Mechanics of Composite Materials*, edited by S. W. TSai, J. M. Whitney, T.-W. Chou, and R. M. Jones, Riga, Latvia SSR, ASME, New York, 1989, pp. 187–196.

[26] Smith, E. C. and Chopra, I., "Formulation and Evaluation of an Analytical Model for Composite Box-Beams," *Journal of American Helicopter Society*, Vol. 36, No. 3, 1991, pp. 23–35.

[27] Birman, V., “Analytical Models of Sandwich Plates with Piezoelectric Strip Stiffners,” *International Journal of Mechanical Sciences*, Vol. 36, No. 6, 1994, pp. 567–578.

[28] Lin, C. Y. and Crawley, E. F., “Aeoelastic Actuation Using Elastic and Induced Strain Anisotropy,” *Journal of Aircraft*, Vol. 32, No. 5, 1995, pp. 1130–1137.

[29] Lagnese, J. E., “Boundary Stabilization of Thin Plates,” *SIAM Studies in Applied Mechanics*, 1989.

[30] Librescu, L. and Na, S., “Dynamic Response Control of Thin-Walled Beams to Blast Pulses Using Structural Tailoring and Piezoelectric Actuation,” *Journal of Applied Mechanics*, Vol. 65, June 1998, pp. 497–504.

[31] Meirovitch, L., *Principles and Techniques of Vibrations*, Prentice Hall, Upper Saddle River, New Jersey, 1997.

[32] Bryson, Jr., A. E. and Ho, Y. C., *Applied Optimal Control: Optimization, Estimation, and Control*, Hemisphere Publishing, Wahsington, D.C., revised printing ed., 1975.

[33] Laub, A. J., “A Schur Method for Solving Algebraic Riccati Equations,” *IEEE Transactions on Automatic Control*, Vol. AC-24, No. 6, 1979, pp. 913–921.

[34] Na, S. and Librescu, L., “Optimal Vibration Control of Thin-Walled Anisotropic Cantilevers Exposed to Blast Loadings,” *Journal of Guidance, Control and Dynamics*, Vol. 23, No. 3, 2000, pp. 491–500.

[35] Dorato, P., Abdallah, C., and Cerone, V., *Linear–Quadratic Control: An Introduction*, Prentice Hall, Englewood Cliffs, NJ, 1995.

Table 4.1: Material properties of piezoelectric(PZT4) and Graphite/Epoxy composite

Parameter	Piezoelectric	Graphite/Epoxy
Elastic constant, Gpa		
C_{11}	139.0^a	207.7
C_{12}	77.8^a	1.73
C_{13}	74.3^a	1.73
C_{22}	139.0	5.53
C_{23}	74.3	1.39
C_{33}	115.0^a	5.53
C_{44}	25.6^a	2.55
C_{55}	25.6	2.55
C_{66}	30.6	3.1
Density, Kg/m^3	7495	1528
Piezoelectric coupling constant, $N/(m \cdot V)$		
$e_{31} = e_{32}$	-5.20	–
e_{33}	15.1	–
$e_{15} = e_{24}$	12.7	–
Dielectric constant, $F/m \times 10^9$		
ϵ_{11}^S	6.75	–
ϵ_{22}^S	6.75	–
ϵ_{33}^S	5.87	–

[a] Independent parameters of the piezoceramic material, see Eqs. (4.10, 4.11)

Table 4.2: Geometric specification of the smart aircraft wing and the piezoceramic patches

Wing parameter	Value	Piezo. patch parameter	Value
Chord length $2b$, m	0.757	Width Δb_p, m	0.252
Depth $2d$, m	0.0997	Thickness Δh_p, m	2.03×10^{-3}
Wall thickness h_s, m	0.0203		
Number of layers	6	Number of layers	1
Lay-up	$[\theta_6]$, CAS		
Aspect ratio $\mathcal{AR}$,	12	Length, m	4.54
Geometric sweep angle Λ_g, deg.	0		

Table 4.3: Essence of the minimax control ($\mu = 10^{10}$, $M_{design} = 0.7$, $\theta_{design} = 105^0$) on the integrated aeroelastic system ($M_{flight} = 0.7$, $\theta_{flight} = 105^0$)

Control strategy	Structure-related eigenvalues		
	1^{st}	2^{nd}	3^{rd}
OL	$0.00149 \pm 0.100j$	$-0.0156 \pm 0.322j$	$-0.0121 \pm 0.490j$
$CL,\ r_c = 10^{-9}$	$-0.00150 \pm 0.100j$	$-0.0156 \pm 0.322j$	$-0.0122 \pm 0.490j$
$CL,\ r_c = 10^{-10}$	$-0.00161 \pm 0.100j$	$-0.0160 \pm 0.322j$	$-0.0123 \pm 0.490j$
$CL,\ r_c = 10^{-11}$	$-0.00242 \pm 0.100j$	$-0.0189 \pm 0.322j$	$-0.0141 \pm 0.490j$

Table 4.4: Parameter variations on the stability of controlled aeorelastic system ($r_c = 10^{-10}$, $\mu = 10^{10}$, $M_{design} = 0.7$, $\theta_{design} = 105^0$)

Parameter variation	$\Delta\theta(\theta_{flight}) : [deg]$				
$\Delta M_{flight}(M_{flight})$	0(105)	15(120)	30(135)	45(150)	-5(100)
0.02(0.77)	✓[a]	✓	✓	✓	×[b]
0.00(0.75)	✓	✓	✓	✓	×
−0.05(0.7)	✓	✓	✓	✓	×
−0.15(0.6)	✓	✓	✓	✓	✓
−0.25(0.5)	×	✓	✓	✓	✓

[a] ✓: Closed-loop stable

[b] ×: Closed-loop unstable

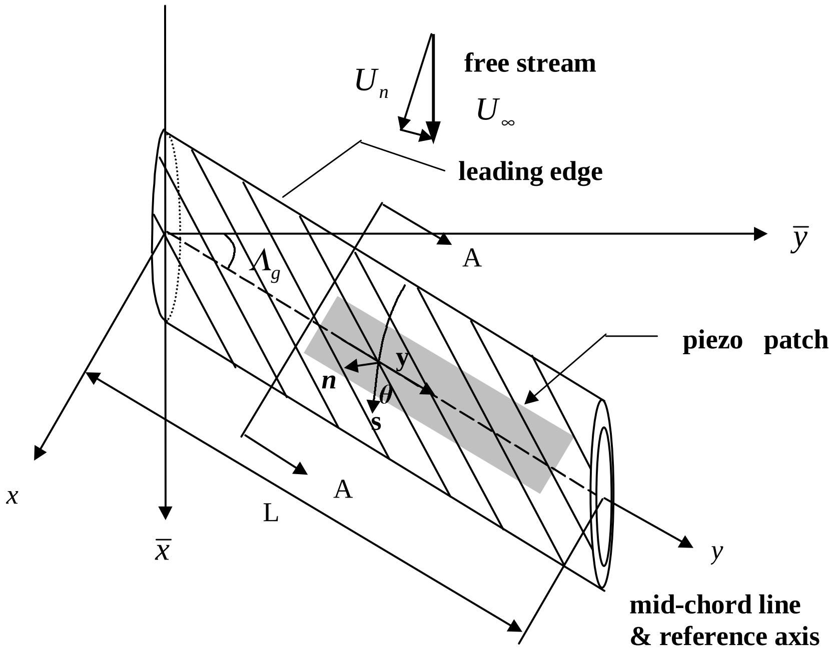

Figure 4.1: Geometry of the smart aircraft wing modeled as a thin-walled beam.

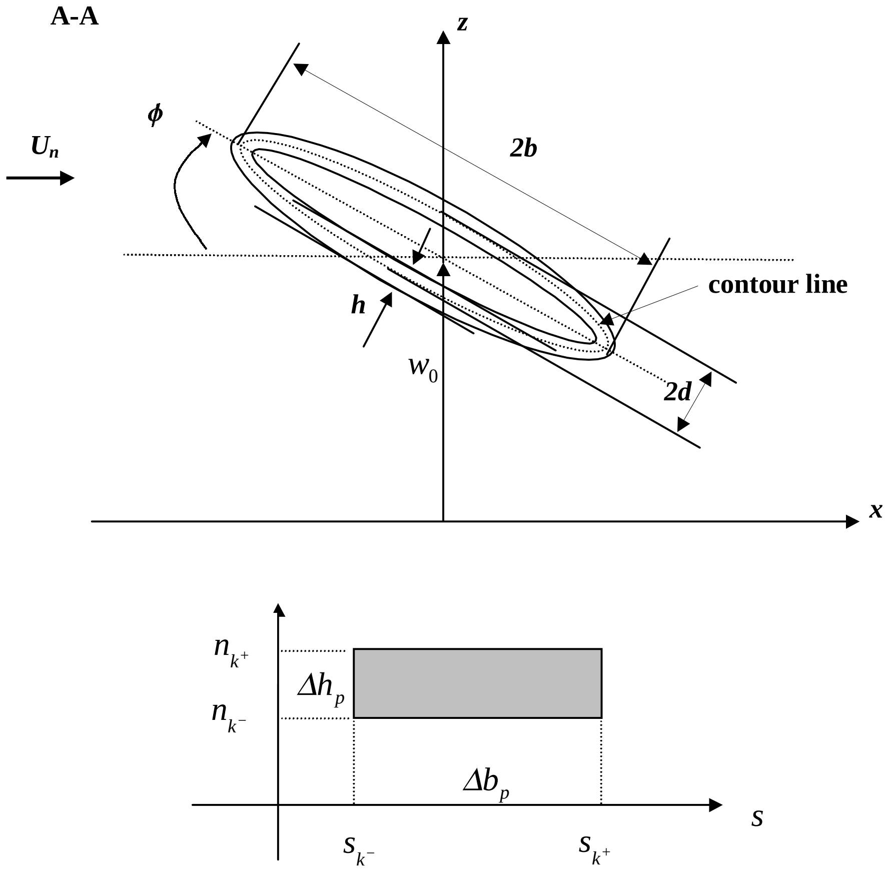

Figure 4.2: Geometric specification of the normal cross-section of the host wing and the piezoceramic patch.

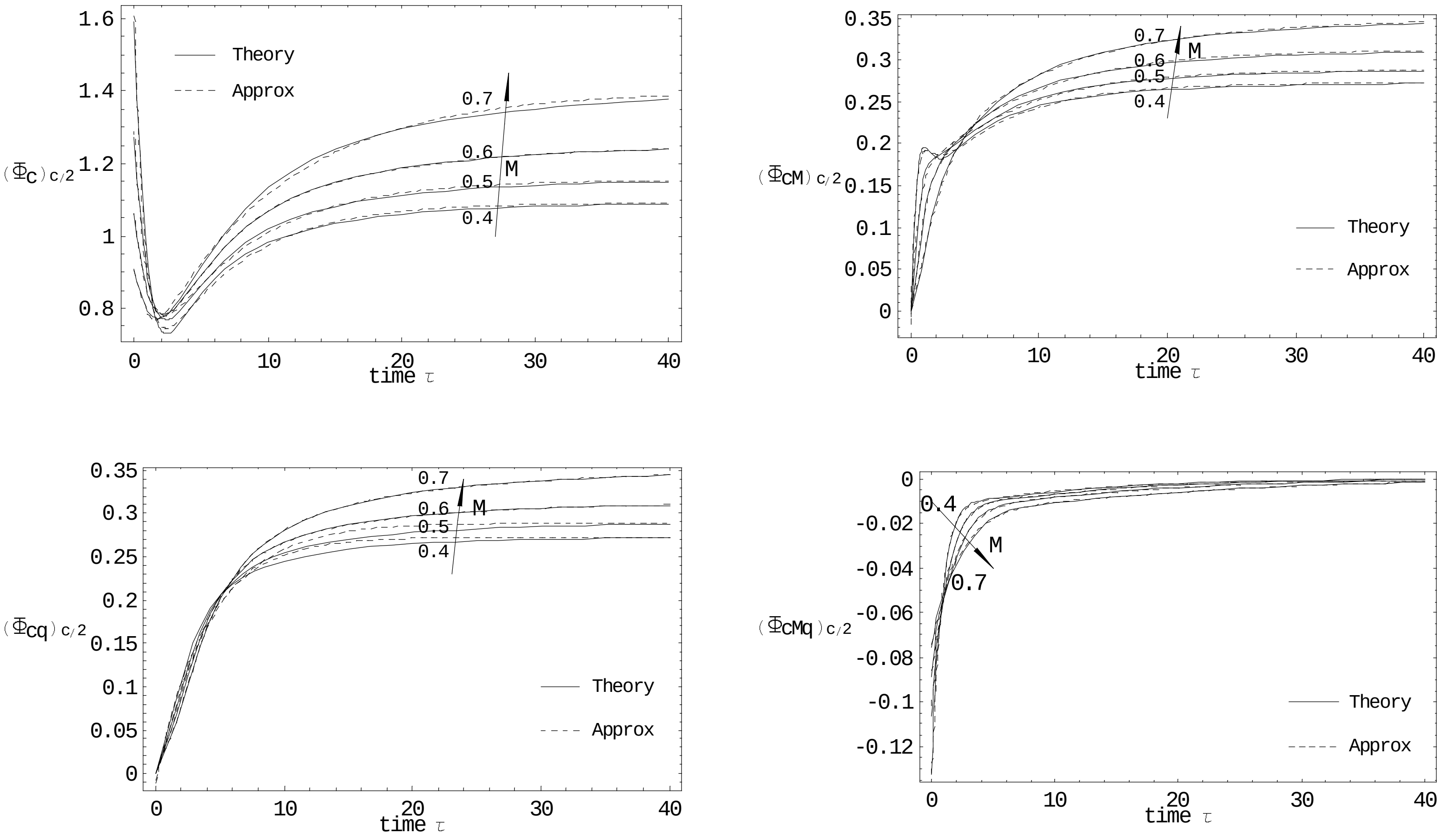

Figure 4.3: Curve fitting of the unsteady 2-D subsonic aerodyanmic indicial functions.

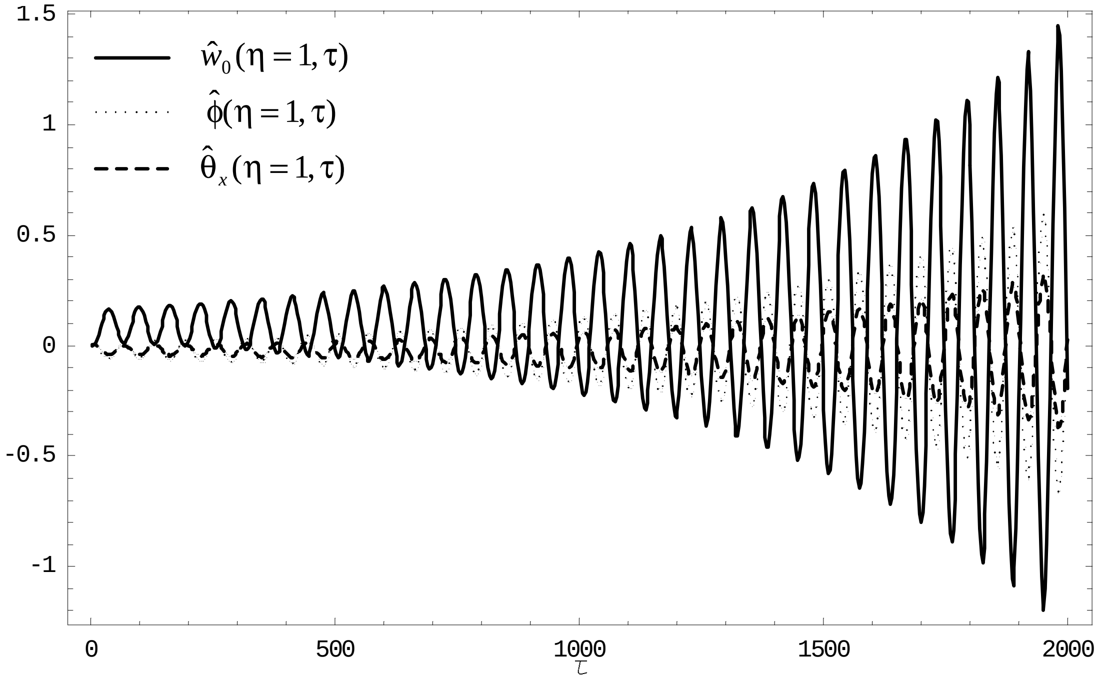

Figure 4.4: Open-loop aeroelastic response(deflection) to a sharp-edged gust ($V_G = 10m/s$, $M_{flight} = 0.7$, $\theta_{flight} = 105^0$).

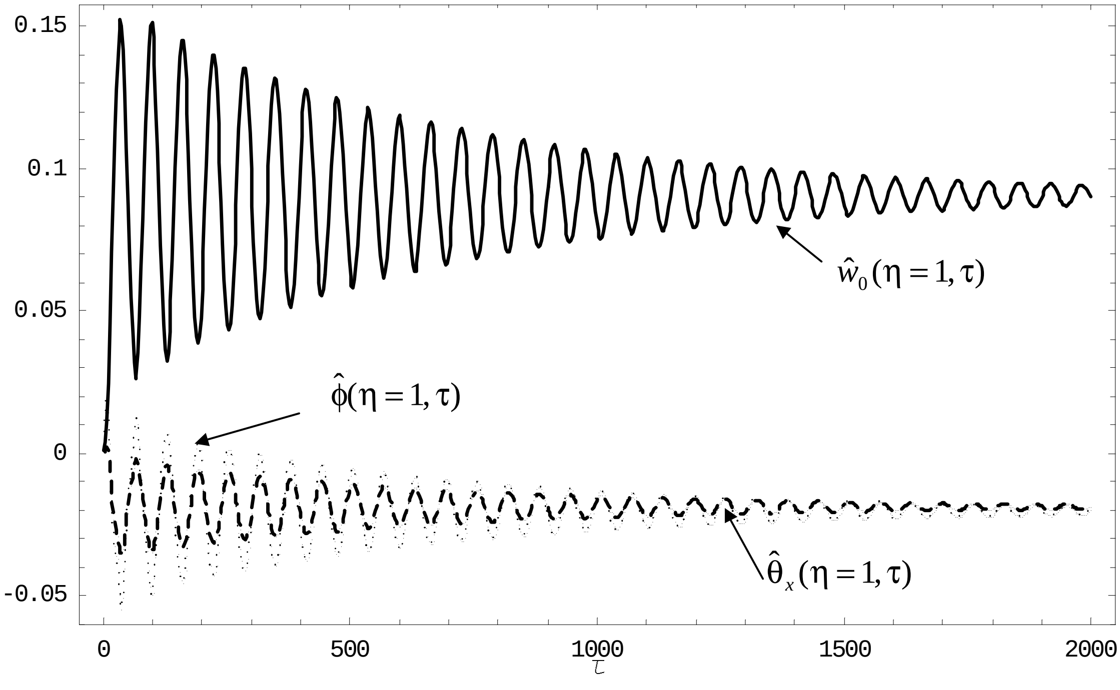

Figure 4.5: Closed-loop aeroelastic response(deflection) to a sharp-edged gust ($V_G = 10m/s$, $M_{flight} = M_{design} = 0.7$, $\theta_{flight} = \theta_{design} = 105^0$, $r_c = 10^{-9}$, $\mu = 10^{10}$).

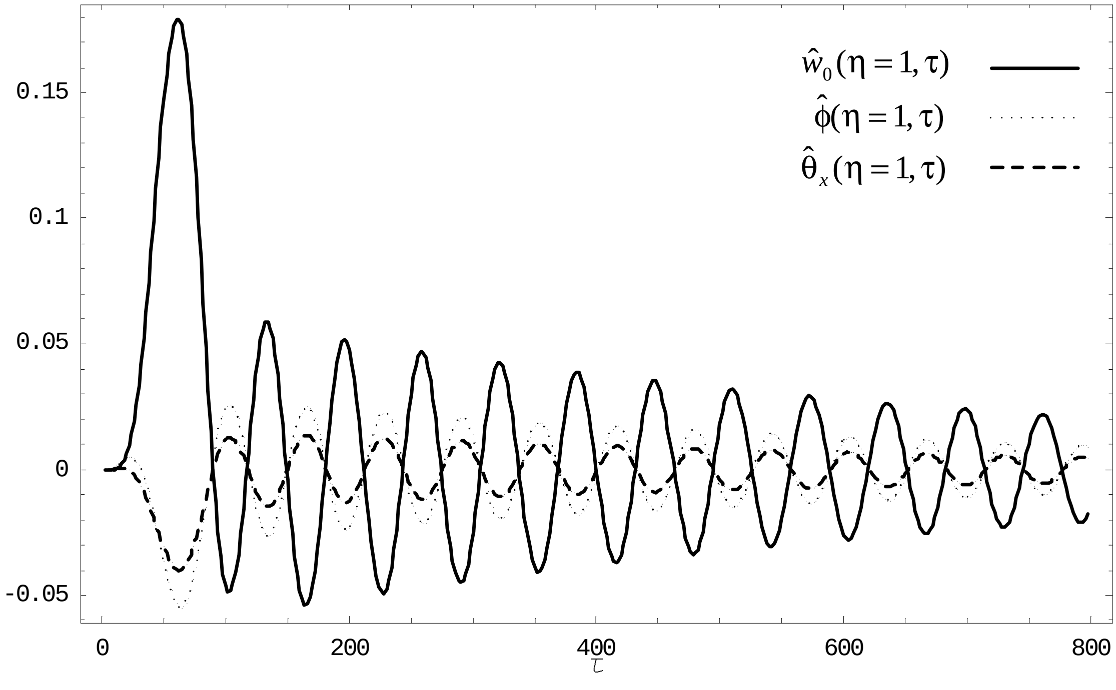

Figure 4.6: Closed-loop aeroelastic response(deflection) to a 1-COSINE gust ($V_G = 15m/s$, $\tau_p = 50$, $M_{flight} = M_{design} = 0.7$, $\theta_{flight} = \theta_{design} = 105^0$, $r_c = 10^{-9}$, $\mu = 10^{10}$).

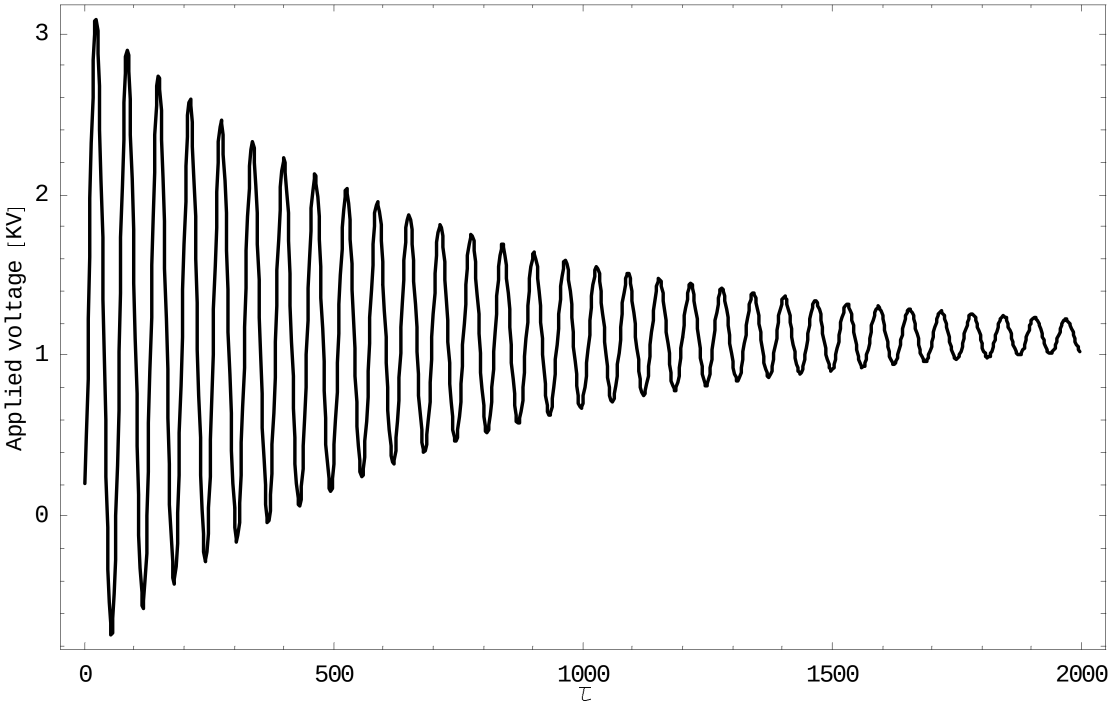

Figure 4.7: Applied voltage for a closed-loop aeroelastic system to a sharp-edged gust ($V_G = 10m/s$, $M_{flight} = M_{design} = 0.7$, $\theta_{flight} = \theta_{design} = 105^0$, $r_c = 10^{-9}$, $\mu = 10^{10}$).

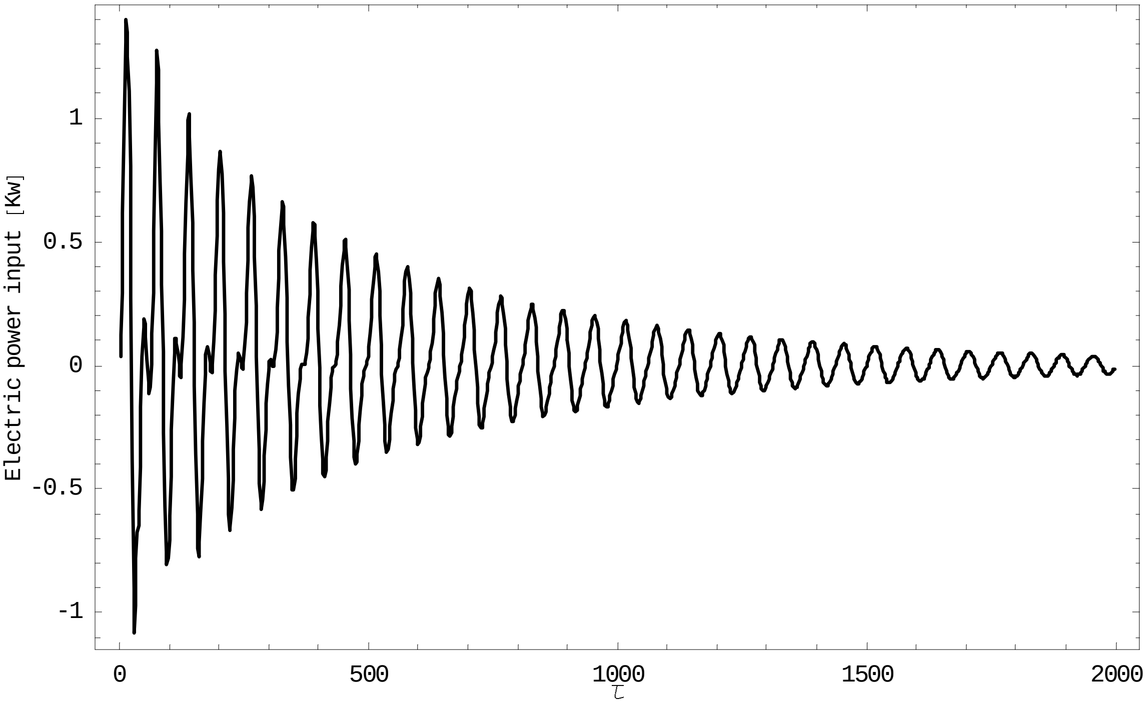

Figure 4.8: Electric power input for a closed-loop aeroelastic system to a sharp-edged gust ($V_G = 10m/s$, $M_{flight} = M_{design} = 0.7$, $\theta_{flight} = \theta_{design} = 105^0$, $r_c = 10^{-9}$, $\mu = 10^{10}$).

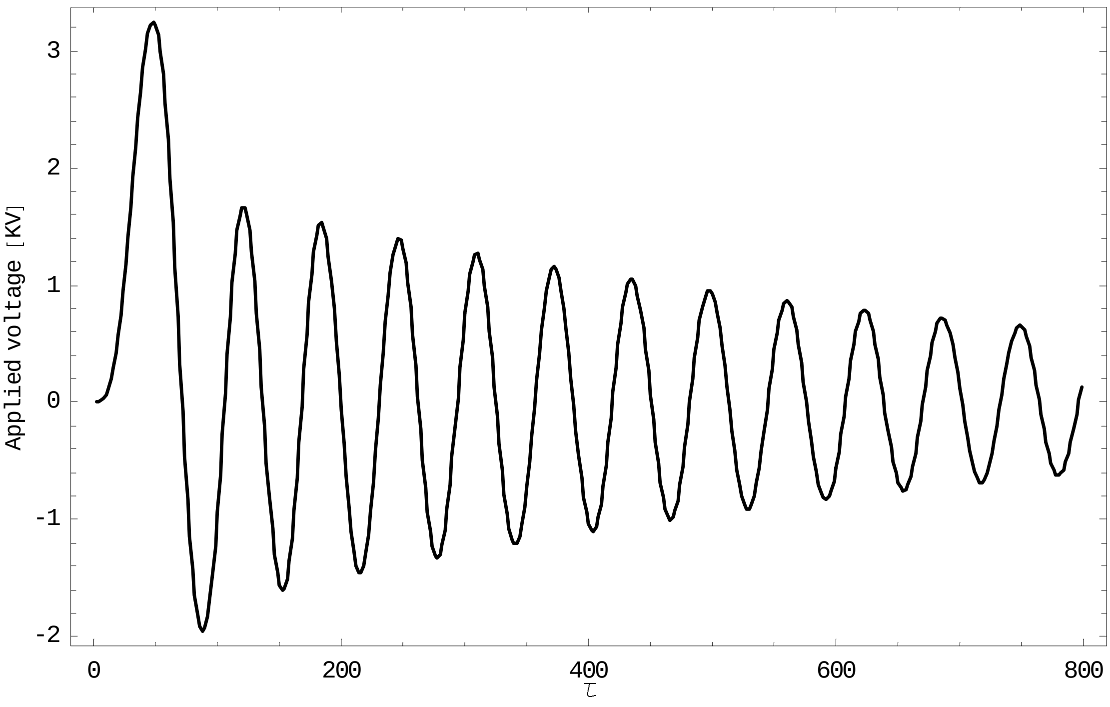

Figure 4.9: Applied voltage for a closed-loop aeroelastic system to a 1-COSINE gust ($V_G = 15m/s$, $\tau_p = 50$, $M_{flight} = M_{design} = 0.7$, $\theta_{flight} = \theta_{design} = 105^0$, $r_c = 10^{-9}$, $\mu = 10^{10}$).

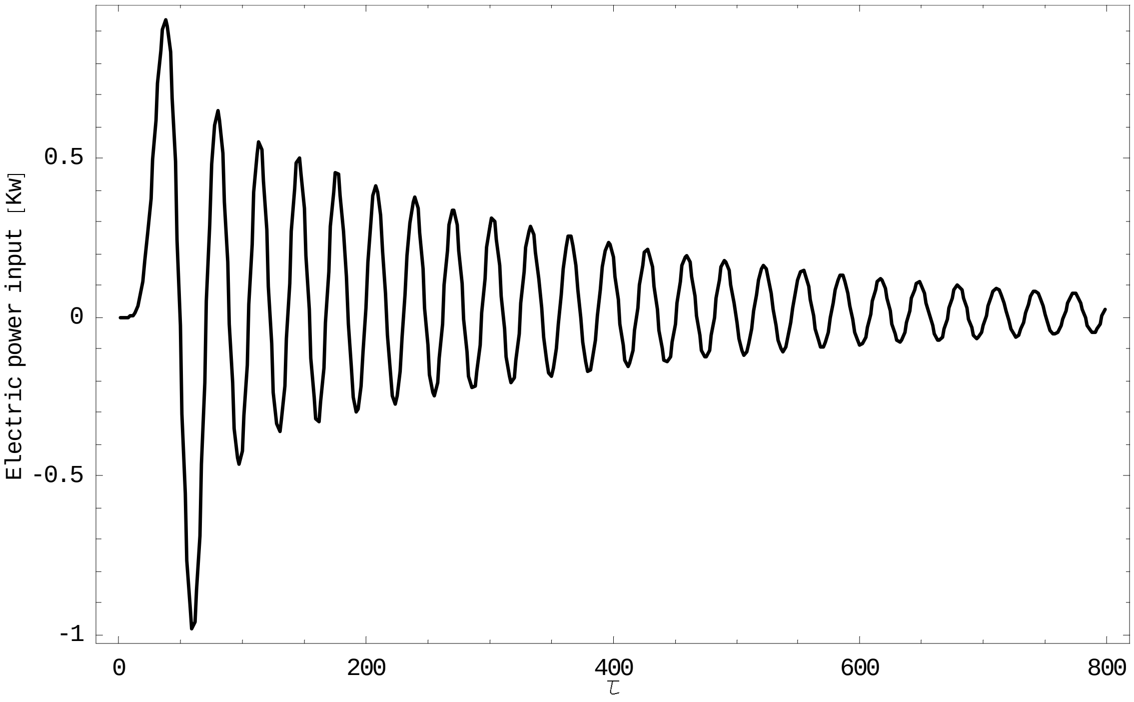

Figure 4.10: Electric power input for a closed-loop aeroelastic system to a 1-COSINE gust ($V_G = 15m/s$, $\tau_p = 50$, $M_{flight} = M_{design} = 0.7$, $\theta_{flight} = \theta_{design} = 105^0$, $r_c = 10^{-9}$, $\mu = 10^{10}$).

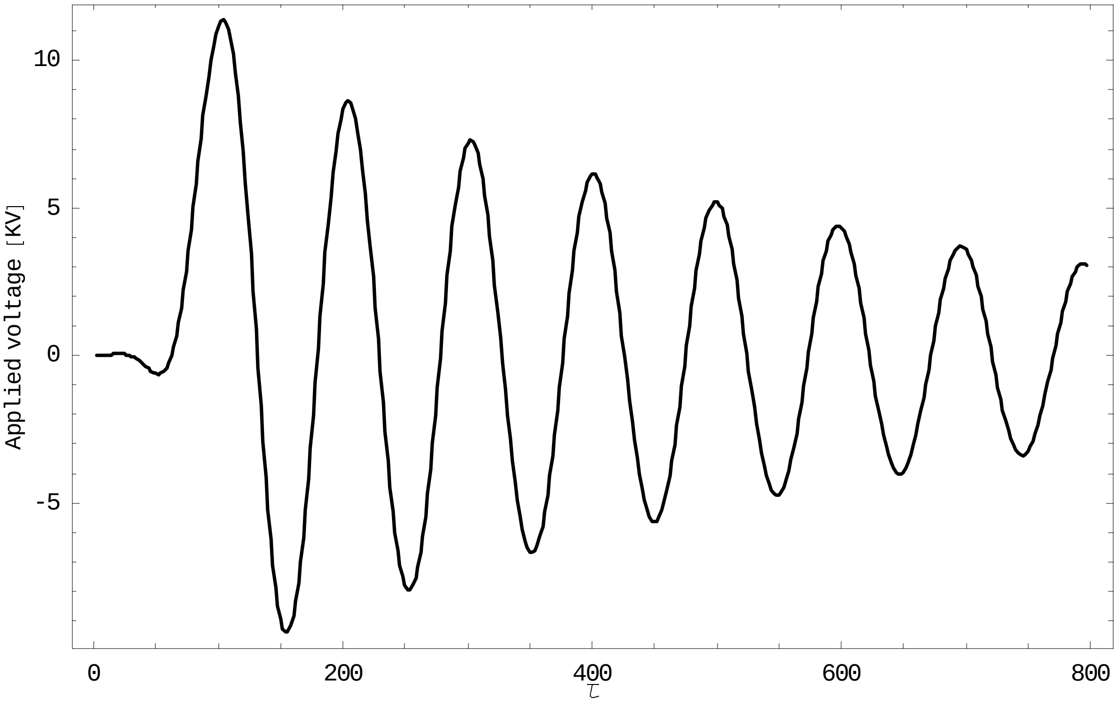

Figure 4.11: Applied voltage for the closed-loop aeroelastic system ($V_G = 10m/s$, $\tau_p = 50$, $M_{flight} = 0.77$, $\theta_{flight} = 135^0$, $M_{design} = 0.75$, $\theta_{design} = 105^0$, $r_c = 10^{-10}$, $\mu = 10^{10}$).

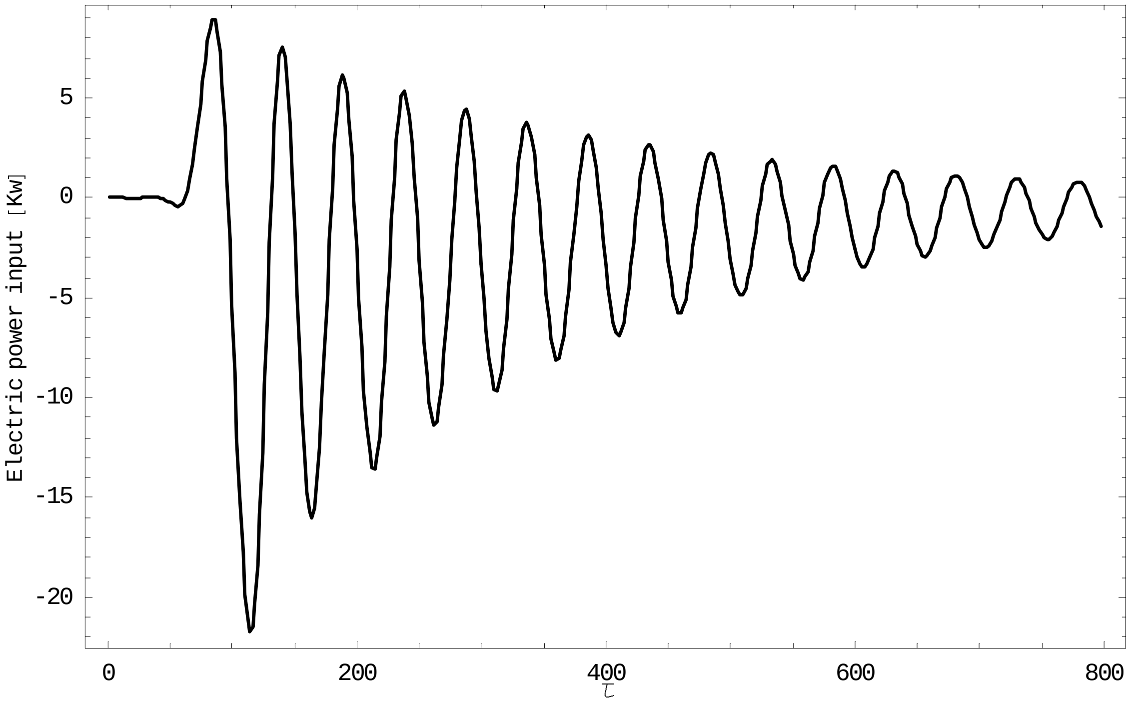

Figure 4.12: Electric power input for the closed-loop aeroelastic system ($V_G = 10m/s$, $\tau_p = 50$, $M_{flight} = 0.77$, $\theta_{flight} = 135^0$, $M_{design} = 0.75$, $\theta_{design} = 105^0$, $r_c = 10^{-10}$, $\mu = 10^{10}$).

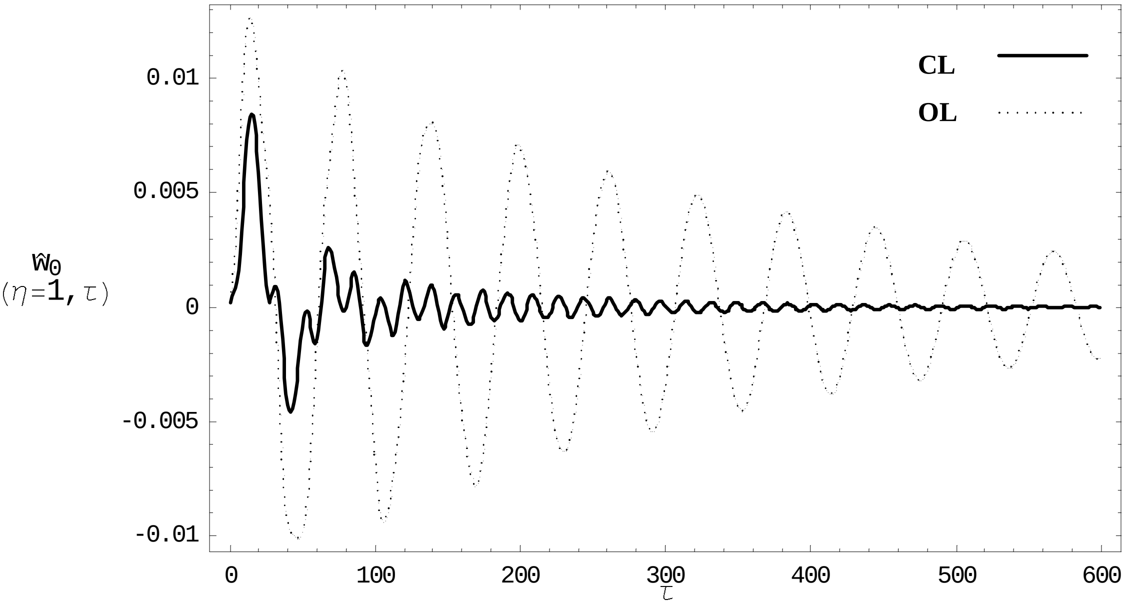

Figure 4.13: Comparison of controlled vs. uncontrolled aeroelastic responses to a blast load ($\hat{P}_m = 10^{-3}$, $\tau_p = 2.5$, $M_{flight} = 0.6$, $M_{design} = 0.75$, $\theta_{flight} = \theta_{design} = 105^0$, $r_c = 10^{-10}$, $\mu = 10^{10}$).

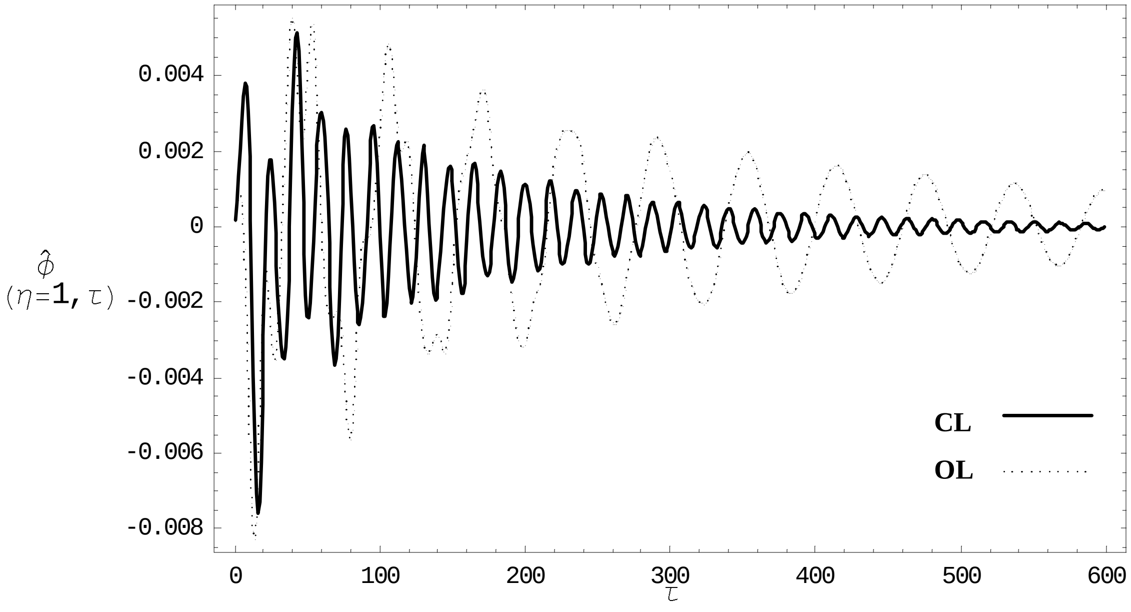

Figure 4.14: Comparison of controlled vs. uncontrolled aeroelastic responses to a blast load ($\hat{P}_m = 10^{-3}$, $\tau_p = 2.5$, $M_{flight} = 0.6$, $M_{design} = 0.75$, $\theta_{flight} = \theta_{design} = 105^0$, $r_c = 10^{-10}$, $\mu = 10^{10}$).

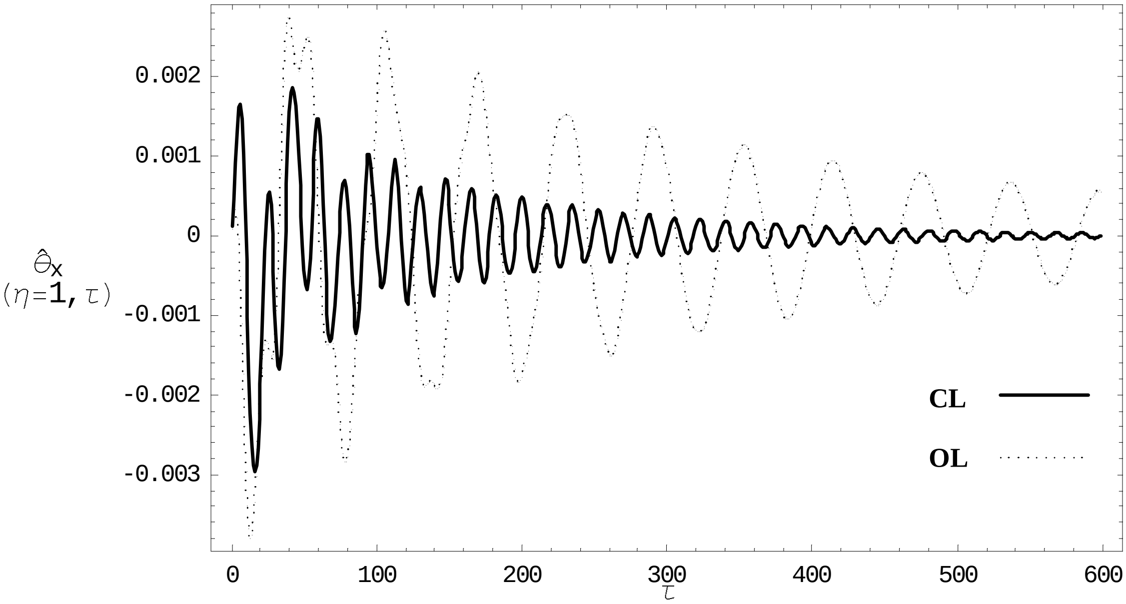

Figure 4.15: Comparison of controlled vs. uncontrolled aeroelastic responses to a blast load ($\hat{P}_m = 10^{-3}$, $\tau_p = 2.5$, $M_{flight} = 0.6$, $M_{design} = 0.75$, $\theta_{flight} = \theta_{design} = 105^0$, $r_c = 10^{-10}$, $\mu = 10^{10}$).

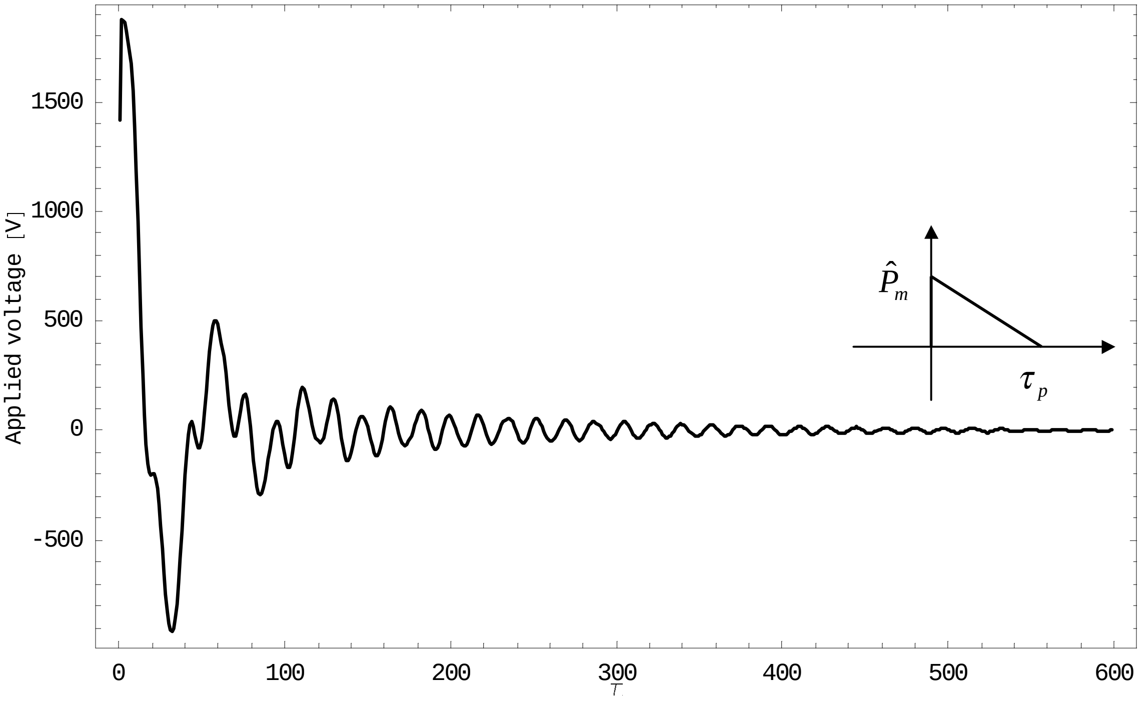

Figure 4.16: Applied voltage for the controlled aeroelastic system to a blast load ($\hat{P}_m = 10^{-3}$, $\tau_p = 2.5$, $M_{flight} = 0.6$, $M_{design} = 0.75$, $\theta_{flight} = \theta_{design} = 105^0$, $r_c = 10^{-10}$, $\mu = 10^{10}$).

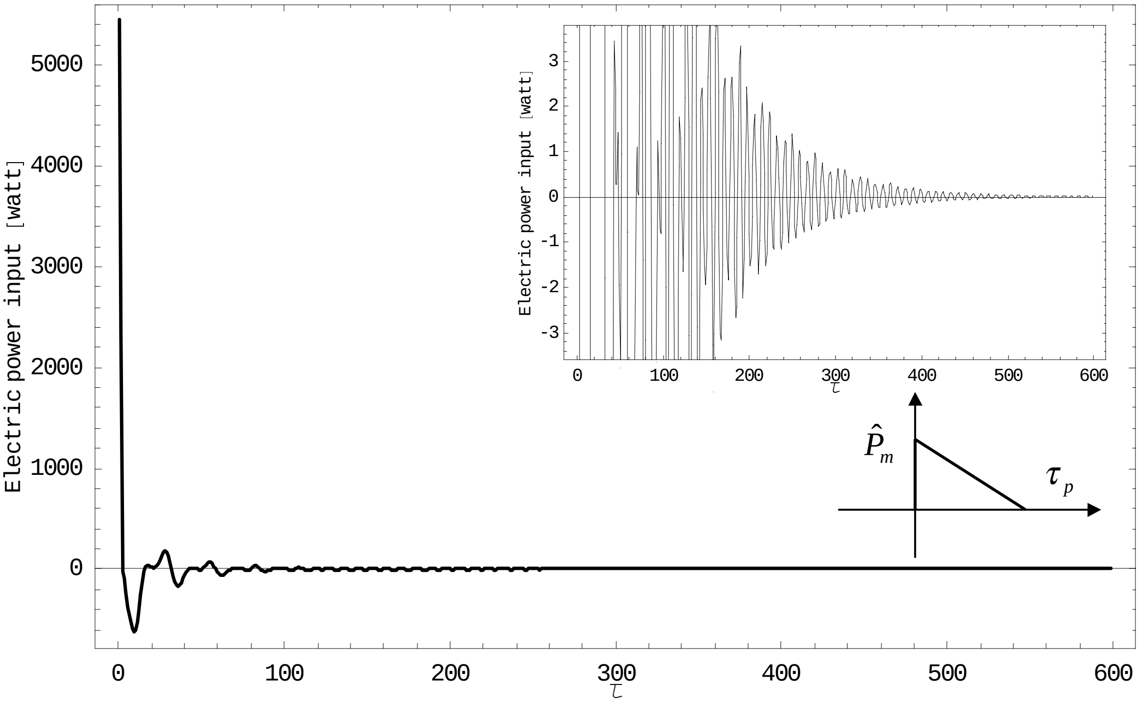

Figure 4.17: Electric power input for the controlled aeroelastic system to a blast load ($\hat{P}_m = 10^{-3}$, $\tau_p = 2.5$, $M_{flight} = 0.6$, $M_{design} = 0.75$, $\theta_{flight} = \theta_{design} = 105^0$, $r_c = 10^{-10}$, $\mu = 10^{10}$).

Chapter 5

Investigation of Shunt Damping on the Aeroelastic Behavior of an Advanced Aircraft Wing

Abstract

Piezoelectric shunt circuits are incorporated into an anisotropic composite aircraft wing and the role of the damping thereby induced is investigated in the context of aeroelastic tailoring. It is revealed that the anisotropy of the host structure has a fundamental influence on the efficiency of the shunt damping. Improper configuration of the shunt circuit may render the otherwise aeroelastic stable system unstable. Due to the potential catastrophic outcomes by flutter, it is advised that special attention should be given to passive damping of aeroelastic systems via shunt circuits.

5.1 Introduction

Damping augmentation via piezoelectric shunt circuit (shunt damping) has been extensively explored towards vibration reduction and control [1, 6–8, 10, 18–21]. It has also been extended to control the aeroelastic response [2, 13, 14]. Unfortunately, as revealed in this chapter, damping augmentation is no longer a *conservative* approach for aeroelastic control, since aeroelastic systems can absorb energy from the ambient flow. Improper configuration of the shunt circuit may induce aeroelastic instability.

5.2 Modeling

5.2.1 Governing Equations in State-Space Form

A single-cell, closed cross-section thin-walled beam model is adopted towards modeling the aircraft wing. The circumferentially asymmetric stiffness (CAS) lay-up [11] is used to generate the preferred bending-twist elastic coupling. A pair of piezoceramic (PZT4) patches are symmetrically mounted on the lower and upper surfaces of the host wing. It is assumed that the poling direction is along the normal of the mounted surface. Parallel RC and parallel RL circuits are introduced to dissipate the converted strain energy. It is assumed that the piezo. patch mounted on the upper surface of the thin-walled beam is connected to a circuit with the same configuration as that of the patch mounted on the lower surface. The geometry of the wing and upper piezoceramic patch are displayed in Figs. 5.1 and 5.2. Notice the introduction of the piezo. patch pair specified as above does not change the CAS elastic coupling characteristics, since the the plane of isotropy of the patch is in $s-y$ plane (see Fig. 5.1).

From the piezoelectric constitutive equations, we get the expressions of the electric charge $\hat{Q}_c$ and current $\hat{I}_c$ that pass across the electrode of the *upper* patch:

$$\hat{Q}_c^+ = \mathcal{A}_Q^+ \hat{\mathbf{x}} + C_p \hat{V}_c^+ \tag{5.1a}$$

$$\hat{I}_c^+ = \mathcal{A}_I^+ \hat{\mathbf{x}} + \frac{U_n}{b} C_p \dot{\hat{V}}_c^+ \tag{5.1b}$$

in which, $\mathcal{A}_I^+$ is a $1 \times (2+l)m$ matrix, C_p is the reduced capacity of the *electrode pair* connected to the upper patch. For the piezoceramic patch mounted on the lower surface, similar results can be derived, except the superscript ”$^+$” is replaced by ”$^-$”. If we further explore the fact that for CAS layup and the symmetric mounting of the *patch pair* and the same configuration of shunt circuits for each patch, we get: $\mathcal{A}_Q^- = -\mathcal{A}_Q^+$, $\mathcal{A}_I^- = -\mathcal{A}_I^+$, then the following analog follows: $\hat{V}_c^+ \leftrightarrow -\hat{V}_c^-$, $\hat{I}_c^+ \leftrightarrow -\hat{I}_c^-$, i.e., whenever the voltage induced on the shunt circuit for the upper patch is $\hat{V}_c$, the corresponding voltage induced on the shunt circuit of the lower patch is $-\hat{V}_c$ (provided that $\hat{V}_c^+(0) = -\hat{V}_c^-(0)$). Therefore, in the following derivation, only the quantities realted to the upper patch will be referred to.

We start from the state-space form of the aeroelastic governing equations (see Eqs. 4.31a, b):

$$\dot{\hat{\mathbf{x}}} = \mathcal{A}_x\hat{\mathbf{x}} + \mathcal{B}_d\hat{\mathbf{w}}_d + \mathcal{B}_c\hat{V}_c + \mathcal{B}_d^0(\tau)\hat{\mathbf{x}}(0) \tag{5.2a}$$

With initial conditions:

$$\hat{\mathbf{x}}(0) = \hat{\mathbf{x}}_0 \tag{5.2b}$$

where $\hat{\mathbf{x}}$ is a $(2+l)m \times 1$ state vector, $\mathcal{A}_x$, $\mathcal{B}_d^0$ are $(2+l)m \times (2+l)m$ matrices, $\mathcal{B}_d$ is a $(2+l)m \times m$ matrix, $\hat{\mathbf{w}}_d$ is a $m \times 1$ the generalized disturbance vector, $\mathcal{B}_c$ is a $(2+l)m \times 1$ vector, $\hat{V}_c$ is the induced voltage on the piezoceramic patch mounted on the upper surface of the host wing. The details of these quantities have been provided in Eq. 4.30.

When the RC circuit displayed in Fig. 5.3 is introduced, by applying the Kirchhoff's current law (Ref. [17], pp. 14), we get:

$$-\frac{\hat{V}_c}{R_c} - C_c\frac{U_n}{b}\dot{\hat{V}}_c = \hat{I}_c \tag{5.3}$$

Combining Eqs. (5.1b, 5.3), we get:

$$\dot{\hat{V}}_c = \frac{-1}{\frac{U_n}{b}[C_c + C_p]}\mathcal{A}_I\hat{\mathbf{x}} - \frac{1}{\frac{U_n}{b}R_c[C_c + C_p]}\hat{V}_c \tag{5.4}$$

Similarly, when the RL circuit displayed in Fig. 5.4 is introduced, we get:

$$\left\{\begin{array}{c}\dot{\hat{V}}_c\\ \ddot{\hat{V}}_c\end{array}\right\}=\left[\begin{array}{cc}0 & 1\\ \dfrac{-1}{(U_n/b)C_p}(\mathcal{A}_I\mathcal{B}_c+\dfrac{1}{L_c(U_n/b)}) & \dfrac{-1}{(U_n/b)C_pR_c}\end{array}\right]\left\{\begin{array}{c}\hat{V}_c\\ \dot{\hat{V}}_c\end{array}\right\}+\left\{\begin{array}{c}\mathbf{0}_{1\times(2+l)m}\\ \dfrac{-1}{(U_n/b)C_p}\mathcal{A}_I\mathcal{A}_x\end{array}\right\}\hat{\mathbf{x}}$$
$$+\left\{\begin{array}{c}\mathbf{0}_{1\times m}\\ \dfrac{-1}{(U_n/b)C_p}\mathcal{A}_I\mathcal{B}_d\end{array}\right\}\hat{\mathbf{w}}_d+\left\{\begin{array}{c}\mathbf{0}_{1\times(2+l)m}\\ \dfrac{-1}{(U_n/b)C_p}\mathcal{A}_I\mathcal{B}^0_d\end{array}\right\}\hat{\mathbf{x}}_0 \tag{5.5}$$

Combining Eqs. 5.2a and 5.4 or 5.2a and 5.5, we get the shunted aeroelastic governing equations corresponding to the RC or RL circuits. In a generic form, they can be written as

$$\dot{\hat{\mathbf{y}}}=\tilde{\mathcal{A}}_y\hat{\mathbf{y}}+\tilde{\mathcal{B}}_y\hat{\mathbf{w}}_d+\tilde{\mathcal{B}}^0_y\hat{\mathbf{y}}_0 \tag{5.6}$$

where state vector $\hat{\mathbf{y}}$ consists of $\hat{\mathbf{x}}$, $\hat{V}_c$ or $\hat{\mathbf{x}}$, $\hat{V}_c$, $\dot{\hat{V}}_c$.

5.2.2 Initial Conditions of $\hat{V}_c$ and $\dot{\hat{V}}_c$

The initial conditions $\hat{V}_c$ and $\dot{\hat{V}}_c$ need to be determined from the initial conditions of the electrode when the shunt circuit is connected to it. Specifically, if $\hat{\mathbf{x}}_0$ is set when the electrode is in open-circuit condition, i.e., $\hat{Q}_c(0)=0$ (see Ref. [16]), $\hat{I}_c(0)=0$, from Eqs. 5.1a and 5.1b, we get:

$$\hat{V}_c(0)=-\frac{1}{C_p}\mathcal{A}_Q\hat{\mathbf{x}}(0);\qquad \dot{\hat{V}}_c(0)=\frac{-1}{(U_n/b)C_p}\mathcal{A}_I\hat{\mathbf{x}}(0) \tag{5.7}$$

if $\hat{\mathbf{x}}_0$ is set when the electrode is in short-circuit condition, by definition, we get $\hat{V}_c(0)=0$, $\dot{\hat{V}}_c(0)=0$.

5.3 Numerical Simulations and Discussion

The capability of shunt-damping on the aeroelastic behavior of an anisotropic composite aircraft wing is investigated in this section. Material specifications of the host structure

(Graphite/Epoxy composite) and the piezoceramic patch are listed in Table 5.1; geometric specifications of the wing is in Table 5.2. In the numerical simulation, the biconvex cross section is adopted. For unsteady subsonic aerodynamic loads, the indicial function based approach [4, 9, 12] is adopted and for each of the 4 indicial function, 3 aerodynamic lag terms are used, i.e., $l = 3$. The first 3 structural modes are actually used in the simulation, i.e., $m = 3$. Notice that due to large amplitudes of the coefficient matrices $\dfrac{1}{U_n/b[C_c + C_p]}\mathcal{A}_I$ and $\dfrac{1}{(U_n/b)C_p}\mathcal{A}_I\mathcal{A}_x$, the system matrix $\tilde{\mathcal{A}}_y$ is not well-conditioned. In order to overcome numerical accuracy problem, Schur decomposition (Ref. [5], pp. 219-210) provided by Mathematica® is used for the matrix inversion. Discrete-time transition matrix based scheme (Ref. [15], pp. 41) is adopted for the temporal discretization of Eq. 5.6. In the actual simulation, it is assumed $\hat{\mathbf{x}}_0 = 0$.

Figures 5.5, 5.6 and 5.7, 5.8, 5.9 display the effect of shunt-damping by a *RC* circuit on enhancing the dynamic aeroelastic response subject to a 1-COSINE gust and a sonic boom, respectively. Figs. 5.10 and 5.11 display the voltage induced on the piezo. patch, while Figs. 5.12 and 5.13 display the energy relation between the *electric* energy converted from *strain* energy and the electric energy actually dissipated (in form of heat) by the resistor. Three observations should be noted: (1)In the case $\theta = 180^0$ (or 0^0), shunt-damping is quite efficient to reduce the transient response intensity and the transient duration. In Fig. 5.5, the maximum peak amplitude of vibration is reduced by about 17%, while in Fig. 5.6, the peak amplitude of acceleration is reduced by about 29% and in all the cases, the transient duration is much less than the counterpart in which the piezo. effect is not accounted for. (2)The energy conversion between strain energy and electric energy is unidirectional (in the presence of the inherent capacity of the electrode and the capacitor in the shunt circuit), this is due to $\hat{P}_{electric}(\tau) \leq 0,\ \text{for all}\ \tau > 0$. (3)Almost all the electric energy converted from the strain energy is dissipated by the resistor.

However, the efficiency of shunt damping on enhancing the aeroelastic behavior may be significantly changed by the alteration of ply orientation, as displayed in Table 5.3. It is observed that in the case $\theta = 180^0$, the damping is the most efficient, while in the case

$\theta = 105^0$, the damping almost has no effect. To be even worse, in the case $\theta = 120^0$, $R_c = 900\,\Omega$, and $C_c = 10^{-9}\,F$, the aeroelastic becomes unstable (onset of flutter occurs). Figs. 5.14, 5.15 and 5.16 display the simulation results for this case. It is remarkable to notice that $\hat{P}_{electric}$ is still negative, implying that the strain energy is unidirectionally converted to the electric energy and almost all the converted electric energy is dissipated by the resistor in the form of heat. From the first principle of thermodynamics, the ultimate energy is provided by the ambient flow. It is interesting to note that analogous to the effect of shunt damping on the aeroelastic response in the context of aeroelastic tailoring, Ref. [3] points out that the *nominal* open-loop damping can significantly influence the closed-loop response and that poor damping model may cause the nominally stable system actually unstable.

5.4 Conclusion

The shunt damping on the dynamic aeroelastic behavior of an anisotropic composite wing is investigated. The numerical simulations reveal that ply orientation has a fundamental influence on the efficiency of the damping. Damping augmentation no longer constitutes a *conservative* approach towards vibration control of the aeroelastic system and improper configuration of the shunt circuit may render the otherwise aeroelastic stable system unstable.

5.5 References

[1] G. S. Agnes. Development of a Modal Model for Simultaneous Active and Passive Piezoelectric Vibration Suppression. *Journal of Intelligent Material Systems and Structures*, 6:482–487, July 1995.

[2] G. S. Agnes and S. Mall. Structural Integrity Issues During Piezoelectric Vibration Suppression of Composite Structures. *Composites PartB: Engineering*, 30:727–738, 1999.

[3] H. T. Banks and D. J. Inman. Significance of Modeling Internal Damping in the Control of Structures. *Journal of Guidance, Control and Dynamics*, 15(6):1509–1512, 1992.

[4] R. L. Bisplinghoff, H. Ashley, and R. L. Halfman. *Aeroelasticity.* Dover Publications, New York, 1996.

[5] G. H. Golub. *Matrix Computations.* The Johns Hopkins University Press, Blatimore, MD, 1983.

[6] N. W. Hagood and E. F. Crawley. Experimental Investigation of Passive Enhancement of Damping for Space Structures. *Journal of Guidance, Control and Dynamics*, 14(6):1100–1109, 1991.

[7] M. J. Lam, D. J. Inman, and W. R. Saunders. Vibration Control Through Passive Constrained Layer Damping and Active Control. In *SPIE Proceedings of Smart Structures and Materials: Passive Damping and Isolation*, volume 3045, pages 60–69, San Diego, CA, 3-4, March 1997.

[8] H. H. Law, P. L. Rossiter, L. L. Koss, and G. P. Simon. Mechanisms in Damping of Mechanical Vibration by Piezoelectric Ceramic-Polymer Composite Materials. *Journal of Materials Science*, 30:2648–55, 1995.

[9] J. Leishman. Indicial lift approximations for two-dimensional subsonic flow as obtained from oscillatory measurements. *Journal of Aircraft*, 30(3):340–351, 1993.

[10] G. A. Lesieutre. Vibration damping and control using piezoelectric materials. *The Shock and Vibration Digest*, 30(3):187–195, May 1998.

[11] L. Librescu and O. Song. Behavior of thin-walled beams made of advanced composite materials and incorporating non-classical effects. *Applied Mechanics Reviews*, 44(11, part 2):S174–S180, 1991.

[12] P. Marzocca, L. Librescu, and G. Chiocchia. Unsteady aerodynamics in various flight speed regimes for flutter/dynamic response analyses. In *Proceeding of the 18th AIAA Applied Aerodynamic Conference*, Denver, CO, August 14-17 2000. AIAA-2000-4229.

[13] A.-M. R. McGowan. A Feasibility Study on Using Shunted Piezoelectrics to Reduce Aeroelastic Response. In *SPIE Proceedings of Smart Structures and Materials*, volume 3674, Newport Beach, CA, 2-4 March 1999.

[14] A.-M. R. McGowan, W. K. Wilkie, and R. W. Moses et al. Aeroservoelastic and Structural Dynamics Research on Smart Structures Conducted at NASA Langley Research Center. In *SPIE's* 5^{th} *Annual International Symposium on Smart Structures and Materials*, San Diego, CA, 1-5, March 1998.

[15] L. Meirovitch. *Principles and Techniques of Vibrations.* Prentice Hall, Upper Saddle River, New Jersey, 1997.

[16] V. Piéfort, N. Loix, and A. Preumont. Modeling of piezolaminated composite shells for vibration control. In *European Conference on Spacecraft Structures, Materials and Mechanical Testing*, Brunschweig, Germany, 4-6, Nov., 1998.

[17] G. Rizzoni. *Principles and Applications of Electrical Engineering.* Richard D. Irwin, Boston, MA, 1993.

[18] D. E. Veley and S. S. Rao. A Comparison of Active, Passive and Hybrid Damping Treatments in Structural Design. In *SPIE Proceedings of Smart Structures and Materials: Passive Damping and Isolation*, volume 2720, pages 184–195, San Diego, CA, 26-27, Feb 1996.

[19] K. W. Wang, J. S. Lai, and W. K. Yu. An Energy-Based Parametric Control Approach for Structural Vibration Suppression via Semi-Active Piezoelectric Networks. *Journal of Vibration and Acoustics*, 118:505–509, July 1996.

[20] S. Y. Wu. Piezoelectric Shunts with Parallel R-L Circuit for Structural Damping Vibration Control. In *SPIE Proceedings of Smart Structures and Materials: Passive Damping and Isolation*, volume 2720, pages 259–269, San Diego, CA, 26-27, Feb 1996.

[21] S. Y. Wu and A. S. Bicos. Structural Vibration Damping Experiments Using Improved Piezoelectric Shunts. In *SPIE Proceedings of Smart Structures and Materials: Passive Damping and Isolation*, volume 3045, pages 40–50, San Diego, CA, 3-4, March 1997.

Table 5.1: Material properties of piezoelectric and graphite/epoxy composite

Parameter	Piezoelectric	Graphite/Epoxy
Elastic constant, Gpa		
C_{11}	139.0	207.7
C_{12}	77.8	1.73
C_{13}	74.3	1.73
C_{22}	139.0	5.53
C_{23}	74.3	1.39
C_{33}	115.0	5.53
C_{44}	25.6	2.55
C_{55}	25.6	2.55
C_{66}	30.6	3.1
Density, Kg/m^3	7495	1528
Piezoelectric coupling constant, $N/(m \cdot V)$		
$e_{31} = e_{32}$	-5.20	–
e_{33}	15.1	–
$e_{15} = e_{24}$	12.7	–
Dielectric constant, $F/m \times 10^9$		
ϵ_{11}^S	6.75	–
ϵ_{22}^S	6.75	–
ϵ_{33}^S	5.87	–

Table 5.2: Geometric specification of the bare aircraft wing and the piezoceramic patches

Wing parameter	Value	Piezo. patch parameter	Value
Chord length $2b$, m	0.757	Width Δb_p, m	0.252
Depth $2d$, m	0.0997	Thickness Δh_p, m	2.03×10^{-3}
Wall thickness h_s, m	0.0203		
Number of layers	6	Number of layers	1
Lay-up	$[\theta_6]$, CAS		
Aspect ratio $\mathcal{R}$,	6	Length, m	2.27
Geometric sweep angle Λ_g, deg.	0		

Table 5.3: Influence of the shunt-damping on the integrated aeroelastic system ($M_{flight} = 0.6$, unit–$R_c : \Omega$; $C_c : F$; $L_c : H$)

Circuit config.	Structure-related eigenvalues		
	1^{st}	2^{nd}	3^{rd}
$\theta = 180^0$, RC/RL			
w/o piezo effect	$-0.0124 \pm 0.0826j$	$-0.00711 \pm 0.493j$	$-0.0136 \pm 0.497j$
$C_c : 10^{-9}$, $R_c : 10^{3.7}$	$-0.0258 \pm 0.0914j$	$-0.0136 \pm 0.498j$	$-0.0223 \pm 0.544j$
$C_c : 10^{-6}$, $R_c : 10^{3.7}$	$-0.0223 \pm 0.0922j$	$-0.0137 \pm 0.498j$	$-0.0149 \pm 0.530j$
$C_c : 10^{-9}$, $R_c : 10^{3}$	$-0.0156 \pm 0.0827j$	$-0.0134 \pm 0.498j$	$-0.0340 \pm 0.507j$
$L_c : 10^{-0.7}$, $R_c : 10^{3}$	$-0.0124 \pm 0.0826j$	$-0.00732 \pm 0.491j$	$-0.0134 \pm 0.497j$
$L_c : 10^{-0.7}$, $R_c : 10^{2.5}$	$-0.0124 \pm 0.0826j$	$-0.00755 \pm 0.491j$	$-0.0134 \pm 0.497j$
$L_c : 10^{-1.7}$, $R_c : 10^{2.5}$	$-0.0124 \pm 0.0826j$	$-0.00713 \pm 0.493j$	$-0.0135 \pm 0.497j$
$\theta = 120^0$, RC/RL			
w/o piezo effect	$-0.00573 \pm 0.176j$	$-0.00910 \pm 0.854j$	$-0.00925 \pm 1.21j$
$C_c : 10^{-9}$, $R_c : 10^{3.7}$	$-0.00527 \pm 0.175j$	$-0.00609 \pm 0.836j$	$-0.0115 \pm 1.23j$
$C_c : 10^{-9}$, $R_c : 10^{3}$	$-0.00554 \pm 0.176j$	$-1.00\times 10^{-5} \pm 0.843j$	$-0.0178 \pm 1.22j$
$C_c : 10^{-9}$, $R_c : 900$	$-0.00556 \pm 0.176j$	$\boxed{8.20 \times 10^{-5} \pm 0.844j}$	$-0.0182 \pm 1.22j$
$L_c : 10^{-0.7}$, $R_c : 10^{2.5}$	$-0.00573 \pm 0.176j$	$-0.00847 \pm 0.856j$	$-0.0113 \pm 0.120j$
$L_c : 10^{-1.7}$, $R_c : 10^{2.5}$	$-0.00573 \pm 0.176j$	$-0.00910 \pm 0.854j$	$-0.00926 \pm 1.21j$
$L_c : 10^{-0.7}$, $R_c : 10^{3}$	$-0.00573 \pm 0.176j$	$-0.00891 \pm 0.856j$	$-0.010 \pm 1.20j$
$\theta = 105^0$, RC/RL			
w/o piezo effect	$-0.00676 \pm 0.292j$	$-0.00997 \pm 0.958j$	$-0.00902 \pm 1.72j$
$C_c : 10^{-9}$, $R_c : 10^{3.7}$	$-0.00664 \pm 0.292j$	$-0.00914 \pm 0.952j$	$-0.00969 \pm 1.72j$
$C_c : 10^{-6}$, $R_c : 10^{3.7}$	$-0.00669 \pm 0.292j$	$-0.00955 \pm 0.953j$	$-0.00937 \pm 1.72j$
$C_c : 10^{-9}$, $R_c : 10^{3}$	$-0.00665 \pm 0.292j$	$-0.00720 \pm 0.954j$	$-0.0119 \pm 1.72j$
$L_c : 10^{-0.7}$, $R_c : 10^{2.5}$	$-0.00676 \pm 0.292j$	$-0.00968 \pm 0.958j$	$-0.0120 \pm 1.71j$
$L_c : 10^{-1.7}$, $R_c : 10^{2.5}$	$-0.00676 \pm 0.29j$	$-0.00997 \pm 0.958j$	$-0.00904 \pm 1.72j$
$L_c : 10^{-0.7}$, $R_c : 10^{3}$	$-0.00676 \pm 0.292j$	$-0.00988 \pm 0.958j$	$-0.0107 \pm 1.71j$

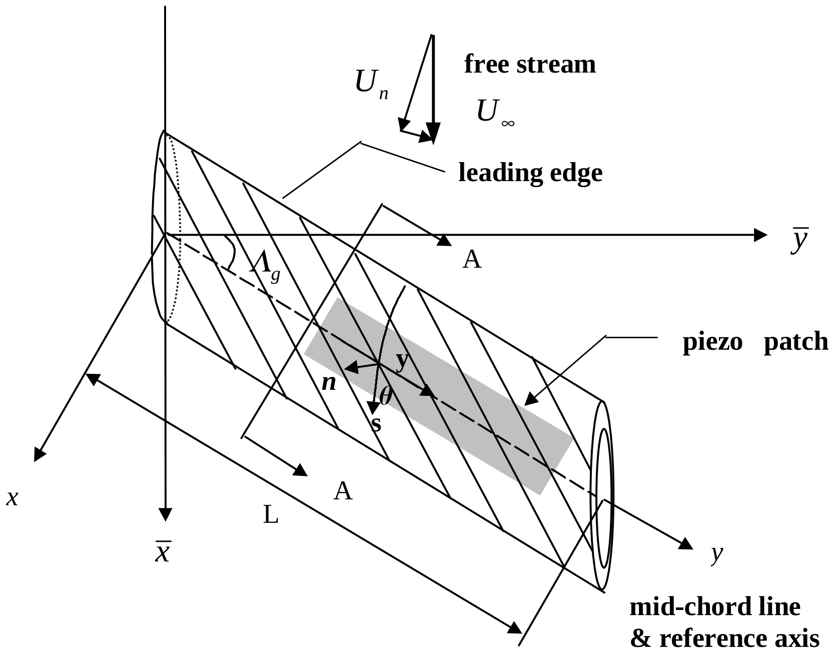

Figure 5.1: Geometry of the anisotropic composite aircraft wing modeled as a thin-walled beam.

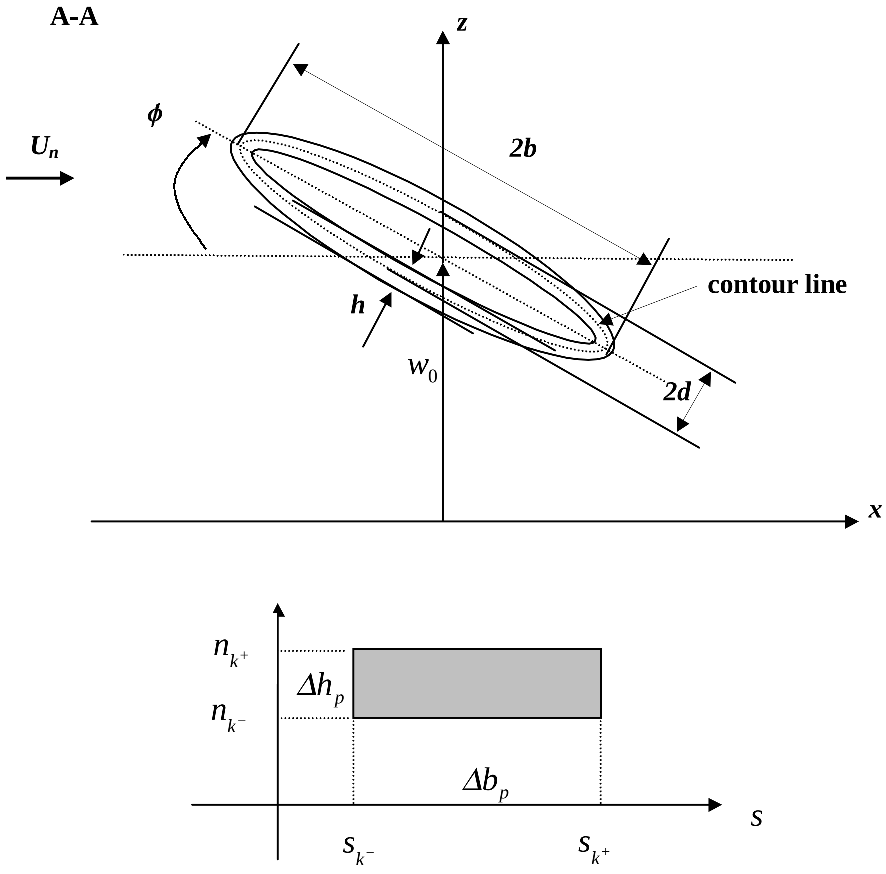

Figure 5.2: Geometric specification of the normal cross-section of the host wing and the piezoceramic patch.

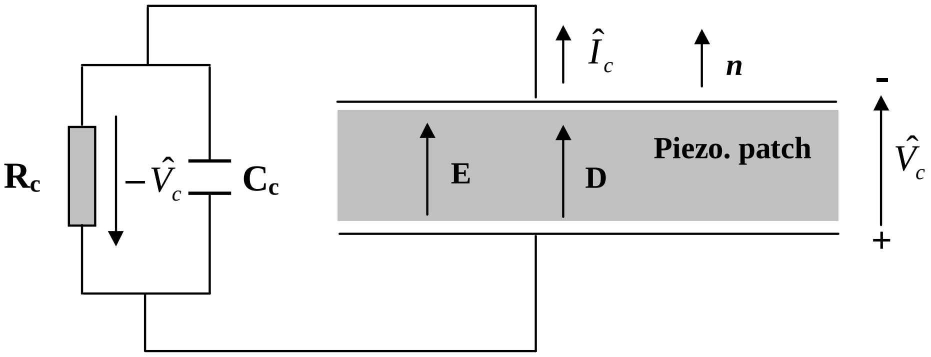

Figure 5.3: Configuration of *RC* circuit connected to the piezoceramic patch.

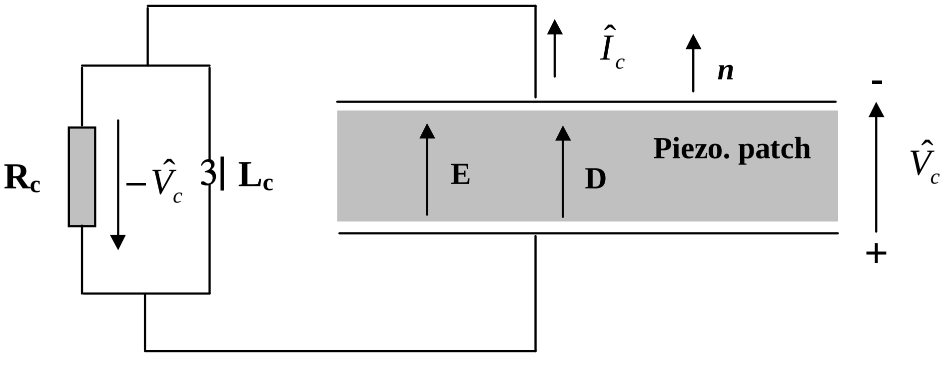

Figure 5.4: Configuration of *RL* circuit connected to the piezoceramic patch.

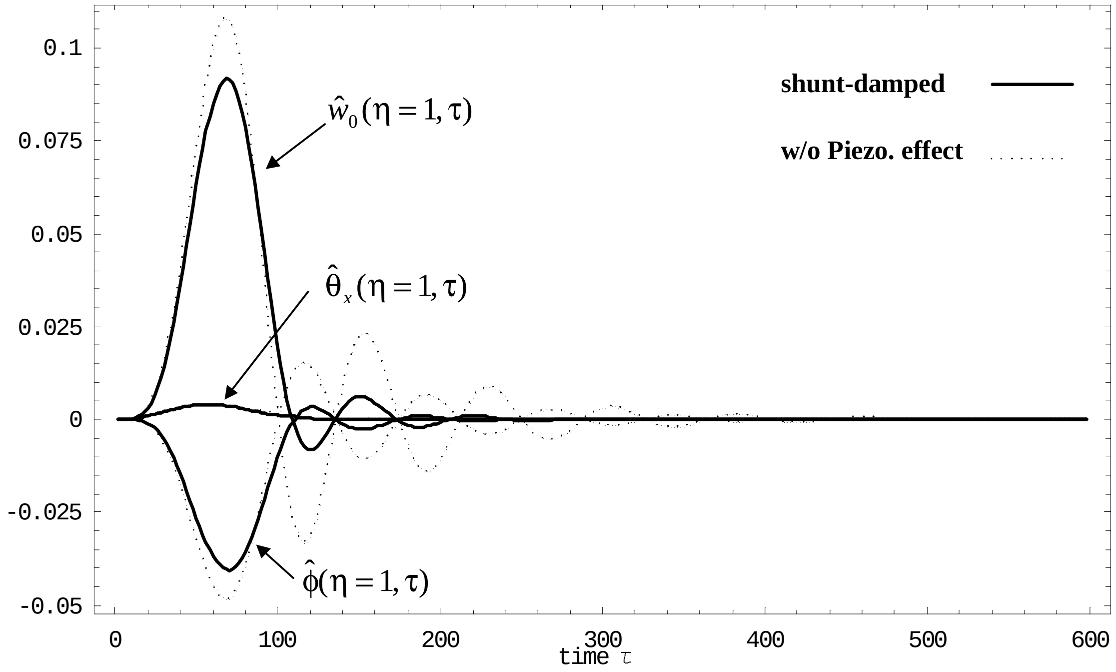

Figure 5.5: Effect of shunt-damping on the dynamic aeroelastic response to a 1-COSINE gust ($V_G = 5m/s$, $M_{flight} = 0.6$, $\theta = 180^0$, $\tau_p = 50$, $C_c = 10^{-9}\,F$, $R_c = 10^{3.7}\,\Omega$).

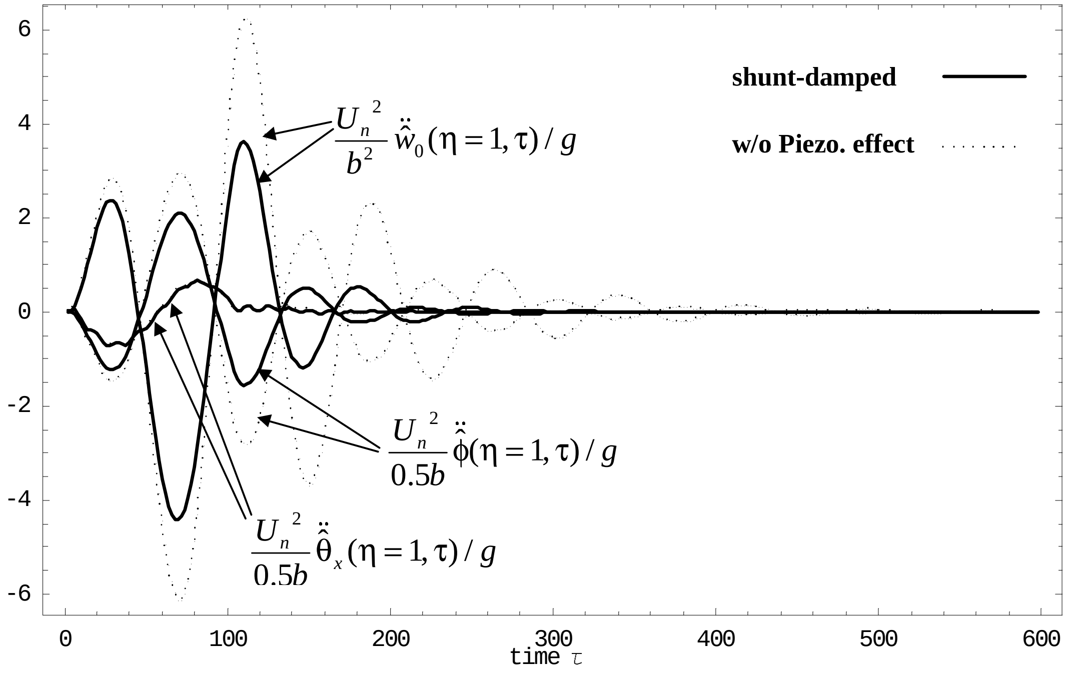

Figure 5.6: Effect of shunt-damping on the dynamic aeroelastic response to a 1-COSINE gust (acceleration) ($V_G = 5m/s$, $M_{flight} = 0.6$, $\theta = 180^0$, $\tau_p = 50$, $C_c = 10^{-9}\,F$, $R_c = 10^{3.7}\,\Omega$, g is the gravitational acceleration).

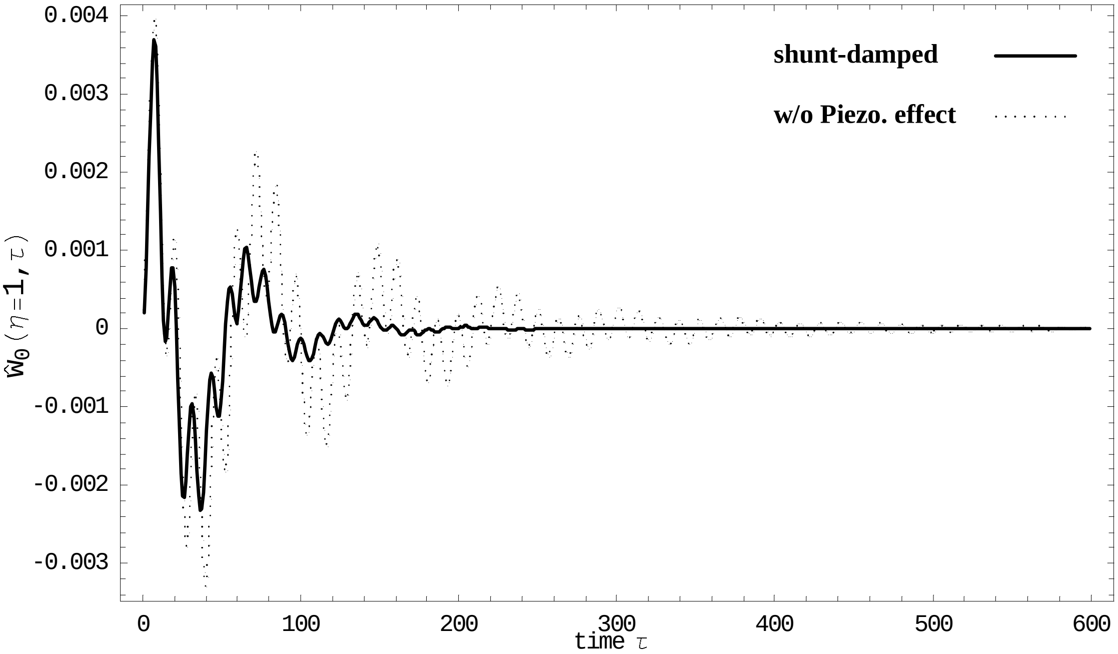

Figure 5.7: Effect of shunt-damping on the dynamic aeroelastic response $\hat{w}_0(\eta = 1, \tau)$ to a sonic boom ($\hat{P}_m = 0.001$, $M_{flight} = 0.6$, $\theta = 180^0$, $\tau_p = 2.5$, $C_c = 10^{-9}\,F$, $R_c = 10^{3.7}\,\Omega$).

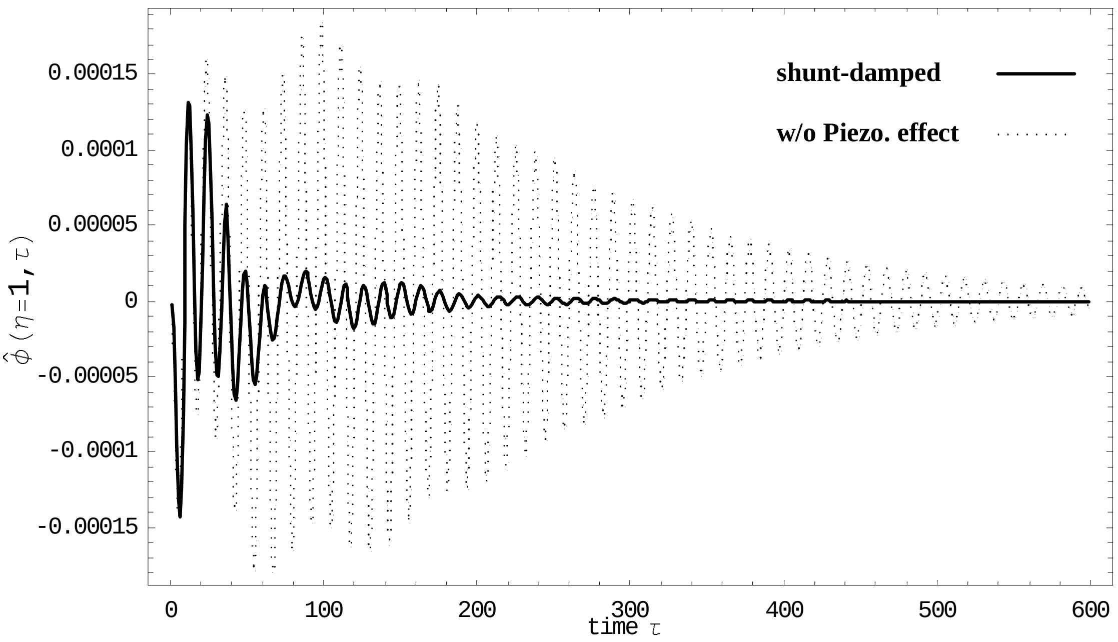

Figure 5.8: Effect of shunt-damping on the dynamic aeroelastic response $\hat{\phi}(\eta = 1, \tau)$ to a sonic boom ($\hat{P}_m = 0.001$, $M_{flight} = 0.6$, $\theta = 180^0$, $\tau_p = 2.5$, $C_c = 10^{-9}\,F$, $R_c = 10^{3.7}\,\Omega$).

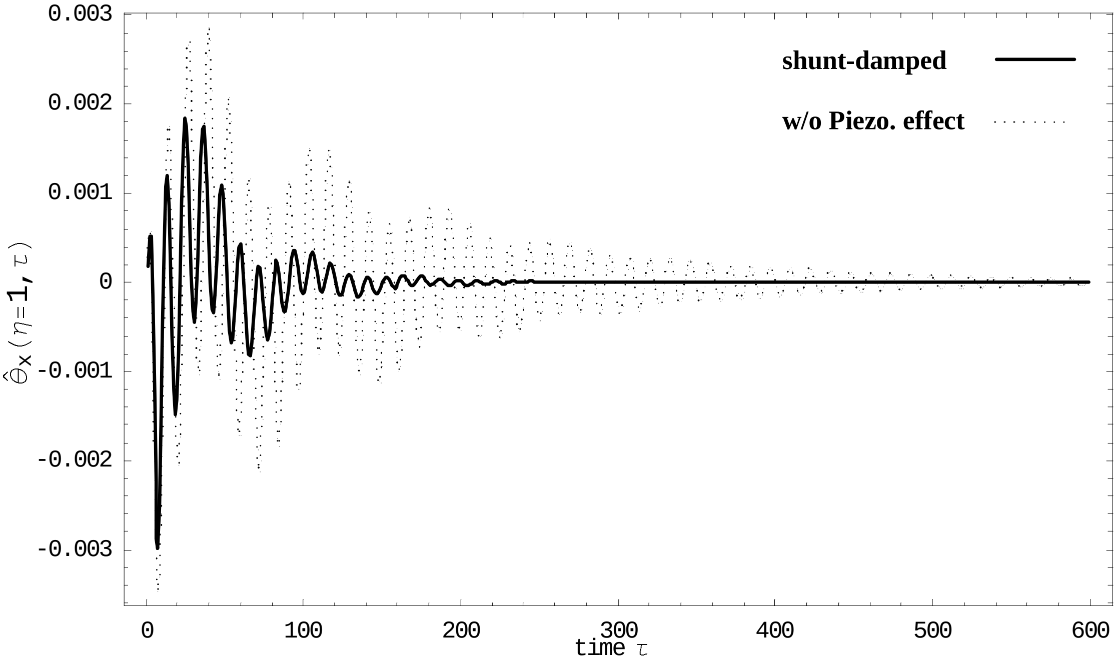

Figure 5.9: Effect of shunt-damping on the dynamic aeroelastic response $\hat{\theta}_x(\eta = 1, \tau)$ to a sonic boom ($\hat{P}_m = 0.001$, $M_{flight} = 0.6$, $\theta = 180^0$, $\tau_p = 2.5$, $C_c = 10^{-9}\,F$, $R_c = 10^{3.7}\,\Omega$).

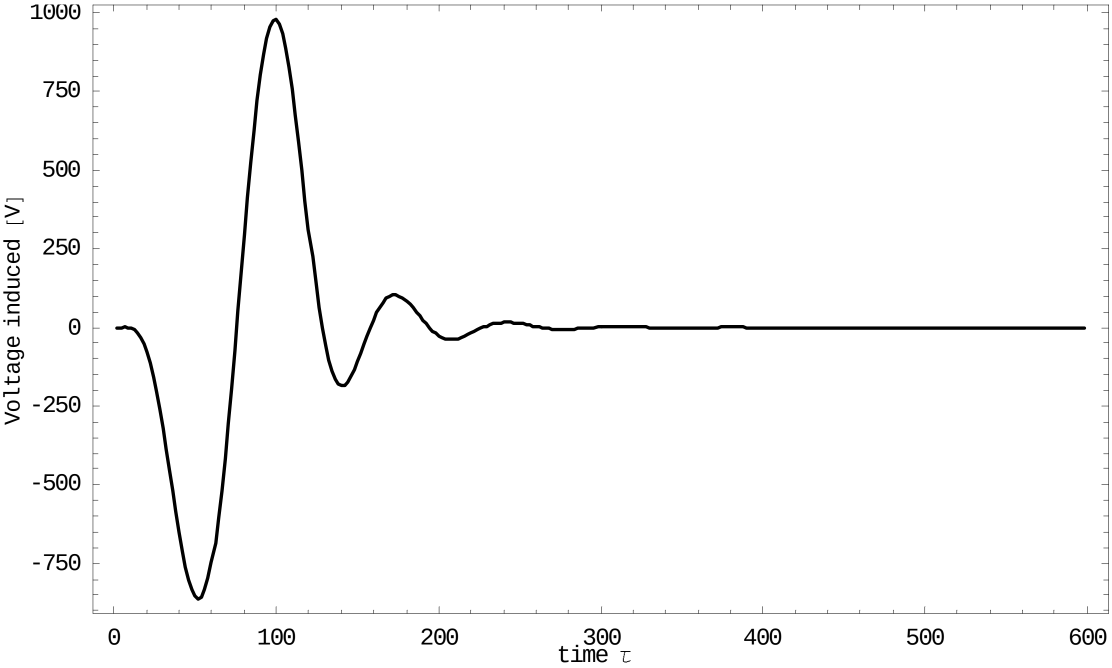

Figure 5.10: Elelctric voltage induced on the piezo. patch by the aeorelastic system subject to a 1-COSINE gust ($V_G = 5m/s$, $M_{flight} = 0.6$, $\theta = 180^0$, $\tau_p = 50$, $C_c = 10^{-9}\,F$, $R_c = 10^{3.7}\,\Omega$).

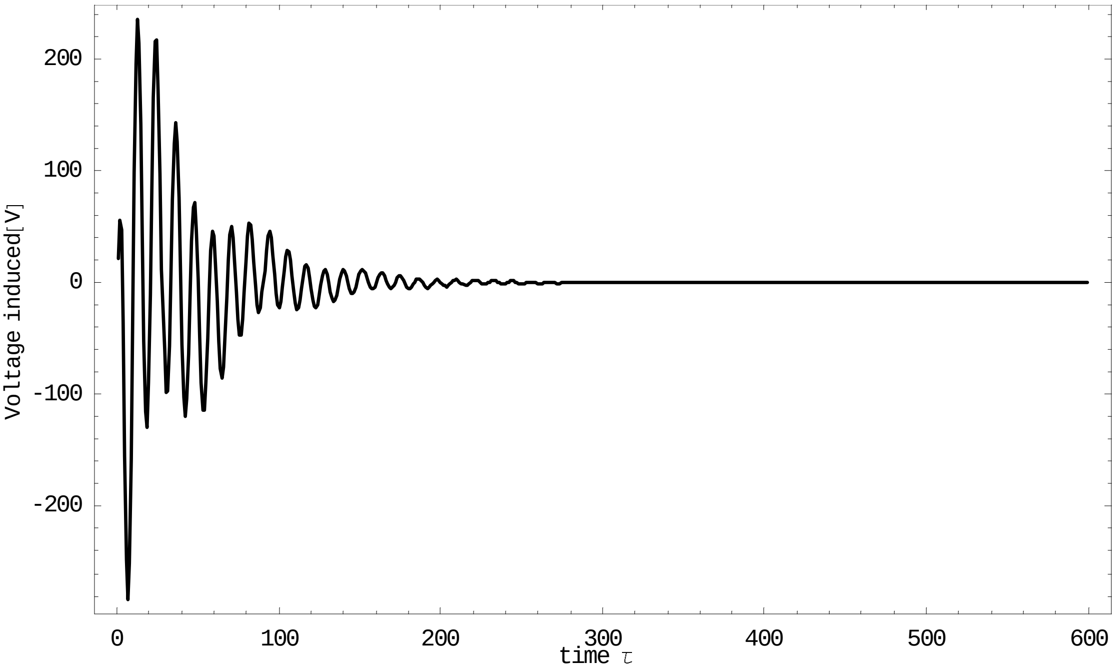

Figure 5.11: Elelctric voltage induced on the piezo. patch by aeorelastic system subject to a sonic boom ($\hat{P}_m = 0.001$, $M_{flight} = 0.6$, $\theta = 180^0$, $\tau_p = 2.5$, $C_c = 10^{-9}\,F$, $R_c = 10^{3.7}\,\Omega$).

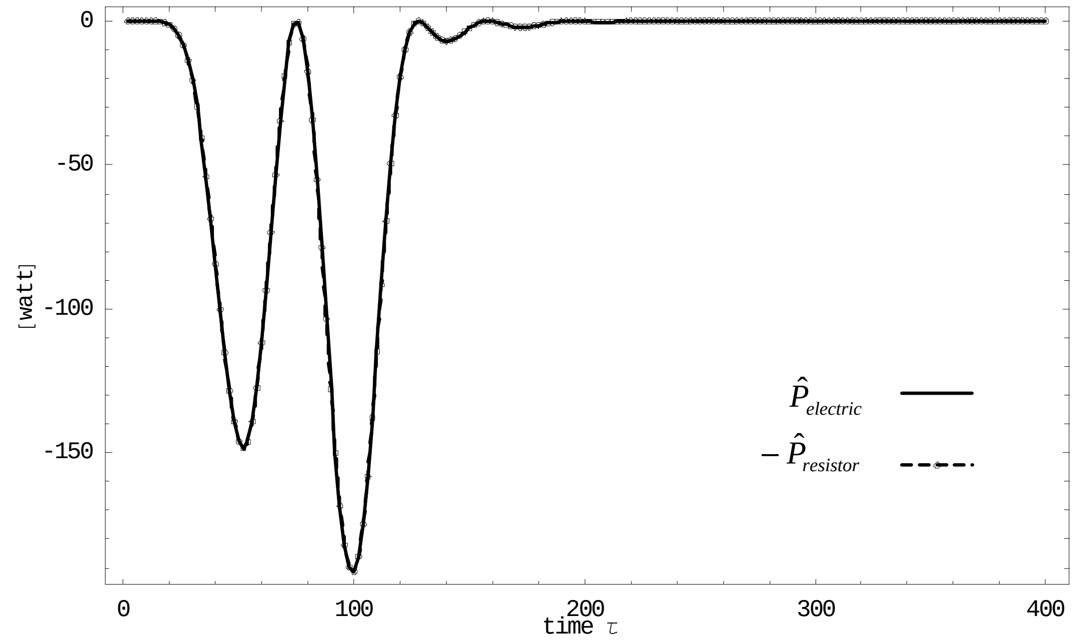

Figure 5.12: Comparison of the total energy converted and the energy dissipated when the aeroelastic system is subject to a 1-COSINE gust ($V_G = 5m/s$, $M_{flight} = 0.6$, $\theta = 180^0$, $\tau_p = 50$, $C_c = 10^{-9}\,F$, $R_c = 10^{3.7}\,\Omega$).

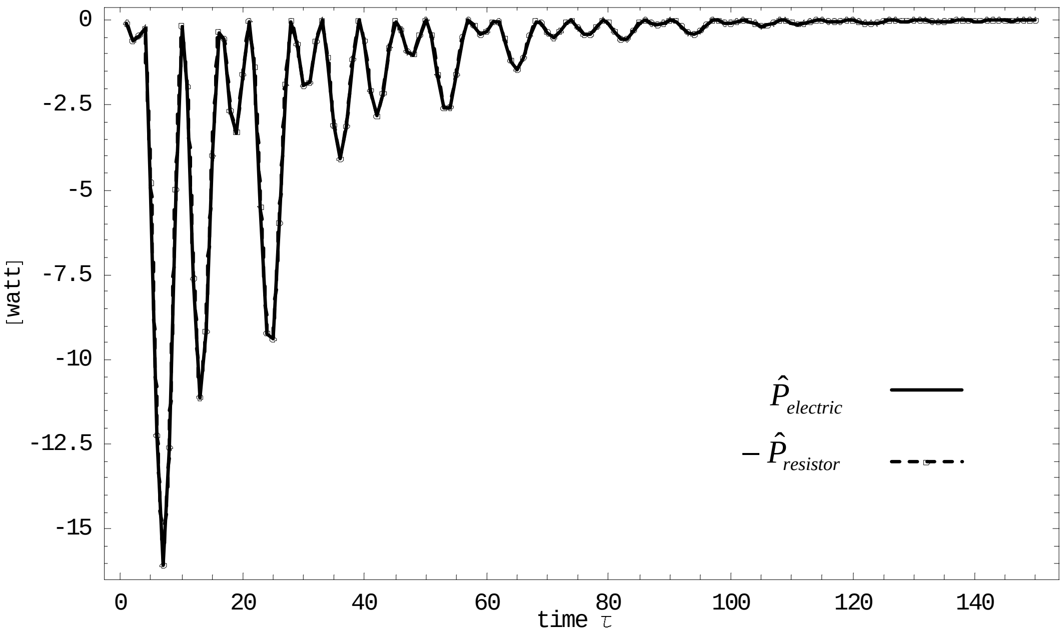

Figure 5.13: Comparison of the total energy converted and the energy dissipated when the aeroelastic system is subject to a sonic boom ($\hat{P}_m = 0.001$, $M_{flight} = 0.6$, $\theta = 180^0$, $\tau_p = 2.5$, $C_c = 10^{-9}\,F$, $R_c = 10^{3.7}\,\Omega$).

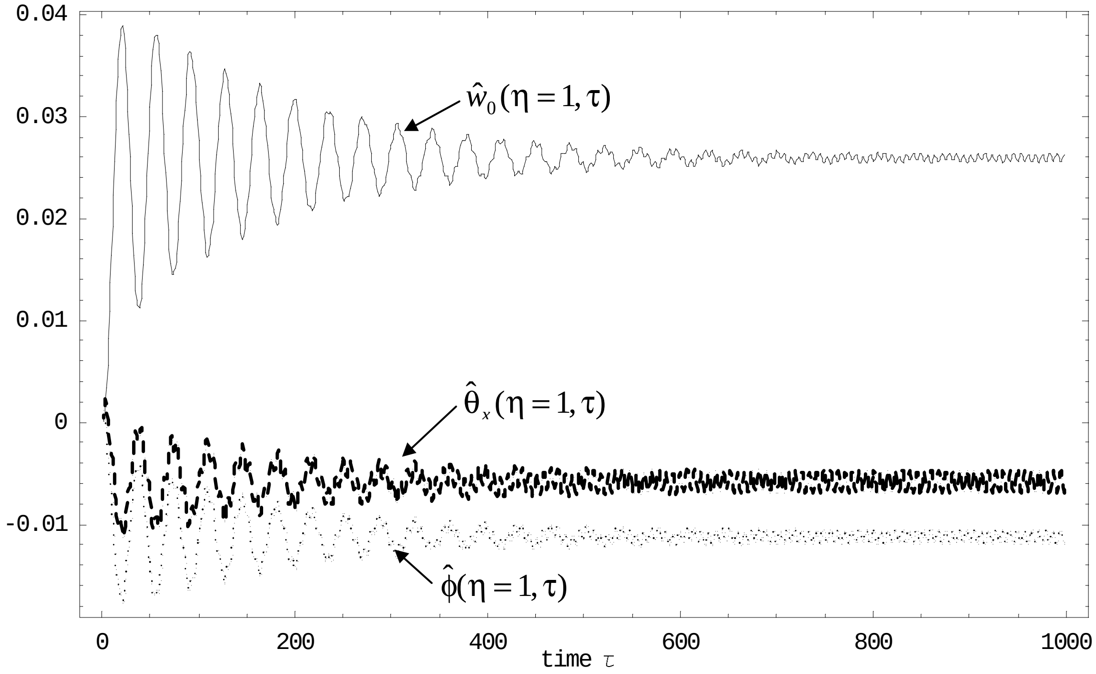

Figure 5.14: Shunt-damped aeroelastic response subject to a sharp-edged gust and featuring the onset of flutter induced by the shunt circuit ($\theta = 120^0$, $C_c = 10^{-9}\,F$, $R_c = 900\,\Omega$, $M_{flight} = 0.6$, $V_G = 10m/s$).

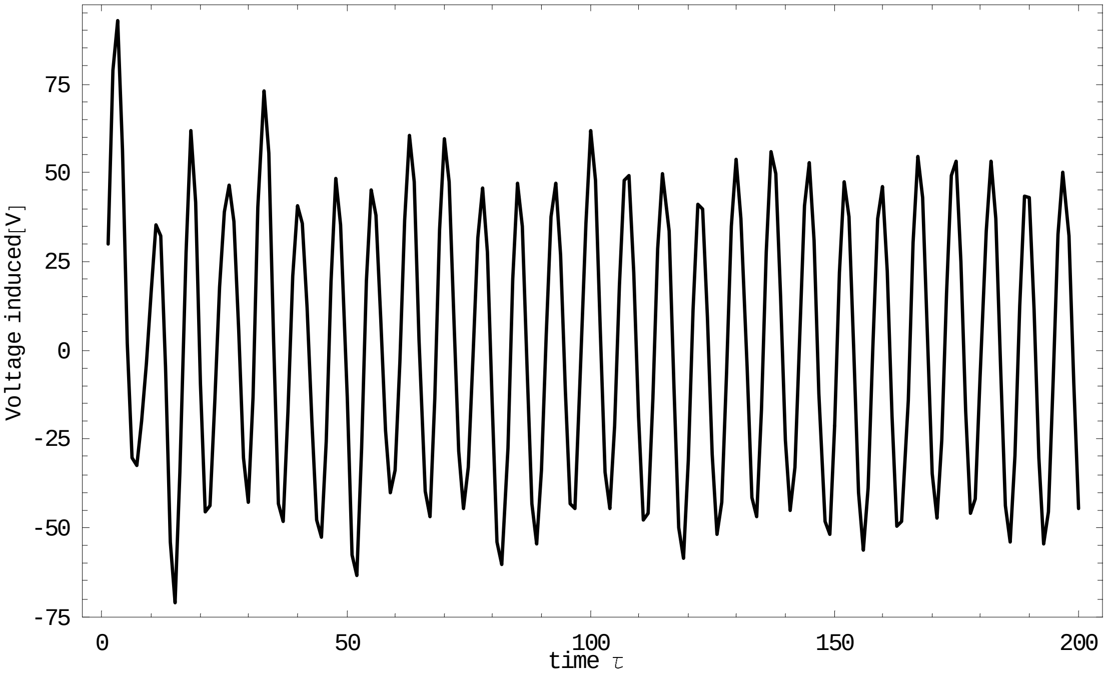

Figure 5.15: Induced voltage on the piezo. patch by the aeroelastic system in flutter ($\theta = 120^0$, $C_c = 10^{-9}\,F$, $R_c = 900\,\Omega$, $M_{flight} = 0.6$, $V_G = 10m/s$).

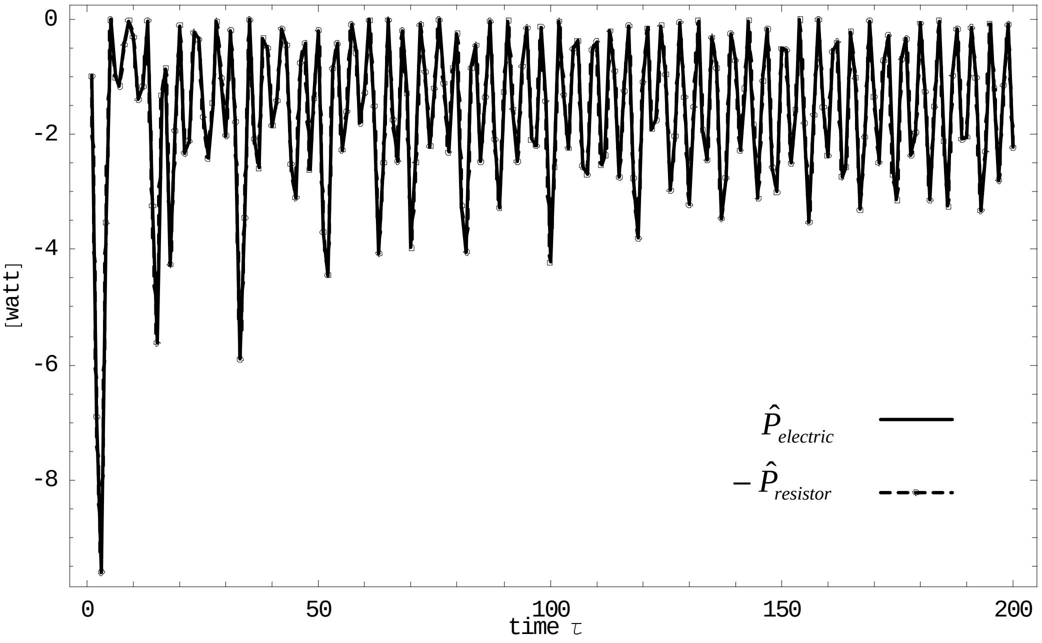

Figure 5.16: Comparison of total energy converted and the energy dissipated when the aeroelastic system is in flutter ($\theta = 120^0$, $C_c = 10^{-9}\,F$, $R_c = 900\,\Omega$, $M_{flight} = 0.6$, $V_G = 10m/s$).

Chapter 6

Conclusions and Recommendations

6.1 Summary

An efficient and comprehensive aeroelastic model based on an analytical anisotropic thin-walled beam model and the concept of indicial functions towards modeling unsteady aerodynamics has been proposed and formulated. The treatment of aeroelasticity of lifting surfaces modeled as anisotropic thin-walled beams appears, to the best of our knowledge, to be addressed for the *first* time in literature. The approach developed in this work facilitates the systematic investigation of aeroelastic static instability (divergence), dynamic instability (flutter), quality of dynamic aeroelastic response, active/passive controls within the aeroelastic tailoring environment and/or smart wing environment. It is also for the *first* time in literature that the investigation has broadly covered in a unified aerodynamic context of cases of incompressible, compressible subsonic, supersonic and hypersonic flight speeds.

Specifically, the major conclusions of this thesis include:

- In the structural part, a refined thin-walled beam model based on an existing thin-walled beam model has been developed and validated. It is clearly demonstrated that, by incorporating 3-D strain effect and the effect of non-uniformity of shear stiffness, the existing thin-walled beam model is capable of providing good and consistent correlation with the experimental results and the predictions by other models; It is the *first* study where this class of thin-walled beam model that has been extensively used towards the study of dynamic response, static aeroelasticity and structural control has been validated against the experimental and theoretical results obtained by other researchers.

- The significant influence of tailoring on the aeroelastic stability boundaries and response has been highlighted. To efficiently use tailoring may need optimization.
- Compressibility at high subsonic speeds has a significant influence on flutter and dynamic aeroelastic response of advanced aircraft wings, hence rendering the aeroelastic design of lifting surfaces and control system more intricate.
- Active control used in conjunction with elastic tailoring demonstrates promising capability towards augmenting the flutter speed, reducing the dynamic aeroelastic response intensity, it also demonstrates robustness over a relatively large range of variations (uncertainty) of major parameters. However, towards the actual implementation of control laws designed thereby, such issues as the limitation of allowable voltage on the piezoelectric actuators, electric power consumption may become serious constraints.
- Within the environment of aeroelastic tailoring, ply orientation has a fundamental influence on efficiency of the shunt damping (passive control). Damping augmentation via shunt circuit *does not* constitute a *conservative* approach towards vibration control on the aeroelastic system. Improper configuration of the shunt circuit may render the otherwise stable aeroelastic system unstable.

6.2 Recommendations for Future Work

The emergence of new composite materials and new structural concepts generates many significant challenges to the aeroelastic discipline. To solve the aeroelastic problems in this new environment will certainly have a profound influence on the safe aeroelastic design of flight vehicles. Listed in the following are only several issues that the author wish to address within a suitable thin-walled beam model in the near future:

- Modeling of damage in the composite aircraft wings and its influence on the aeroelastic instability and response;
- Efficient, yet robust control mechanism towards the aeroelastic vibration control that can address such important issues as: control input saturation, power consumption;
- Implication of geometric and material non-linearities on the characteristics of post-critical behavior of advanced aircraft wings.

VITA

Zhanming Qin was born on Dec. 26, 1969, P. R. China. He graduated from Xi'an Jiaotong University with B.S. in 1992, and from Beijing University of Aeronautics and Astronautics (BUAA) with M.S. in 1995. He then joined the faculty of BUAA as an assistant professor from May 1995 to Aug. 1996. Having completed two contracted research projects, he was enrolled as a Ph.D. student in Virginia Polytechnic Institute and State University at Aug. 1996, and completed his PhD degree at Sept. 2001. At that the same time, he also completed a M.S. degree in Computer Science at the same university.